5-2020

MONTE CARLO CHARACTERIZATION OF THE NUCLEAR RADIATION EMITTED BY THE SURFACE OF THE MOON

Fahad Zaman
University of Tennessee, fzaman@vols.utk.edu

To the Graduate Council:

I am submitting herewith a dissertation written by Fahad Zaman entitled "MONTE CARLO CHARACTERIZATION OF THE NUCLEAR RADIATION EMITTED BY THE SURFACE OF THE MOON." I have examined the final electronic copy of this dissertation for form and content and recommend that it be accepted in partial fulfillment of the requirements for the degree of Doctor of Philosophy, with a major in Nuclear Engineering.

Lawrence Townsend, Major Professor

We have read this dissertation and recommend its acceptance:

Lawrence Heilbronn, Jason Hayward, Thomas Handler

Accepted for the Council:

Dixie L. Thompson

Vice Provost and Dean of the Graduate School

(Original signatures are on file with official student records.)

MONTE CARLO CHARACTERIZATION OF THE NUCLEAR RADIATION EMITTED BY THE SURFACE OF THE MOON

A Dissertation Presented for the

Doctor of Philosophy

Degree

The University of Tennessee, Knoxville

Fahad Zaman
May 2020

DEDICATION

For my father, Abdullah, and my mother, Hana, for everything.

For my third-grade teacher, Sahar, for igniting my passion towards space.

ACKNOWLEDGEMENTS

I consider myself the luckiest for having Dr. Lawrence Townsend as my mentor and advisor. As a researcher and future mentor, I consider Dr. Townsend as my role model. Throughout my career as a nuclear engineering student from an undergraduate to a PhD student, he taught me countless skills that I could not have done this work without. Through his dedication, humility, and integrity, he helped in not only shaping me as a researcher, but also as person. He was always welcoming to my questions and inquiries in meetings, calls, and emails. I cannot recall a single incident throughout the five years I have been his student where he was not eagerly helping me, or a single meeting where I did not laugh at the stories he tells. However, as his last PhD student, I am still not sure whether I was the student he was waiting for before peacefully retiring, or the one who drove him to retirement.

Another person whom I could not show enough appreciation to is Dr. Wouter de Wet. He was not only a great friend, but also like a second mentor to me. He spent countless hours teaching me tons of skills in computation, transport codes, and research in general. He taught me how to use the HETC-HEDS code used in this dissertation. He also helped me in brainstorming many parts of this work.

In addition, there are four professors in the nuclear engineering department at the University of Tennessee that I would like to acknowledge in this dissertation: Dr. Lawrence Heilbronn, Dr. Jason Hayward, Dr. Ondrej Chvala, and Dr. Ronald Pevey. I will always be in debt to Dr. Heilbronn for helping me throughout my career as a nuclear engineer since I was an undergraduate student. He helped me in multiple aspects of this this dissertation. Dr. Hayward's determination on teaching me the research skills, from knowing how to have an overview of the literature to being precise in terminology, helped me greatly in this work. Dr. Chvala, to whom I

owe many thanks, was very kind in aiding me run the MCNP6 simulations using the cluster, which were at the core of this dissertation. Dr. Pevey was very generous in helping me with the Monte Carlo computational methods that were very important to this work.

I would like to thank my colleagues at the CRaTER team, especially Dr. Harlan Spence, Sonya Smith, Dr. Nathan Schwadron, Dr. Andrew Jordan, Dr. Jody Wilson, and Dr. Mark Looper, for their fruitful discussions and enormous support. I also thank my dearest friend Naser Burahmah for supporting me throughout my PhD career and helping me in running the PHITS simulations used in this work.

Finally, I would like to thank the National Aeronautic Space Administration (NASA) for funding this work through sub-award 11-1071 with the University of New Hampshire under the NASA CRaTER contract NNG11PA03C. I also thank Kuwait Foundation for the Advancement of Sciences (KFAS) for helping relief the remaining financial fees as a PhD student for three semesters through Abdulaziz H. Al Sagar Development Center at Kuwait Chamber of Commerce and Industry.

ABSTRACT

With neither a significant magnetic field nor an atmosphere, the Moon is exposed to a harsh radiation environment containing the galactic cosmic rays (GCRs) and the solar energetic particles (SEPs). When these particles strike the lunar surface, they create cascades of secondaries and eject "albedo" particles. The lunar albedo radiation consists of the scattered primary particles and secondaries created by the primary particles' interactions. This dissertation uses MCNP6, a general-purpose Monte Carlo transport code that is widely used in the nuclear physics and engineering communities, to study the behavior of the albedo particles coming off the lunar surface, primarily protons, neutrons, electrons, positrons, gamma rays, deuterons, tritium ions, helium-3 ions, and alpha particles, by generating the energy and angular distributions of each albedo species. The maximum depth reached by any particle leading to the creation of an albedo particle is also calculated as a function of albedo particle energy and emission angle. Also, to characterize the elemental composition of the lunar regolith, variations in albedo production are studied in hypothetical scenarios with increased abundances of hydrogen, oxygen, sodium, magnesium, aluminum, silicon, calcium, titanium, manganese, and iron. The results obtained from MCNP6 are compared to two transport codes frequently used in space radiation applications: PHITS and HETC-HEDS. Finally, the generated spectra are applied to the Cosmic Ray Telescope for the Effects of Radiation (CRaTER) instrument aboard the Lunar Reconnaissance Orbiter (LRO), which has been monitoring the lunar radiation environment since its launch in 2009, to characterize the observed albedo proton population as a function of spacecraft altitude and orientation, and to compare the measured absorbed doses to the ones modeled by MCNP6. The contribution of each albedo species to the total absorbed dose is also calculated to better understand the effects of lunar albedo radiation.

TABLE OF CONTENTS

LIST OF TABLES

LIST OF FIGURES

1. INTRODUCTION

It has been almost fifty years since the last human visit to the lunar surface, and since then, the absence of a practical motive made it difficult for humans to decide to go back to the Moon. However, it was feasible to send instruments to lunar orbit and the surface. Many scientific discoveries have been made since the Apollo missions that changed our understanding of the Moon, prominently the discovery of lunar hydrogen near the poles where the permanently shadowed regions (PSRs) reside. The presence of hydrogen on the Moon was proved using modified spectroscopy techniques (Saal et al., 2008), epithermal neutron detection (Feldman et al., 1998), infrared measurements (Pieters et al., 2009), and active detection methods (Colaprete et al., 2010). The first and only attempt to soft land a robotic spacecraft close to the poles has failed and thus, with the exception of the intentional crash landing of the Lunar Crater Observation and Sensing Satellite (LCROSS) equipment on the Lunar Reconnaissance Orbiter (LRO) in 2009 (Colaprete et al., 2010), the lunar poles remain unvisited so far. However, NASA plans to send humans back to the Moon through its Artemis program during this decade, with the lunar South Pole being the front-running landing location (Honeycutt et al., 2019).

One of the main challenges facing a long-term stay on the lunar surface is the harsh space radiation environment, which consists of galactic cosmic rays (GCRs), solar energetic particles (SEPs), and the unique source of radiation coming off the lunar surface. The Moon has neither a significant magnetic field nor an atmosphere, and thus GCRs and SEPs interact directly with the lunar surface, either scattering or creating cascades of secondaries which include neutrons, protons, photons, electrons, positrons, muons, pions, and light ions.

The exact nature of lunar surface radiation is not fully characterized, and it is thus important to study the behavior of the particles leaving the lunar surface. In addition to their importance from

a radiation protection standpoint, these particles could be utilized to locate lunar volatiles, mainly hydrogen, and to characterize the elemental composition of the lunar regolith by examining the differences in their spectra with increased or decreased abundances of different elements. Ideally, this could be achieved by taking various measurements in different locations on the lunar surface. Because we are presently unable to do this, we use Monte Carlo (MC) simulations, which with their unique advantages provide us with a valuable alternative. MC codes cover a wider range of energies and angles than could be attained in a laboratory.

This dissertation uses MCNP6 (Goorley et al., 2016), a general-purpose MC transport code widely used in the nuclear physics and engineering communities, to study the behavior of these particles coming off the lunar surface: protons, neutrons, electrons, positrons, gamma rays, deuterons, tritium ions, helium-3 ions, and alpha particles. MCNP6 will be described in further detail in the next chapters.

Definition of Terms

This work will refer to any particle leaving the lunar surface to free space as an "albedo" particle, a term used in previous (Armstrong, 1972) and recent (Looper et al., 2013; Spence et al., 2013; Schwadron et al., 2016; Mesick et al., 2018) papers concerned with radiation coming off the surface of the Moon. The albedo particles could be either reflected primary particles or secondaries created by the primary particles' interactions. The literature sometimes refers to albedo particles as the "leakage" of particles (Gasnault et al., 2000; McKinney et al., 2006; Prettyman et al., 2006; Ota et al., 2011). Also, since this work simulates a hypothetical regolith with increased content of hydrogen, it will refer to the regular hydrogen-free regolith as "dry" regolith, and the hydrogenated regolith as "wet" regolith. In addition, this dissertation will use the description "maximum production depth" to refer to the maximum depth reached by any particle leading to the creation

of an albedo particle and not necessarily to the production depth of the albedo particle itself. Finally, some papers in the literature multiply the GCR flux source term by the surface current per source particle and report the results as albedo "flux". Since the particles that leave the lunar surface to free space do not propagate or lose any energy in any material, and for simplicity purposes, the terms "flux" and "surface current" will be used interchangeably in this dissertation in describing the number of albedo particles per source particle, although the accurate term in all cases is "surface current".

Justification and Originality

There are several studies that used MC simulations to study the radiation coming off the lunar regolith. Many of these papers focused on albedo neutrons and gamma rays due to the presence of *in situ* measurements starting from the Apollo era, which provide an opportunity of comparing modeled results to measured data. These studies focused on benchmarking MC results against measurements, characterizing the elemental composition of the lunar regolith, and helping in gamma-ray and neutron spectroscopy. One study (McKinney et al., 2006) used MCNPX, a previous version of MCNP, to compare the modeled neutron density in the lunar regolith to measurements taken by the Apollo 17 astronauts. The neutron albedo flux, described as "neutron leakage flux" in their paper, was reported as a function of neutron energy from the thermal range up to 10 GeV. Another more sophisticated study (Prettyman et al., 2006) used MCNPX to study albedo gamma rays (described in their work as gamma ray leakage) coming off various regolith compositions taken from different Apollo and Luna samples. These were then compared to the data collected by the gamma ray spectrometer aboard the Lunar Prospector. Also, another paper (Yamashita et al., 2008) used Geant4, an open-source MC transport code, to estimate the production rates of albedo neutrons and photons and support the measurements to be collected by

SELENE, the Japanese lunar orbiter. It is worth noting that the source term used in these studies was normalized and did not include anything heavier than GCR helium. A recent study (Mesick et al., 2018) showed an agreement between Geant4 and MCNP6 albedo neutron flux spectra. Other MC codes, like FLUKA (De Angelis et al., 2007) and PHITS (Ota et al., 2011), were also used to generate albedo neutron spectra. In addition, since the launch of the Cosmic Ray Telescope for the Effects of Radiation (CRaTER) instrument aboard the LRO spacecraft (Spence et al., 2010), there has been an increased interest in understanding the behavior of albedo protons. A paper with the best comparison to this work in its collective nature (Looper et al., 2013) used Geant4 to model the energy and angular distribution of multiple albedo particles emitted by the lunar surface, including protons, and compared the resulting energy-deposit spectra with measurements observed by the CRaTER instrument.

This dissertation aims to extend on the previous work by using MCNP6, which has its own enhancements in high energy physics, to create the spectra of multiple albedo species, both neutral and charged, as a function of angle, energy, and depth, for various scenarios with different elemental compositions. This effort should provide a better understanding of the nature of lunar radiation, help in characterizing the chemical composition of the lunar regolith, create a benchmarking database for other codes, and assist both previous and future missions in data analyses. PHITS and HETC-HEDS, MC codes that will be described in further detail in later chapters, are used to provide comparisons between the results of some albedo spectra using similar geometries and identical source terms. Finally, the results will be applied to the CRaTER instrument which is currently orbiting the Moon. The CRaTER instrument's field of view as a function of altitude and orientation will be modeled using MCNP6. Then, both the angular and energy distributions will be incorporated into an MCNP6 model of the CRaTER instrument. These

steps will determine what the CRaTER instrument should be observing at various altitudes and orientations. They will also provide a comparison between the absorbed doses calculated by MCNP6 and the ones measured by the CRaTER instrument.

Outline of Dissertation

This dissertation is divided into eight chapters. The first chapter, this chapter, gives a background and an overview of the literature and the goals of this dissertation. Chapter 2 explains the methodology followed in this work, mainly the computational methods. It provides the details of the source term, geometries, material composition, tallies, and scenarios used in the MC simulations, along with all assumptions and justifications. It also describes each MC transport code used in this work in further detail. Chapters 3-7 present and discuss the results of the simulations. Chapter 3 illustrates the results of albedo particles from dry regolith, while Chapter 4 is concerned with the results from wet regolith. Chapter 5 shows the results of albedo particle emissions for nine different scenarios, each with a modeled regolith that has an increased content of one major lunar element, to help characterize the composition of lunar regolith by studying the possible changes in albedo behavior in each scenario. These major lunar elements are oxygen, sodium, magnesium, aluminum, silicon, calcium, titanium, manganese, and iron. Chapter 6 compares the albedo results of MCNP6 with PHITS and HETC-HEDS with similar geometries and identical source terms. Chapter 7 shows the results of the CRaTER instrument's field of view and the resulting modeled observations for different altitudes and orientations. It also compares MCNP6 modeled absorbed dose rates to the ones measured by the CRaTER instrument. Finally, Chapter 8 gives the conclusions and recommendations for future work.

2. COMPUTATIONAL METHODS

The main transport code used to generate the results in this work is MCNP6, while PHITS and HETC-HEDS transport codes were used primarily for data comparisons. Each of these codes is described in this chapter. In general, MC codes require the following inputs to run: a geometry, a source term, and material specification.

2.1 MCNP6

The Monte Carlo N-Particle (MCNP) code is a general-purpose MC radiation transport code developed by Los Alamos National Laboratory. MCNP version 6.1, which merged the capabilities of MCNPX and MCNP5, was used for the MCNP part of the simulations in this work. This version has its own enhancements in physics models for high energy applications, and thus provides an excellent opportunity to study the space radiation environment, especially since the flux of GCR ions peak at around ~1 GeV/n. *Goorley et al. [2016]* provides a detailed description of the features of the version of MCNP used in this work.

2.1.1 Simulations

The MCNP6 simulations in this work were divided into three different geometries. First, there are the sophisticated runs that model the entire lunar surface to produce the albedo spectra as a function of particle type, energy, emission angle, and maximum production depth, for different regolith compositions. These runs require a substantial amount of time, need a large number of processing units, and create the main product of this dissertation. Second, there are the runs that model the energy deposited, or absorbed dose, in the detectors of the CRaTER instrument from GCR and albedo radiation for LRO altitudes of 50 km. This could be done ideally by adding a model of the CRaTER instrument at the desired altitude to the existing MCNP6 model of the lunar

surface. However, since the CRaTER instrument is extremely small relative to the size of the Moon, combining the two geometries lead to undesirable statistics when tallying the albedo particles reaching the CRaTER instrument. Thus, to simulate the dose at the detectors of the CRaTER instrument, an additional sphere was added to the sophisticated runs at an altitude of 50 km to determine the angle and energy of albedo particles as they strike the CRaTER instrument. These spectra were then normalized and used as a directed source term in separate relatively quicker runs simulating only the CRaTER instrument. The CRaTER instrument will be described in further detail in subsection 2.1.3. Finally, there are the runs that model the "albedo" field of view of the CRaTER instrument for different altitudes, orientations, and detector coincidences. Here, both the Moon and the CRaTER instrument are included in the geometry. However, these runs do not include any material and are relatively faster to run. Here, an arbitrary isotropic source term is placed on one of the detectors of the CRaTER instrument; then, the angle at which a particle strikes the lunar surface from the CRaTER instrument is tallied. This backtracks the probability distribution of an albedo particle reaching the CRaTER instrument from the lunar surface as a function of emitted angle and detector coincidence. The results of this part are applied to the albedo spectra to get an estimation of the distribution of the albedo particles reaching the CRaTER instrument. To sum up, the first type of runs generates the albedo spectra of each studied particle emitted by the lunar surface. The second type of runs studies the absorbed dose in the CRaTER instrument from GCR and albedo particles. The third type of runs calculates the probability of any particle leaving the lunar surface and reaching multiple detectors aboard the CRaTER instrument, which gives an estimate of the albedo particles reaching the detectors for different altitudes and orientations.

2.1.2 Albedo Spectra

The geometry used to generate the albedo spectra consists of a sphere with a radius of 1,737 km, which is approximately the volumetric mean radius of the Moon. Here, the surface roughness of the Moon was assumed to be smoothed out at satellite altitudes, and thus lunar craters and other topographic features were not taken into consideration when building the lunar geometry. The elemental composition used to represent the lunar regolith depends on the scenario studied. The basic scenario of a dry regolith uses the average composition of 10 different lunar soil samples obtained from *Lawrence et al. [2006]*. These samples were chosen because they cover all the locations visited by the sample return missions. The elemental composition used in the dry regolith scenario is listed in Table 2.1, which contains samples taken from the six Apollo missions, the three Luna sample return missions, and ferroan anorthosite (FAN), a material widely used in MC simulations to represent the lunar regolith (Gasnault et al., 2000; Yamashita et al., 2008; Looper et al., 2013; Crites et al. 2013). Since the average composition of all ten samples was used in the simulations, the lunar elemental composition was assumed to be homogenous with no local or regional variations in all scenarios and simulations. It is worth noting that none of the samples listed in Table 2.1 contain hydrogen. The absence of significant concentrations of hydrogen in the Apollo and Luna samples is due to the fact that none of the landing locations were near the PSRs, where the presence of relatively higher concentrations of hydrogen is expected.

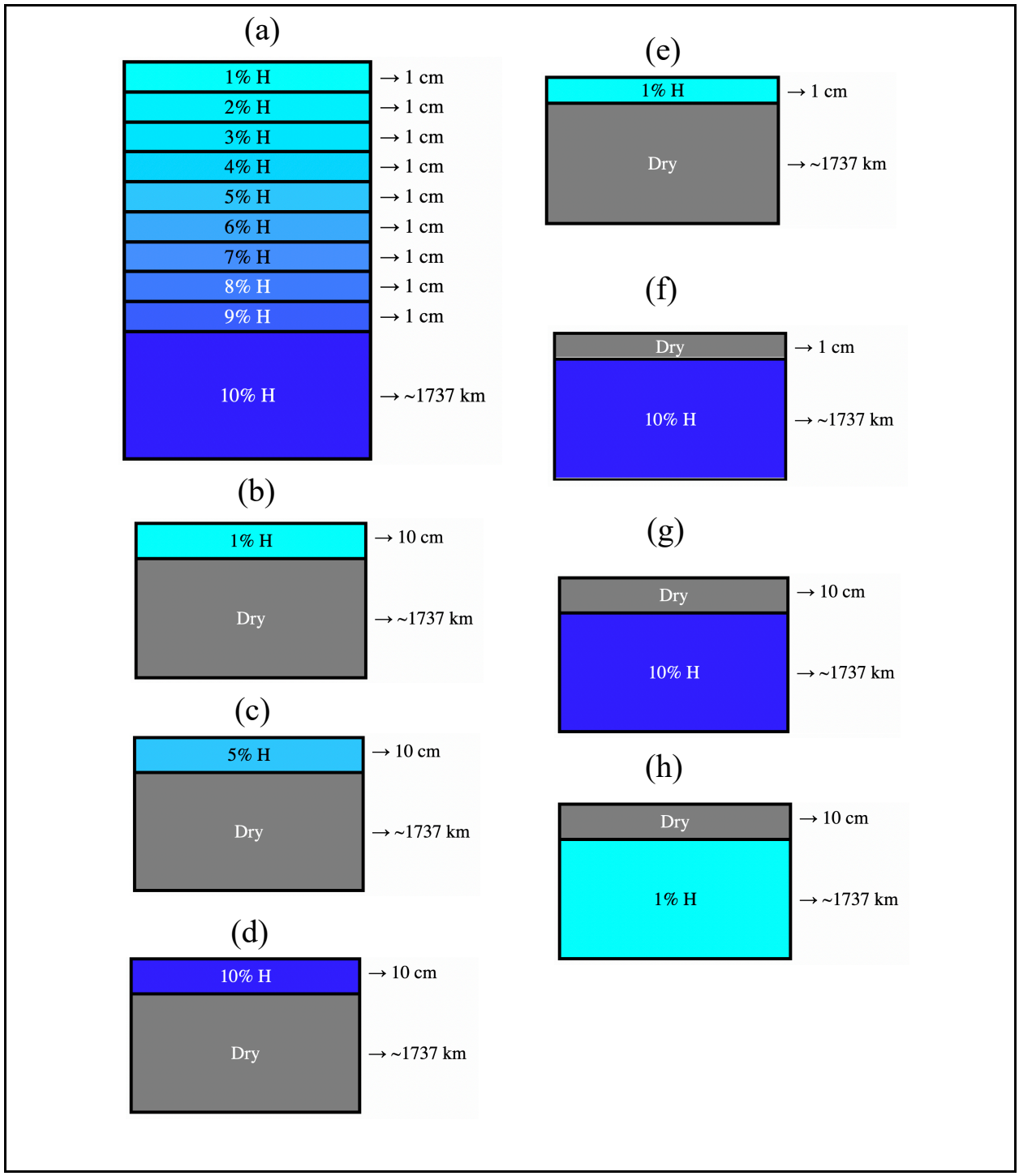

Figure 2.1 The wet case scenarios: (a) Fully wet regolith where hydrogen content increases with depth, (b) top wet 10-cm layer with 1% hydrogen, (c) top wet 10-cm layer with 5% hydrogen, (d) top wet 10-cm layer with 10% hydrogen, (e) top wet 1-cm layer with 1% hydrogen, (f) top dry 1-cm layer above a wet layer with 10% hydrogen, (g) top dry 10-cm layer above a wet layer with 10% hydrogen, and (h) top dry 10-cm layer above a wet layer with 1% hydrogen. Note that these drawings are not scale and their rectangular shape is not representative of the spherical model used. All percentages are in weight fractions.

Table 2.1. The elemental composition of the dry lunar regolith taken from six Apollo samples, three Luna samples, and FAN expressed in weight fraction. The average composition was used in MCNP6 the runs (Lawrence et al., 2006).

Element	A11	A12	A14	A15	A16	A17	L16	L20	L24	FAN	Average Composition
O	0.4252	0.4326	0.4527	0.4331	0.4599	0.4426	0.4203	0.4401	0.4237	0.456	0.4367
Na	0.0035	0.003	0.0052	0.003	0.0035	0.0032	0.0026	0.0029	0.0021	0.0045	0.0032
Mg	0.0478	0.0628	0.0567	0.066	0.0362	0.06	0.0529	0.0584	0.0595	0.0051	0.0556
Al	0.0666	0.0642	0.0921	0.0758	0.1442	0.1002	0.083	0.1204	0.0633	0.1763	0.0900
Si	0.1963	0.216	0.2248	0.2206	0.2098	0.2079	0.2074	0.2113	0.2122	0.2066	0.2118
Ca	0.0839	0.0704	0.0765	0.0748	0.1041	0.0878	0.0822	0.1051	0.0791	0.1359	0.0849
Ti	0.0476	0.0156	0.0102	0.0088	0.0032	0.017	0.0198	0.003	0.0062	0.0008	0.0146
Mn	0.0016	0.0016	0.001	0.0015	0.0005	0.0012	0.0016	0.0008	0.0019	0	0.0013
Fe	0.1275	0.1336	0.0808	0.1164	0.0387	0.08	0.1302	0.058	0.152	0.0148	0.1019

Since the exact nature, distribution, location, and depth of lunar hydrogen is not fully understood, this work studies the changes in lunar albedo for different wet regolith scenarios that vary in the depth, vertical location, and concentration of hydrogen. Different concentrations of hydrogen are added by weight fraction to the modeled dry regolith. The following wet regolith scenarios have been simulated in this work:

1- A fully wet regolith where hydrogen concentration increases with depth. The first top 1-cm layer contains 1% hydrogen, and each subsequent 1-cm layer contains an additional 1% hydrogen until reaching a saturation of 10% hydrogen below 9 cm of regolith. This scenario was chosen under the assumption that hydrogen evaporates faster at shallower depths.

2- A top wet 1-cm layer with 1% hydrogen above a fully dry regolith.

3- A top wet 10-cm layer with 1% hydrogen above a fully dry regolith.

4- A top wet 10-cm layer with 5% hydrogen above a fully dry regolith.

5- A top wet 10-cm layer with 10% hydrogen above a fully dry regolith.

6- A top dry 1-cm layer above a wet regolith with 1% hydrogen.

7- A top dry 10-cm layer above a wet regolith with 1% hydrogen.

8- A top dry 10-cm layer above a wet regolith with 10% hydrogen.

Table 2.2 lists the elemental composition used in the wet regolith scenario and Figure 2.1 shows a schematic of each wet scenario.

Table 2.2. The elemental compositions of different wet regolith layers expressed in weight fraction.

Element	Dry	10% H	9% H	8% H	7% H	6% H	5% H	4% H	3% H	2% H	1% H
H		0.1	0.09	0.08	0.07	0.06	0.05	0.04	0.03	0.02	0.01
O	0.438	0.393	0.397	0.402	0.406	0.41	0.415	0.419	0.424	0.428	0.432
Na	0.003	0.003	0.003	0.003	0.003	0.003	0.003	0.003	0.003	0.003	0.003
Mg	0.056	0.05	0.051	0.051	0.052	0.052	0.053	0.053	0.054	0.054	0.055
Al	0.09	0.081	0.082	0.083	0.084	0.085	0.085	0.086	0.087	0.088	0.089
Si	0.212	0.191	0.193	0.195	0.197	0.199	0.201	0.203	0.205	0.208	0.21
Ca	0.085	0.076	0.077	0.078	0.079	0.08	0.081	0.081	0.082	0.083	0.084
Ti	0.015	0.013	0.013	0.013	0.014	0.014	0.014	0.014	0.014	0.014	0.014
Mn	0.001	0.001	0.001	0.001	0.001	0.001	0.001	0.001	0.001	0.001	0.001
Fe	0.102	0.092	0.093	0.094	0.095	0.096	0.097	0.098	0.099	0.1	0.101

Also, to characterize the variations in lunar albedo with increased concentrations of the major lunar elements, this work tests several hypothetical scenarios with increased content of oxygen, sodium, magnesium, aluminum, silicon, calcium, titanium, and iron. Each of these elements had an increase of 10% by weight fraction added to average weight fraction of the dry regolith. For example, the average weight fraction of iron is ~10% in a dry regolith and ~20% in the hypothetical scenario with increased content of iron. Table 2.3 shows the elemental compositions used in each of these scenarios.

Table 2.3. The elemental compositions of the scenarios studying the increased concentrations of the major lunar elements expressed in weight fraction. Numbers in bold represent the fraction of the enriched element.

Element	Dry	+10% O	+10% Na	+10% Mg	+10% Al	+10% Si	+10% Ca	+10% Ti	+10% Mn	+10% Fe
O	0.438	**0.538**	0.393	0.39	0.389	0.381	0.389	0.392	0.393	0.388
Na	0.003	0.003	**0.103**	0.003	0.003	0.003	0.003	0.003	0.003	0.003
Mg	0.056	0.046	0.05	**0.156**	0.049	0.049	0.05	0.05	0.05	0.049
Al	0.09	0.074	0.081	0.08	**0.19**	0.079	0.08	0.081	0.081	0.08
Si	0.212	0.174	0.191	0.189	0.189	**0.312**	0.189	0.19	0.191	0.188
Ca	0.085	0.07	0.076	0.076	0.076	0.074	**0.185**	0.076	0.076	0.075
Ti	0.015	0.012	0.013	0.013	0.013	0.013	0.013	**0.115**	0.013	0.013
Mn	0.001	0.001	0.001	0.001	0.001	0.001	0.001	0.001	**0.101**	0.001
Fe	0.102	0.084	0.092	0.091	0.091	0.089	0.091	0.092	0.092	**0.202**

For all simulated scenarios, an isotropic GCR spectrum for a period of a solar minimum activity was chosen as a source term. During solar minimum, the SEP flux decreases while the GCR ion flux peaks (Townsend et al, 1990, 1992). One of the unique features of this work is that it includes a large source term covering multiple GCR ions (not only protons and alphas) starting from GCR hydrogen and going up to GCR nickel. To generate the source term, the Badhwar-O'Neill 2014 Galactic Cosmic Ray Flux Model was used for a solar modulation parameter of 500 MV (Slaba et al., 2014). Figure 2.2 shows the energy spectrum of the source term used for all the simulations that study the spectra of albedo particles emitted by the lunar surface.

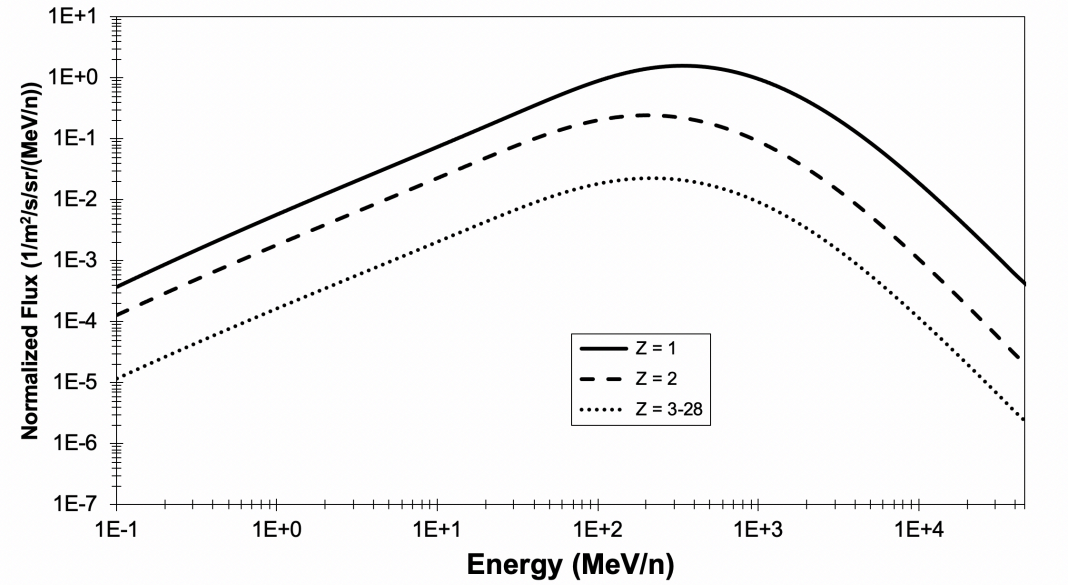

Figure 2.2. The GCR source term used in all simulations. It was generated using the Galactic Cosmic Ray Flux Model for a solar modulation parameter of 500 MV (Slaba et al., 2014).

The following particles were transported in all runs: photons, electrons, positrons, pions (positive, negative, and neutral), muons (positive and negative), neutrons, protons, deuterons, tritium ions, helium-3 ions, alphas, and heavy ions. To account for computation times and resources, a lower energy cutoff of 10 keV was set for all particles. This means that all the results are reported for energies above 10 keV and neither thermal nor the full range of epithermal neutrons is included. Also, the recommended default physics models were turned on up to 10 GeV. The F1 tally was chosen to report albedo spectra as current integrated over a surface in units of particles per source particle. Using the energy and cosine cards in MCNP6, the current was reported as a function of emitted particle energy and angle off the local normal vector of the lunar sphere. The cell flagging card was used to determine the maximum depth of any process leading to the albedo particle flagged. This helps in determining the depth that passive spectroscopy instruments probe in the regolith when characterizing the lunar composition. To achieve this,

additional layers of spheres were added at different depths below the surface. If an albedo particle or its any of its predecessors crosses any of these inner layers, it will be reported as flagged from the corresponding surface. The double counting was accounted for in a separate calculation. The results will thus be also reported as a function of maximum production depth. Finally, the density of the lunar surface varies between 0.89 g/cm^3 (Carrier et al., 1973) up to ~3 g/cm^3 (McKay et al., 1991; Yamashita et al., 2008). The density chosen for all runs in this work is 1.5 g/cm^3. The thickness of the geometry, which is in hundreds of kilometers, is assumed to cover all the nuclear interactions and secondary particles production for the chosen density. Varying the density by 33% did not show significant differences in lunar albedo spectra. Also, no differences were observed when reporting the depth results in unit of g/cm^2 for different densities.

2.1.3 The CRaTER Instrument

The CRaTER instrument was launched into lunar orbit aboard the LRO in 2009 to study the radiation environment near the lunar surface. Since then its data have been used by many studies (Case et al., 2010; Looper et al., 2013; Schwadron et al., 2016, 2018; Spence et al., 2013; Wilson et al., 2012). It consists of 3 pairs of silicon detectors, separated by two volumes of tissue equivalent plastic (TEP) with different thicknesses as shown in Figure 2.3. Each pair consists of a thin odd-numbered silicon detector and a thick even-numbered silicon detector. The thin detectors are ~150 micron thick and operate with high gain amplifiers, making them sensitive to a low linear energy transfer (LET) ranging between 0.09 and 85 keV/μm. The thick detectors are ~1000 micron thick, operate with low gain amplifiers, and are sensitive to a relatively higher LET ranging between 2.3 keV/μm to 2.2 MeV/μm. The CRaTER instrument has two ends, one facing deep space, and the other facing the lunar surface. Starting from the deep space end lies the D1/D2 detector set, followed by a TEP section ~54 mm thick, the D3/D4 detector set, another TEP section

~27 mm thick, and the D5/D6 detector set facing the lunar surface. Each detector has a radius of 1.75 cm, while the TEP volumes vary very slightly from that radius. *Spence et al. [2010]* gives a full description of the CRaTER instrument.

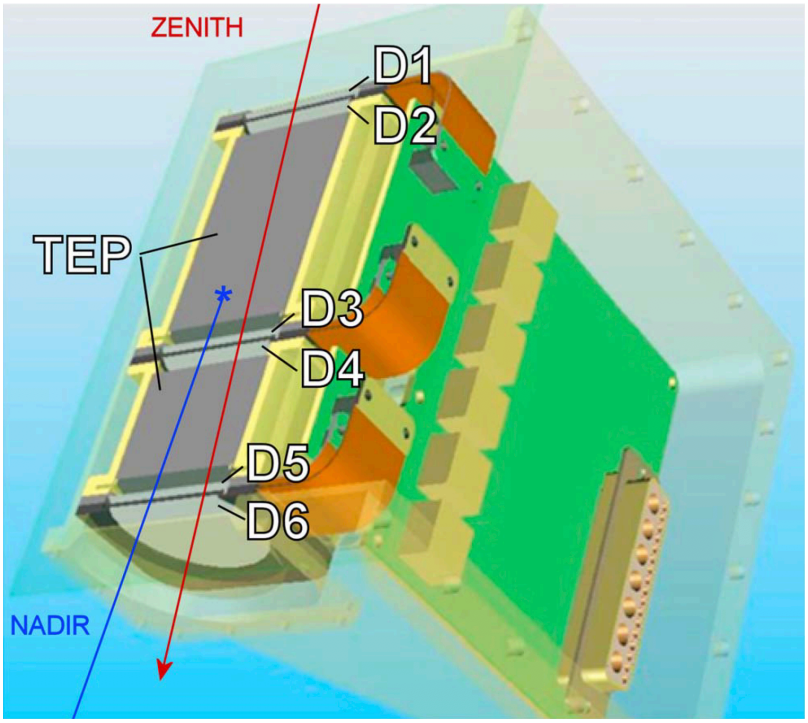

Figure 2.3. Transparent layout of the CRaTER instrument obtained from *Spence et al. [2010]* and labeled by *Wilson et al. [2012]*.

The CRaTER instrument is capable of differentiating between different GCR particles and albedo protons by examining the ratio of the unequal energies deposited in different sets of detectors. For example, when a GCR proton enters from deep space and passes through multiple sets of detectors starting from the D1/D2 set, it registers a higher LET in the lower sets of detectors than the upper ones due to the energy lost in the TEP volumes. Each GCR ion has a distinctive energy deposit ratio in different sets of detectors. On the other hand, when an albedo proton passes

through multiple sets of detectors, it registers a higher LET in the upper sets of detectors. Plotting a histogram of the energy deposited in D4 versus energy deposited in D6 for D4+D6 coincidence events shows a distinctive clustering from GCR ions and albedo protons as illustrated in Figure 2.4 (Wilson et al., 2012).

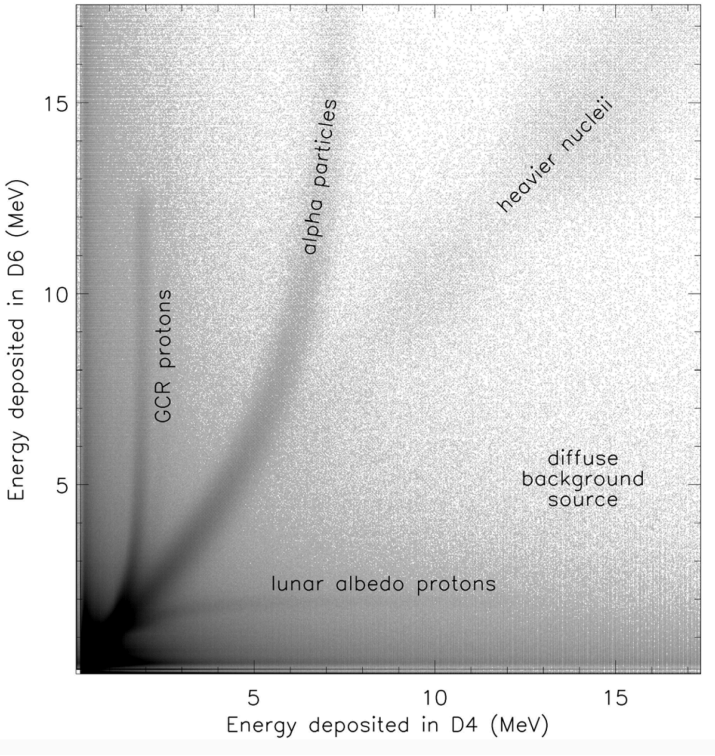

Figure 2.4. Two-dimensional histogram of coincidences triggering D4 and D6 detectors measured by the CRaTER instrument obtained from *Wilson et al. [2012]*.

2.1.4 The CRaTER Instrument Field of View

Since coincidence detections are important aspects of the CRaTER instrument dataset, determining the instrument's field of view of as a function of detector coincidence, altitude, and orientation is necessary. To achieve this, MCNP6 was used with a geometry consisting of the CRaTER instrument and a sphere having the lunar radius. The CRaTER instrument MCNP6 model

consists of a stack of cylinders with radii of 1.75 cm and the exact thicknesses of the detectors and TEP volumes. Because the altitude and the orientation of the CRaTER instrument vary throughout the mission, four different scenarios were examined:

1- The CRaTER instrument model placed 50 km away from the lunar surface facing the nadir.
2- The CRaTER instrument model placed 50 km away from the lunar surface facing the limb.
3- The CRaTER instrument model placed 180 km away from the lunar surface facing the nadir.
4- The CRaTER instrument model placed 180 km away from the lunar surface facing the limb.

Due their complicated geometry, the CRaTER instrument box and the LRO spacecraft were not included in MCNP6 model. Also, since these runs are purely geometric, the simulations in this part did not include any material. To determine the field of view, an arbitrary isotropic disk source was placed at the bottom of either D2 or D4 detector. Then, a surface flagging card was used to flag only the particles passing through the D6 detector. Finally, the F1 tally and the cosine card were used to determine the probability of a particle reaching the lunar surface as a function of striking angle.

2.1.5 The CRaTER Instrument Energy Deposit

The CRaTER instrument is capable of measuring absorbed dose in different sets of detectors near the lunar surface coming from deep space and from the lunar surface. This provides an opportunity to compare the simulated results of energy deposited to the observed measurements. To determine the energy deposited in the modeled CRaTER detector, a geometry consisting of

only the CRaTER instrument was used in the simulations. However, the lunar surface was not included in these runs, and the material composition of different detector elements were added. In addition, a 1.5-cm thick aluminum coat was added around the CRaTER instrument to simulate the surrounding instrument shielding. Table 2.4 lists the components and elemental compositions used in the modeled CRaTER geometry. Multiple source terms were used to determine the contribution of GCR ions and each albedo species to the total absorbed dose. Because the lunar surface provides shielding from GCR radiation, the GCR source term used in previous parts was adjusted to account only for the radiation reaching the detector at an altitude of 50 km. Also, the source term of each albedo species was run separately after being normalized from the previously calculated spectra at an altitude of 50 km. The F6 tally was used to determine the energy deposited in different detectors.

Table 2.4. The components used in the MCNP6 model of the CRaTER instrument. In MCNP6, all of these components were modeled as cylinders in the geometries with a radius of 1.75 cm. A void cylinder is added between each of these components. The thicknesses of the void volumes are added to the cumulative thickness.

Component	Thickness (mm)	Cumulative Thickness (mm)	Elemental Composition (weight fraction)
Top Aluminum Shield	0.8128	0.8128	~100% Al
D1 Detector	0.148	3.3238	100% Si
D2 Detector	1	7.6838	100% Si
Upper TEP	53.967	65.5938	10.33% H, 76.93% C, 3.3% N, 6.94% O, 1.14% F, & 1.37% Ca
D3 Detector	0.149	69.2968	100% Si
D4 Detector	1	73.8648	100% Si
Lower TEP	26.98	112.7448	10.33% H, 76.93% C, 3.3% N, 6.94% O, 1.14% F, & 1.37% Ca
D5 Detector	0.149	124.7938	100% Si
D6 Detector	1	128.8538	100% Si
Bottom Aluminum Shield	0.81026	132.026	~100% Al

2.2 Other MC Codes

Although MCNP6 in the main code used in most parts of this work, using other MC codes with similar geometries provide a useful comparison between different codes. Two additional MC codes were used in this work: PHITS and HETC-HEDS.

2.2.1 PHITS

The Particles and Heavy Ion Transport code System (PHITS) is a general-purpose MC code developed by the Japan Atomic Energy Agency in collaboration with other institutes (Niita et al., 2006; Sato et al. 2018). It has been validated and utilized in several papers studying space radiation (Sato and Niita, 2006; Puchalska et al, 2012; Matthiä et al., 2016). This work uses PHITS version 3.1 to compare the angular and energy spectra of albedo neutrons, protons, and lights ions with those obtained from MCNP6. The geometry, elemental composition, and source term used in PHITS simulations are identical to the ones used in MCNP6. Both the fully dry and fully wet regolith scenarios were simulated, and the physics models were kept as default in both cases.

2.2.2 HETC-HEDS

The High Energy Transport Code – Human Exploration and Development of Space (HETC-HEDS) is a three-dimensional MC code that extends on the previous HETC code (Gabriel et al., 2000) to include the proper modules for high-energy heavy-charged particles transport. *Townsend et al. [2010a]* provides a very detailed description of the HETC-HEDS code. Previous studies validated and used HETC-HEDS for space applications, including simulations of the CRaTER instrument (Charara et al., 2008; Sihver et al., 2008; Townsend et al., 2010a, 2010b; Porter et al., 2014; de Wet and Townsend, 2017). In this work, HETC-HEDS is used to compare the energy distributions of albedo neutrons and protons with the spectra generated from MCNP6 and PHITS. The geometry consists of a slab with a thickness of 10 meters, and the exact source term and elemental composition of lunar regolith used in the previous runs.

3. RESULTS FROM DRY REGOLITH

The distributions of albedo particles are reported as a function of four properties: particle type, energy, emitted angle, and maximum production depth. This chapter starts with the 2-D spectra first, showing the energy, angular, and depth distributions. It then follows by relating these properties in 3D plots, or more accurately heat maps, in which one property appears on the x-axis, another on the y-axis, and the fluxes are presented on a color gradient.

3.1 Energy Distribution

Figure 3.1 shows the energy spectra of the albedo particles studied in this work. The neutral particles dominate the spectra, especially at lower energies. They are followed by charged particles which in general decrease in flux the heavier the charged particle is. Albedo ions heavier than alpha particles were not included in this spectrum, and the total flux of all heavier ions added together was an order of magnitude lower than albedo alpha flux. The individual spectrum of each albedo species with the relative errors are available in Appendix A.

Albedo neutrons are created mainly through the spallation reactions caused by the energetic GCR particles. Their energy spectrum in Figure 3.1 shows the resonance effects around epithermal energies and the dominance of neutrons at high energies. Albedo photons are produced mainly through nuclear interactions, bremsstrahlung, decay of particles, electron-positron annihilation, and neutron scattering reactions. The energy spectrum of albedo photons shows some characteristic peaks in energies lower than ~10 MeV. The most prominent peak is the annihilation peak at 511 keV, followed by other peaks caused by inelastic neutron scattering, decay of radioactive fragments, and neutron capture reactions. Since neutrons below 100 keV were not included in the simulations, some peaks caused by low-energy neutron capture reactions are expected to be underestimated. Also, this work initially used the default list of particles transported

by MCNP6, which caused an underproduction of high energy photons. *Ratliff et al. [2017]* noted a similar problem caused by the default exclusion of neutral pions, a source of high energy photons through particle decay. Turning on neutral pions in this work helped in solving the problem of the underestimation of high-energy photons.

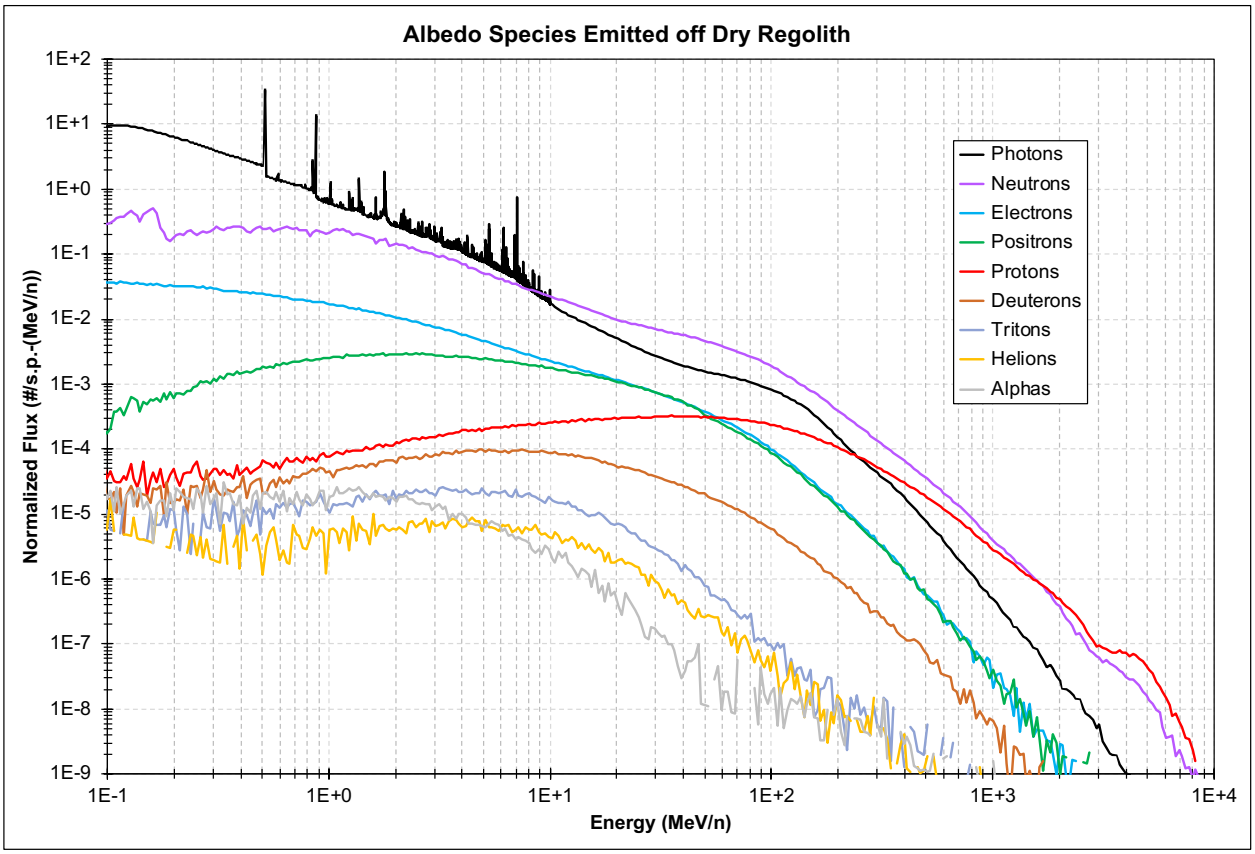

Figure 3.1. The energy spectra of the studied albedo species.

Albedo electrons and positrons are produced mainly by nuclear interactions, particle decay, pair production, Compton recoil, photoelectric effect, and knock-on reactions. They have similar energy spectra down to ~10 MeV, where albedo electrons gradually dominate over albedo positrons. Albedo protons are either scattered primary GCR protons, or secondary protons created by nuclear interactions in the regolith. They peak at ~60 MeV and dominate above ~1 GeV along with albedo neutrons. Other light ions are also produced by nuclear interactions and their energy spectra showed a relatively higher uncertainty in their fluxes implying a much lower production compared to other albedo species.

3.2 Angular Distribution

The normalized flux of each albedo species as function of emission angle off surface normal (0 degrees off normal corresponds to the zenith direction and 90 degrees correspond to the shallowest angle off the lunar surface) is shown in Figure 3.2. Taking the behavior of albedo neutrons as an example helps shed light on the angular behavior of other albedo species. Figure 3.3 shows the angular distribution of albedo neutrons without accounting for differences in solid angle. A drop in the flux at lowest angles off normal and another at highest angles are observed. The first drop exists because the solid angle decreases dramatically at lower angles than higher angles. This is illustrated in Figure 3.4. The solid angle between 0 and 1 degree off surface normal is smaller than the solid angle between 89 and 90 degrees by a factor of ~115. In other words, there is a smaller surface area for particles going straight up relative to particles emitted at shallower angles.

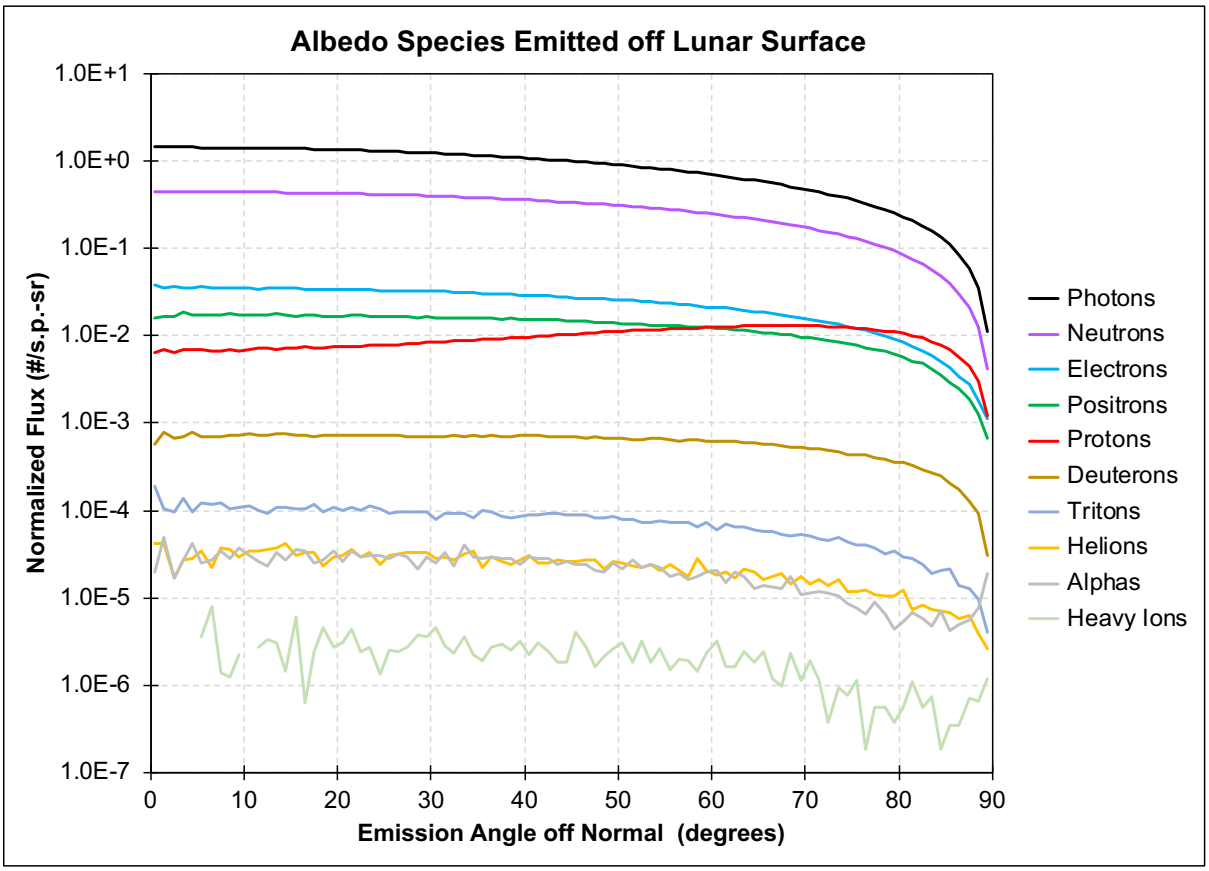

Figure 3.2 The angular spectra from all albedo species.

The other drop in flux at higher angles is expected since it relates directly to the distance required by the particle to reach the surface. From the same point in the lunar regolith, the shortest distance to the surface is straight up, which corresponds to 0 degrees off normal, while shallower angles require a larger distance to reach the surface. Normalizing for solid angle adjusts the drop in smaller angles off normal, as shown in Figure 3.2. With the exception of albedo protons, all other particles peak at 0 degree off normal and drop continuously until reaching 90 degrees. This correlates directly with the probability of propagating through the lunar regolith to reach the lunar surface.

The main reason behind the proton peak at higher angles off normal is due to the presence of protons in the source term. Most of the albedo protons leaving at shallow angles have very high energies. Unlike all other albedo particles which are created inside the regolith, albedo protons consist of a large portion of scattered GCR protons that leave the lunar surface at very high angles off normal. A similar behavior could be expected from heavier ions like alpha particles; however, the statistics were not high enough to reach a proper conclusion. Figure 3.2 also includes the angular behavior of albedo heavy ions, and it is clear from the plot that they leave the surface with a much smaller magnitude than other albedo species. The individual angular spectrum of each albedo species is presented in Appendix B, along with their corresponding relative errors.

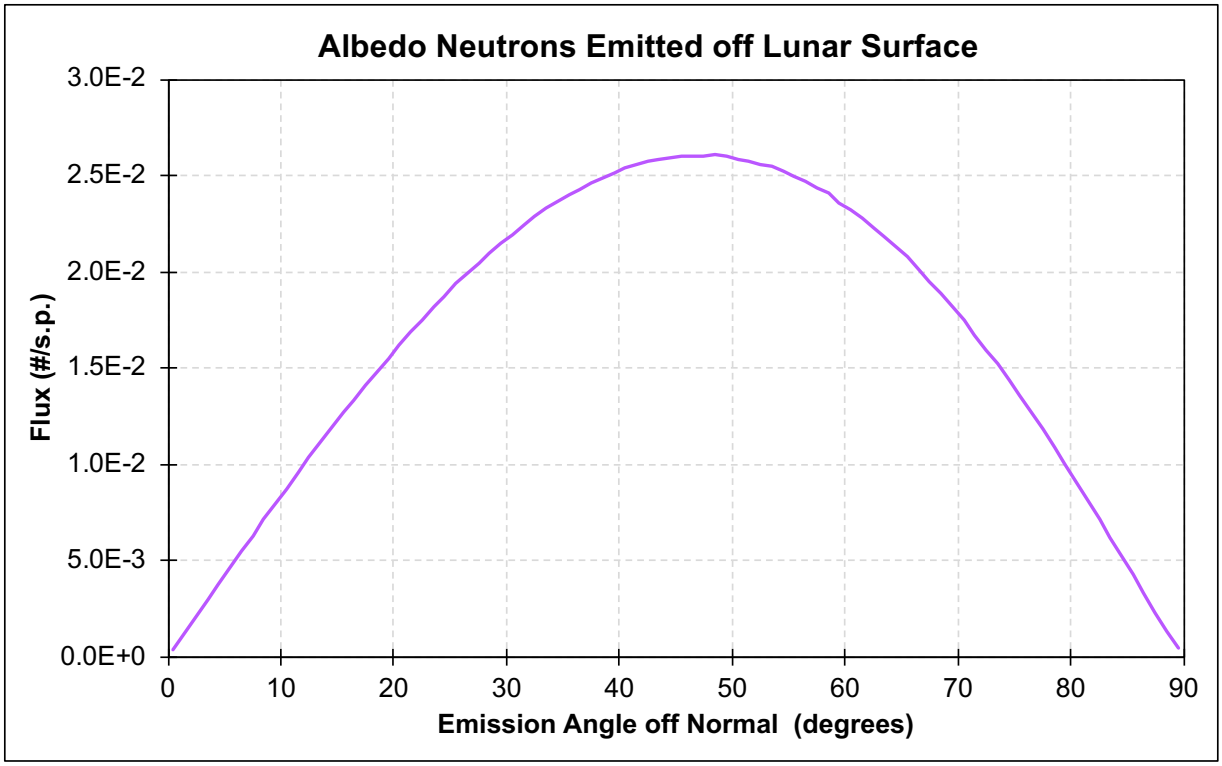

Figure 3.3. The angular distribution of albedo neutrons without normalization for solid angle.

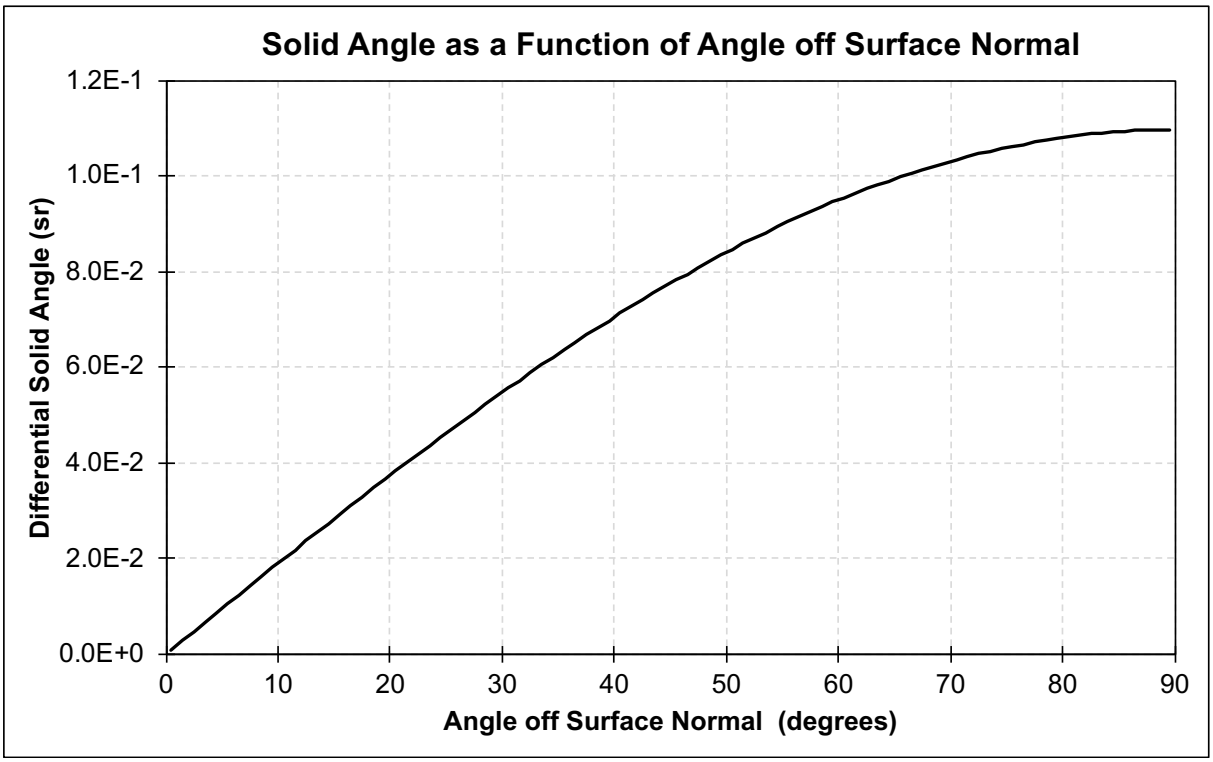

Figure 3.4 The differential solid angle as a function of angle off surface normal.

3.3 Maximum Production Depth Distribution

Figure 3.5 shows the flux of each albedo particle as a function of maximum production depth from all angles and all energies studied. Recall that this is the maximum depth reached by any process leading to the production of the albedo particle before leaving the lunar surface and not the depth where the albedo particle itself was necessarily produced. Figure 3.6 presents the same results in units of percentage relative to the total flux at the surface to provide a comparison between the different albedo species. Appendix C contains all the individual plots with their relative errors. The fluxes of albedo neutrons, photons, electrons, and positrons peak at some depth in the regolith, while other species tend to decrease continuously with depth. To understand these features, it important to describe what is happening to the behavior of albedo particles inside the regolith before reaching the surface. There are two factors contributing to the flux of albedo

particles as they leave the lunar surface: the rate of production of secondary particles in the regolith and the probability of a secondary particle to reach the lunar surface. The production of GCR-induced secondary particles peaks as some depth, while the probability of leaving the lunar surface decreases with increasing depth. As illustrated in Figure 3.7, these two factors combine to produce a local peak in flux of albedo particles reaching the surface. The blue "penetration curve" in Figure 3.7 shifts to the right with neutral particles since they have a higher probability of propagating through lunar regolith, and thus this shifts their albedo peak to deeper locations in the regolith. Since charged particles have a relatively higher stopping power, the penetration curve shifts more to the left the heavier the particle is. Therefore, albedo electrons and positrons have an albedo peak in a relatively shallower depth than neutral particles, while other light ions do not have an observable albedo peak at any depth implying that the penetration curve shifts heavily to the left and totally dominates over the green "production curve". The only exception to this behavior is albedo protons and alphas since there is an additional factor to the equation, which is the scattering of GCR primaries that also count as albedo particles. However, no local albedo peak in the regolith was observed for either particles above the lower limit studied in this work, which is 0.15 g/cm^2.

Table 3.1 gives a summary of the depth ranges of the peak production for each albedo species (local maximum in Figure 3.6), the depth ranges where 50% and 99% of the albedo production processes occur, and the maximum production depth range observed in MCNP6 with a relative error of less than 10%. For example, if we assume a local density of 2 g/cm^2, then albedo photon production processes will peak at a depth around ~7.5 cm, 99% of albedo photons will reach the surface from processes occurring at a maximum depth of ~50 cm, and the maximum depth reach by any interaction leading an albedo photon (with a relative error of <10%) is between 2 to 3 meters in the regolith. It is important to note that all these results are for albedo particles

with energies above 10 keV. Particles with lower energies are assumed to peak at different depths and might reach the surface from an even deeper location in the regolith.

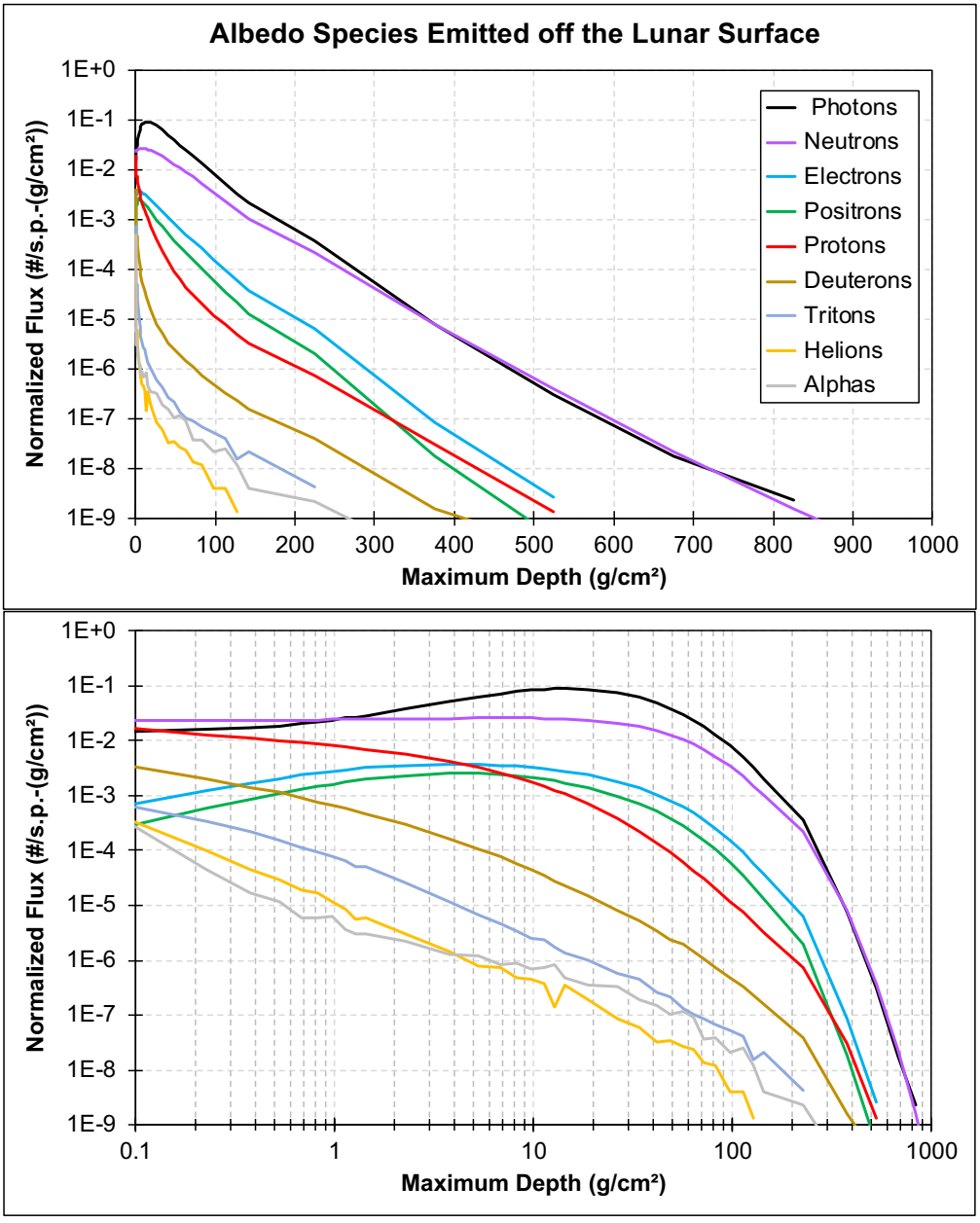

Figure 3.5. The differential albedo particle flux as a function of maximum production depth in a semilogarithmic plot (top) and a logarithmic plot (bottom).

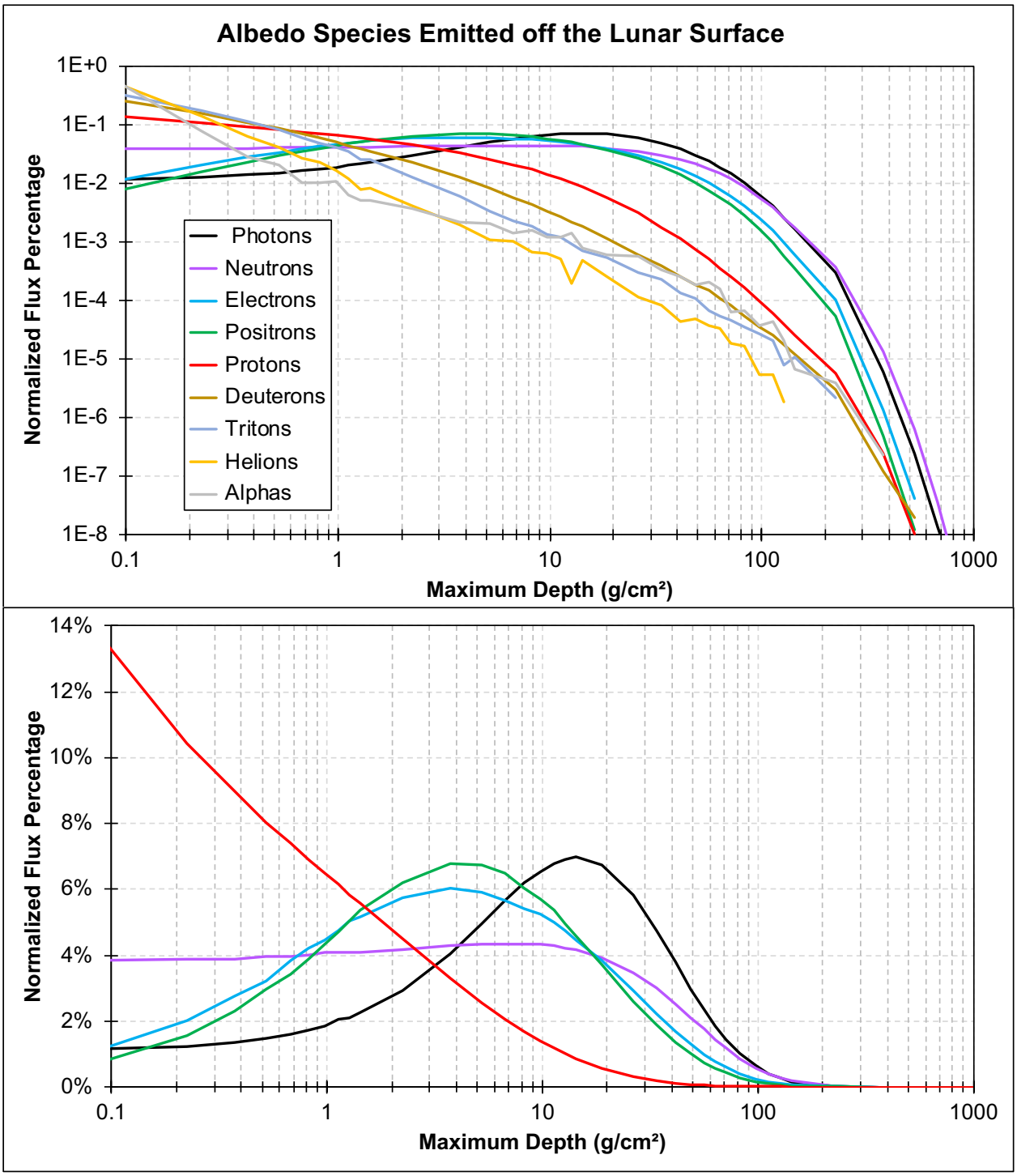

Figure 3.6. The percentage relative to the total flux of each albedo species as a function of maximum production depth in a logarithmic plot for all species (top) and a semilogarithmic plot for selected species (bottom).

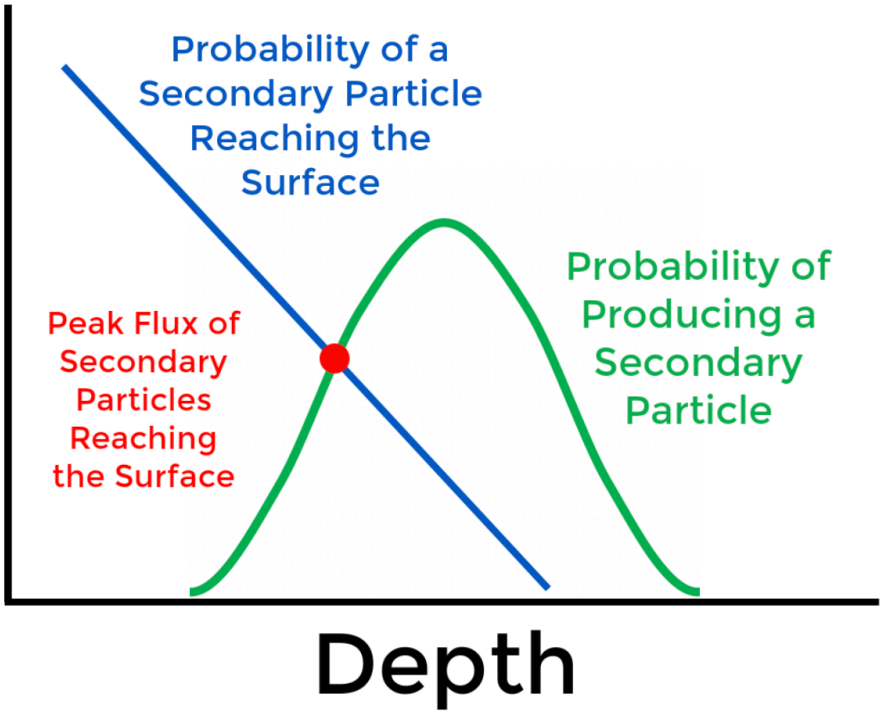

Figure 3.7. The factors contributing to the flux of albedo particles reaching the lunar surface.

Table 3.1. Summary of the depth ranges of albedo particles for different parameters of interest.

Albedo Species	Maximum Depth Range of Peak Production (g/cm^2)	Maximum Depth Range Reached by 50% of the Particles (g/cm^2)	Maximum Depth Range Reached by 99% of the Particles (g/cm^2)	Maximum Depth Range Reached by Any Particles with <10% Relative Error (g/cm^2)
Neutrons	6-7.5	4.5-6	90-105	600-750
Photons	13.5-15	10.5-12	90-105	450-600
Electrons	3-4.5	4.5-6	67.5-75	150-300
Positrons	3-4.5	4.5-6	67.5-75	150-300
Protons	Surface	0.75-0.9	15-22.5	300-450
Deuterons	Surface	0.3-0.45	9-10.5	150-300
Tritons	Surface	0.15-0.3	4.5-6	90-105
Helions	Surface	0-0.15	1.5-3	22.5-30
Alphas	Surface	0-0.15	4.5-6	60-67.5

3.4 Energy-Depth Relationship

Figures 3.8 to 3.23 show three-dimensional plots of the energy and depth distributions of each albedo species for selected angles. The maximum depth reached by the albedo particle production processes is on the x-axis, and the energy of the albedo particle as it leaves the surface is on the y-axis. The temperature gradient in the plot represents the normalized flux in units of (#/s.p.-MeV-sr-(g/cm^2)). Three angular regions were selected in this part: 0-10 degrees off surface normal, which are the albedo particles going upwards, 40-50 degrees representing the particles leaving at the midpoint between the zenith and the surface, and 80-90 degrees, which are the particles leaving at very shallow angles off the lunar surface. From the same point in the lunar regolith, the particles leaving in the region between 0 and 10 degrees generally travel the least distance to reach the lunar surface, while the particles leaving between 80 and 90 degrees travel the longest distance to the surface. Also, since GCRs interact with the lunar surface at angles pointing downward into the surface, and since fragmentation usually creates forward directed fragments, particles leaving in the region between 0 and 10 degrees (or their predecessors in general) should undergo a very large scattering angle leading to a substantial energy loss prior to leaving the surface. This will be also discussed in the next section.

Albedo Neutrons

Observing the behavior of albedo neutrons in Figure 3.8 shows that the observed albedo neutron flux peak at ~7 g/cm^2 is caused mainly by albedo neutrons with energies below ~1 MeV. As the probability of low energy particles reaching the lunar surface decreases, this peak starts to gradually fade away as seen in Figures 3.10 and 3.11 until it disappears at large angles off surface normal. Figure 3.11, which shows the albedo neutrons leaving at angles glancing the lunar surface,

suggests that energetic albedo neutrons are created closer to the surface and the absence of the peak in flux implies the dominance of the penetration curve over the production curve in Figure 3.7. In other words, the production of albedo neutrons leaving at glancing angles is not increasing enough at deeper locations in the regolith to overcome the minimum distance required to reach the surface. On the other hand, the production of albedo neutrons leaving at upward angles is high enough at ~7 g/cm^2 and close enough to the lunar surface to create a local peak in flux.

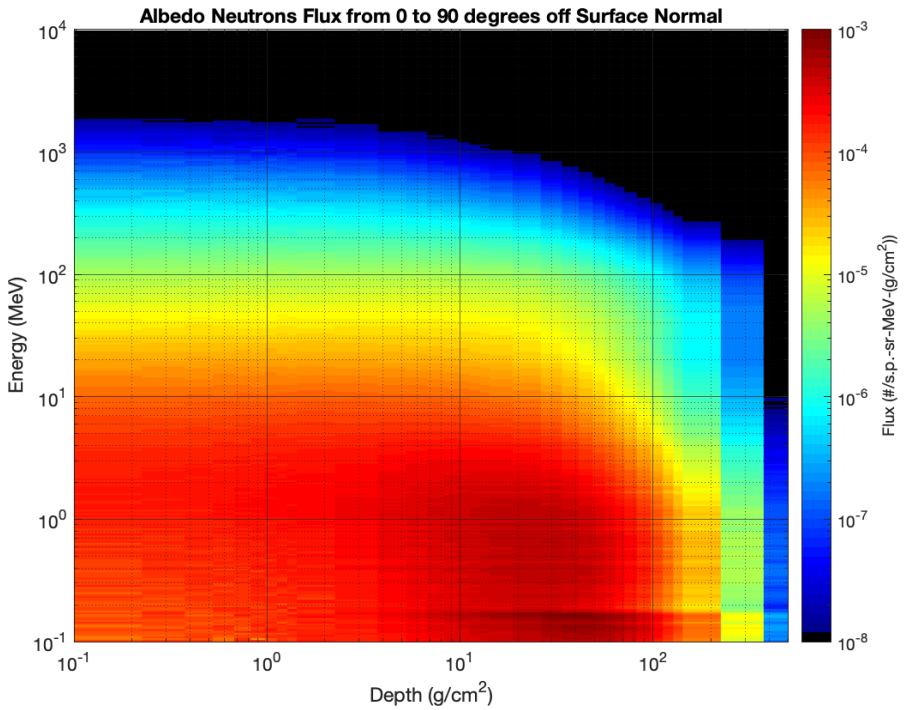

Figure 3.8. Albedo neutron flux as a function of energy and maximum production depth for all angles off surface normal.

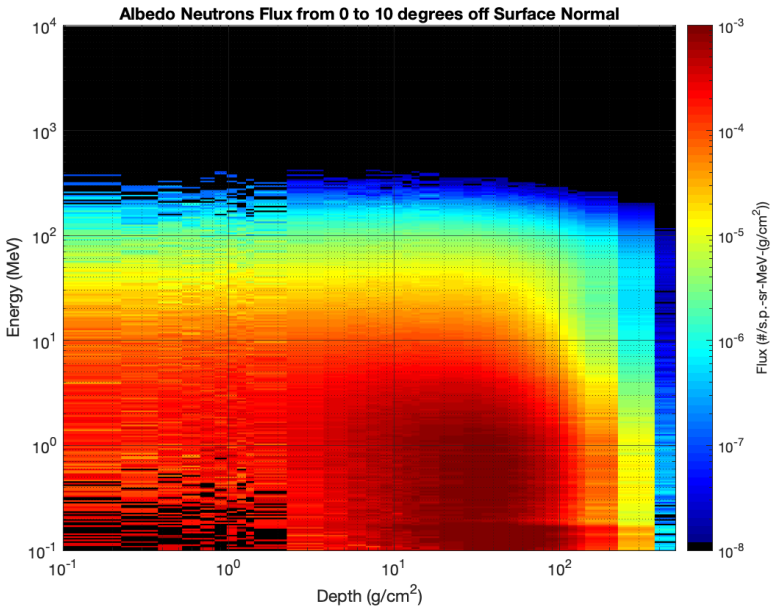

Figure 3.9. Albedo neutron flux as a function of energy and maximum production depth for angles between 0 and 10 degrees off surface normal.

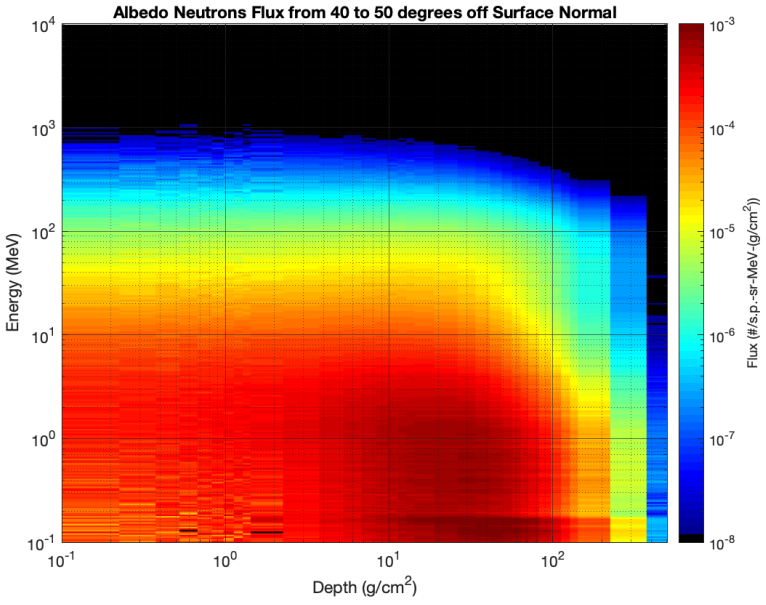

Figure 3.10. Albedo neutron flux as a function of energy and maximum production depth for angles between 40 and 50 degrees off surface normal.

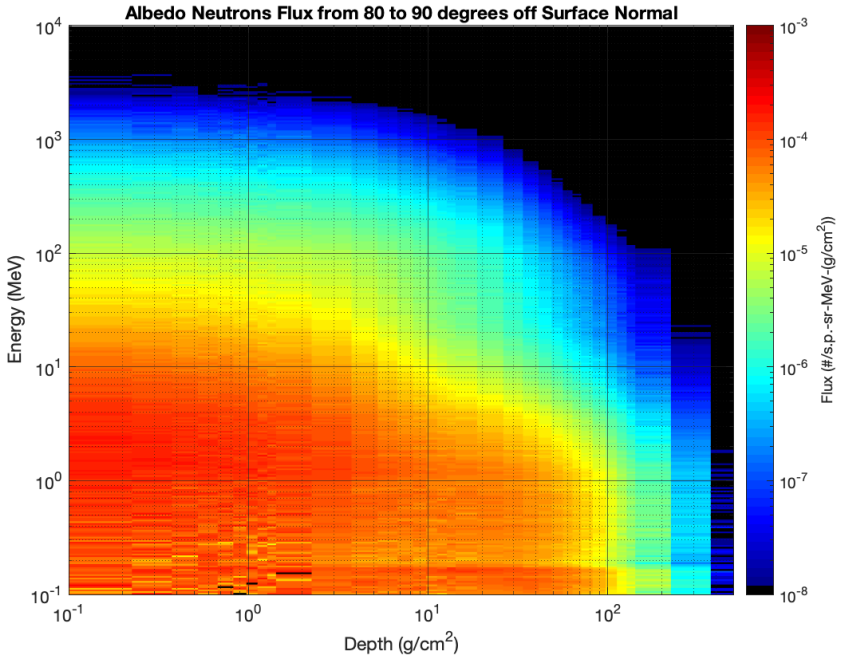

Figure 3.11. Albedo neutron flux as a function of energy and maximum production depth for angles between 80 and 90 degrees off surface normal.

Albedo Photons

The behavior of albedo photons, illustrated in Figures 3.12 to 3.15, shows a similar trend although the peak in flux at low energies does not fade away even at shallower angles off the surface. This implies that the shift in the penetration curve is small relative to albedo neutrons. Albedo photons leaving at glancing angles transit more material to the surface, which explains the shift in energy and depth between Figure 3.13 (photons leaving upwards) and Figure 3.15 (photons leaving at glancing angles).

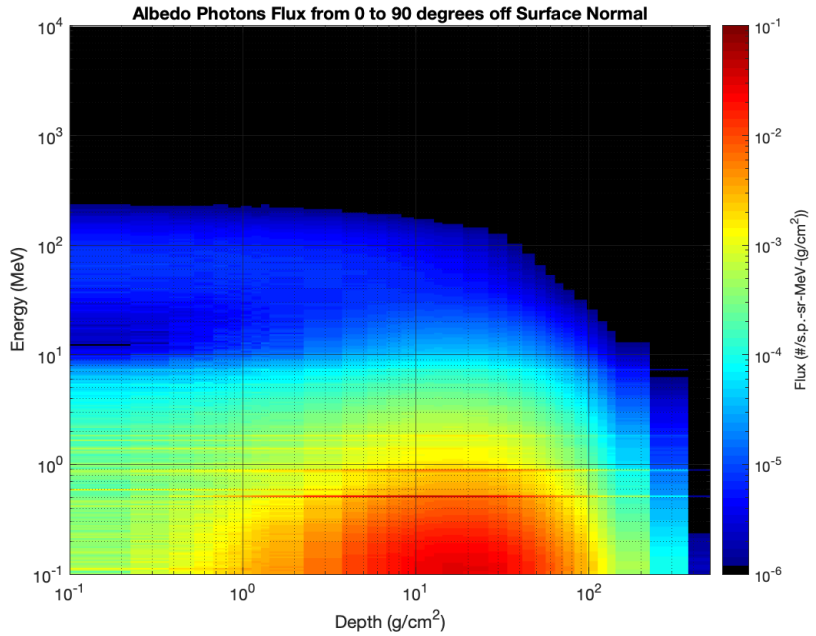

Figure 3.12. Albedo photon flux as a function of energy and maximum production depth for all angles off surface normal.

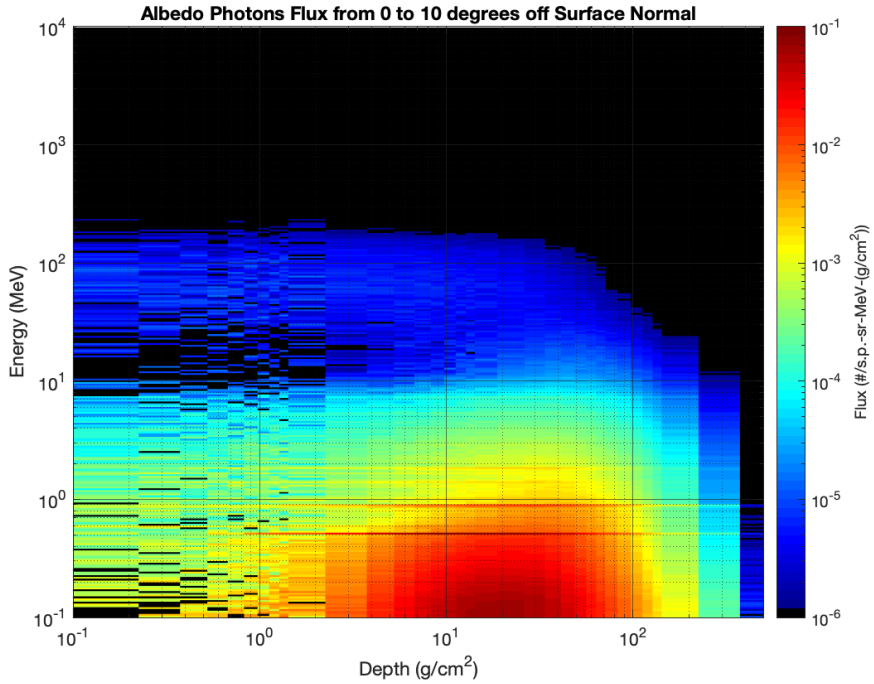

Figure 3.13. Albedo photon flux as a function of energy and maximum production depth for angles between 0 and 10 degrees off surface normal.

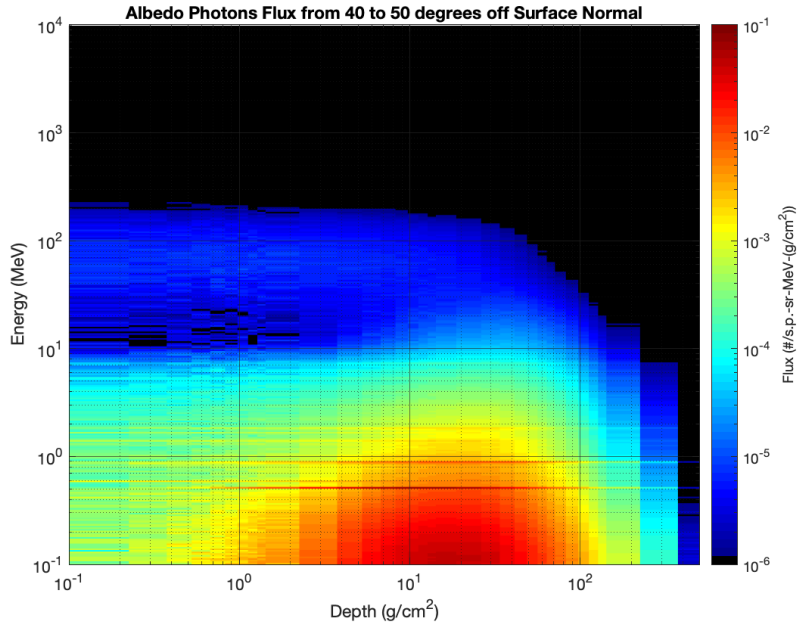

Figure 3.14. Albedo photon flux as a function of energy and maximum production depth for angles between 40 and 50 degrees off surface normal.

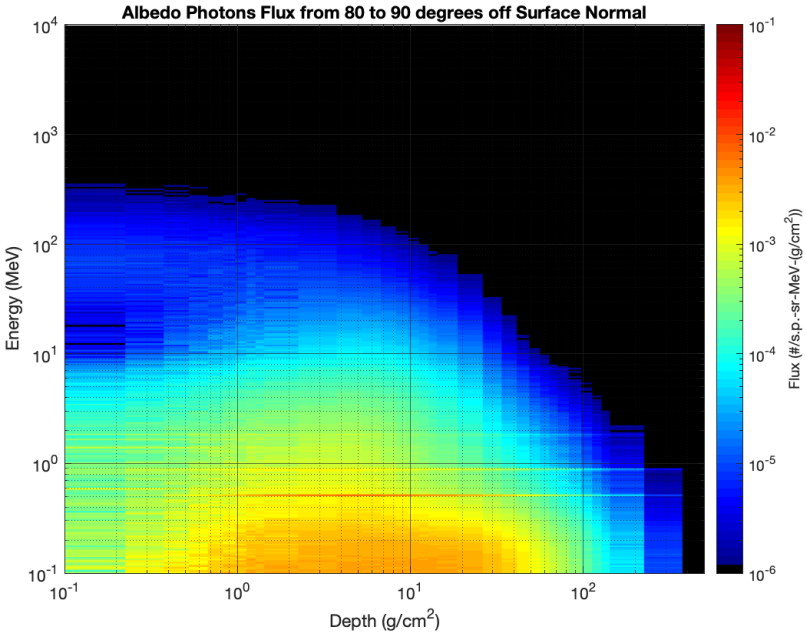

Figure 3.15. Albedo photon flux as a function of energy and maximum production depth for angles between 80 and 90 degrees off surface normal.

Albedo Electrons

The behavior of albedo electrons in Figures 3.16 to 3.19 is also similar to the previously discussed particles. Electrons with lower energies peak at ~5 g/cm^2 in upward directed angles. High energy electrons are only observed at shallow angles and by processes that occur near the surface, implying they are created by the spallation reactions of the glancing GCR ions at the upper layers of the regolith.

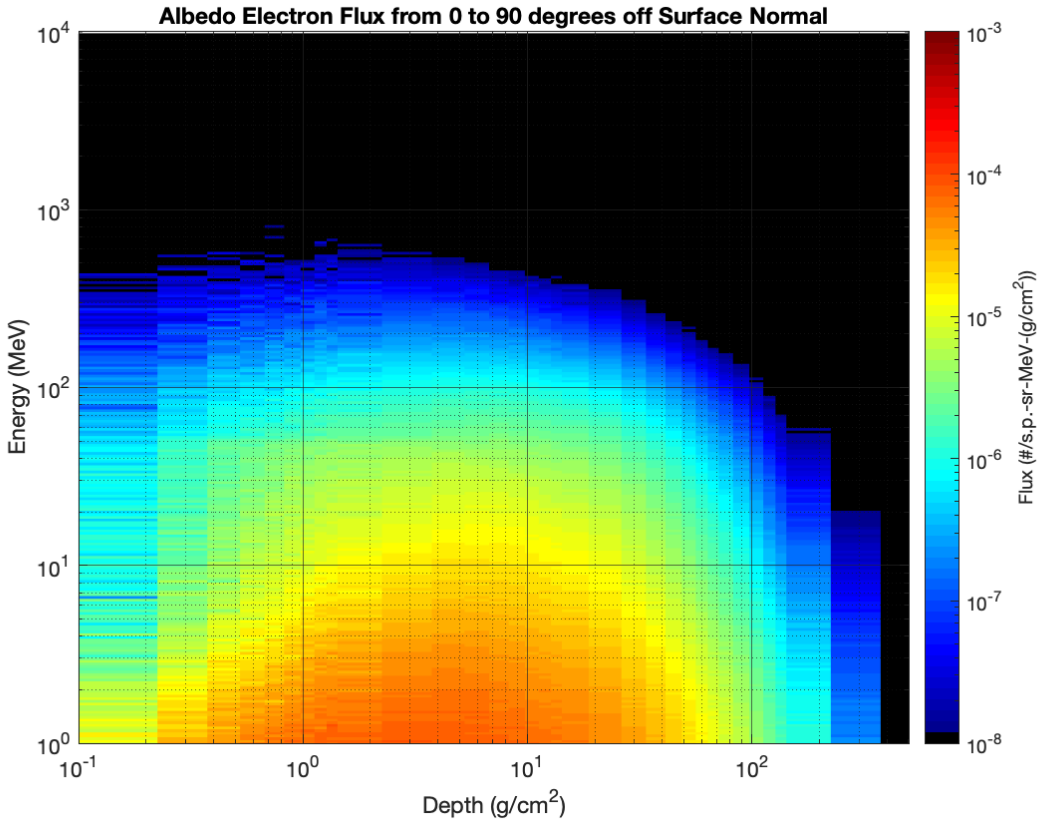

Figure 3.16. Albedo electron flux as a function of energy and maximum production depth for all angles off surface normal.

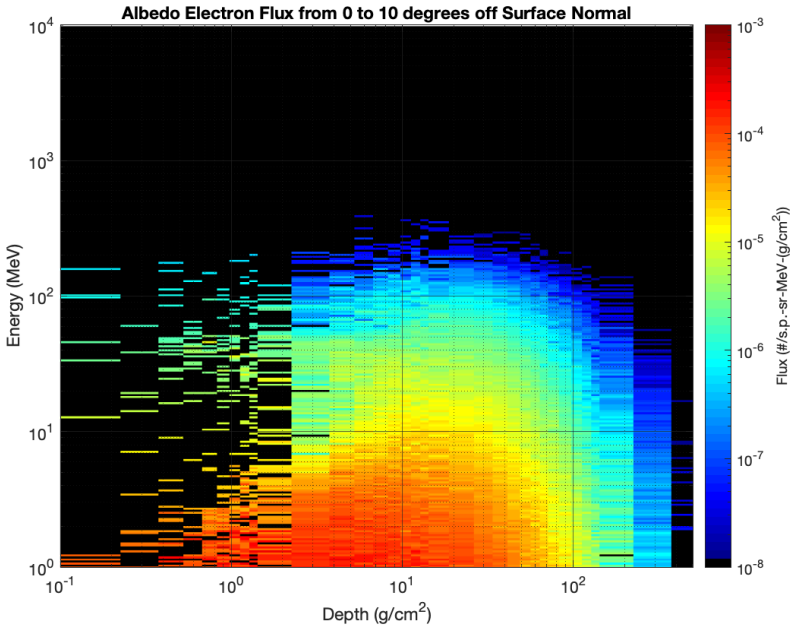

Figure 3.17. Albedo electron flux as a function of energy and maximum production depth for angles between 0 and 10 degrees off surface normal.

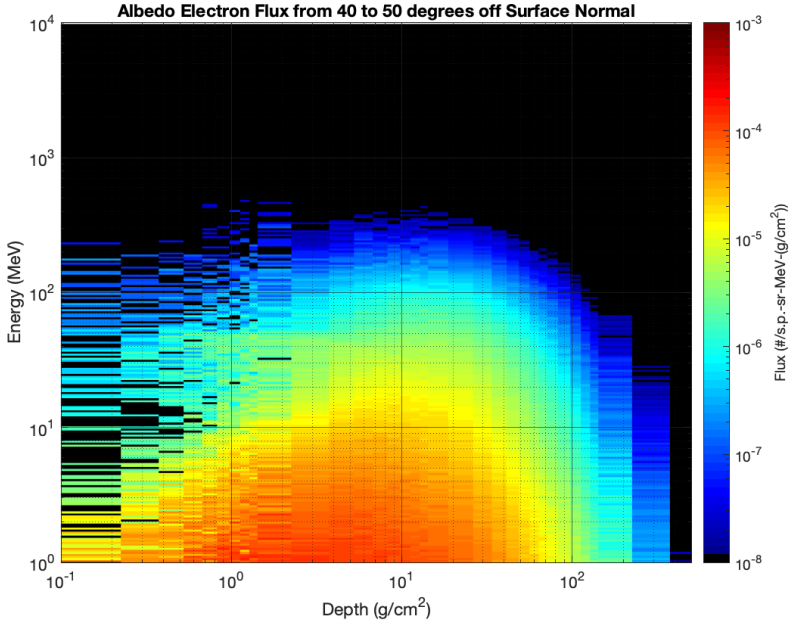

Figure 3.18. Albedo electron flux as a function of energy and maximum production depth for angles between 40 and 50 degrees off surface normal.

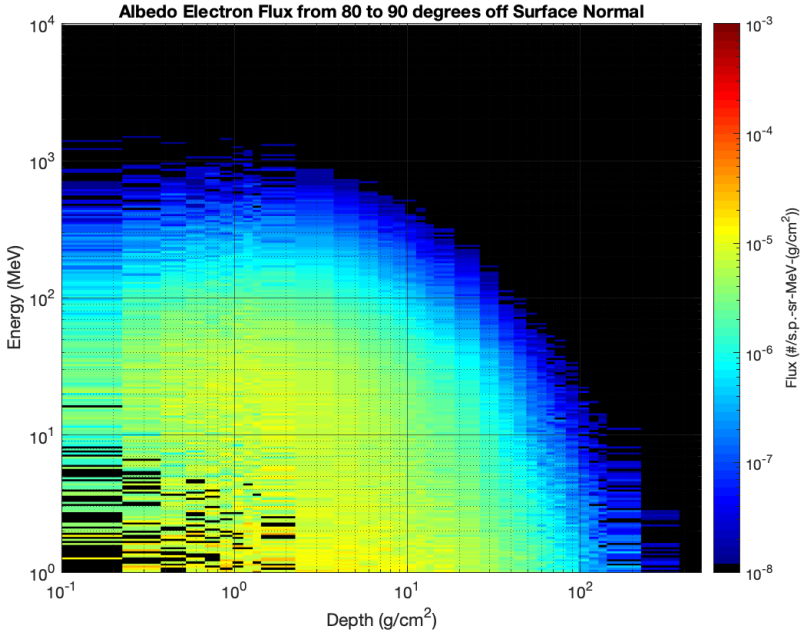

Figure 3.19. Albedo electron flux as a function of energy and maximum production depth for angles between 80 and 90 degrees off surface normal.

Albedo Protons

Figures 3.20 to 3.23 show the behavior of albedo protons, which peak as a function of energy and not depth, in all angular regions. Upward going albedo protons have relatively lower energies than albedo protons leaving at glancing angles and come from processes occurring at much deeper locations. Low-energy protons at very shallow depths are probably lower energy fragments with large scattering angles and those coming from deeper location are the energetic fragments that were able to reach the lunar surface after losing a substantial amount of energy. Observing the behavior of albedo protons leaving at very shallow angles off the lunar surface in Figure 3.23 shows the clear scattering of GCR protons at very shallow depths which are represented by the fluxes with GeVs of energy in the upper left corner of the plot. Figure 2.23 also

shows that energetic fragments that made it to the surface are from a relatively shallower depths compared to the upward directed albedo protons.

The energy-depth plots of albedo positrons were not included in this section since they behave similarly to albedo electrons. Also, the lights ion plots were not included for statistical reasons. Appendix D includes the energy-depth plots from all angular ranges for the four albedo species discussed in this part.

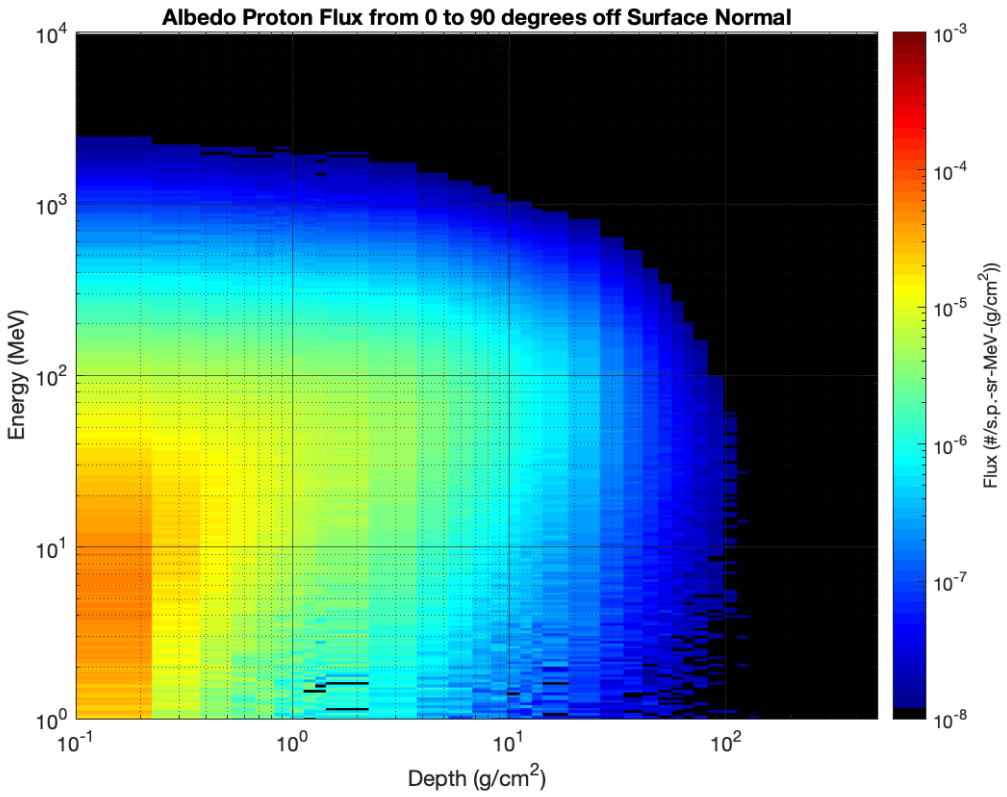

Figure 3.20. Albedo proton flux as a function of energy and maximum production depth for all angles off surface normal.

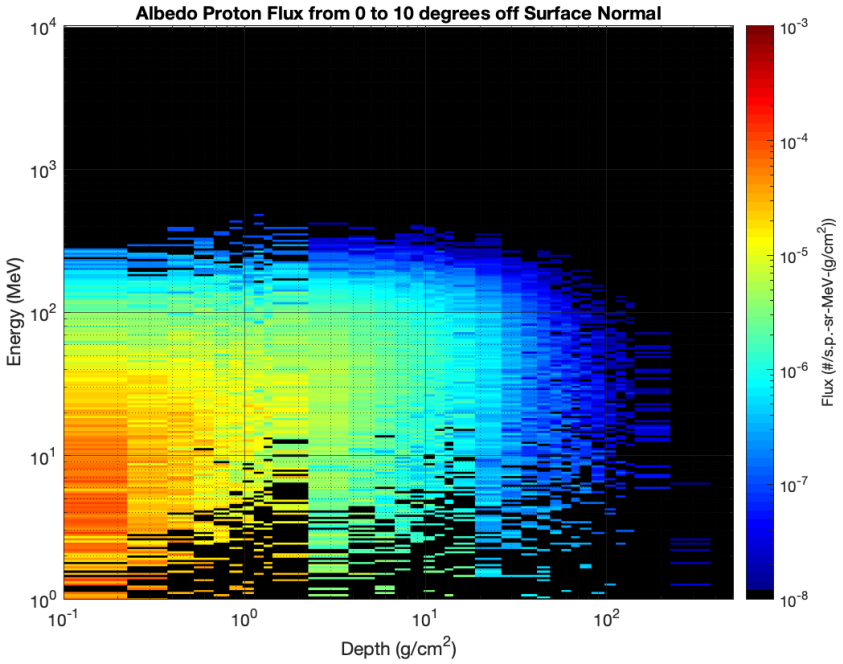

Figure 3.21. Albedo proton flux as a function of energy and maximum production depth for angles between 0 and 10 degrees off surface normal.

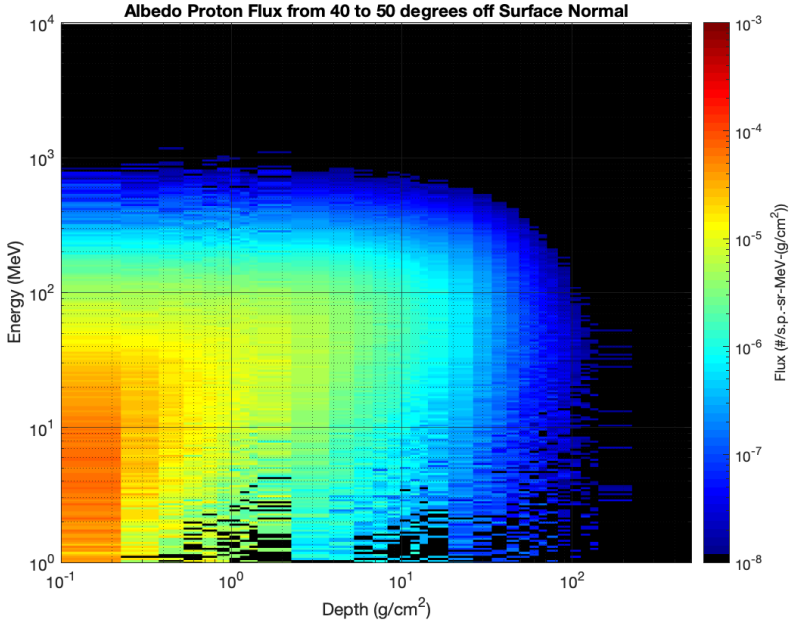

Figure 3.22. Albedo proton flux as a function of energy and maximum production depth for angles between 40 and 50 degrees off surface normal.

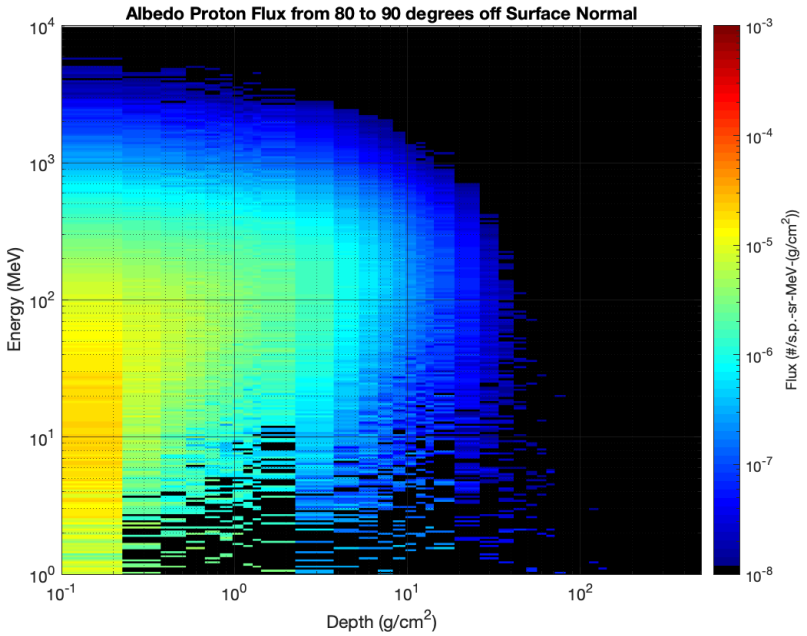

Figure 3.23. Albedo proton flux as a function of energy and maximum production depth for angles between 80 and 90 degrees off surface normal.

3.5 Energy-Angle Relationship

Figures 3.24 to 3.30 show three-dimensional plots of the energy and angular distributions of albedo neutrons, photons, electrons, and protons. The angle off normal of the albedo particle as it leaves the lunar regolith is on the x-axis, and its corresponding energy is on the y-axis.

Albedo Neutrons

Taking a closer look at the behavior of albedo neutrons in Figure 3.24 shows that high energy neutrons are only emitted at very high angles off normal and most of lower energy neutrons are emitted generally straight up. Figure 3.25 presents the albedo neutrons that were only created in the upper few millimeters of the regolith, and it is clear that these are mostly fast neutrons created by the fragmentation processes involving glancing GCR ions, as observed in the previous section, with the most energetic neutrons appearing at the shallowest angles off surface.

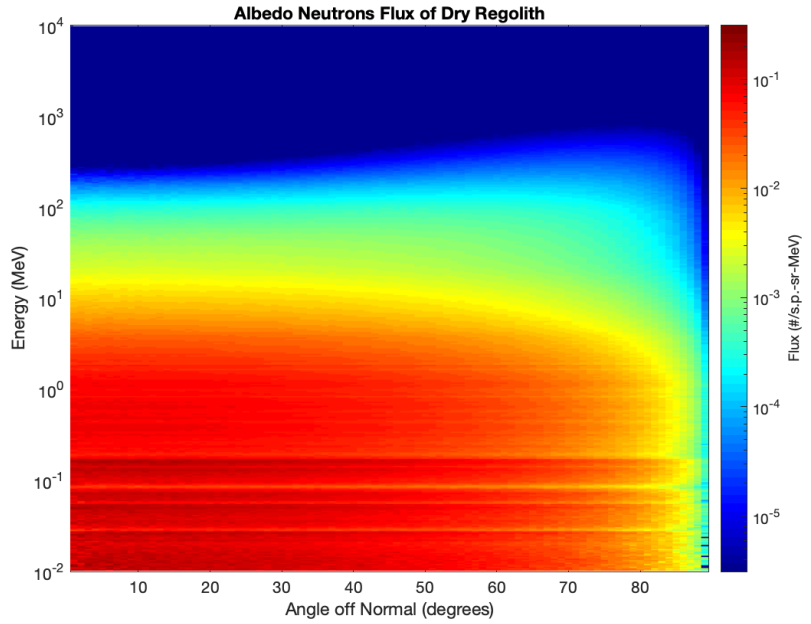

Figure 3.24. Albedo neutron flux as a function of energy and emitted angle coming from all depths.

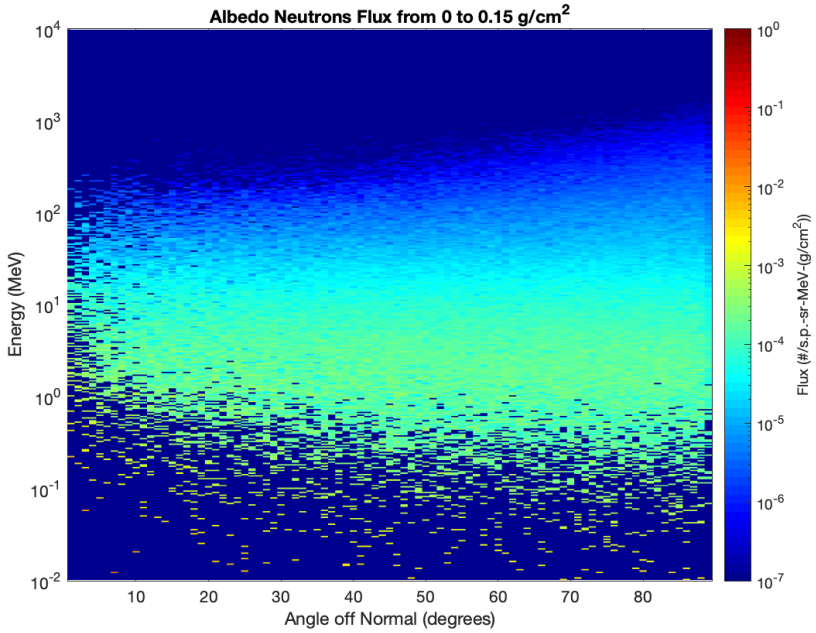

Figure 3.25. Albedo neutron flux as a function of energy and emitted angle reaching a maximum production depth of 0.15 g/cm^2.

Albedo Photons

The behavior of albedo photons, illustrated in Figure 3.26, shows a larger population of albedo photons at lower energies. It also shows the discrete photopeaks and the decrease in flux at higher angles off normal at all energy ranges unlike other albedo species. Taking a closer look at the photons created in the thin upper layer of the regolith give an insight to the processes creating the albedo photons. As seen in Figure 3.27, two distinctive energy regimes are apparent in the upper millimeters of the regolith: higher energy photons in the order of tens of MeVs, and a lower energy range in the order of hundreds of keVs. The high energy photons are created by the decay of neutral pions. This was verified in an MCNP6 run with neutral pions turned off. The results presented in Figure 3.28 show that photons with higher energies disappeared from all emission angles at the upper few centimeters of regolith when neutral pions are turned off.

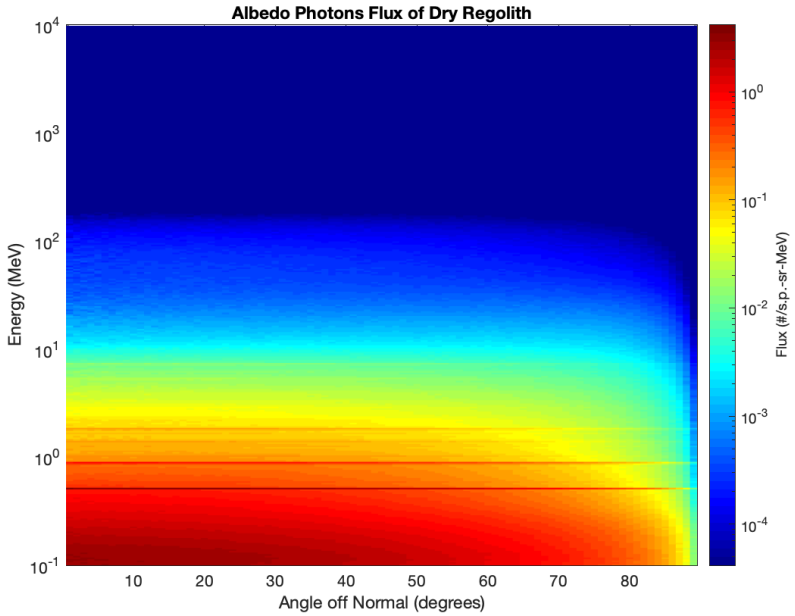

Figure 3.26. Albedo photon flux as a function of energy and emitted angle coming from all depths.

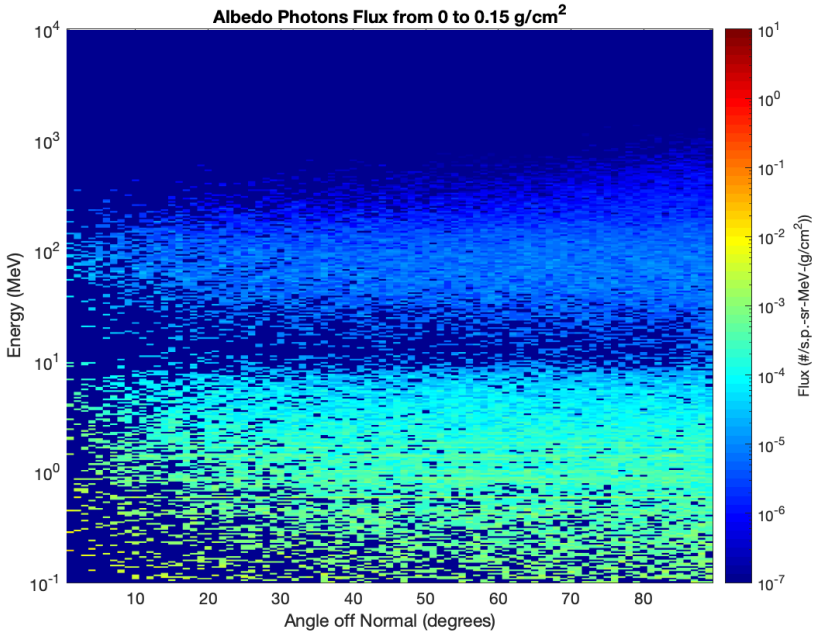

Figure 3.27. Albedo photon flux as a function of energy and emitted angle reaching a maximum production depth of 0.15 g/cm^2.

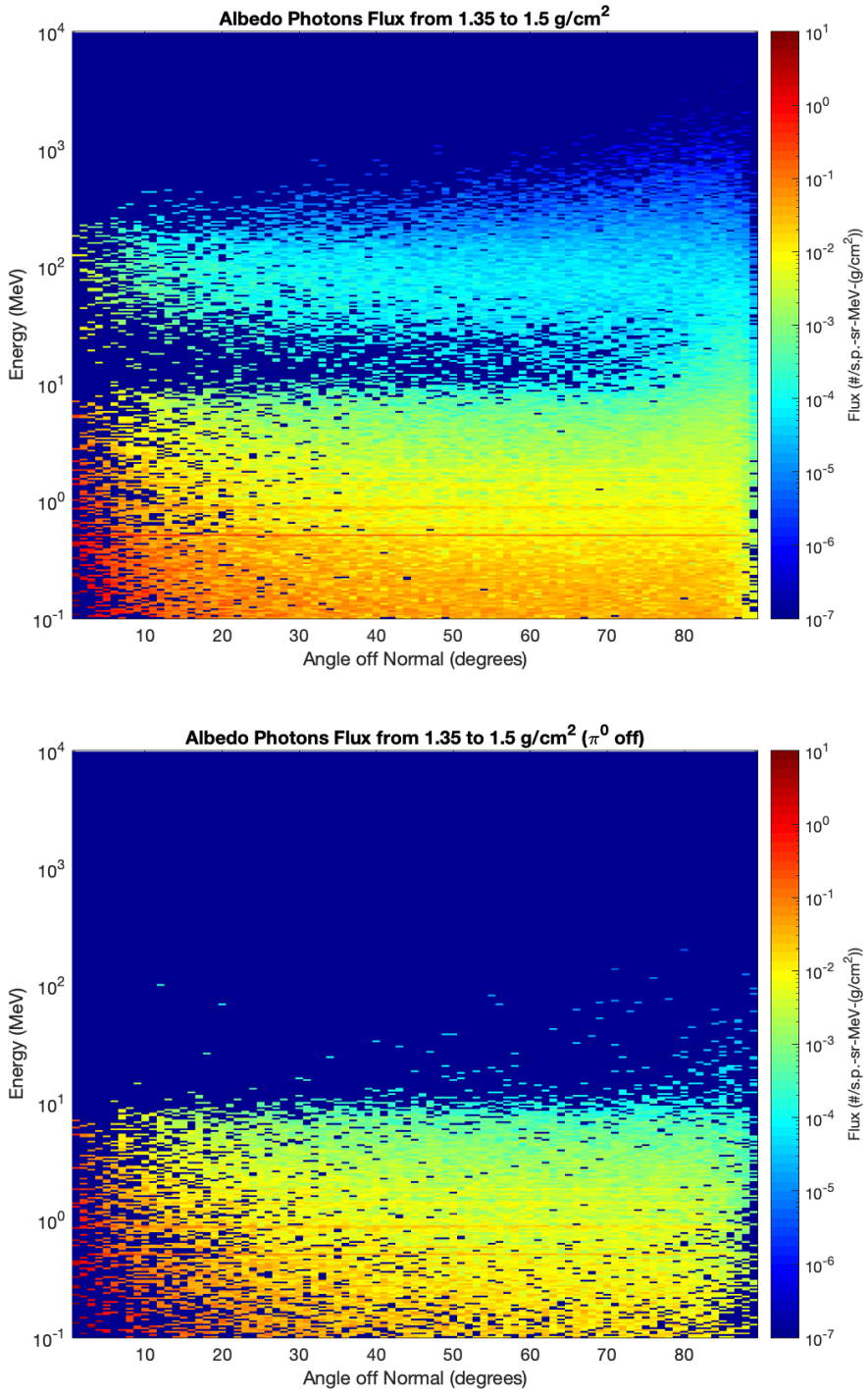

Figure 3.28. Albedo photon flux as a function of energy and emitted angle reaching a maximum production depth range between 1.35 to 1.5 g/cm^2 with neutral pions turned on (top) and off (bottom).

Albedo Electrons and Protons

Figure 2.29 illustrates the behavior of albedo electrons, which peaks at lower energies and emission angles off surface normal. The behavior of albedo protons, shown in Figure 3.30, is heavily affected by the presence of GCR protons in the source term. The increase observed at higher angles off surface normal and at higher energies consists of scattered GCR protons and the forward directed fragments created by glancing GCR ions.

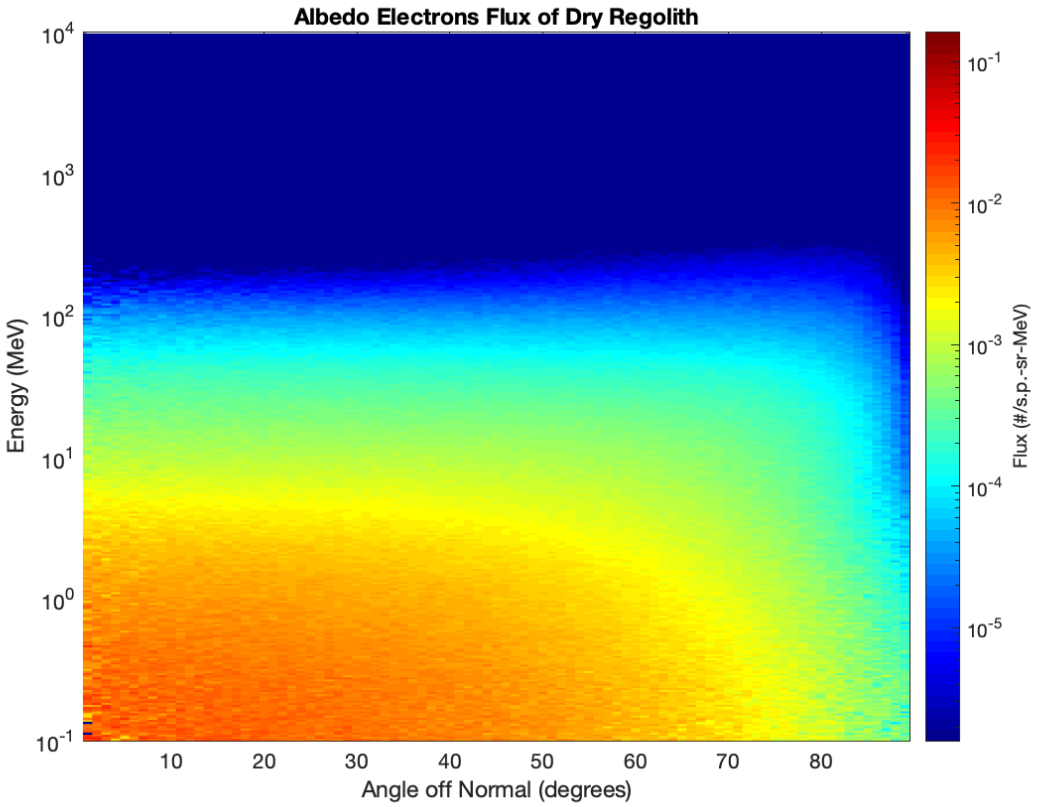

Figure 3.29. Albedo electron flux as a function of energy and emitted angle coming from all depths.

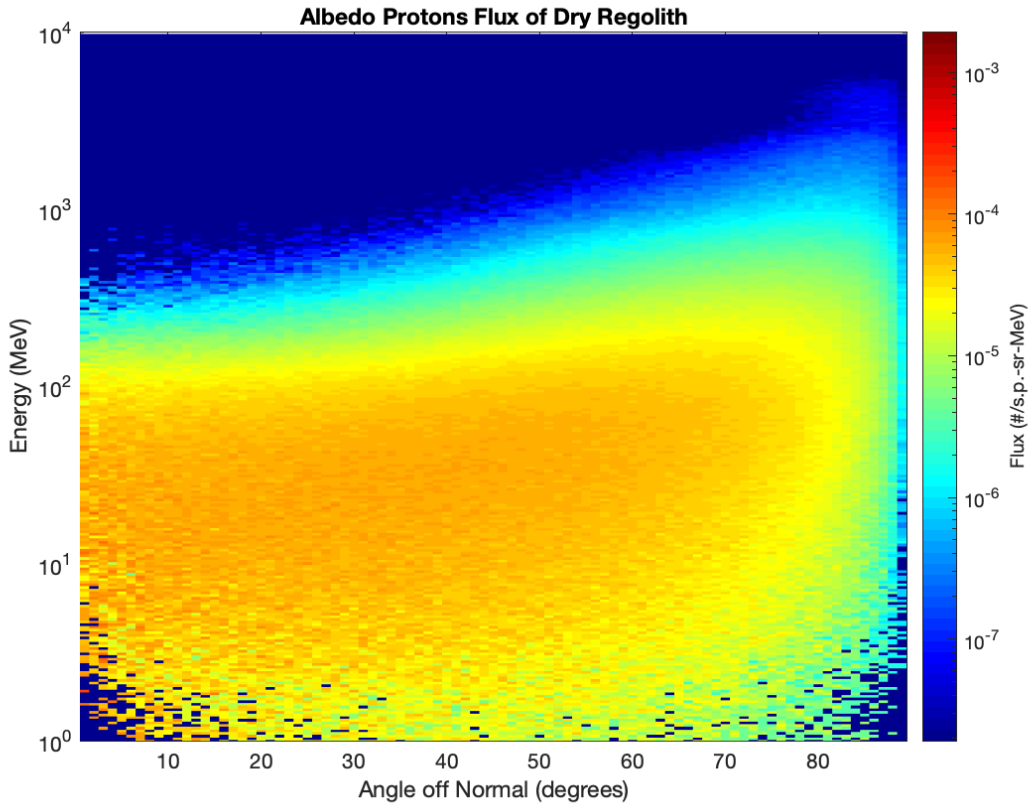

Figure 3.30. Albedo proton flux as a function of energy and emitted angle coming from all depths.

Angular Spectra of Energetic Albedo Particles

Figures 3.31 to 3.34 show the angular distribution for energies above and below 100 MeV to better illustrate the effects of the glancing GCR ions on the production of albedo particles. Both albedo neutrons and electrons show a peak at shallow angle in energies above 100 MeV as shown in Figures 3.31 and 3.32. This implies that these are produced by the fragmentation occurring at the top layers of the regolith. Energic albedo protons show a similar behavior where the peak at higher angles in Figure 3.33 appears to be sharper than the one covering all energies. However, low energy protons behave similarly to other albedo species with low energies, where the peak caused by the glancing GCR ions is no longer observed. Also, Figure 3.34 shows that high energy

photons do not have any peak like other albedo particles, which is reasonable since most these photons are decay products of neutral pions and not the result of nuclear spallation processes.

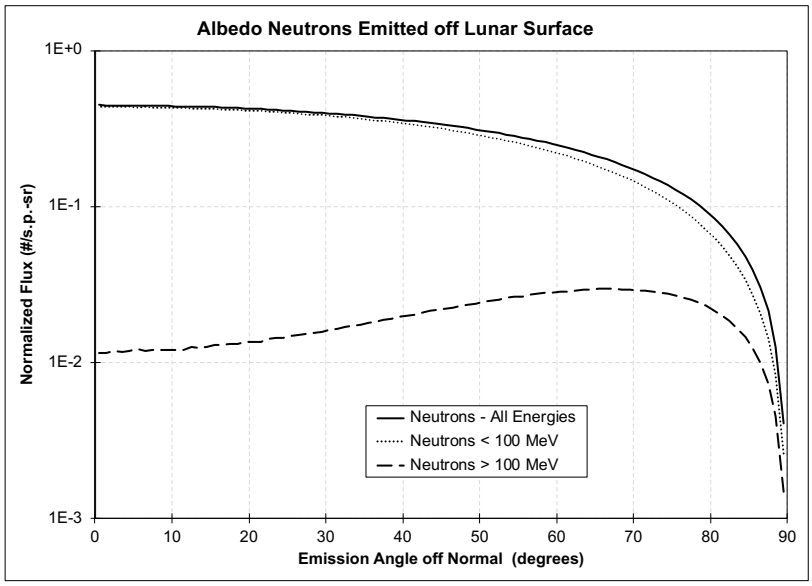

Figure 3.31. The angular distribution of albedo neutrons for two different energy ranges.

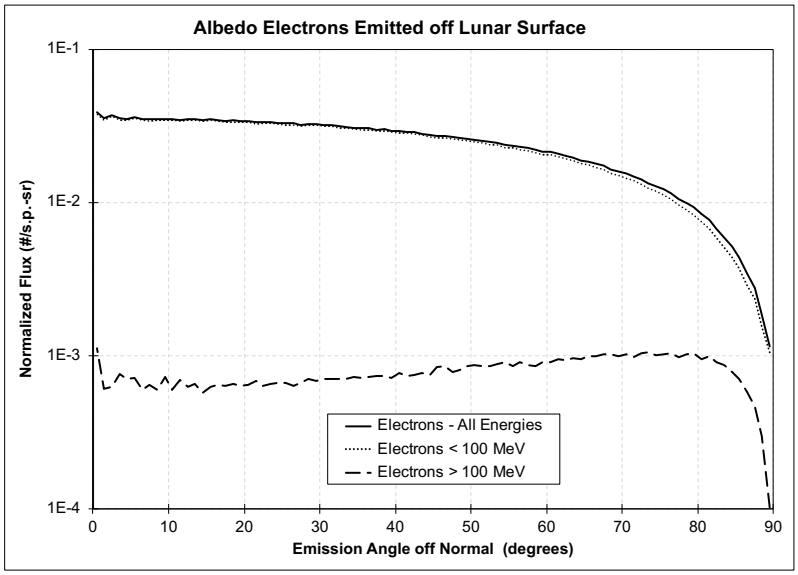

Figure 3.32. The angular distribution of albedo electrons for two different energy ranges.

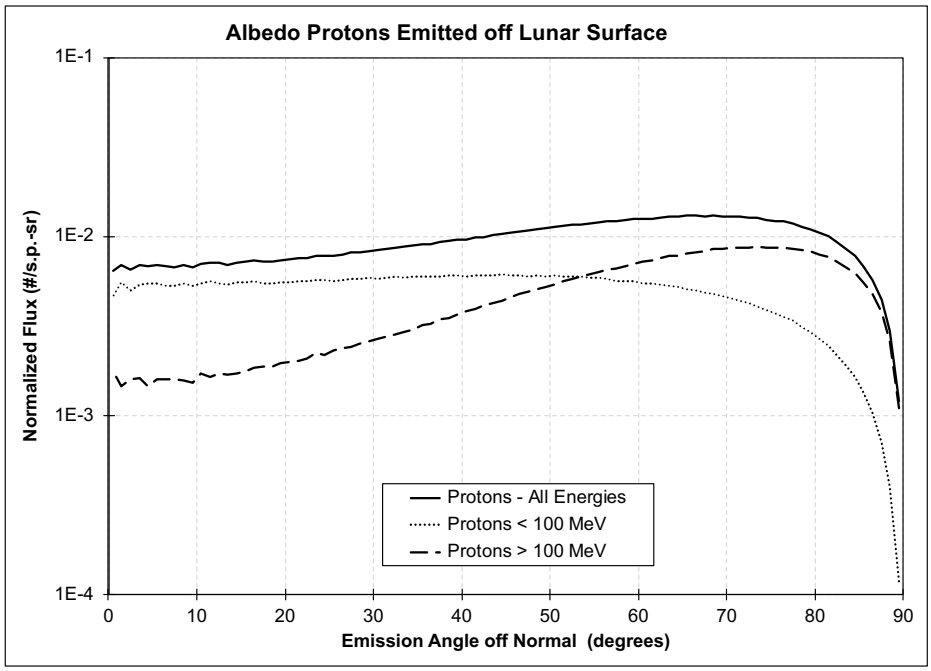

Figure 3.33. The angular distribution of albedo protons for two different energy ranges.

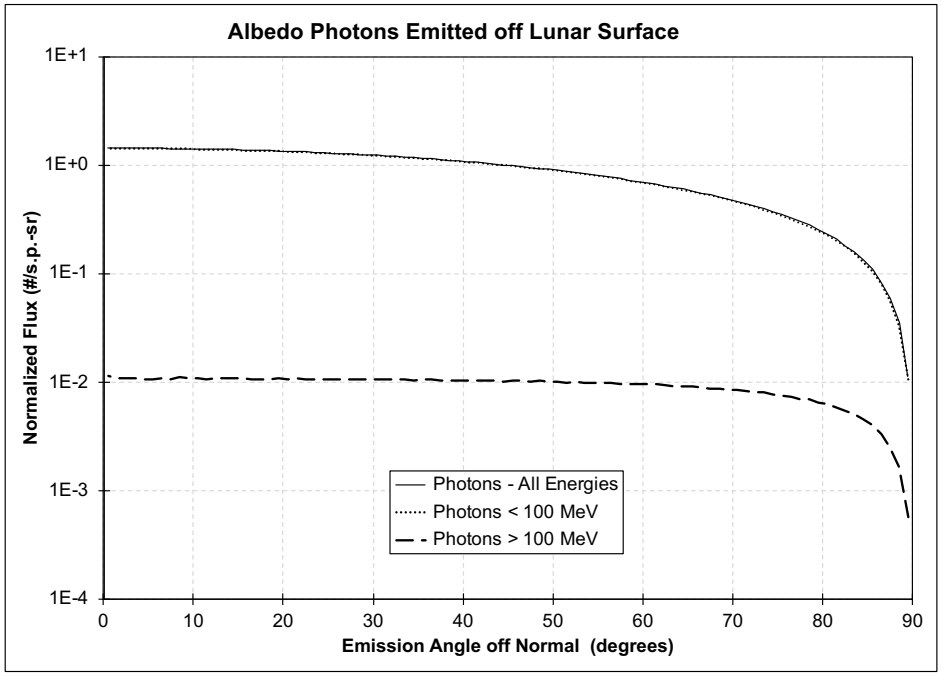

Figure 3.34. The angular distribution of albedo photons for two different energy ranges.

Effects from Glancing GCR Ions

To verify the effects from glancing GCR ions on albedo production ever further, three additional runs were transported with monodirectional GCR source terms: a run with a source pointing directly downwards in a 90 degree angle towards the lunar regolith, a run with a glancing source term pointing at 15 degrees off the lunar surface, and a run with very glancing source term pointing at 5 degrees off the lunar surface. The results displayed in Figures 3.35 to 3.40 show that albedo species with the highest energies appear only with glancing source terms. For example, as shown in Figure 3.36, albedo protons created by the downward directed GCR ions peak at an energy of ~400 MeV and albedo neutrons peak at ~500 MeV, while those created by glancing GCR ions peak at energies in the order of GeVs for both protons and neutrons. Observing the changes in the angular spectra in Figures 3.38 to 3.40 shows that albedo protons, neutrons, and electrons populate heavily at shallower angles (high angles off surface normal) when glancing GCR source terms strike the lunar surface. Also, the downward directed GCR source term creates significantly less protons leaving at shallower angles.

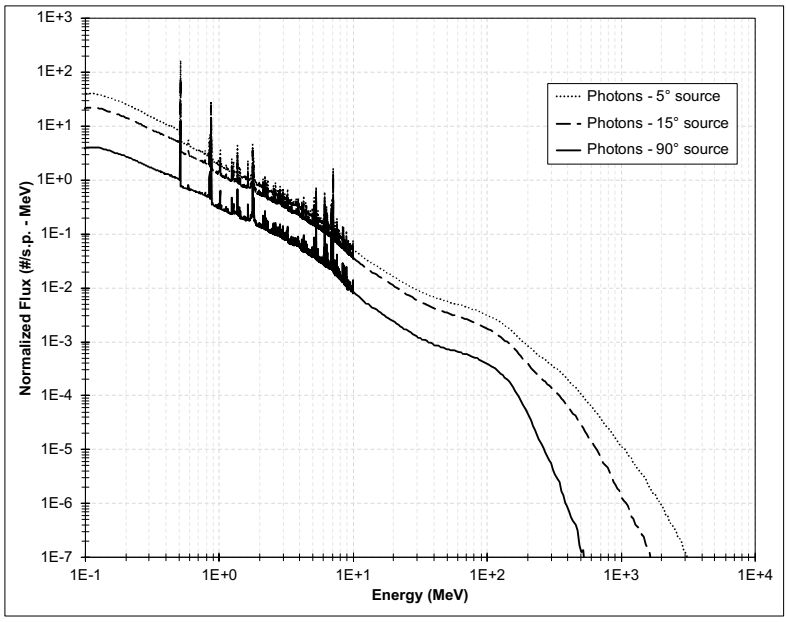

Figure 3.35. The energy distribution of albedo photons from three monodirectional source terms pointing towards the regolith: 5 degrees off lunar surface, 15 degrees off lunar surface, and directly downward 90-degree source term.

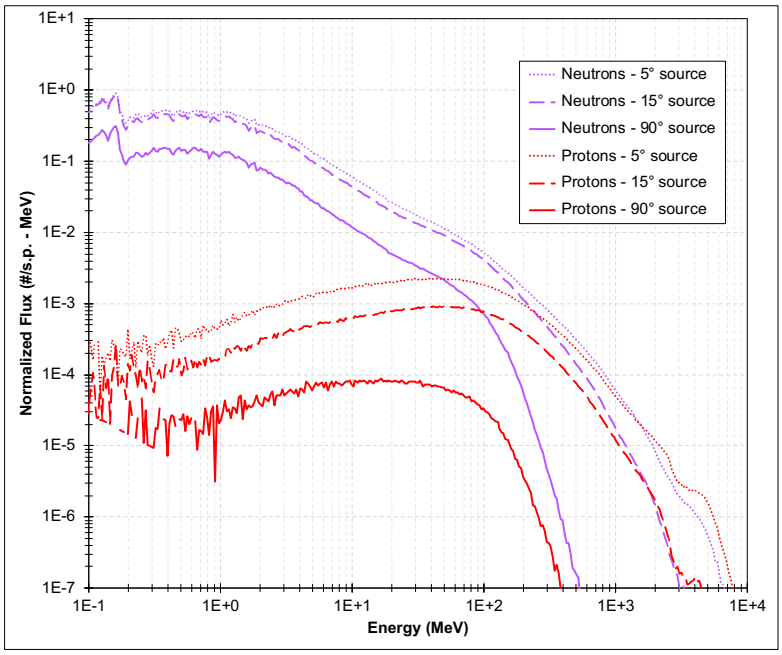

Figure 3.36. The energy distribution of albedo neutrons and protons from three monodirectional source terms pointing towards the regolith: 5 degrees off lunar surface, 15 degrees off lunar surface, and directly downward 90-degree source term.

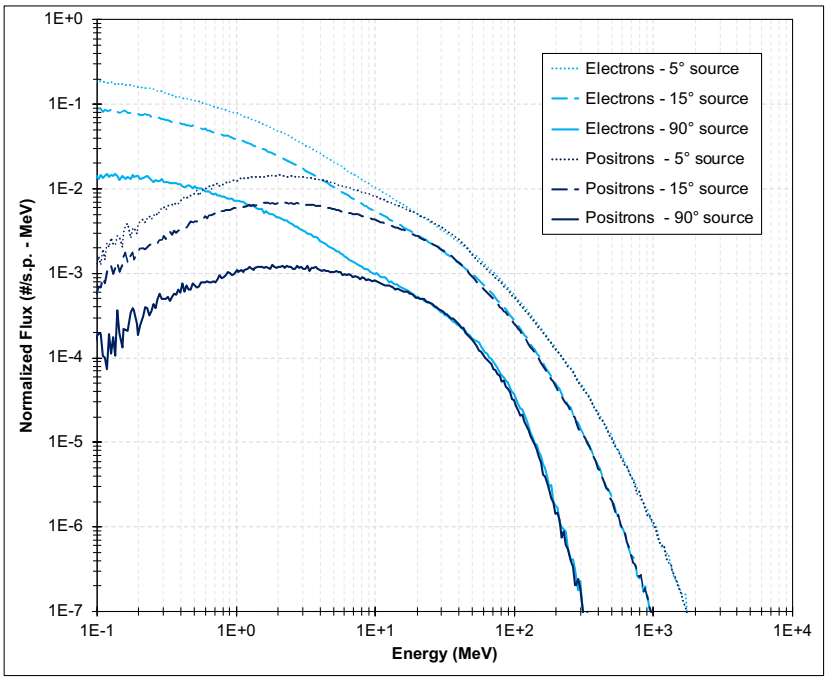

Figure 3.37. The energy distribution of albedo electrons and positrons from three monodirectional source terms pointing towards the regolith: 5 degrees off lunar surface, 15 degrees off lunar surface, and directly downward 90-degree source term.

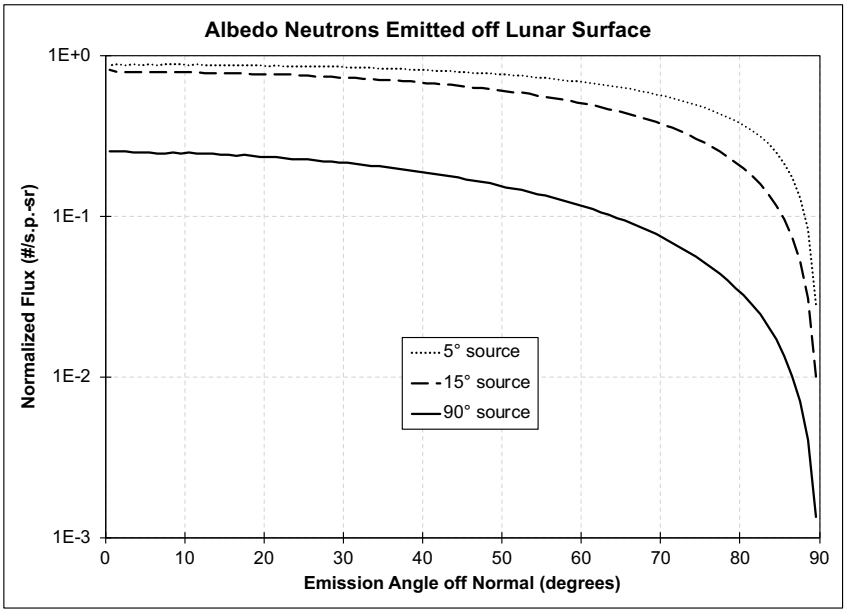

Figure 3.38. The angular distribution of albedo neutrons from three monodirectional source terms pointing towards the regolith: 5 degrees off lunar surface, 15 degrees off lunar surface, and directly downward 90-degree source term.

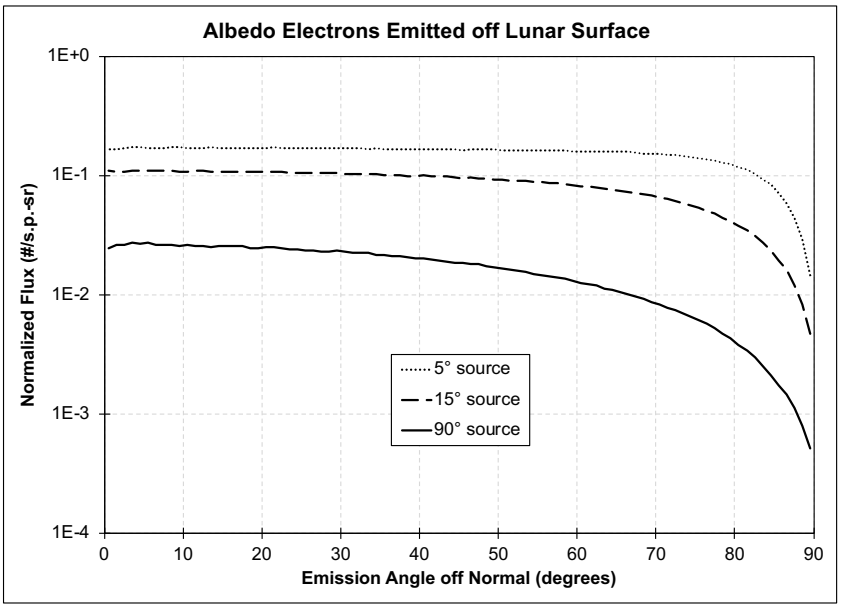

Figure 3.39. The angular distribution of albedo electrons from three monodirectional source terms pointing towards the regolith: 5 degrees off lunar surface, 15 degrees off lunar surface, and directly downward 90-degree source term.

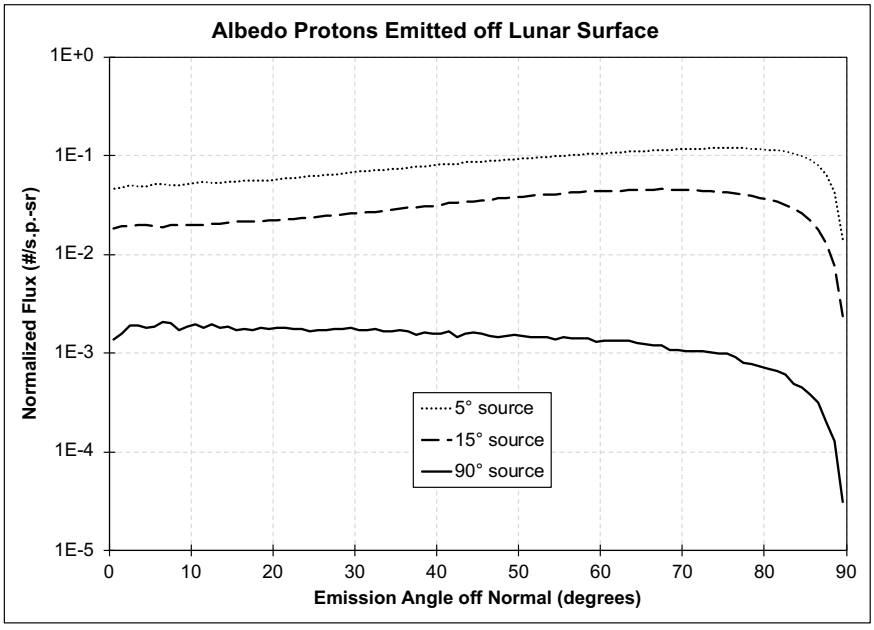

Figure 3.40. The angular distribution of albedo protons from three monodirectional source terms pointing towards the regolith: 5 degrees off lunar surface, 15 degrees off lunar surface, and directly downward 90-degree source term.

4. ALBEDO PARTICLES EMITTED BY WET REGOLITH

This chapter discusses the results of albedo particles emitted by different scenarios of wet regolith. Since albedo protons from wet regolith are of importance to the CRaTER instrument, they will be primarily discussed in this chapter. All the scenarios of wet regolith addressed here are illustrated in Figure 2.1.

4.1 Energy Distribution of Albedo Particles

The energy distribution of albedo particles from a fully wet and a fully dry regolith, illustrated in Figure 4.1, shows minor differences in the behavior of albedo electrons, positrons, and photons, and significant variations in the behavior of albedo protons and neutrons. The flux of albedo photons decreases slightly at lower energies, which is expected since hydrogen replaces the heavier elements in the regolith. The decrease in high-z elements leads to a lower production of photons by bremsstrahlung and neutron interactions. The general suppression of photons between 100 keV and ~2 MeV should not to be viewed as a distinct characteristic of hydrogen in the regolith, because it applies to an increased abundance of other low-z materials as well. The characteristic 2.22-MeV gamma ray peak of hydrogen, which is the energy released following the neutron capture by a hydrogen atom, was not distinctively observed in the wet scenarios of the simulations.

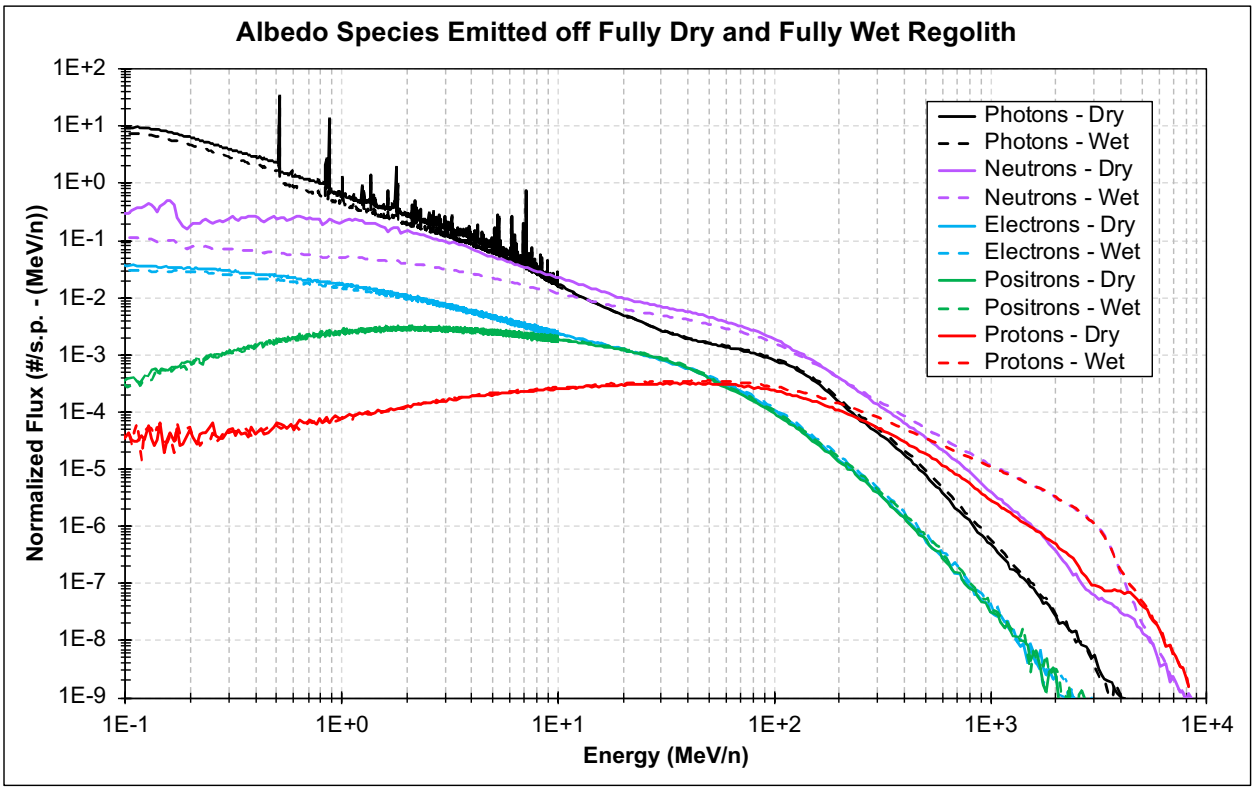

Figure 4.1 The energy distribution of albedo protons, neutrons, electrons, and positrons emitted from a fully dry and fully wet regolith.

The decrease in albedo neutron flux in wet regolith is due to the moderation effects created by the neutron-proton nuclear scattering. Significantly more neutrons are escaping the surface from a dry regolith, while many more neutrons are reaching the lower energy cutoff in a wet regolith. However, it is not clear why an increase in albedo neutron flux is seen above 200 MeV in a wet regolith. MCNP6 reports a higher neutron production created from nuclear interactions in a dry regolith (~28 per source particle) than a wet regolith (~17 per source particle) which is expected due to the presence of more high-z material. The increase in albedo neutrons above 200 MeV could be an artifact of the MCNP6 version 1 code, and further investigation is required to understand this abnormal behavior.

The behavior of high-energy albedo protons is enhanced when hydrogen is present in the regolith. The simulations show that the increased production of protons in the wet regolith is caused by recoil elastic scattering. Thus, when heavy GCR ions break up in the regolith, they produced energetic neutrons and protons, which in turn push the hydrogen nuclei in upper layers of the regolith out of the surface, creating an enhanced albedo proton flux. When simulating only GCR protons as a source term, no significant changes in the albedo proton flux were observed.

4.2 Albedo Protons

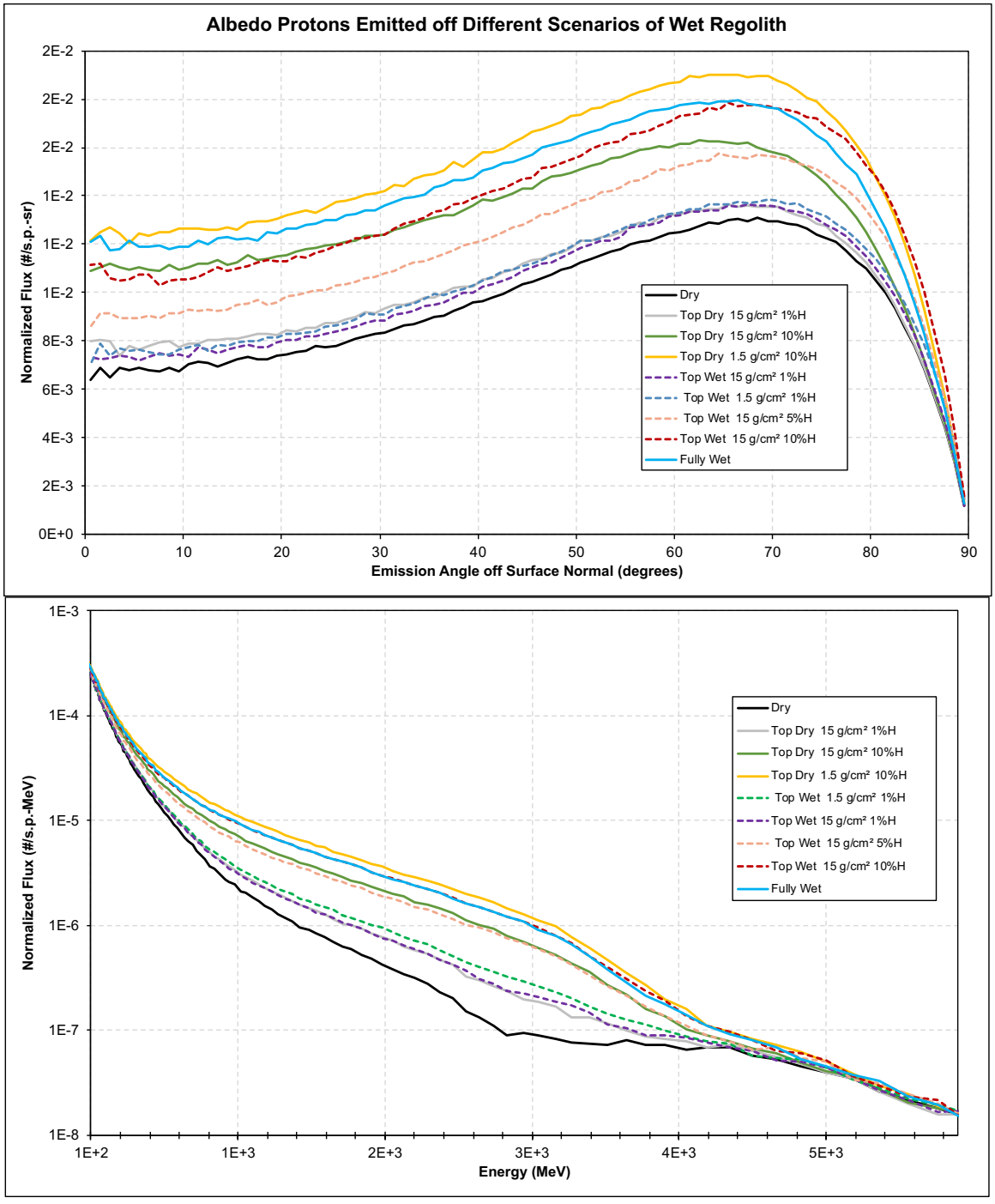

Figure 4.2 The angular (top) and energy (bottom) distribution of albedo protons emitted off dry and various scenarios of wet regolith.

The angular distributions of albedo protons in all the scenarios studied in this work are presented in Figure 4.2. In all angles, the dry regolith produces the least relative amount of albedo protons. Interestingly, a regolith with a 1.5-g/cm^2 top dry layer above a 10% wet regolith produces the highest number of albedo protons at most angles. Recall that the simulated fully wet regolith gradually increases in hydrogen concentration. At 5 g/cm^2, the weight fraction of hydrogen is 4% in the fully wet regolith and 10% in the top dry case (the yellow curve in Figure 4.2). A similar trend is observed in the energy spectrum in Figure 4.2, where the yellow curve dominates for almost all energies. Also, at 70 degrees off normal, the case for a top 10% wet 15-g/cm^2 layer above dry regolith (red dotted curve) starts dominating over the fully wet case for the albedo proton spectrum. This implies that the location of high concentrations of hydrogen is a crucial factor for albedo proton production, especially in the upper 15 g/cm^2 layer. Another interesting trend is observed when comparing a top 5% wet 15 g/cm^2 layer (pink dotted curve) with a top dry 15 g/cm^2 dry layer above 10% wet regolith (green curve). Both cases have similar energy spectra; however, the angular distribution shows that the top dry case dominates over the top wet case up to 70 degrees off normal. This indicates that the maximum fragmentation of GCR ions happens in deeper locations within the regolith, and when deeper hydrogen gets knocked out of the lunar surface, it is affected by the probability of propagating though the lunar regolith and thus more protons are observed going straight up (the shortest distance to surface). Therefore, if an instrument is pointing at the nadir, it has a high probability of probing deep in the regolith. Figures 4.3 to 4.7 give an insight to the maximum production depth distribution for multiple scenarios of wet regolith. In each of these figures, the depth distribution of the dry regolith is included at the top for comparison. Figure 4.3 shows the behavior of a fully wet regolith, where the hydrogen content increases gradually with depth. It is clear that there is an increased flux of high energy protons that remains

constant until it drops sharply below ~20 g/cm^2. On the other hand, Figure 4.4 shows the behavior of the top 10% wet 15-g/cm^2 layer case. Here, more high energy protons are observed relative to the fully wet case at the upper 5 g/cm^2 layer of the regolith. A significant drop follows below 15 g/cm^2, which is the boundary line between wet and dry regolith. Figure 4.5 illustrates the behavior of the top 1% wet 10-cm layer, and it shows no significant enhancements in albedo proton flux. This is also apparent in Figure 4.1 where although the cases with 1% H show some increase in albedo protons flux, this increase is too small relative to the 10% case. This indicates that not only is the location of lunar hydrogen is very important, but also its concentration in the regolith. Finally, Figures 4.6 and 4.7 present the maximum depth distribution of scenarios with a top dry layer above a 10% wet regolith. In both cases, the enhancement in albedo proton flux appears to come directly from the wet side of the regolith. A sharp increase in the behavior of albedo proton production processes is observed beyond the boundary line between dry and wet regolith, implying again that these are the product of the elastic scattering between lunar hydrogen and fragmented GCR protons and neutrons.

To sum up, MCNP6 results show that the flux of albedo protons increases when GCR ions heavier than protons interact with a wet regolith. Although it is possible that the fluxes of albedo protons from a wet regolith are exaggerated by artifacts in the code, the mechanism of albedo protons production through elastic scattering is reasonable. The analyses show the importance of the magnitude of hydrogen concentrations in the upper 15 g/cm^2 layer of the regolith.

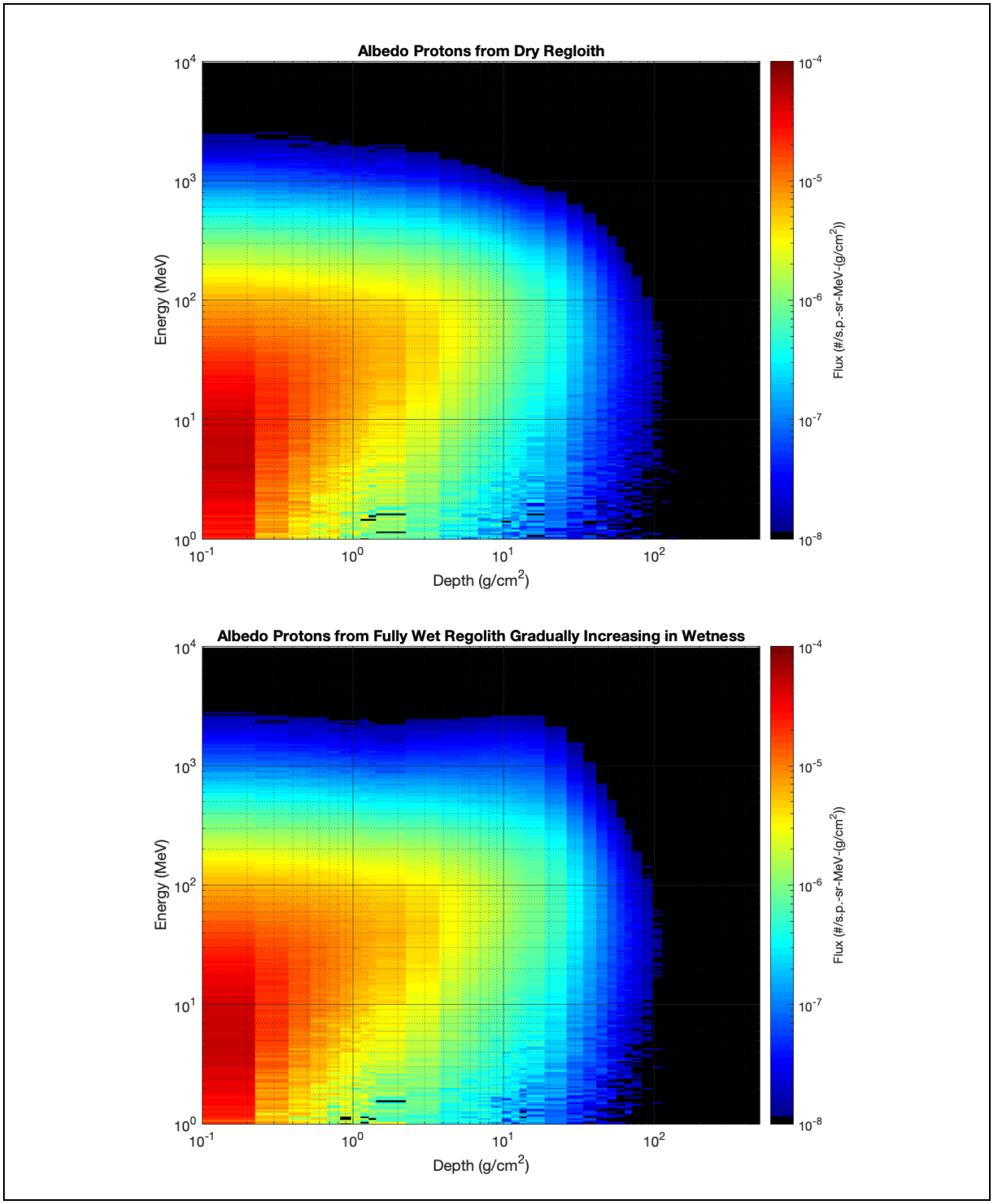

Figure 4.3 The maximum depth distribution of albedo protons emitted by a fully dry (top) and a fully wet (bottom) regolith.

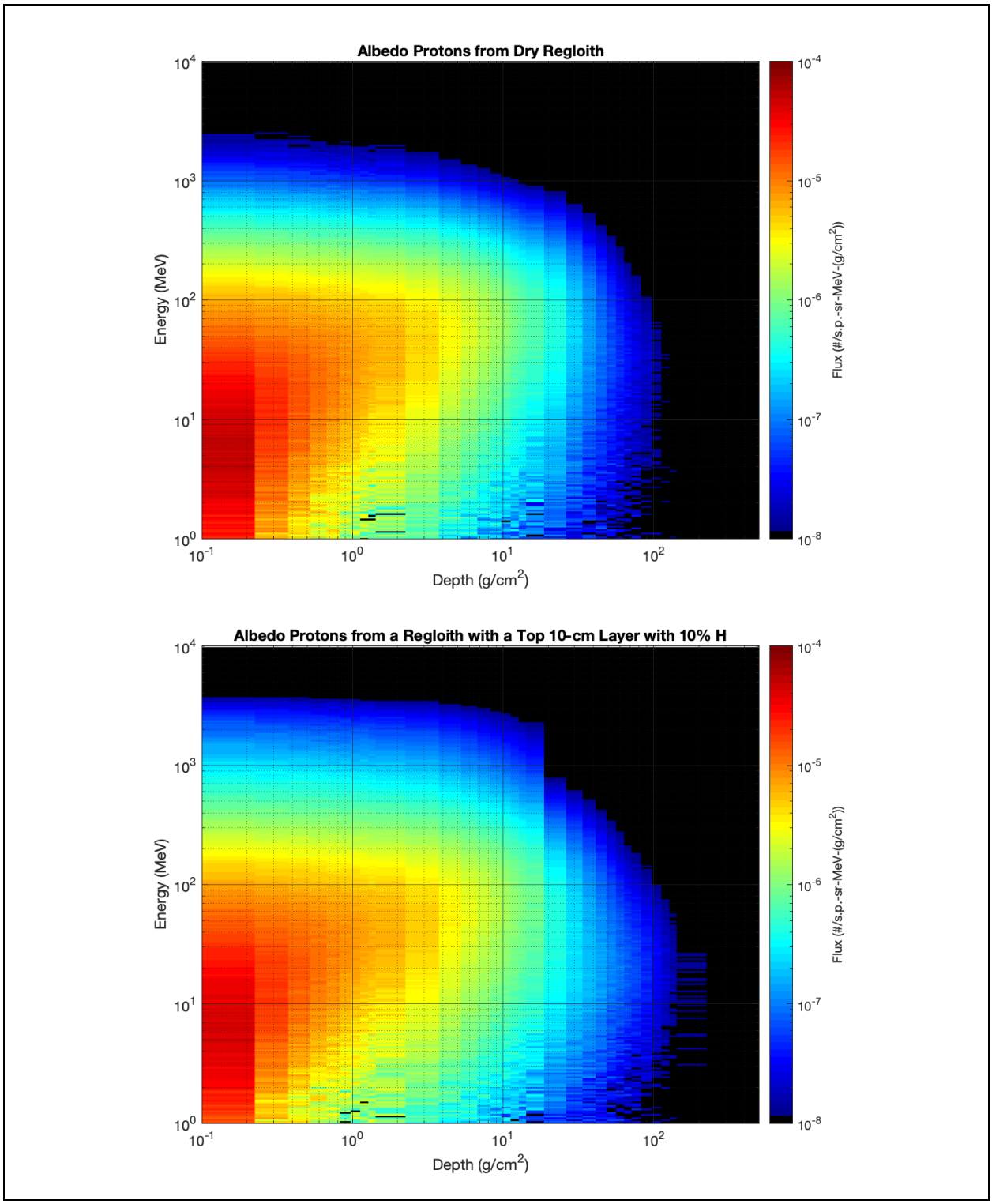

Figure 4.4 The maximum depth distribution of albedo protons emitted by a fully dry regolith (top) and a regolith with top-10 cm wet layer with 10% H (bottom).

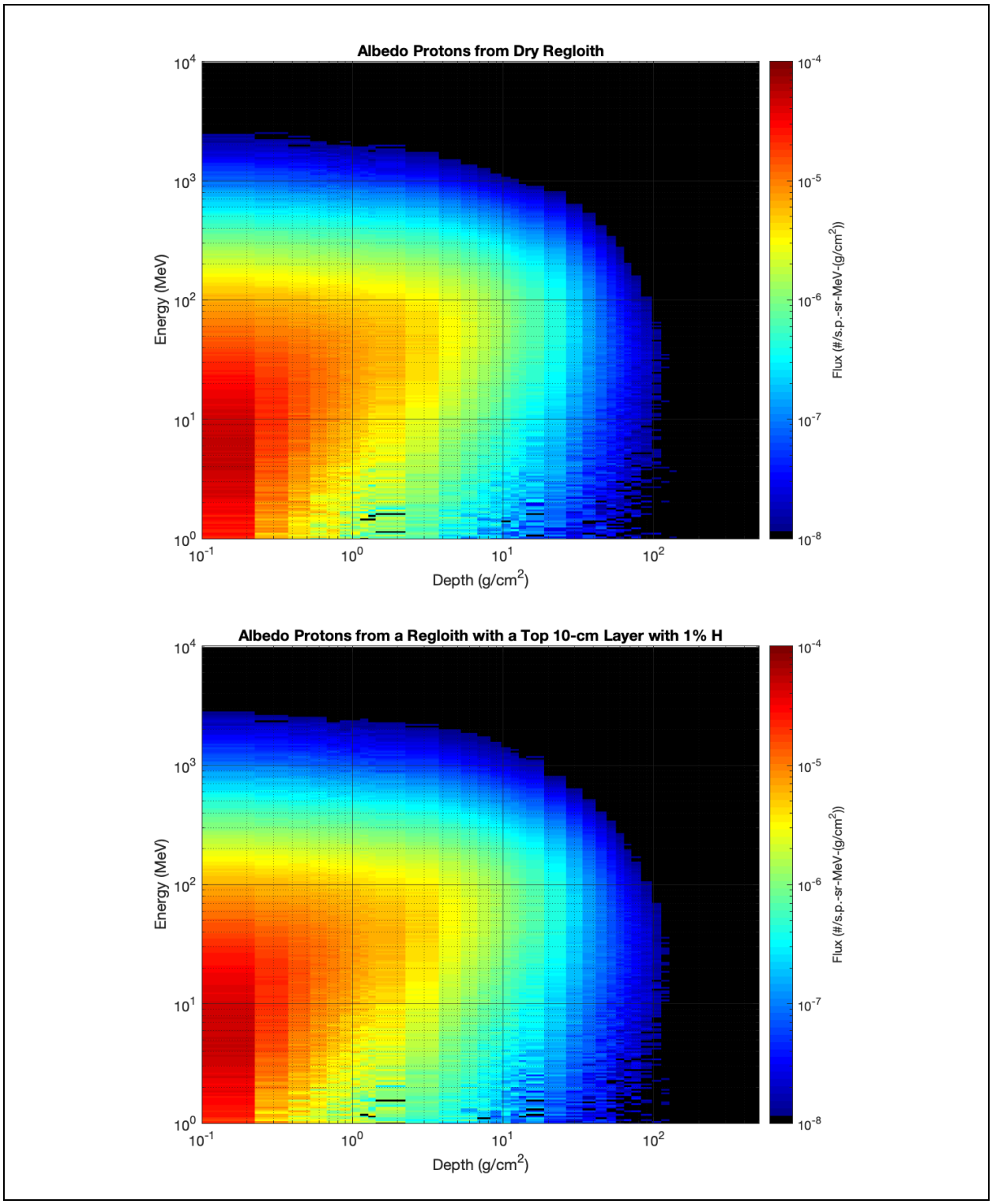

Figure 4.5 The maximum depth distribution of albedo protons emitted by a fully dry regolith (top) and a regolith with a top 10-cm wet layer with 1% H (bottom).

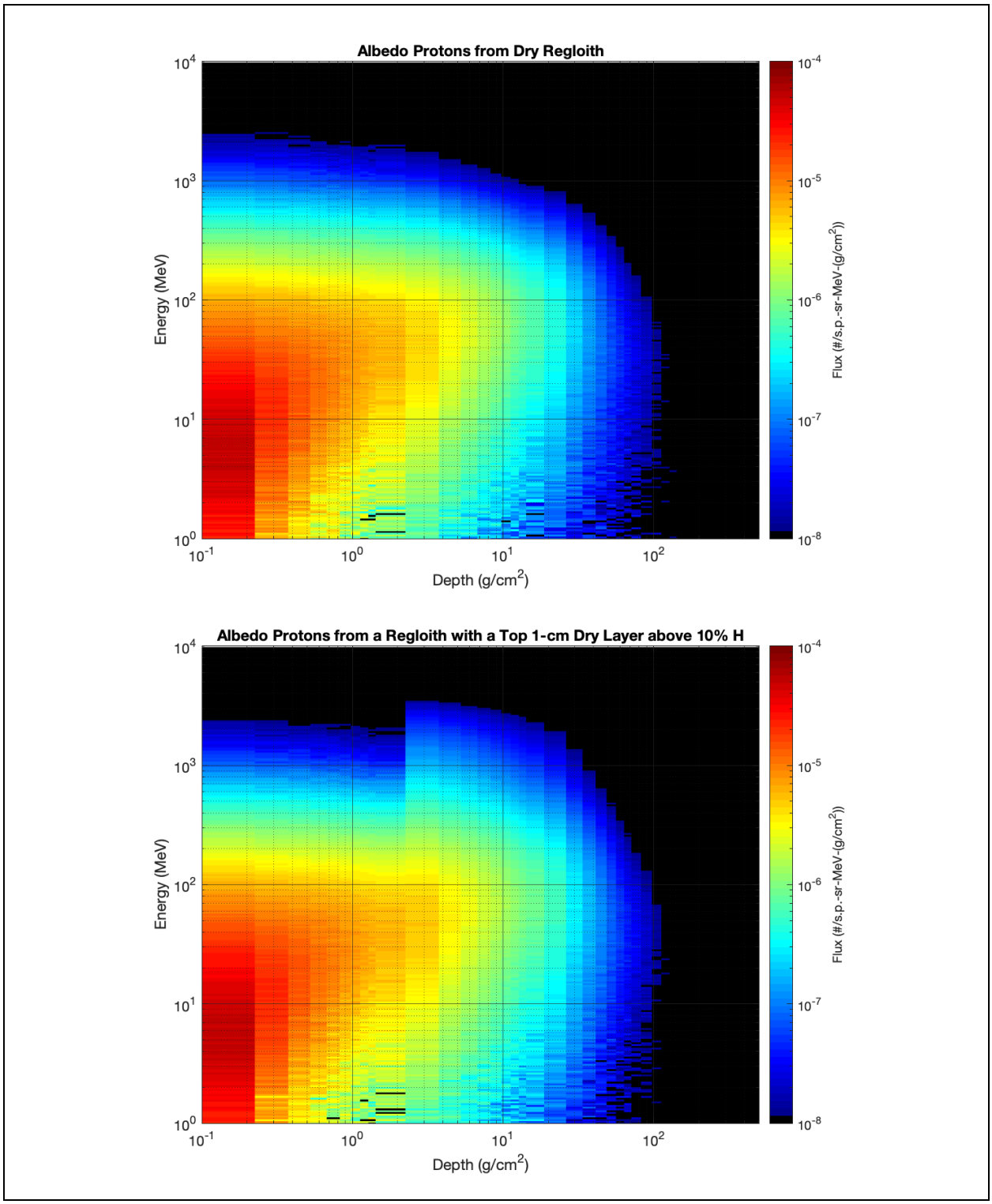

Figure 4.6. The maximum depth distribution of albedo protons emitted by a fully dry regolith (top) and a regolith with top dry 1-cm layer above a wet regolith with 10% H (bottom).

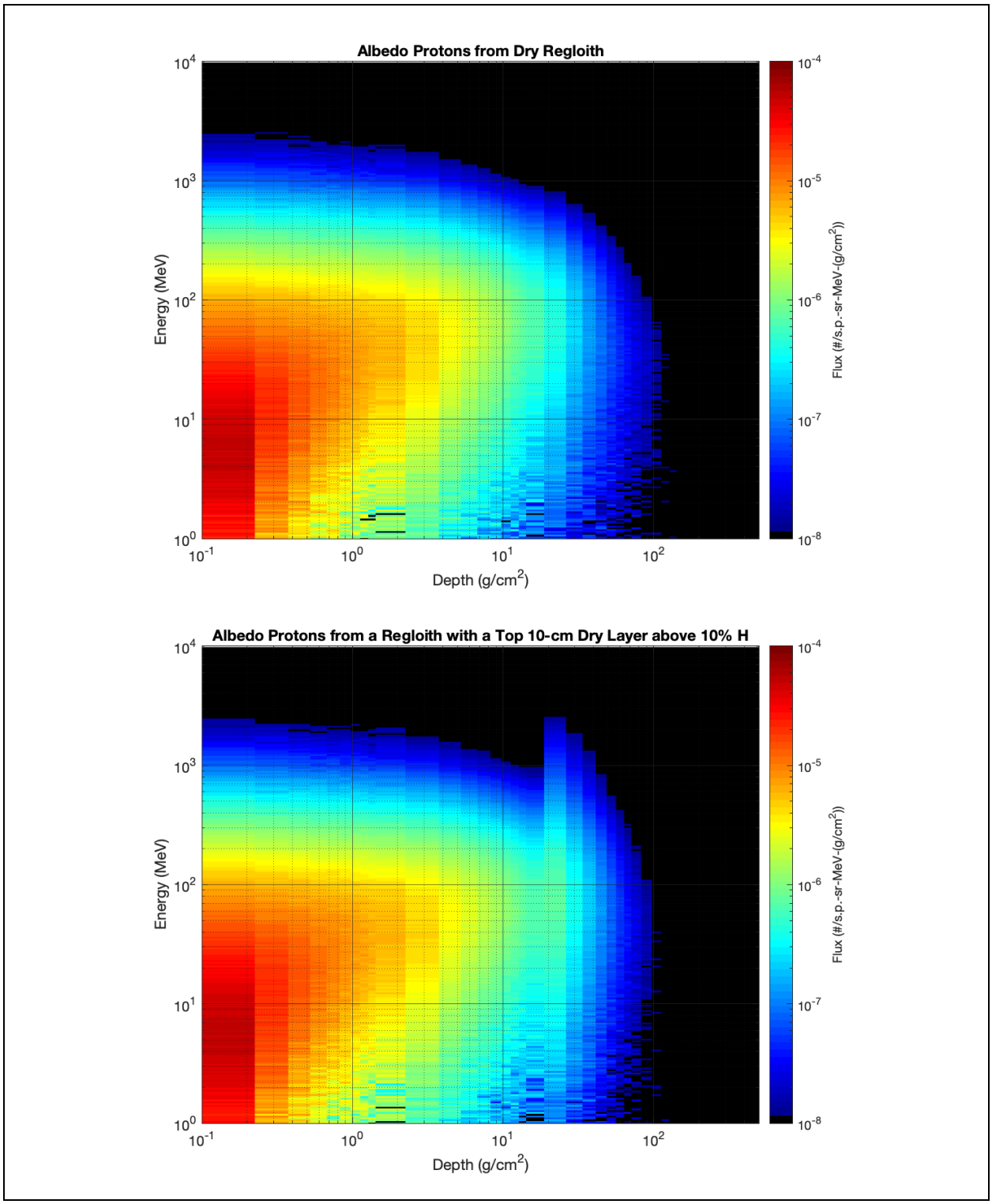

Figure 4.7 The maximum depth distribution of albedo protons emitted by a fully dry regolith (top) and a regolith with top dry 10-cm layer above a wet regolith with 10% H (bottom).

5. CHARACTERIZATION OF MAJOR LUNAR ELEMENTS

This chapter presents the changes in the behavior of albedo particles emitted by different scenarios of regolith with increased content of major lunar elements. Each of the scenarios studied contains an additional 10% weight fraction of one of the major lunar elements. This chapter answers the question: what happens to the behavior of albedo particles if there was an increased content of oxygen, sodium, magnesium, aluminum, silicon, calcium, manganese, titanium, or iron in the lunar regolith?

5.1 Albedo Charged Particles

Figures 5.1 and 5.2 show the behavior of albedo electrons and positrons respectively, where no obvious changes are observed in the increased abundance of any major lunar element. This implies that albedo electrons and positrons with energies above 100 keV might not be a suitable candidate for lunar regolith characterization.

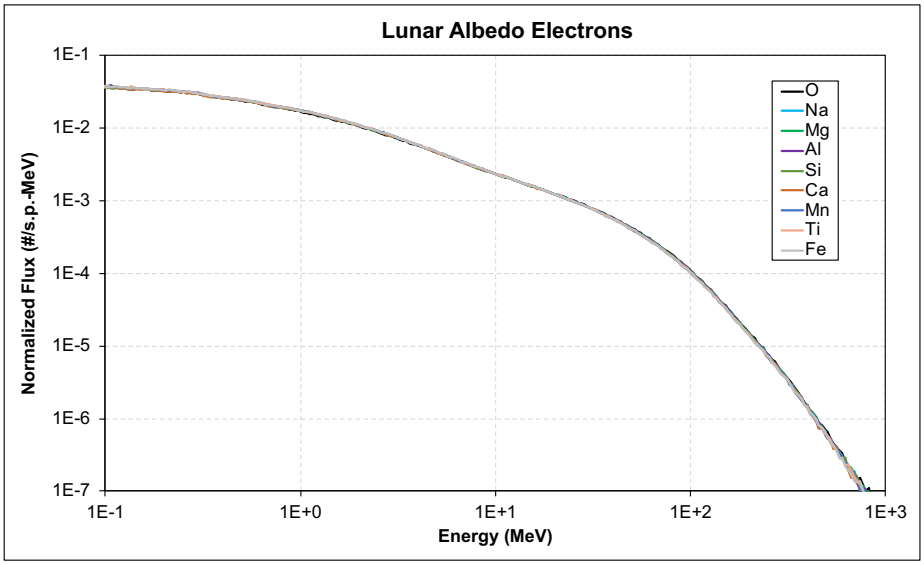

Figure 5.1. The energy spectrum of albedo electrons emitted from nine different scenarios, each with a modeled regolith that has an increased content of the specified element.

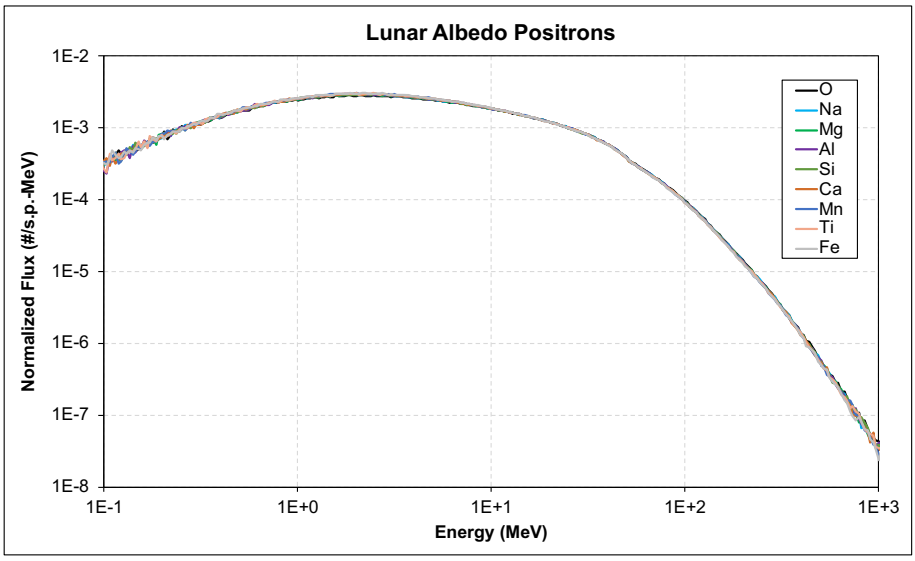

Figure 5.2. The energy spectrum of albedo positrons emitted from nine different scenarios, each with a modeled regolith that has an increased content of the specified element.

The behavior of albedo protons is illustrated in Figure 5.3. Similar to other charged particles, no apparent changes are observed in any of the major elements. This is in contrast with regolith that is rich with hydrogen as seen in the previous chapter, which showed an enhancement in albedo proton flux. It is worth noting that a recent paper studying measurements made by the CRaTER instrument, which is susceptible to albedo protons, showed visible mare features of the lunar regolith (Wilson et al., 2020). The results of this MCNP6 simulation hereby suggest that albedo protons are probably not the reason behind the variations in the lunar map observed by the CRaTER instrument. Figure 5.4 shows the behavior of albedo deuterons, which also does not show any distinctive changes in the fluxes of any modeled scenario. Last, the behavior of albedo alpha particles is presented in the Figure 5.5. Although the statistics are not high enough to conclude that the behavior of a certain lunar element stands out, all scenarios show a similar trend in general and thus albedo alphas might also not be a suitable candidate for the elemental characterization of the lunar regolith.

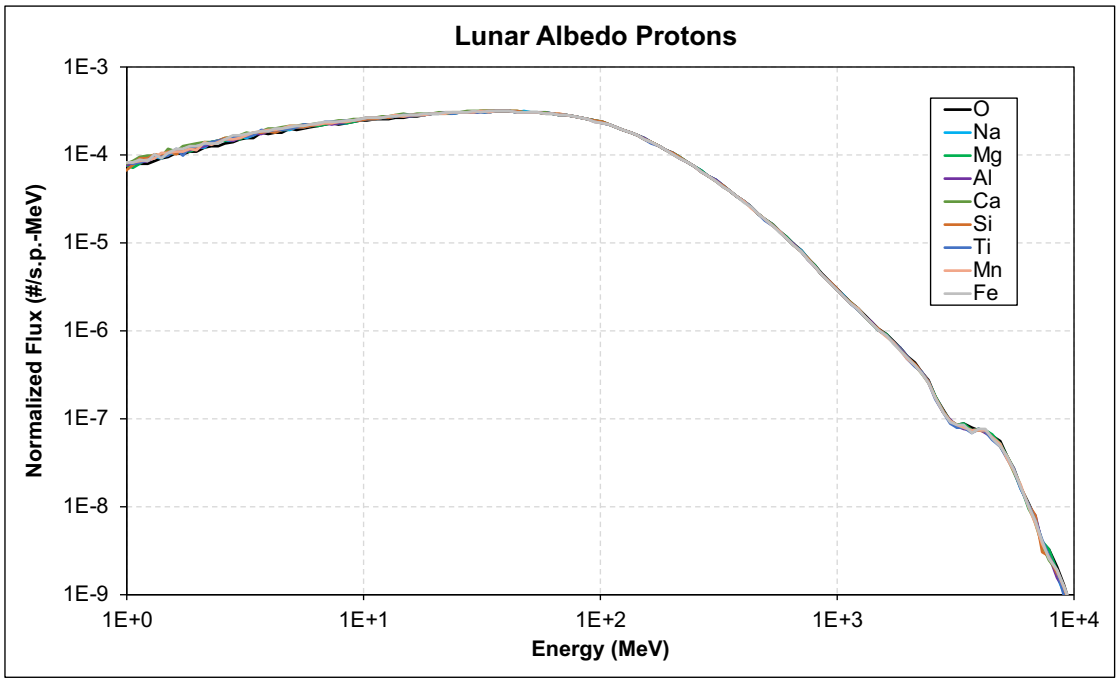

Figure 5.3. The energy spectrum of albedo protons emitted from nine different scenarios, each with a modeled regolith that has an increased content of the specified element.

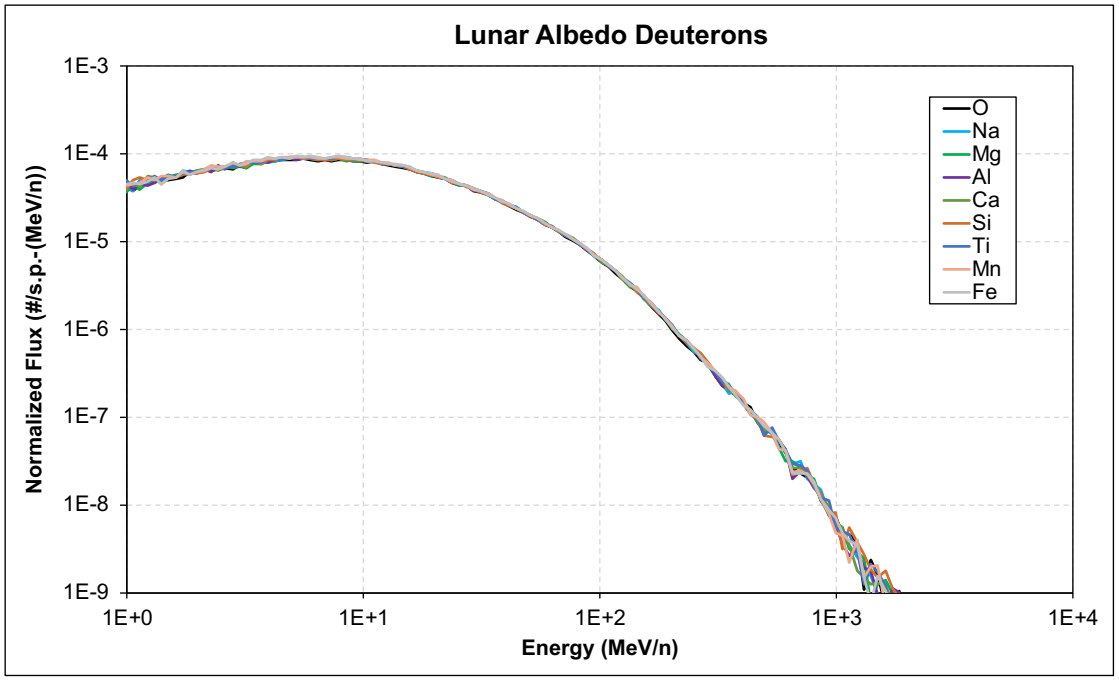

Figure 5.4 The energy spectrum of albedo deuterons emitted from nine different scenarios, each with a modeled regolith that has an increased content of the specified element.

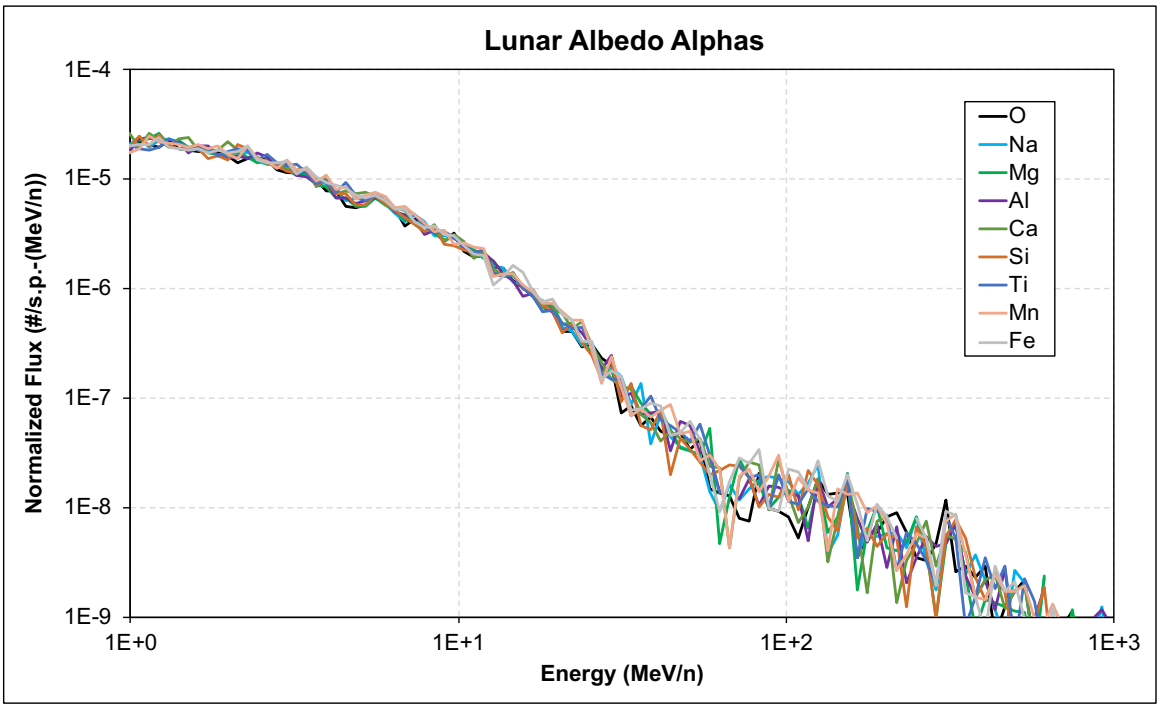

Figure 5.5. The energy spectrum of albedo alphas emitted from nine different scenarios, each with a modeled regolith that has an increased content of the specified element.

5.2 Albedo Neutrons

The behavior of albedo neutrons is presented in Figure 5.6. Variations in the behavior of albedo neutrons start to be distinctive for albedo neutrons with energies below 10 MeV. These energies lie in the resonance regions of the neutron reaction cross sections. The energy and strength of the resonance peaks are highly dependent on the type of element scattering the neutron. Thus, although albedo neutrons with higher energies do not show any variations with any major lunar element, neutrons with energies below 10 MeV (and even more so with energies below 1 MeV) show distinctive features that help in characterizing the elemental composition of the lunar regolith if the absorption and scattering cross sections were taken into consideration.

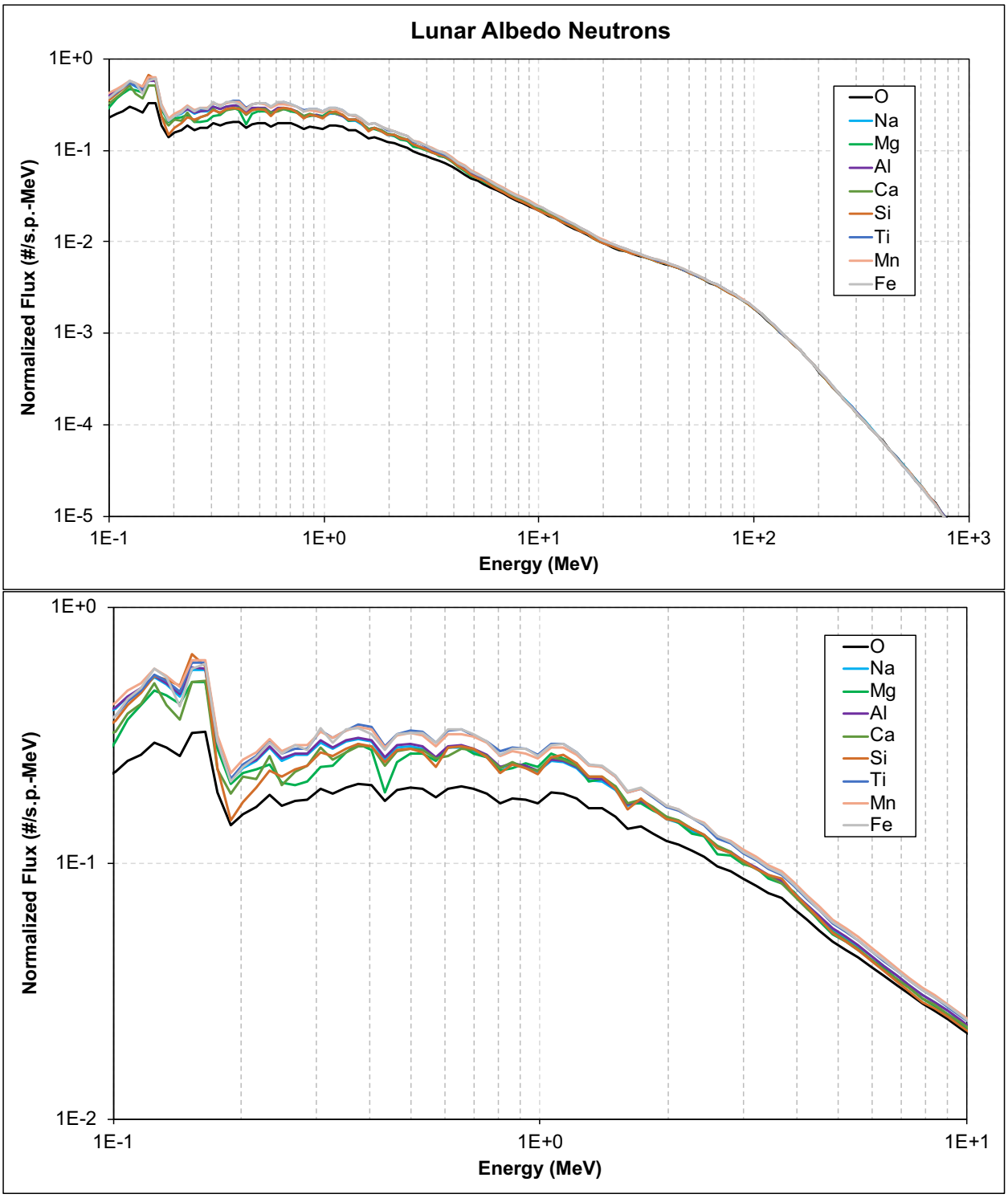

Figure 5.6. The energy spectrum of albedo neutrons emitted from nine different scenarios, each with a modeled regolith that has an increased content of the specified element for all energies studied (top) with a focus on the low energy part of the spectrum (bottom).

5.3 Albedo Photons

Along with low-energy albedo neutrons, albedo photons are excellent candidates for the characterization of lunar elemental composition. Figure 5.9 shows variations in many photopeaks, each being a characteristic of a specific lunar element. To better assess the variations in these photopeaks, the fractional difference in the albedo photon flux between each enriched scenario and the dry regolith has been calculated and presented in Figures 5.8 to 5.18. The specific neutron reactions leading to the release of the characteristic albedo photopeaks added to some of the figures were obtained from *[Reedy, 1978]*. However, the reactions leading to other distinctive photopeaks are yet to be determined. In general, neutral particles are the frontrunners for elemental characterization of lunar regolith due to the low-energy neutron interactions with the nuclei of the lunar elements. The albedo charged particles studied in this work with energies above 100 keV did not show any observable differences that might be useful for spectroscopy purposes.

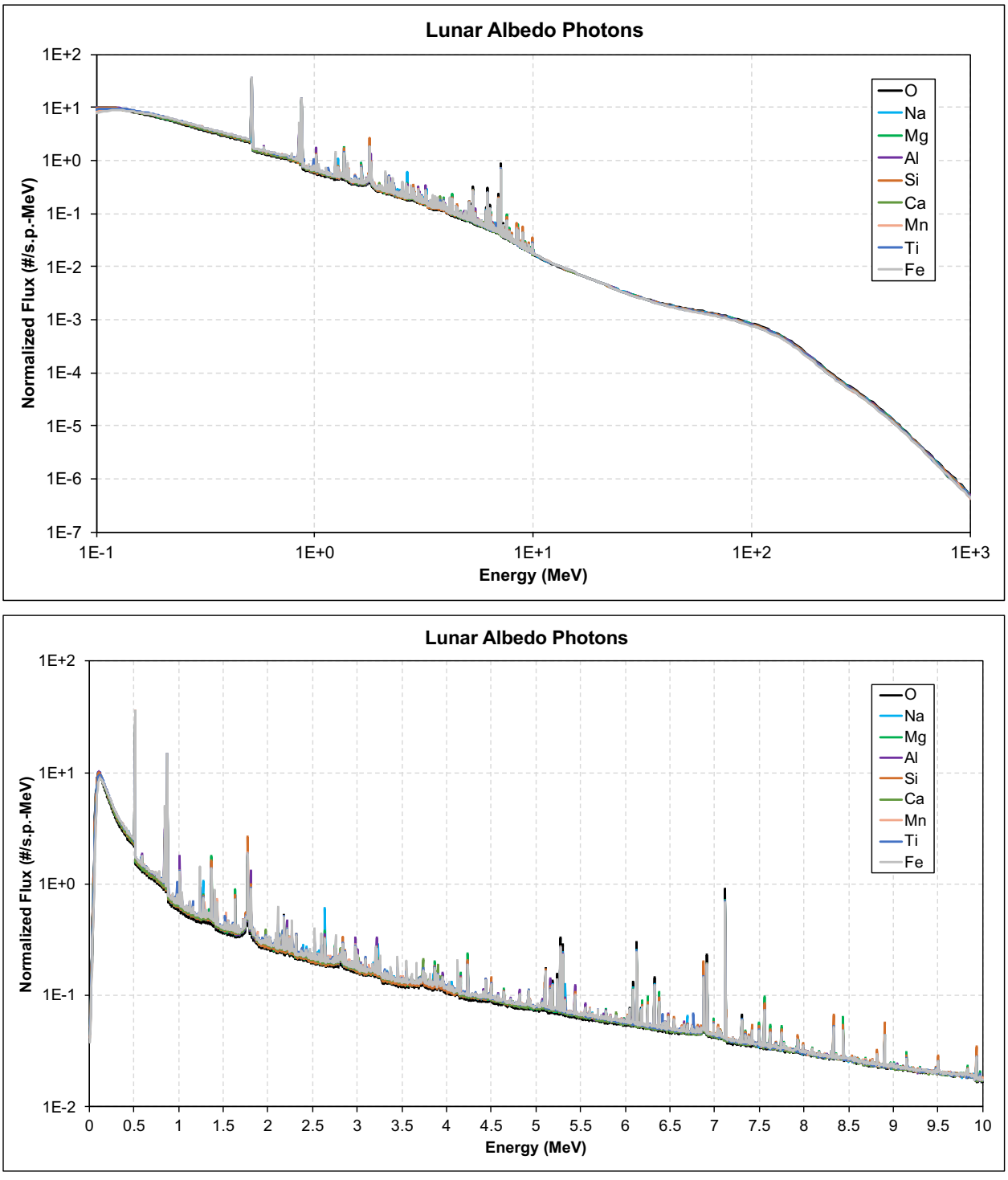

Figure 5.7. The energy spectrum of albedo photons emitted from nine different scenarios, each with a modeled regolith that has an increased content of the specified element for all energies studied (top) with a focus on the low energy part of the spectrum (bottom).

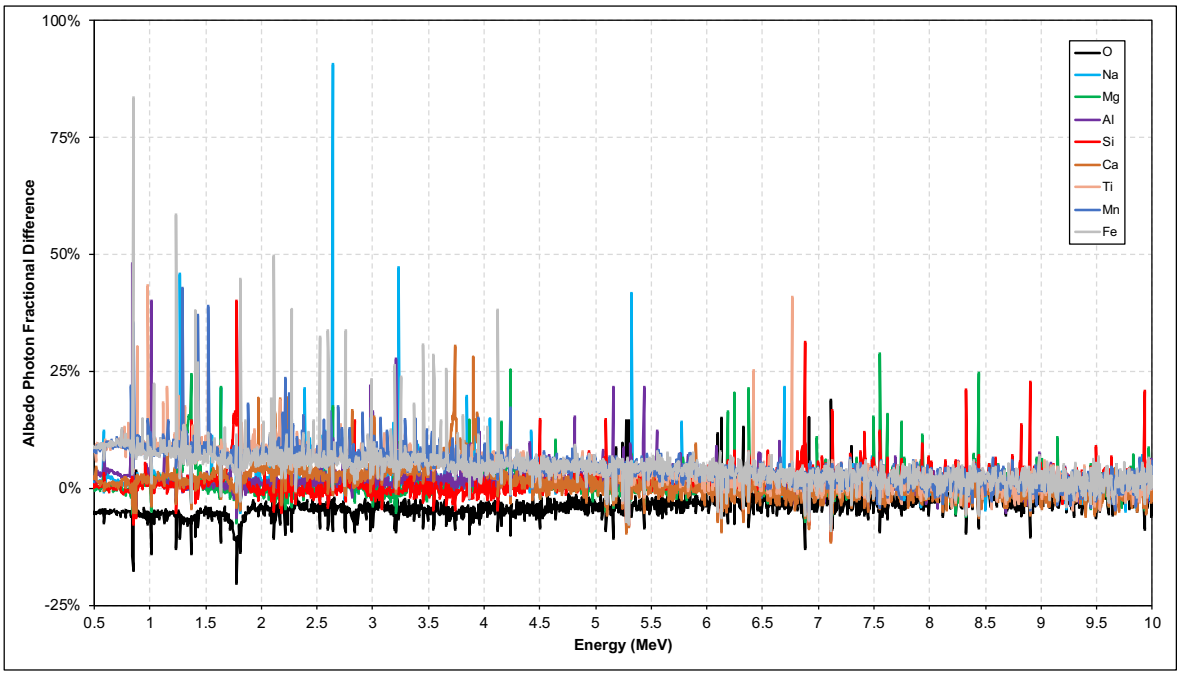

Figure 5.8. The fractional difference in the albedo photon flux of regolith that has an increased content of the specified element vs dry regolith.

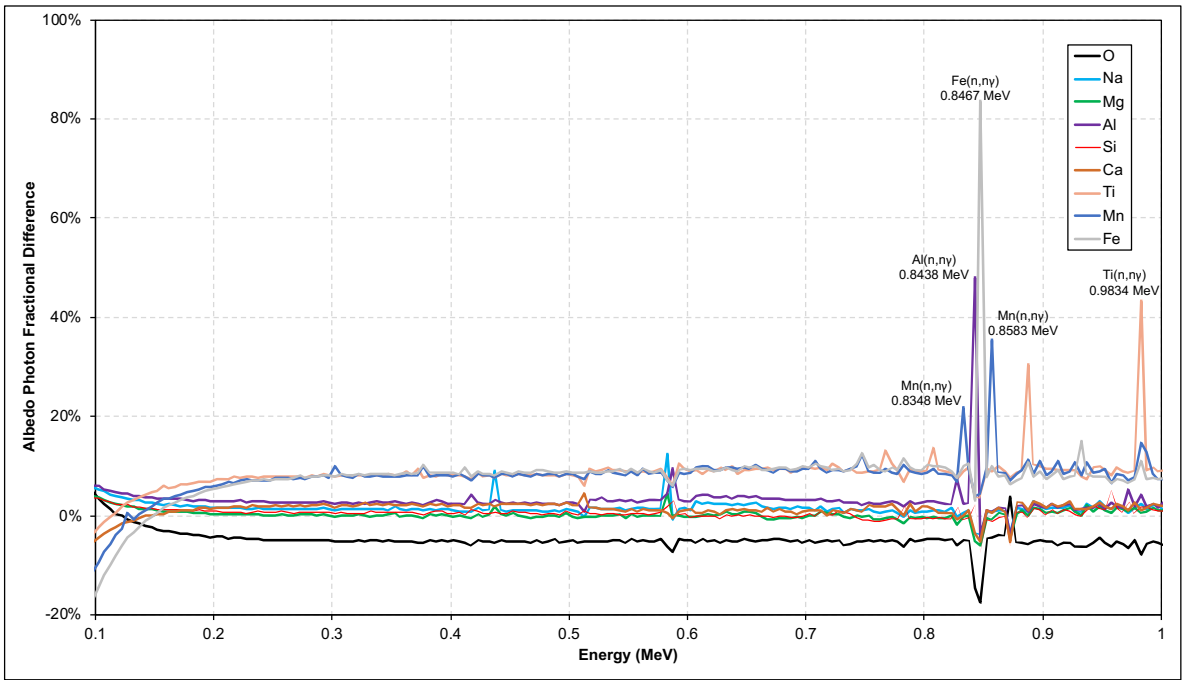

Figure 5.9. The fractional difference in the albedo photon flux of regolith that has an increased content of the specified element vs dry regolith for albedo photon energies below 1 MeV. The neutron reactions leading the chosen photopeaks are obtained from [*Reedy, 1978]*.

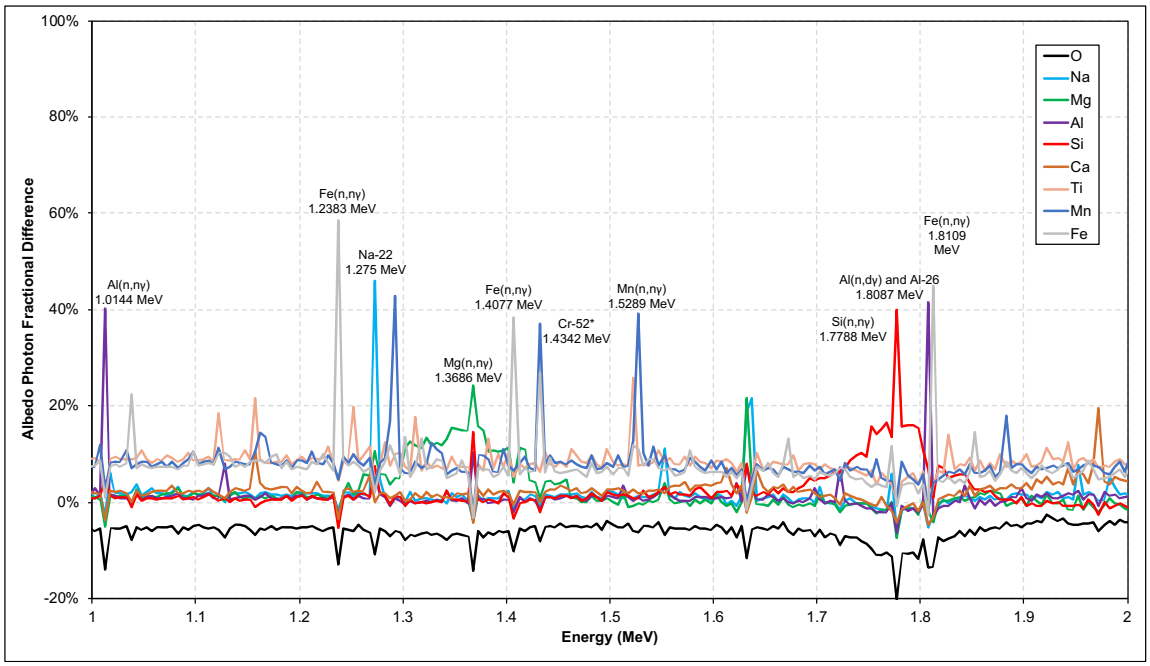

Figure 5.10. The fractional difference in the albedo photon flux of regolith that has an increased content of the specified element vs dry regolith for albedo photon energies between 1 and 2 MeV. The neutron reactions leading the chosen photopeaks are obtained from [*Reedy, 1978]*.

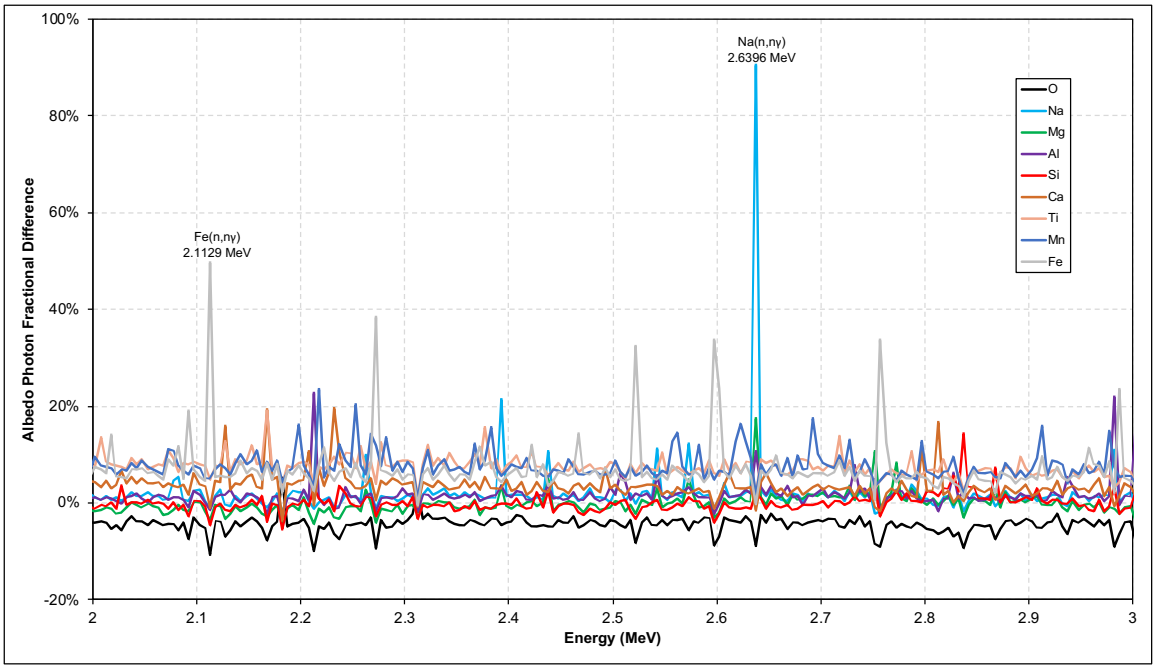

Figure 5.11. The fractional difference in the albedo photon flux of regolith that has an increased content of the specified element vs dry regolith for albedo photon energies between 2 and 3 MeV. The neutron reactions leading the chosen photopeaks are obtained from [*Reedy, 1978]*.

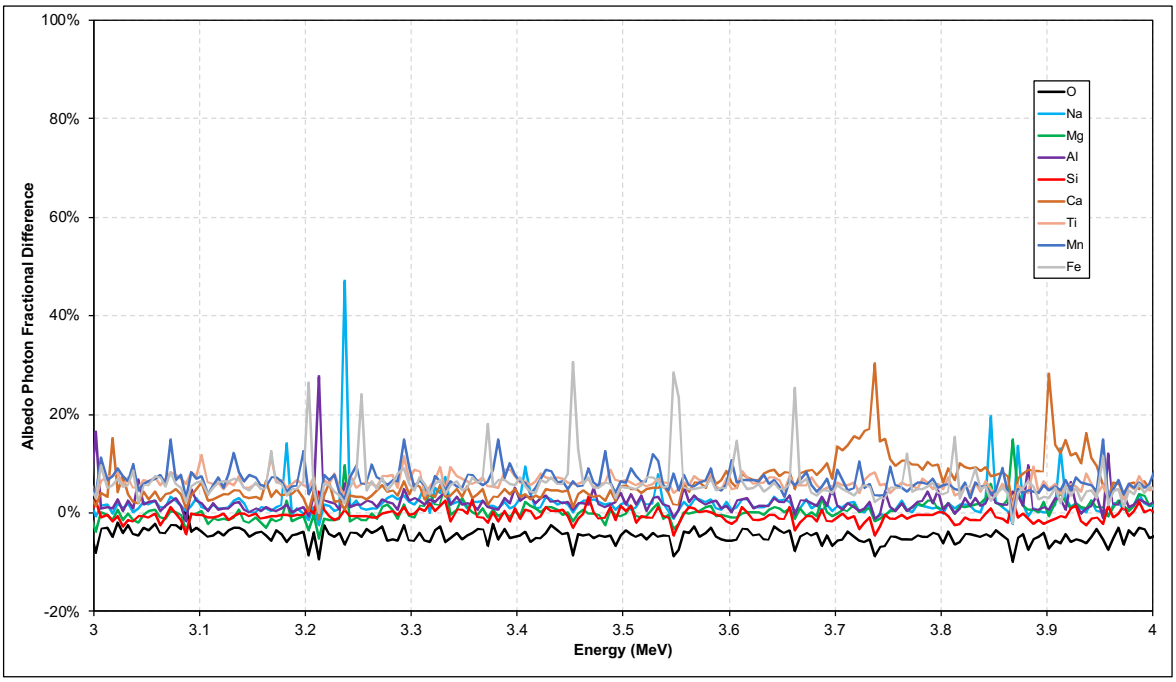

Figure 5.12. The fractional difference in the albedo photon flux of regolith that has an increased content of the specified element vs dry regolith for albedo photon energies between 3 and 4 MeV.

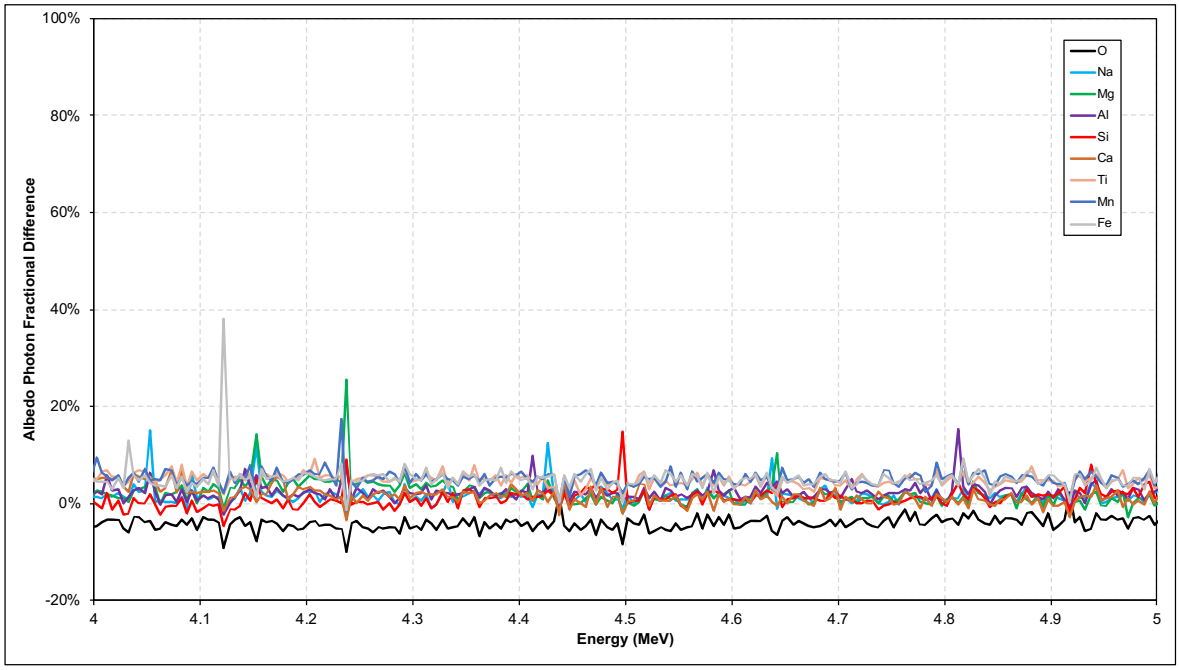

Figure 5.13. The fractional difference in the albedo photon flux of regolith that has an increased content of the specified element vs dry regolith for albedo photon energies between 4 and 5 MeV.

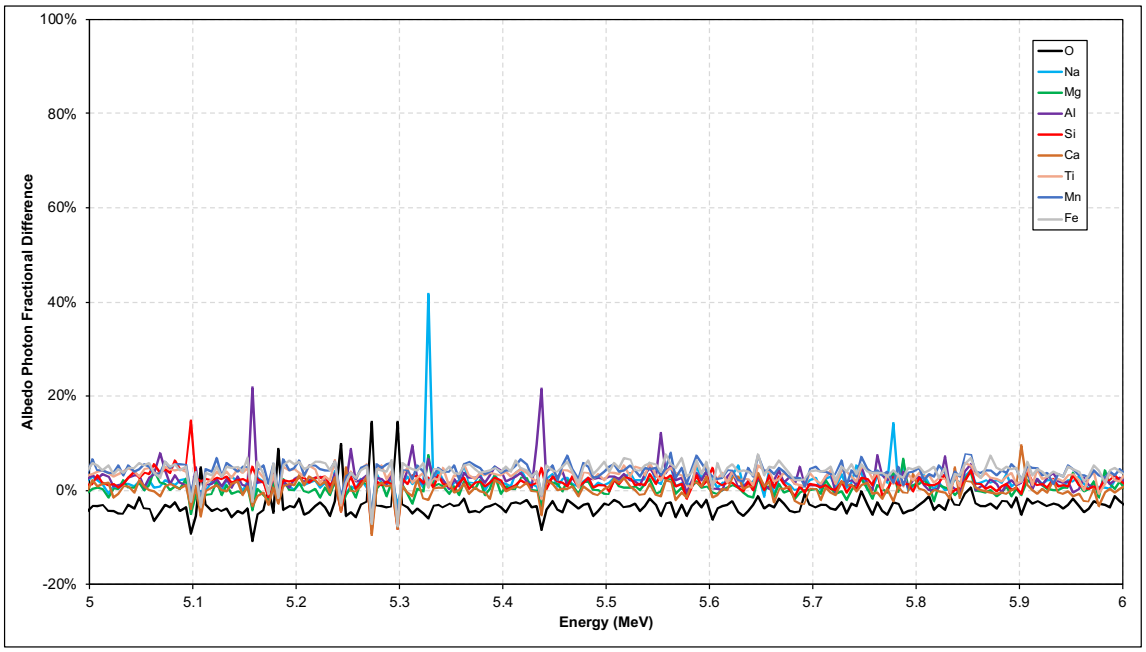

Figure 5.14. The fractional difference in the albedo photon flux of regolith that has an increased content of the specified element vs dry regolith for albedo photon energies between 5 and 6 MeV.

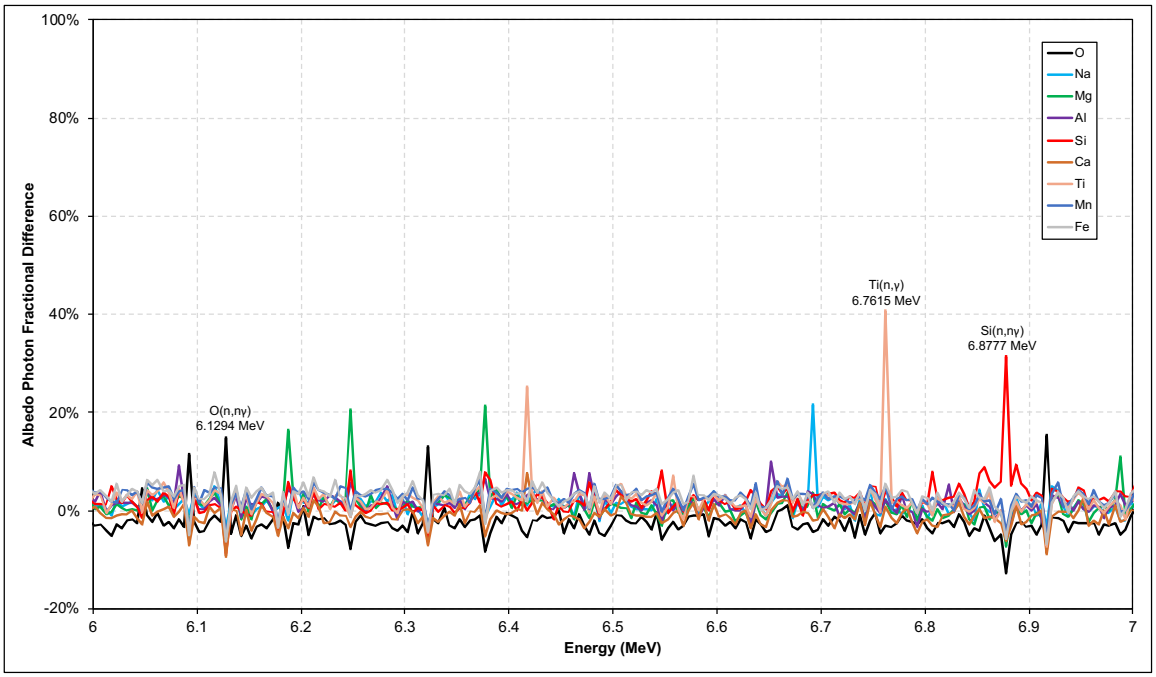

Figure 5.15. The fractional difference in the albedo photon flux of regolith that has an increased content of the specified element vs dry regolith for albedo photon energies between 6 and 7 MeV. The neutron reactions leading the chosen photopeaks are obtained from [*Reedy, 1978]*.

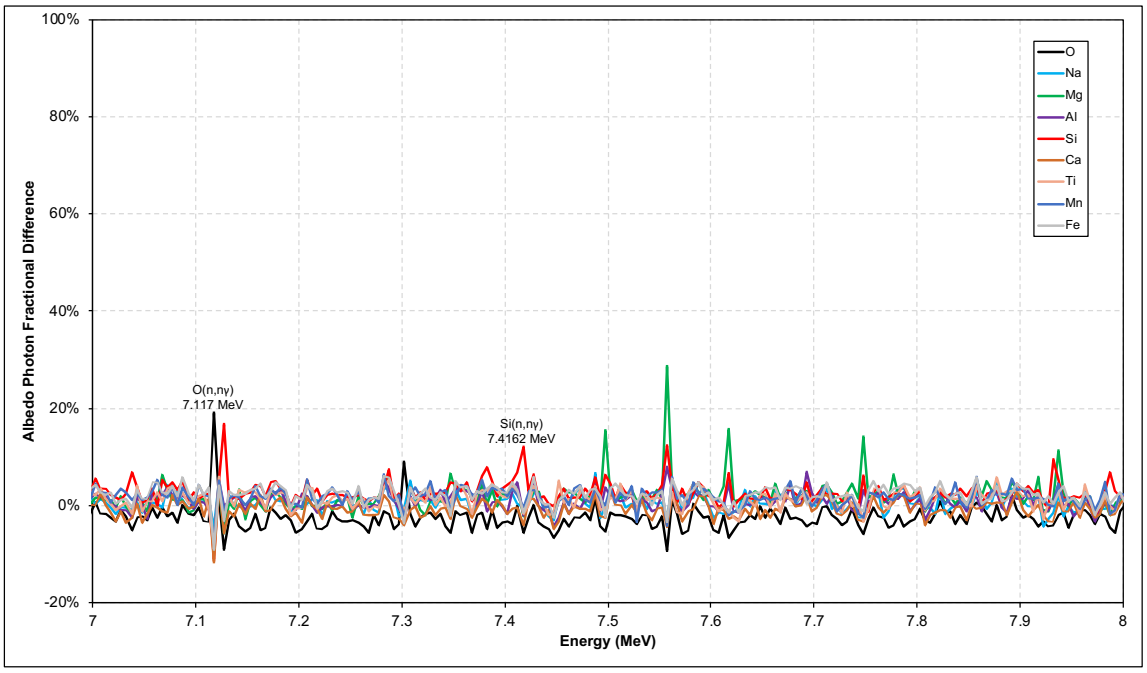

Figure 5.16. The fractional difference in the albedo photon flux of regolith that has an increased content of the specified element vs dry regolith for albedo photon energies between 7 and 8 MeV. The neutron reactions leading the chosen photopeaks are obtained from [*Reedy, 1978]*.

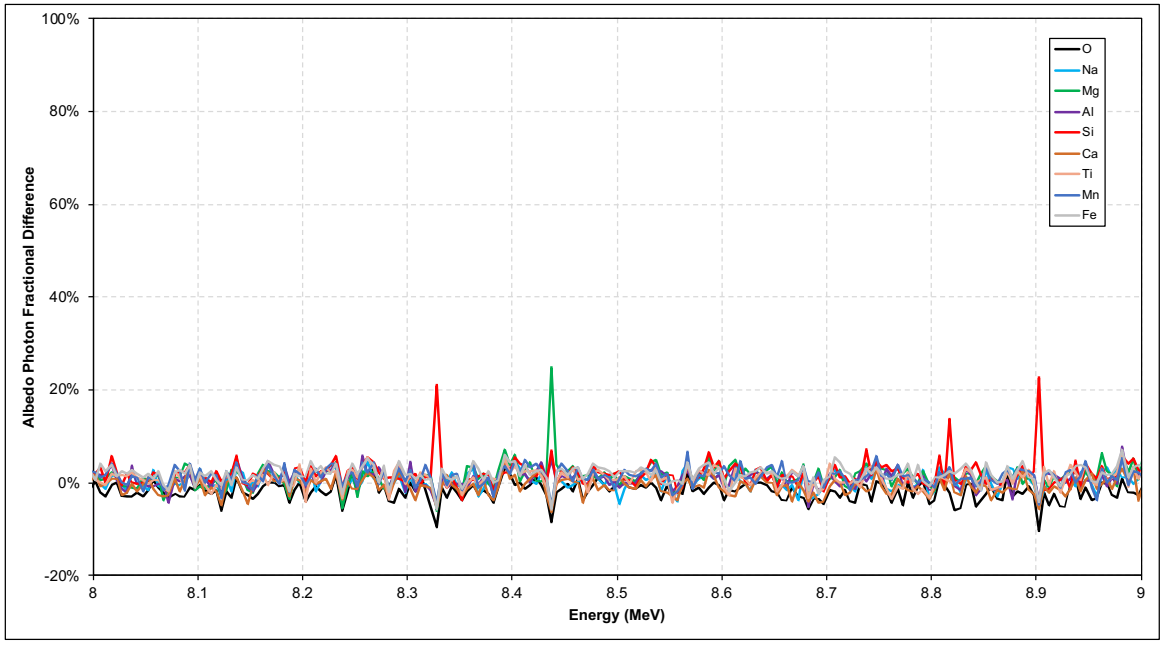

Figure 5.17. The fractional difference in the albedo photon flux of regolith that has an increased content of the specified element vs dry regolith for albedo photon energies between 8 and 9 MeV.

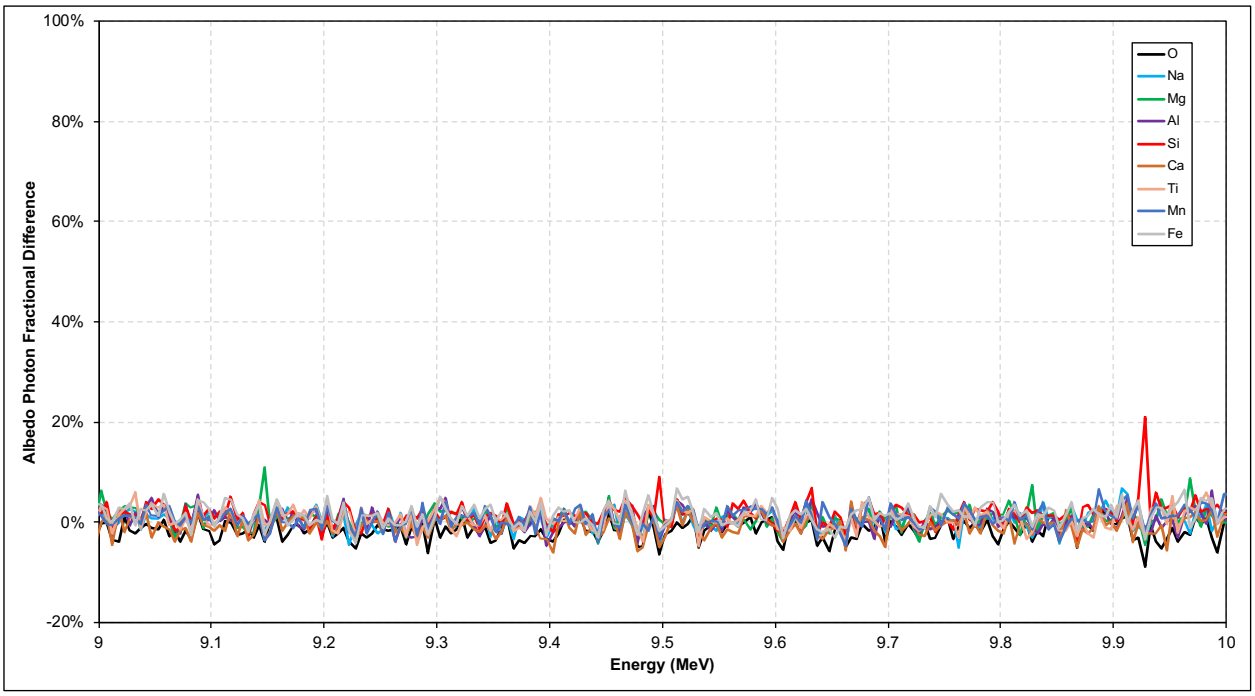

Figure 5.18. The fractional difference in the albedo photon flux of regolith that has an increased content of the specified element vs dry regolith for albedo photon energies between 9 and 10 MeV.

6. RADIATION TRANSPORT CODE COMPARISONS

The results of albedo particle spectra generated using PHITS and HETC-HEDS in comparison with MCNP6 are presented in this chapter. The wet regolith case used for comparison between all codes consisted of a regolith containing 10% hydrogen by weight fraction uniformly distributed in all depths.

6.1 Albedo Neutrons

Figure 6.1 shows a general agreement between MCNP6, PHITS, and HETC-HEDS when comparing the generated energy spectra of albedo neutrons. HETC-HEDS reports slightly higher neutrons populations at all energy ranges, which is possibly due to differences in the geometries. Results from MCNP6 are similar to PHITS at higher energies, but differ slightly at lower energies. This is expected since the physics models differ between the codes. The angular distribution of albedo neutrons displayed in Figure 6.2 also shows a similar trend when comparing MCNP6 to PHITS, where the relative increase in albedo neutrons seen in the energy spectrum is also apparent. The results from HETC-HEDS were not included in the angular distribution due to the differences in the simulation geometries. When comparing albedo neutron fluxes from dry and wet regolith, as shown in Figures 6.3 and 6.4, neither the results from PHITS nor HETC-HEDS show the abnormal increase at high energies observed with MCNP6. The drop in albedo neutron flux due to moderation effects is only observed at the epithermal energy range in PHITS. On the other hand, similar to MCNP6, the drop in HETC-HEDS start emerging within few hundreds of MeV.

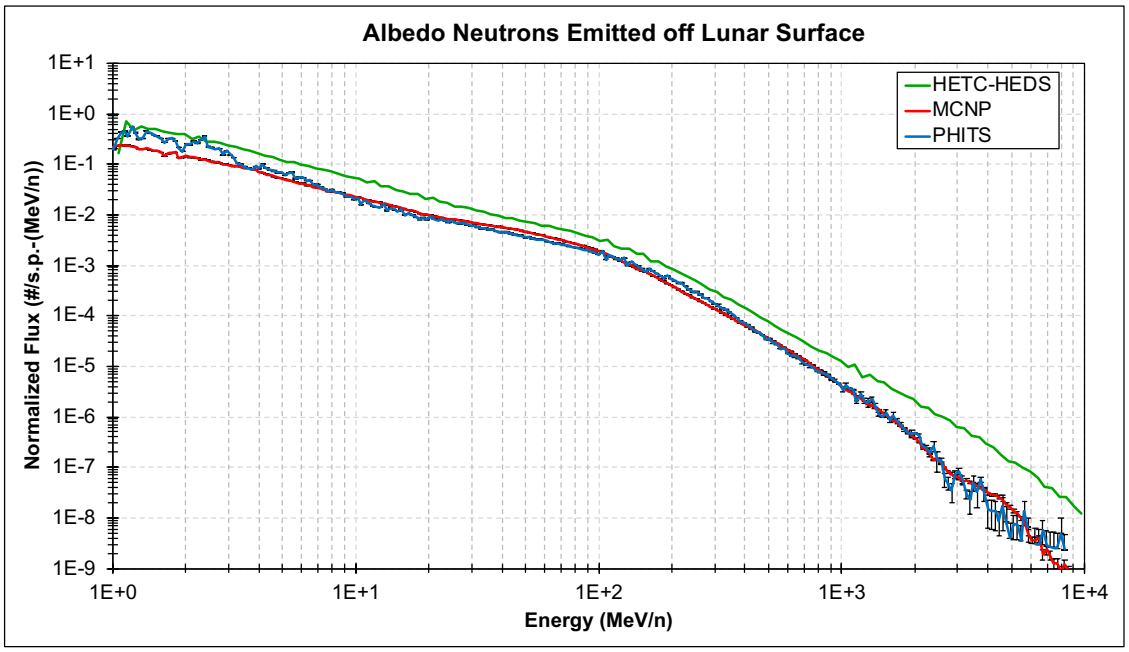

Figure 6.1. The energy distribution of albedo neutrons emitted off a dry regolith compared between MCNP6, PHITS, and HETC-HEDS.

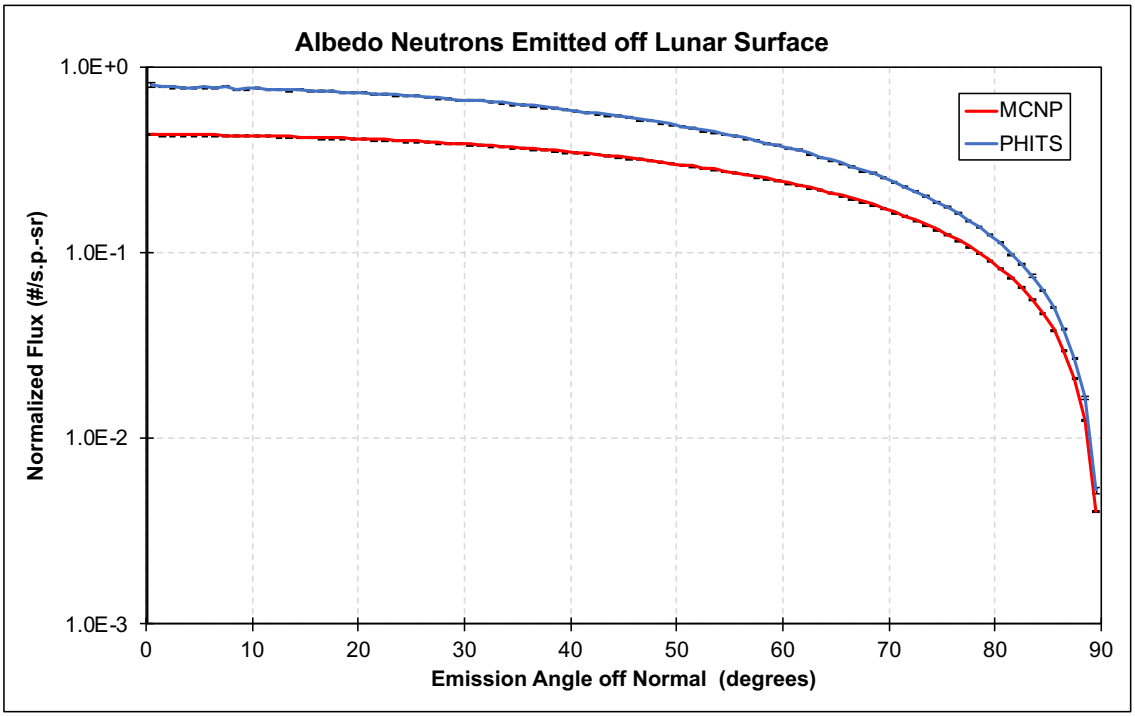

Figure 6.2. The angular distribution of albedo neutrons emitted off a dry regolith compared between MCNP6 and PHITS.

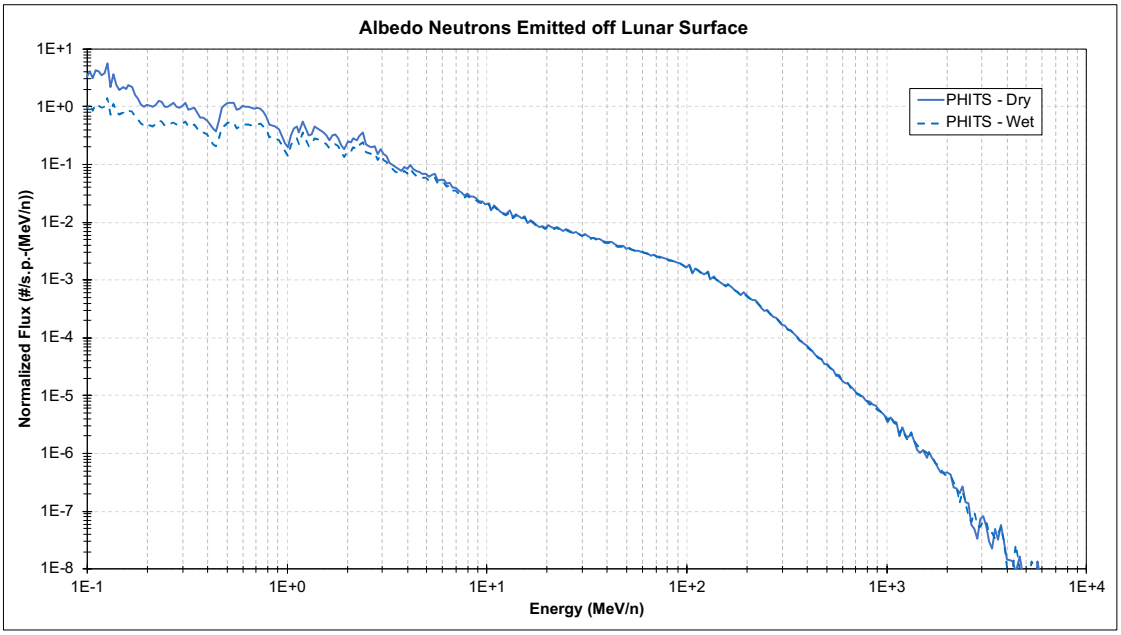

Figure 6.3. A comparison between the energy distribution of albedo neutrons emitted off a dry and a wet regolith generated using PHITS.

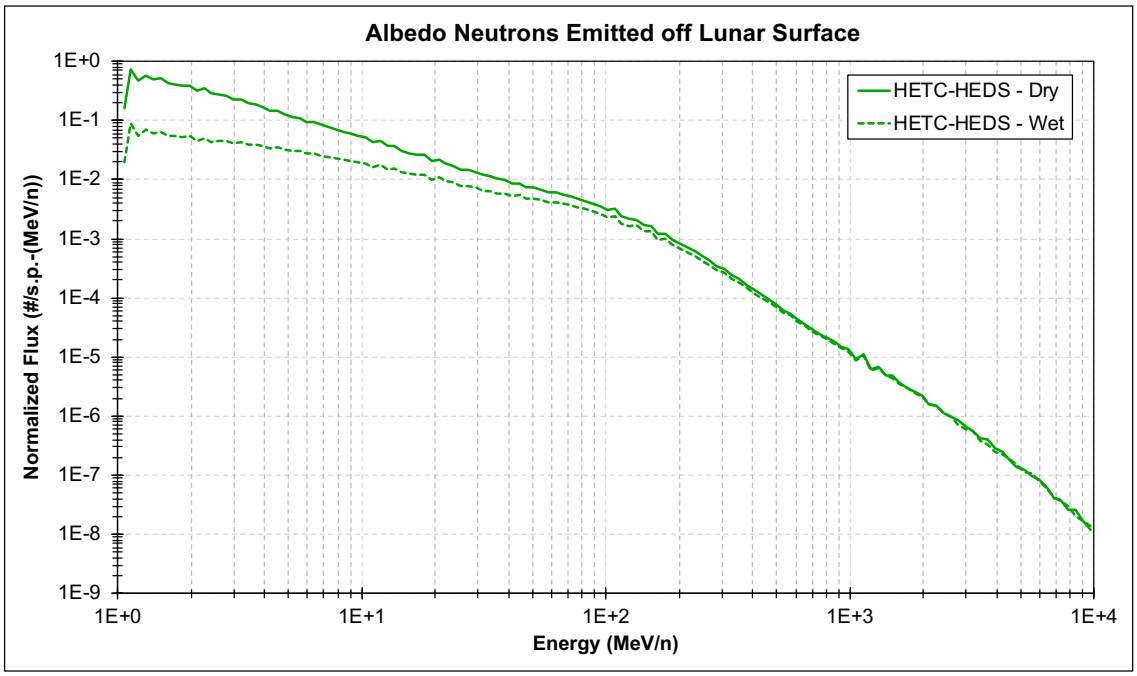

Figure 6.4. A comparison between the energy distribution of albedo neutrons emitted off a dry and a wet regolith generated using HETC-HEDS.

6.2 Albedo Protons

Figure 6.5 illustrates the energy spectra of albedo protons generated from MCNP6, PHITS, and HETC-HEDS. The results show a general agreement in the trend between the codes, especially with the albedo proton peak around several tens of MeV. Similar to albedo neutrons, HETC-HEDS reports relatively higher albedo production in all energy ranges, which might also be due to geometrical reasons. Analyzing the results from the wet case, displayed in Figures 6.6 and 6.7, does not show any visible differences in both PHITS and HETC-HEDS when comparing wet to dry regolith, unlike MCNP6. Note that all the runs in this chapter used the default models in each code. Since many protons are produced from elastic scatterings in wet regolith in MCNP6, one possible reason behind the differences observed is differences in the elastic scattering models between different codes. Another possible explanation is that the increase in proton flux, observed only in MCNP6, is due to artifacts in the code itself, although an increase was measured and is expected from a regolith rich with hydrogen (Schwadron et al., 2012).

The comparison between MCNP6 and PHITS when it comes to angular distributions of albedo protons is displayed in Figure 6.6. Again, there is a good agreement between the two codes when it comes to the asymmetric behavior of albedo protons. PHITS reports slightly higher protons at lower angles off normal, which are the protons leaving the lunar surface with relatively lower energies compared to the other angles. This implies again the both MCNP6 and PHITS agree on the higher energy end and differ slightly in the lower energy end.

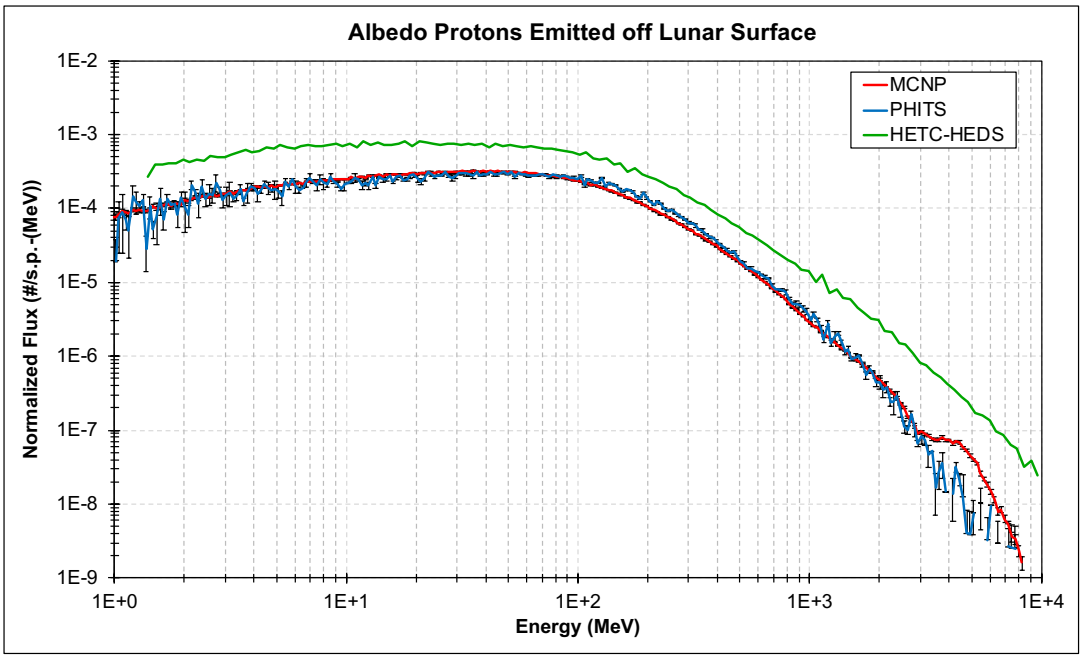

Figure 6.5. A comparison between the energy distribution of albedo protons emitted off a dry regolith generated using MCNP6, PHITS, and HETC-HEDS.

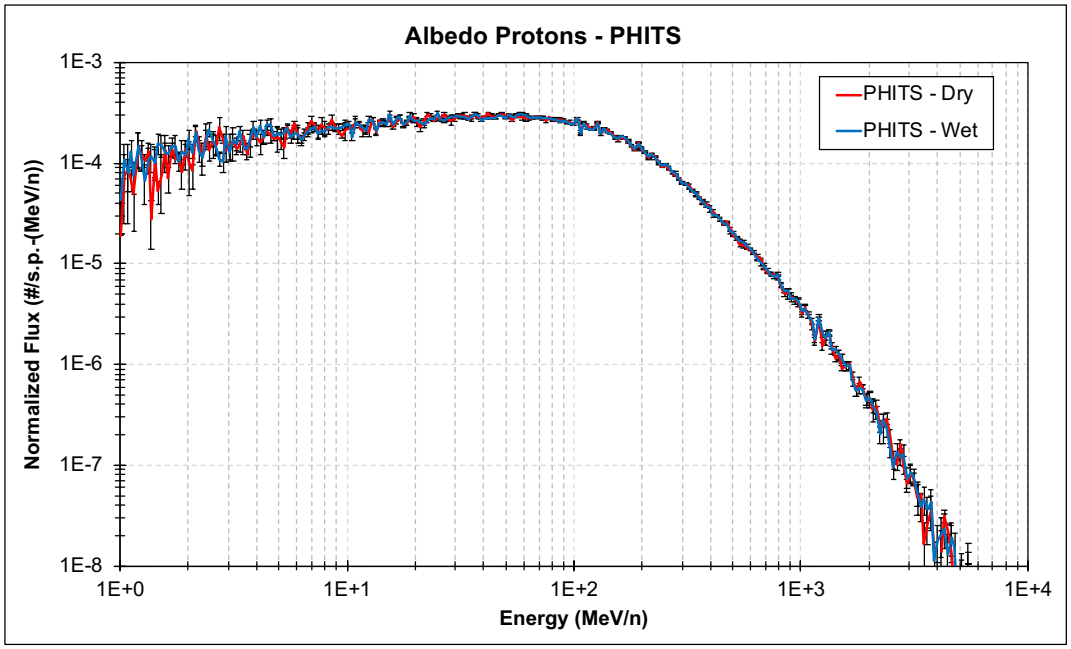

Figure 6.6. A comparison between the energy distribution of albedo protons emitted off a dry and a wet regolith generated using PHITS.

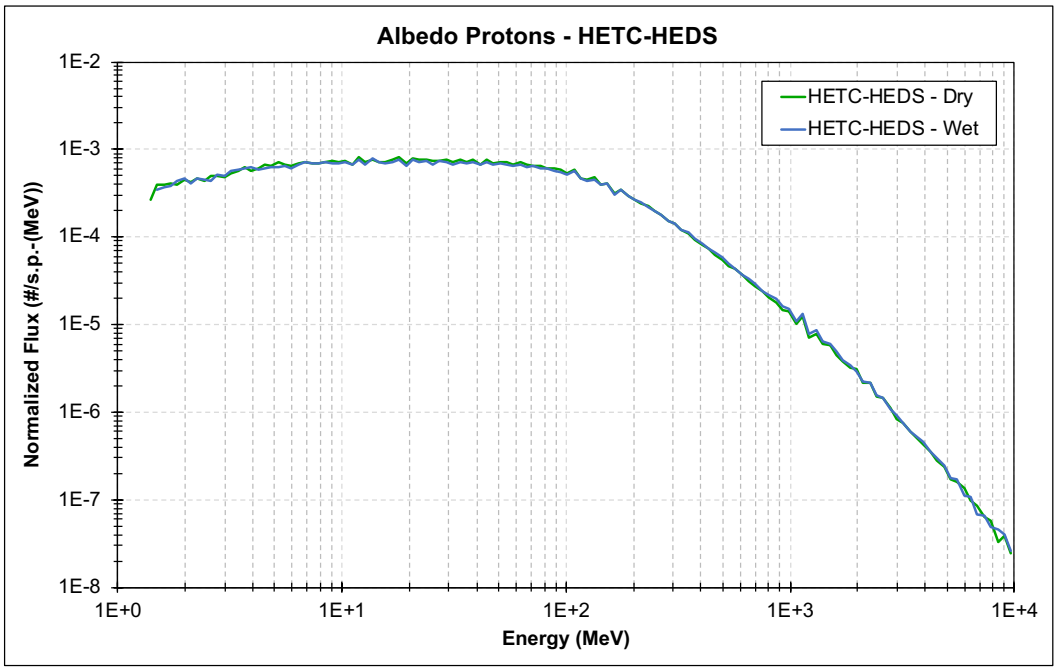

Figure 6.7. A comparison between the energy distribution of albedo protons emitted off a dry and a wet regolith generated using HETC-HEDS.

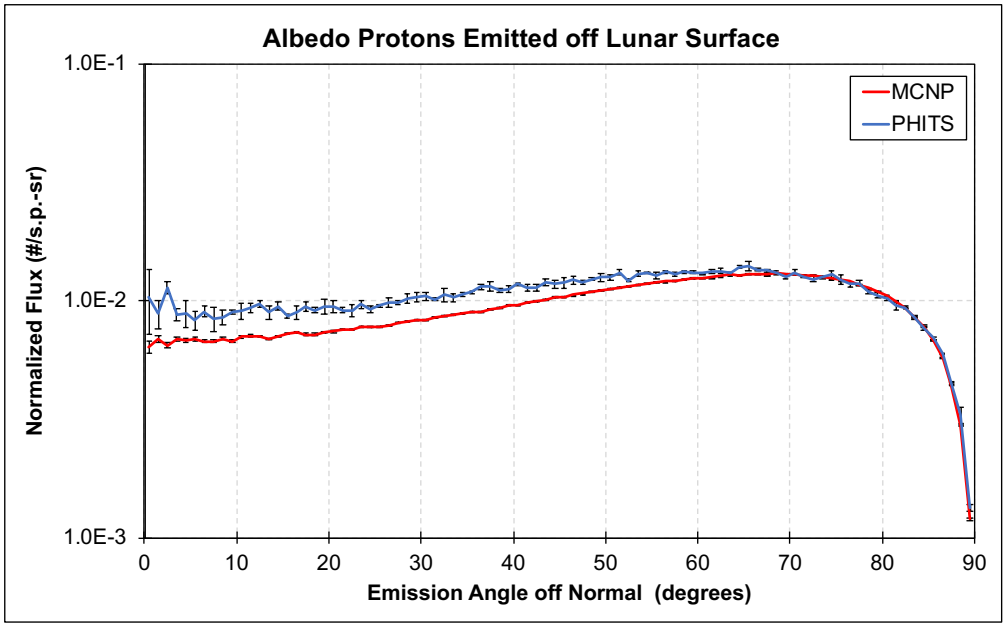

Figure 6.8. The angular distribution of albedo protons emitted off a dry regolith compared between MCNP6 and PHITS.

6.3 Other Albedo Particles

Figures 6.9 to 6.11 show comparisons between MCNP6 and PHITS in generating the energy spectra of other albedo species. There is a general agreement between all the results. The behavior of albedo deuterons generated using PHITS differ slightly from MCNP6. Results of particles heavier than deuterons were not included due to low statistics.

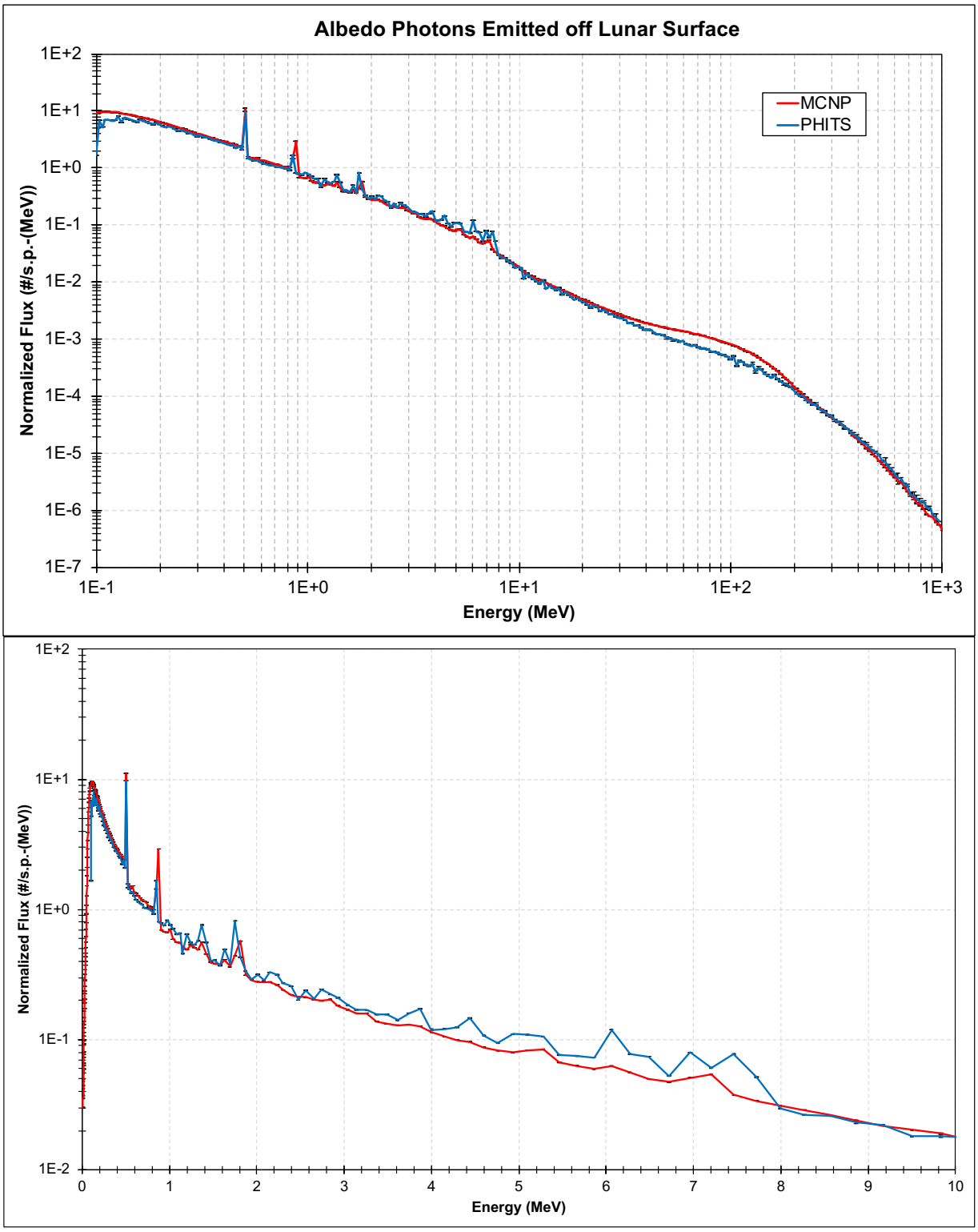

Figure 6.9. The energy distribution of albedo photons emitted off a dry regolith compared between MCNP6 and PHITS for a wide range of energies (top) and up to 10 MeV (bottom).

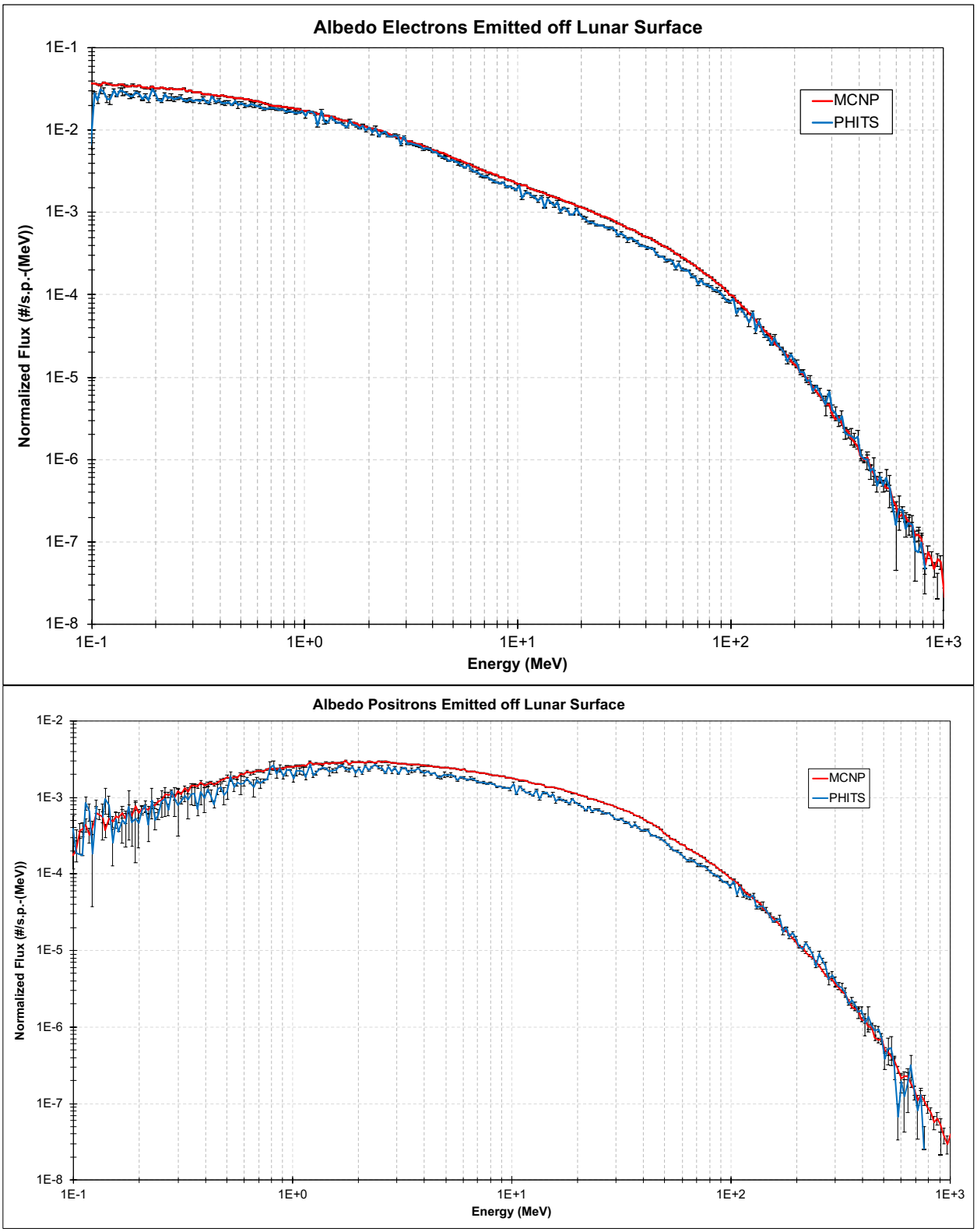

Figure 6.10. The energy distribution of albedo electrons (top) and positrons (bottom) emitted off a dry regolith compared between MCNP6 and PHITS.

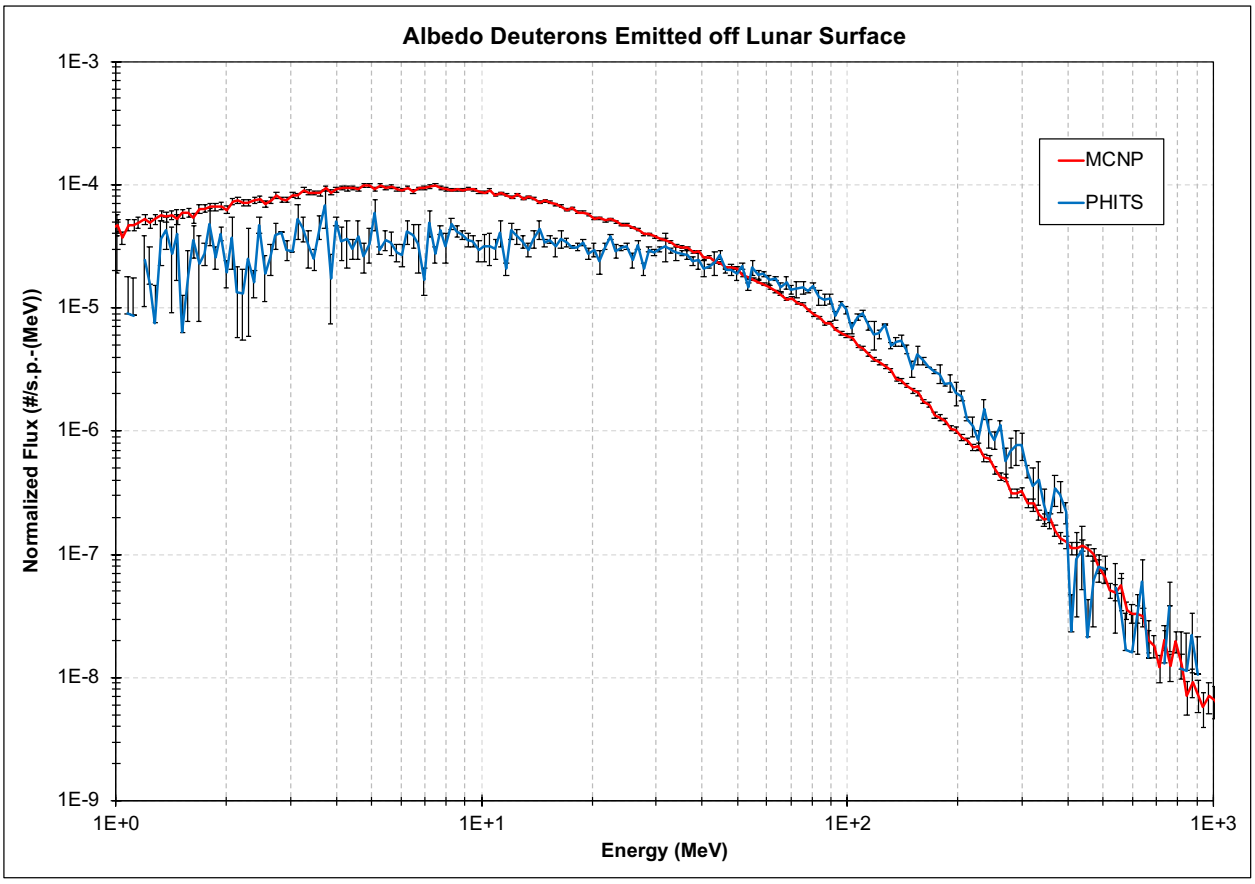

Figure 6.11. The energy distribution of albedo deuterons emitted off a dry regolith compared between MCNP6 and PHITS.

7. THE CRATER INSTRUMENT

This chapter applies the results obtained from the previous chapters to the CRaTER instrument. First, the field of view of the CRaTER instrument is calculated and reported as a function of altitude, orientation, and detector coincidence. Then, the angular distribution of the albedo particles is incorporated into the field of view of the CRaTER instrument. Finally, the dose from GCR ions and albedo particles in the upper and lower sets of detectors is calculated using MCNP6 and compared to the measurements taken by CRaTER instrument.

7.1 Field of View

The CRaTER instrument observes a range of albedo protons that depends highly on its field of view. The field of view in turn depends on altitude, orientation, and detector coincidence. Since the LRO spacecraft orbits at varying altitudes over the lunar surface, two altitudes were chosen in this study to understand the changes in the observed proton albedo: 50 km mean altitude, and 180 km far extreme altitude. Also, as seen in Figure 7.1, an albedo proton could trigger a D6/D4 coincidence, which covers a relatively wider field of view, and a D6/D2 coincidence, which requires an albedo proton with a relatively higher energy to pass through two volumes of TEP. In addition, the CRaTER instrument could face either the lunar nadir or the lunar limb, and the field of view varies significantly between these two orientations. This is illustrated in Figure 7.2. Here, the angular distribution of albedo particles becomes a crucial factor in determining the particles that are able to reach the detectors of the CRaTER instrument.

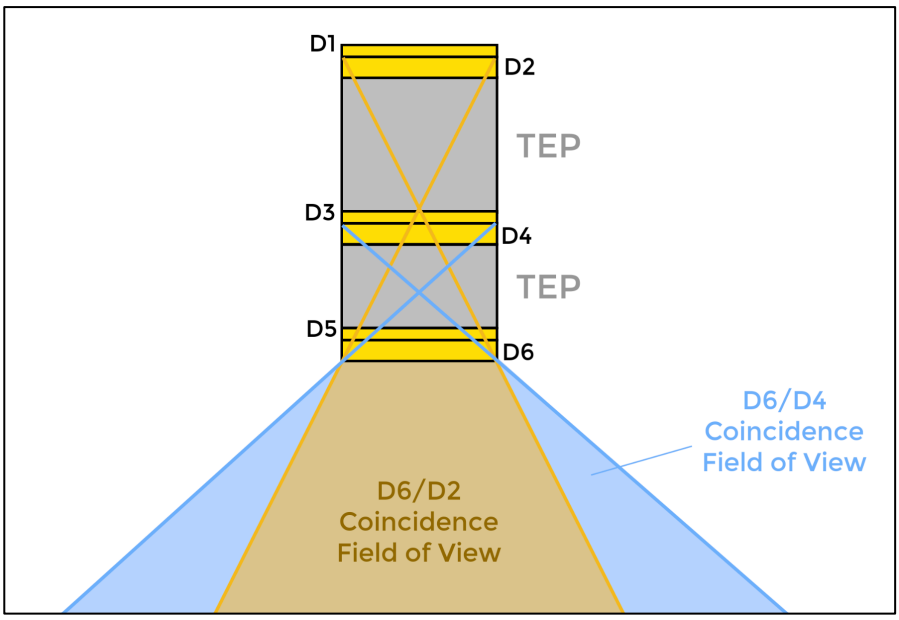

Figure 7.1. Illustrative layout of the CRaTER instrument demonstrating the field of view as a function of detector coincidence. The yellow rectangles represent the silicon detectors and the gray rectangles represent the TEP volumes. The top set of detectors (D1 and D2) faces deep space and the lower set (D5 and D6) faces the lunar surface. An albedo proton reaching D4 and passing through D6 has a wider field of view than a proton reaching D2 and passing through D6. However, the albedo proton should have a higher energy to reach D2 since it passes through two TEP volumes. Note that the dimensions in this figure are not to scale.

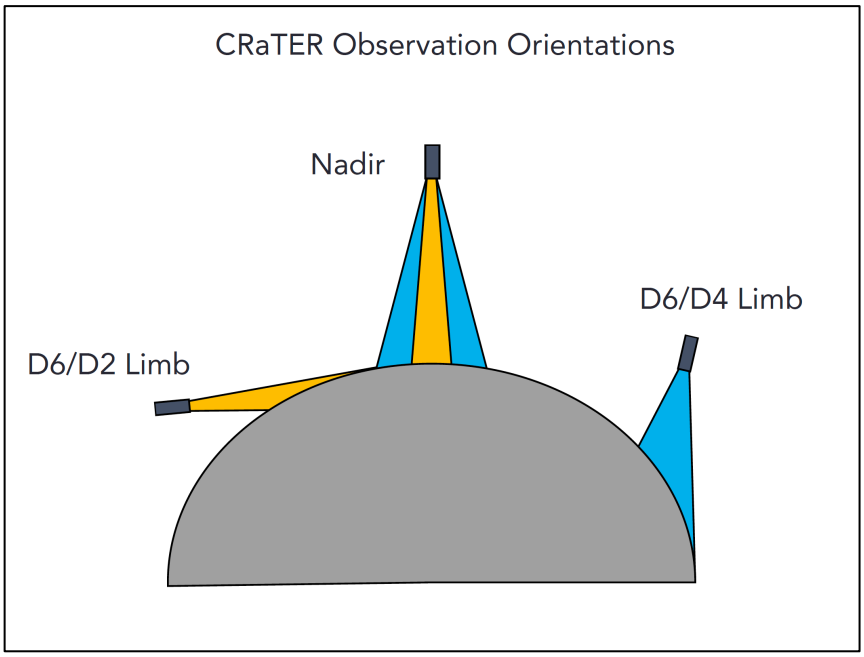

Figure 7.2. Illustrative diagram demonstrating the different orientations of the CRaTER instrument obtained from *[de Wet et al., 2019]*.

The field of view of the CRaTER instrument as a function of altitude, detector coincidence, and orientation was calculated using MCNP6. Figures 7.3 and 7.4 show the probability of an albedo particle leaving the lunar surface and triggering multiple detectors at a certain emission angle. The emission angle is the angle of an albedo particle as it leaves the lunar surface. Recall that this calculation is purely geometrical. For example, taking into account the exact dimensions of the CRaTER instrument and using simple trigonometry, the maximum albedo angle required to trigger D6/D2 coincidence when facing the nadir is calculated to be ~16°, while for D6/D4 coincidence it is calculated to be ~32°. The probabilities obtained using MC methods show field of views that are in a good agreement with the angles calculated using trigonometric methods. The results from MCNP6 also show the exact probability of reaching multiple detectors for each emission angle for the nadir and the limb orientation. Note that the actual field of view is slightly different than the geometrical one due to the curvature of the lunar surface. This is illustrated in the probability of albedo particles reaching the CRaTER instrument at 180 km in comparison to 50 km when observing lunar nadir in Figures 7.3 and 7.4, where the probability at 180 km covers a wider range of angles.

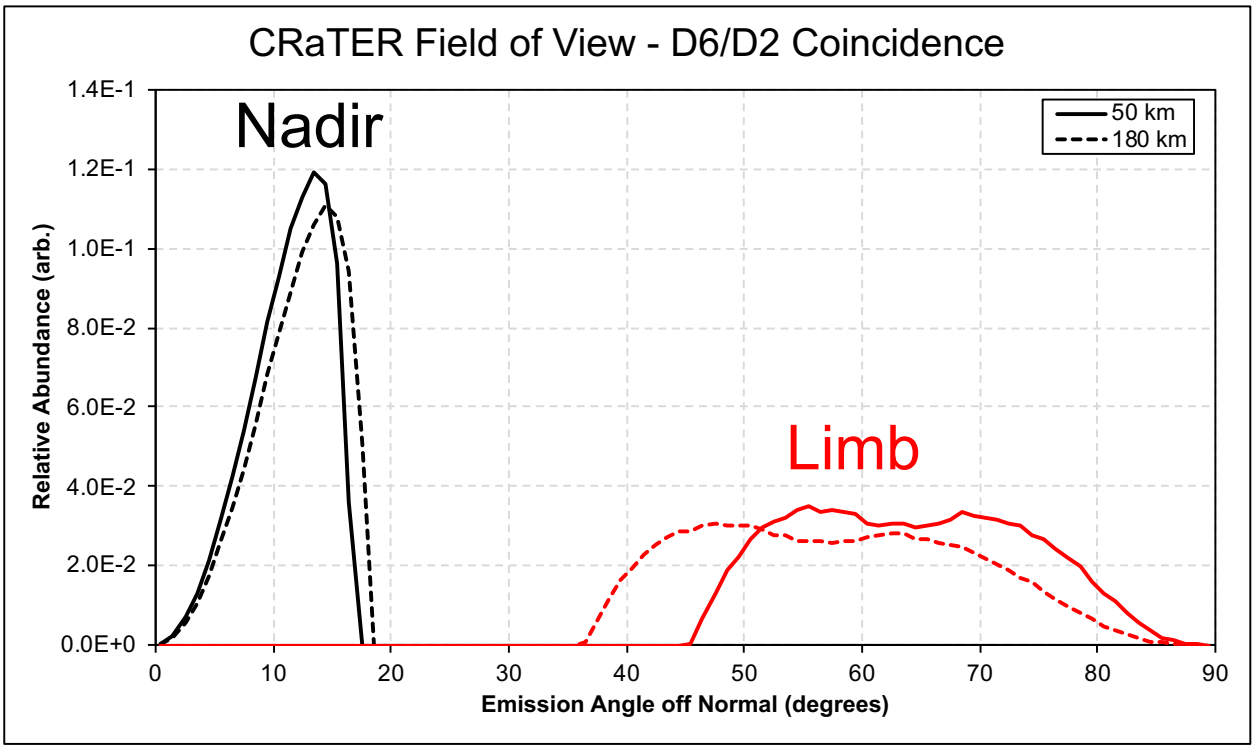

Figure 7.3. The probability of an albedo particle triggering D6/D2 coincidence at the CRaTER instrument as a function of surface emission angle off normal.

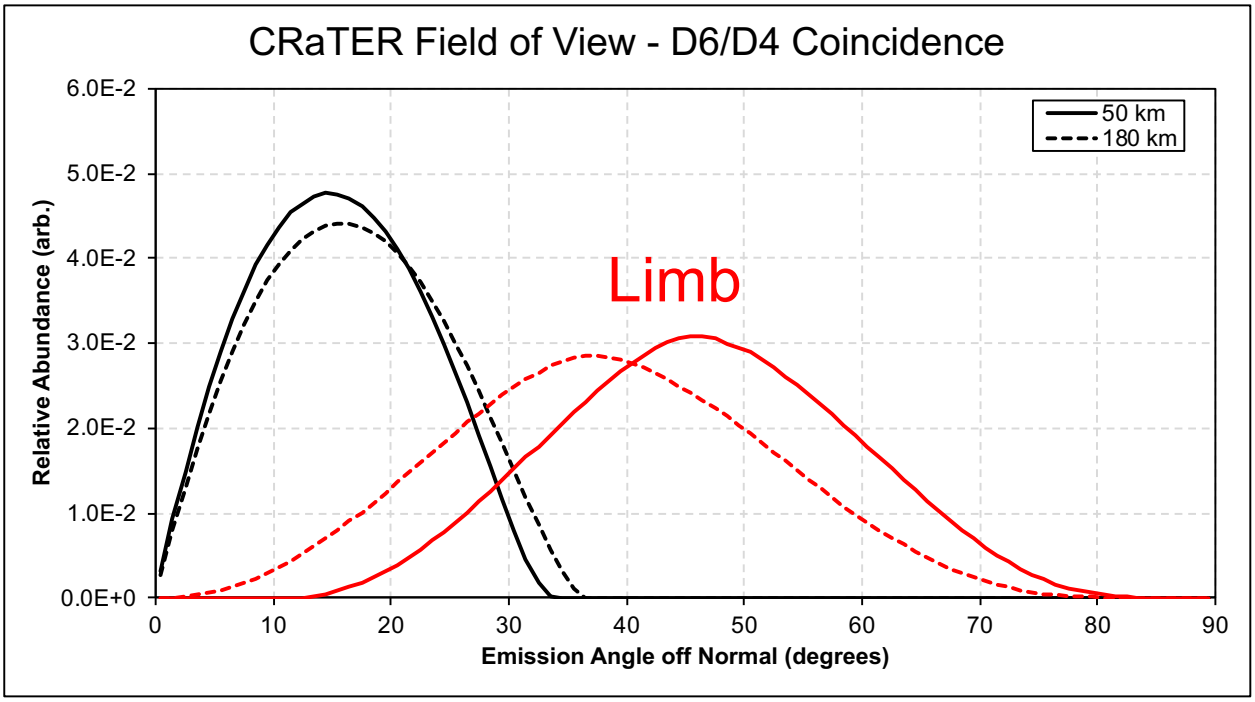

Figure 7.4. The probability of an albedo particle triggering D6/D4 coincidence at the CRaTER instrument as a function of surface emission angle off normal.

7.2 Observable Albedo Range

The next step is to incorporate the angular distribution of albedo protons into the CRaTER instrument field of view for each altitude, orientation, and detector coincidence to characterize the albedo proton population measured by the telescope. In the previous chapters, the albedo proton angular spectrum was calculated as a function of emission energy and maximum production depth. Using the results calculated in Figures 7.3 and 7.4, it is possible to determine the probability of each albedo proton reaching multiple detectors. In addition to the limited field of view in each coincidence detection, there is a threshold energy that the proton must have to register a count in multiple detectors. The proton threshold energy is ~64 MeV for the D6/D4 coincidence and ~114 MeV for the D6/D2 coincidence (Spence et al., 2010). Taking all these factors into consideration, it is possible then to calculate maximum depth distribution and estimate how deep in the lunar regolith is the CRaTER instrument probing for each altitude and orientation. These distributions are presented in Figures 7.5 to 7.12. In each of these figures, the top plot shows the maximum depth distribution for a specific altitude and orientation for all energies, while the bottom plot shows only the particles above the threshold energy for the corresponding detector coincidence. Analyzing these results shows that the CRaTER instrument is able to probe up to 10s of g/cm^2 deep in the regolith, and the detections from the top 10 g/cm^2 are almost uniform. Observations from the lunar limb cover a wider range of energies than the lunar nadir. When it comes to a dry regolith, protons with very high energies (in the GeV range) appear mostly when observing lunar limb. This is in agreement with the previous distributions which show that high-energy protons are scattered GCR protons and come primarily at shallower angles off the lunar surface.

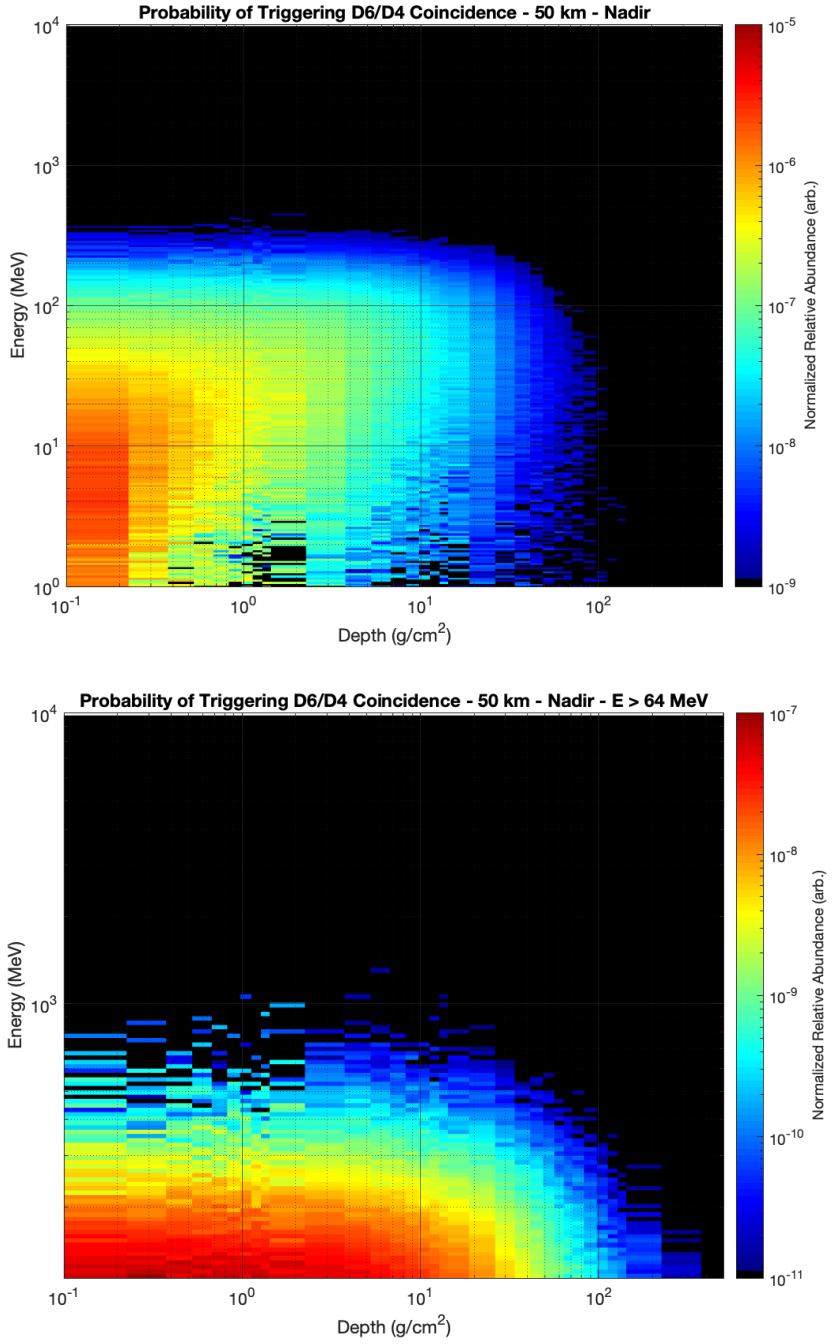

Figure 7.5. The maximum depth distribution of albedo protons triggering D6/D4 coincidence when facing the lunar nadir at altitude of 50 km for all modeled energies (top) and above the threshold energy of 64 MeV (bottom).

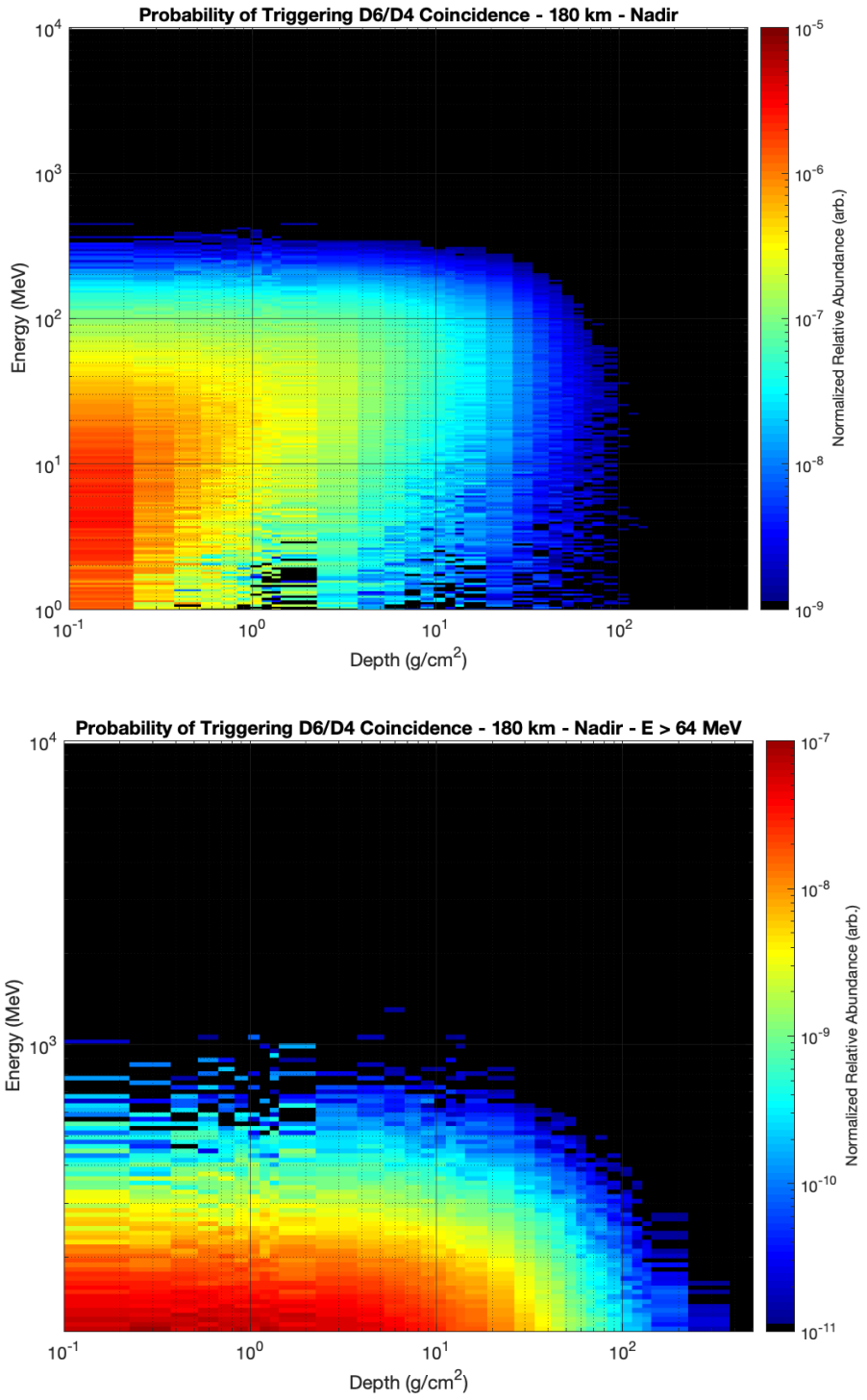

Figure 7.6. The maximum depth distribution of albedo protons triggering D6/D4 coincidence when facing the lunar nadir at altitude of 180 km for all modeled energies (top) and above the threshold energy of 64 MeV (bottom).

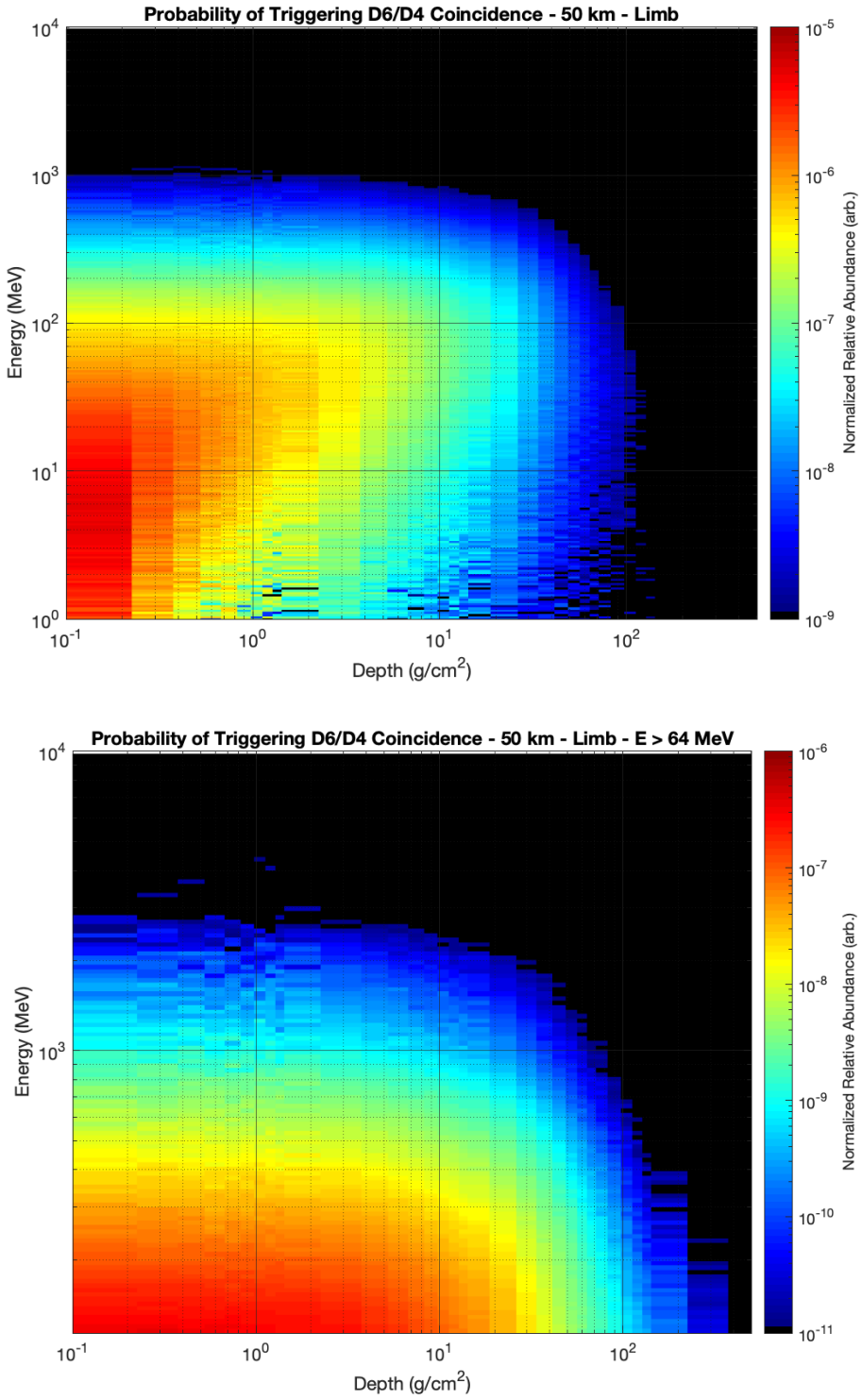

Figure 7.7. The maximum depth distribution of albedo protons triggering D6/D4 coincidence when facing the lunar limb at altitude of 50 km for all modeled energies (top) and above the threshold energy of 64 MeV (bottom).

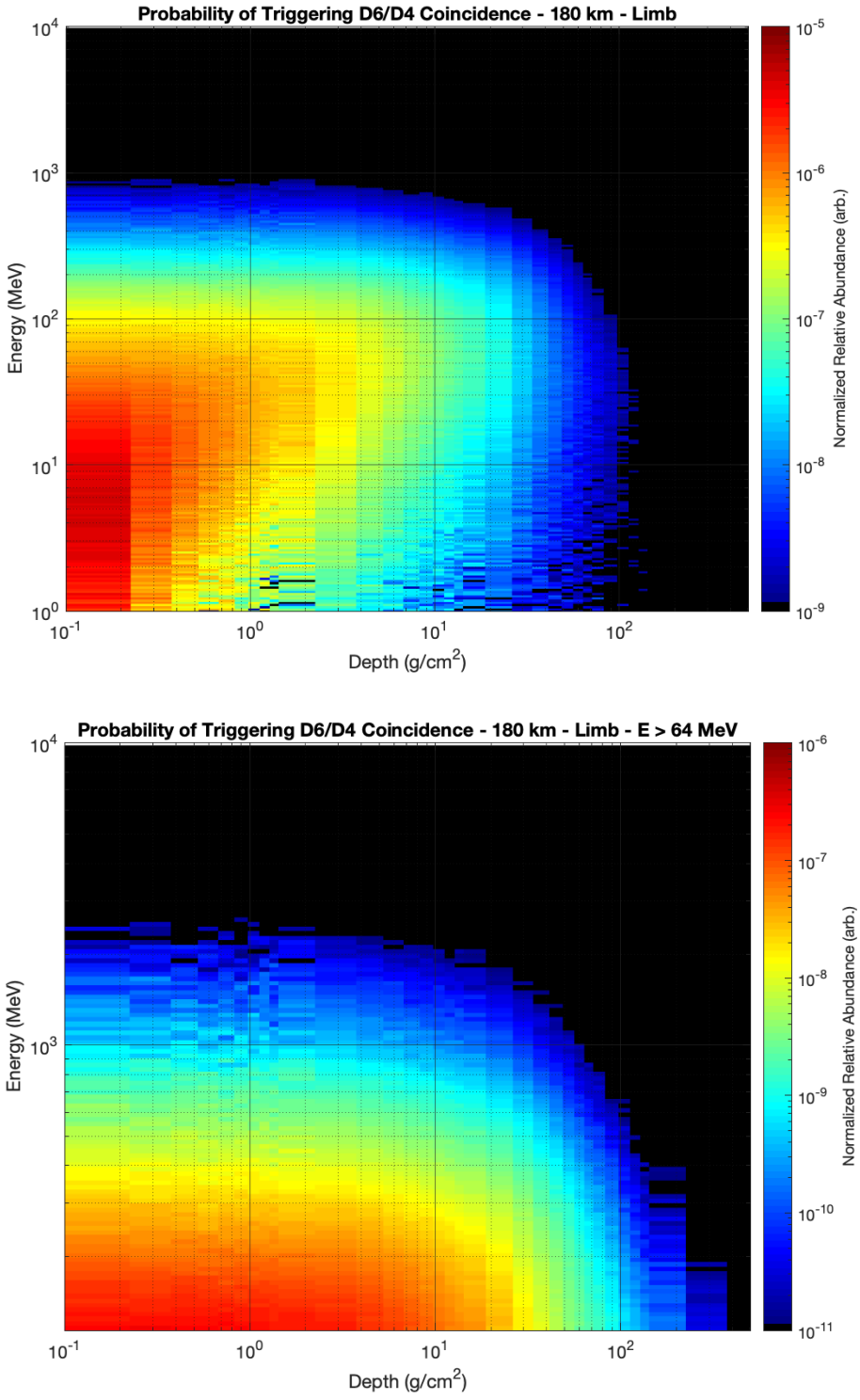

Figure 7.8. The maximum depth distribution of albedo protons triggering D6/D4 coincidence when facing the lunar limb at altitude of 180 km for all modeled energies (top) and above the threshold energy of 64 MeV (bottom).

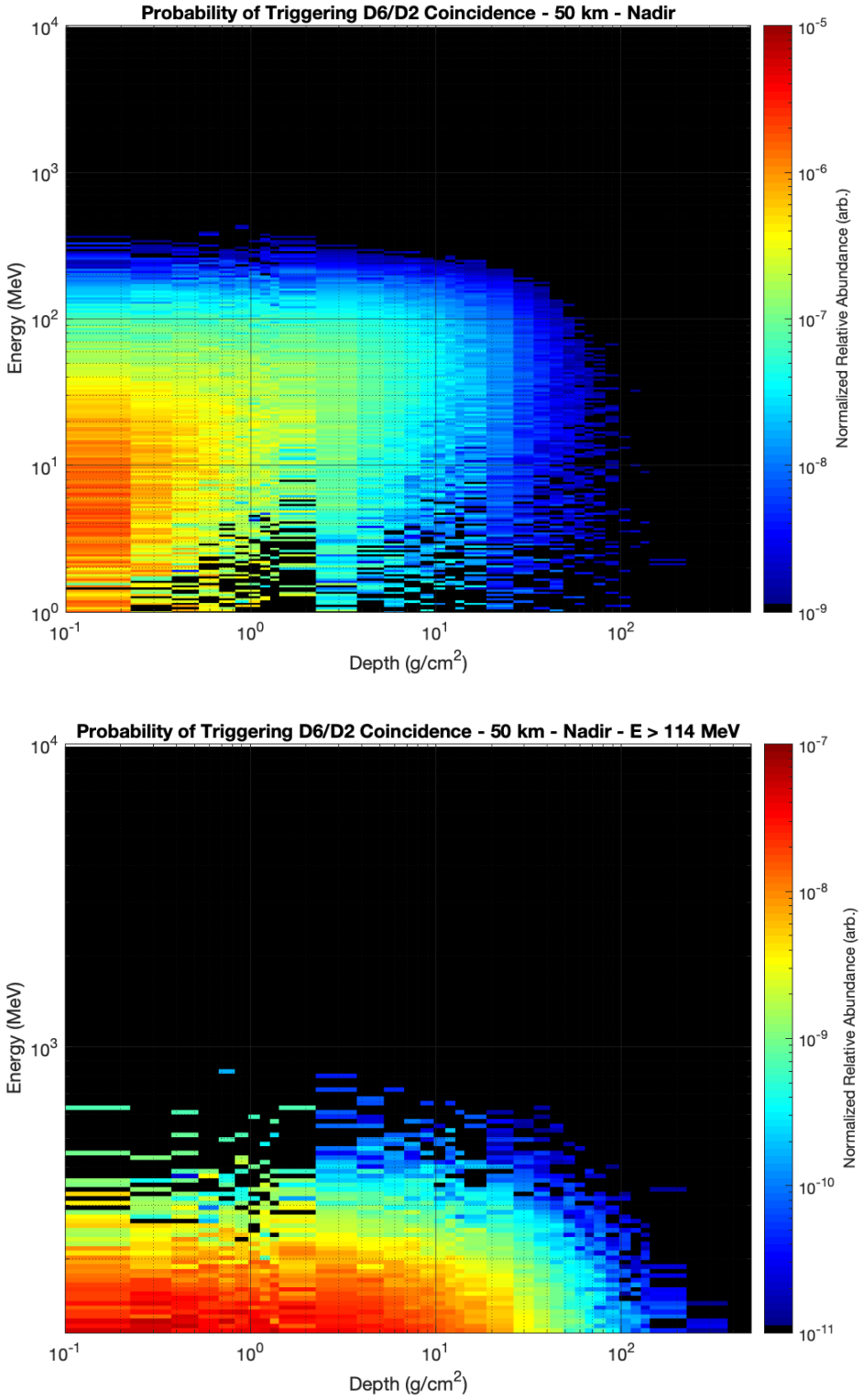

Figure 7.9. The maximum depth distribution of albedo protons triggering D6/D2 coincidence when facing the lunar nadir at altitude of 50 km for all modeled energies (top) and above the threshold energy of 114 MeV (bottom).

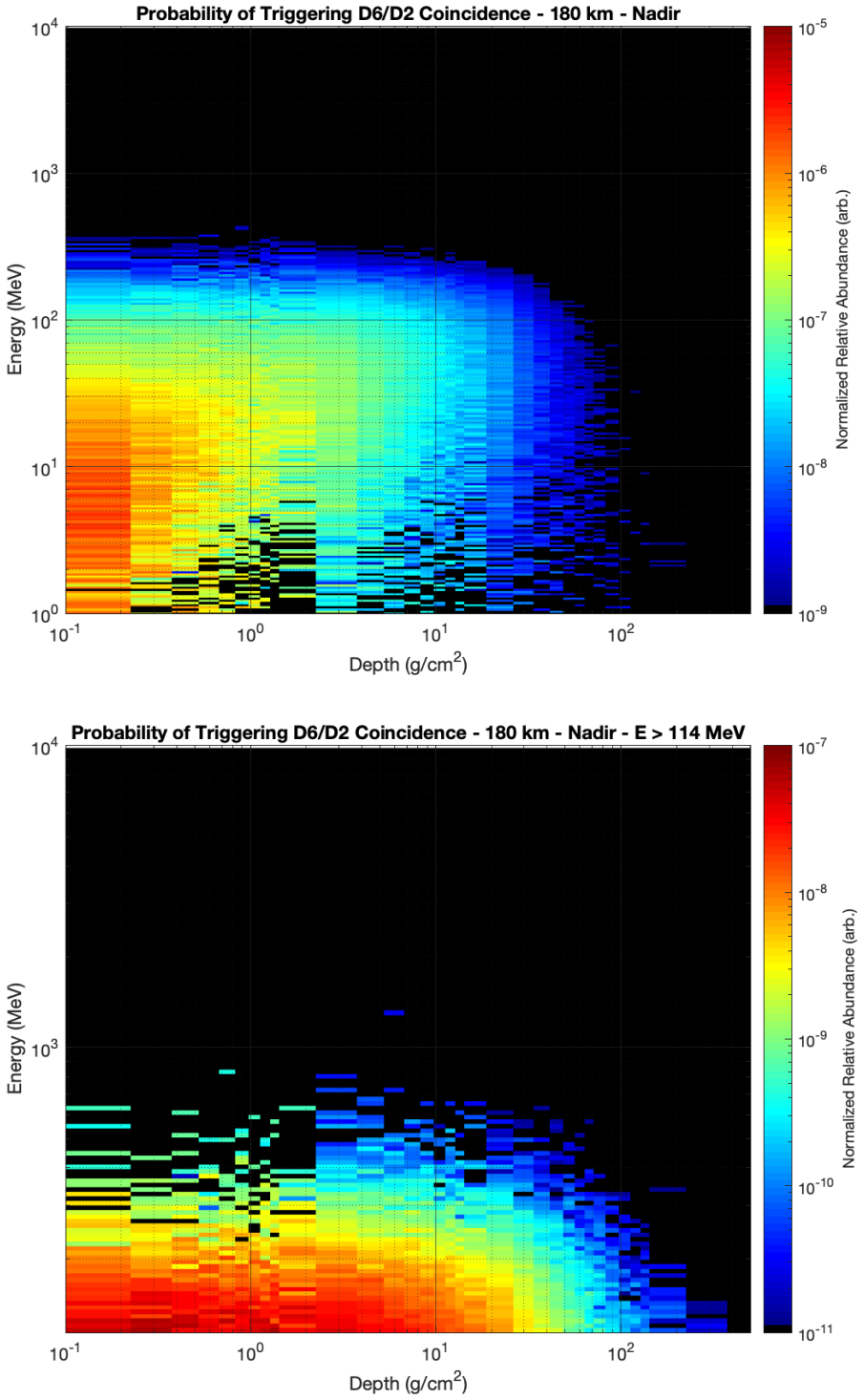

Figure 7.10. The maximum depth distribution of albedo protons triggering D6/D2 coincidence when facing the lunar nadir at altitude of 180 km for all modeled energies (top) and above the threshold energy of 114 MeV (bottom).

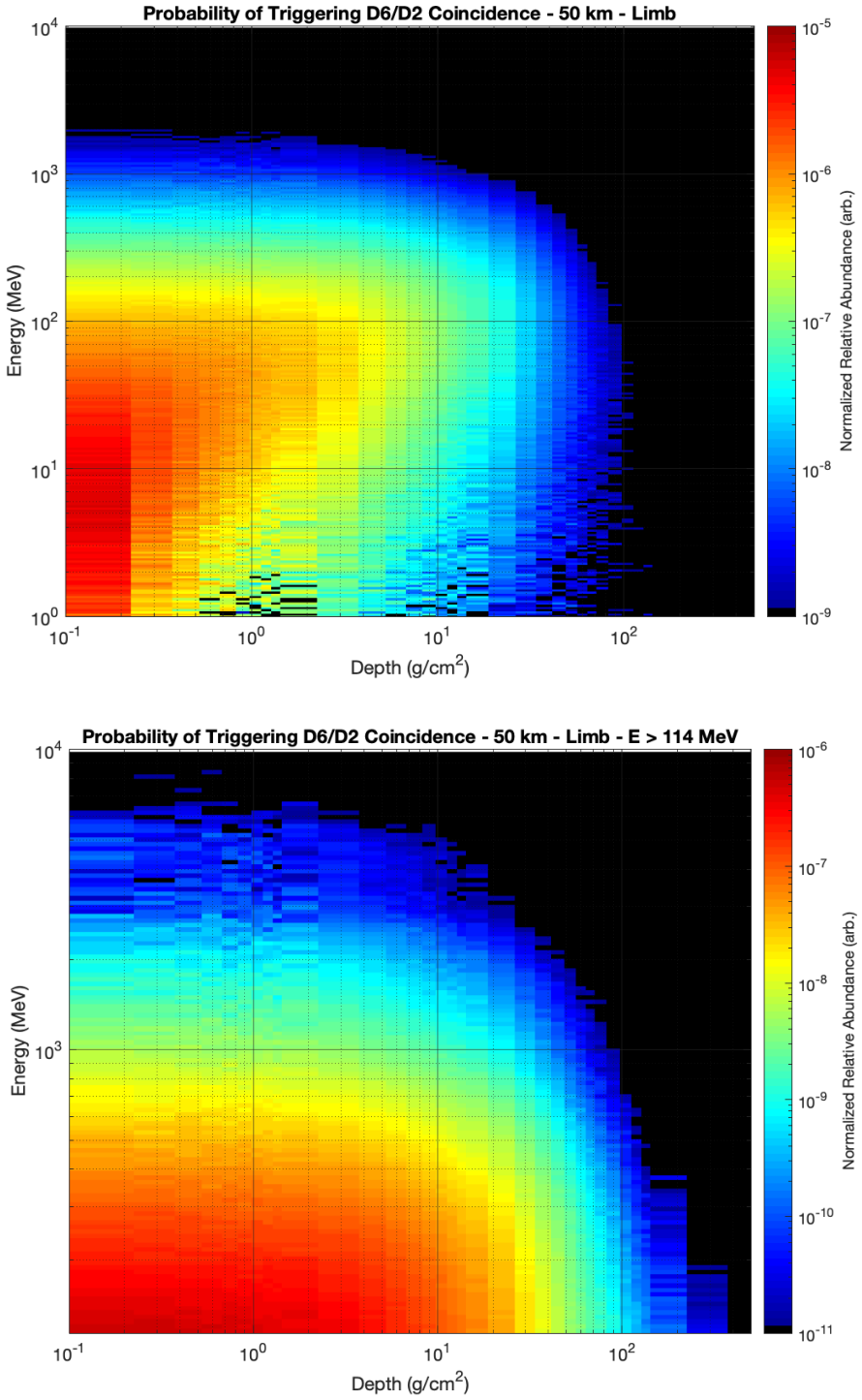

Figure 7.11. The maximum depth distribution of albedo protons triggering D6/D2 coincidence when facing the lunar limb at altitude of 50 km for all modeled energies (top) and above the threshold energy of 114 MeV (bottom).

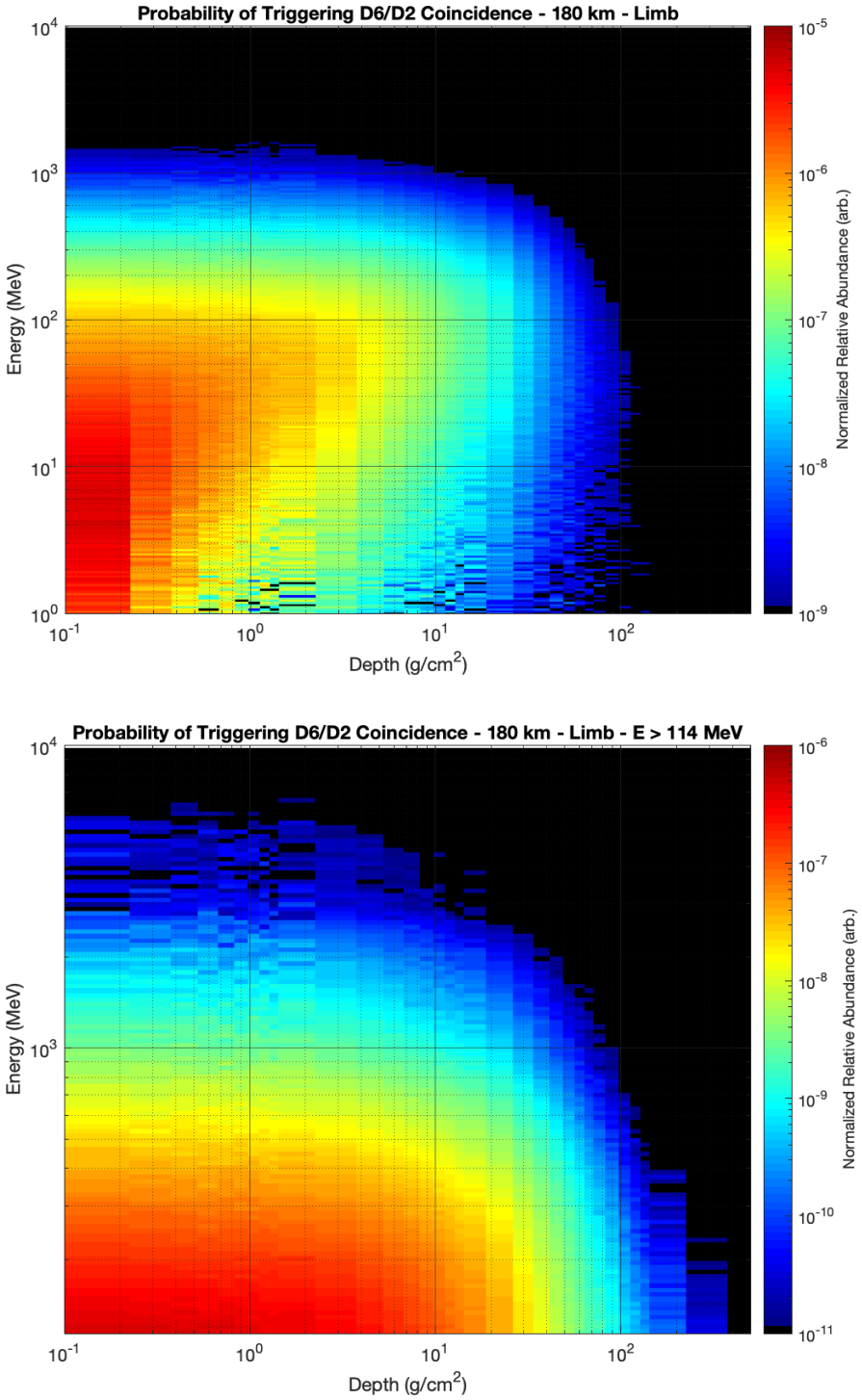

Figure 7.12. The maximum depth distribution of albedo protons triggering D6/D2 coincidence when facing the lunar limb at altitude of 180 km for all modeled energies (top) and above the threshold energy of 114 MeV (bottom).

Wet Regolith

Figures 7.13 to 7.20 show the maximum depth distributions of albedo protons from a fully wet regolith as a function of CRaTER's altitude, orientation, and coincidence detection taking into account the threshold energies. Since MCNP6 spectra show an enhancement the population of high energy albedo protons, a similar behavior is observed in these plots. An increase in the population of high energy protons appear in all orientations. However, since scattered GCR protons also populate the detections observed when facing the lunar limb, hunting for subsurface protons seems more optimal facing the lunar nadir, especially since the high energy protons from dry regolith are negligible at this orientation. Thus, any high energy proton observed is probably due to lunar hydrogen according to MCNP6 calculations. It is important to note though that other codes did not show a similar enhancement from a wet regolith, although there was a good agreement between all the codes when it comes to dry regolith.

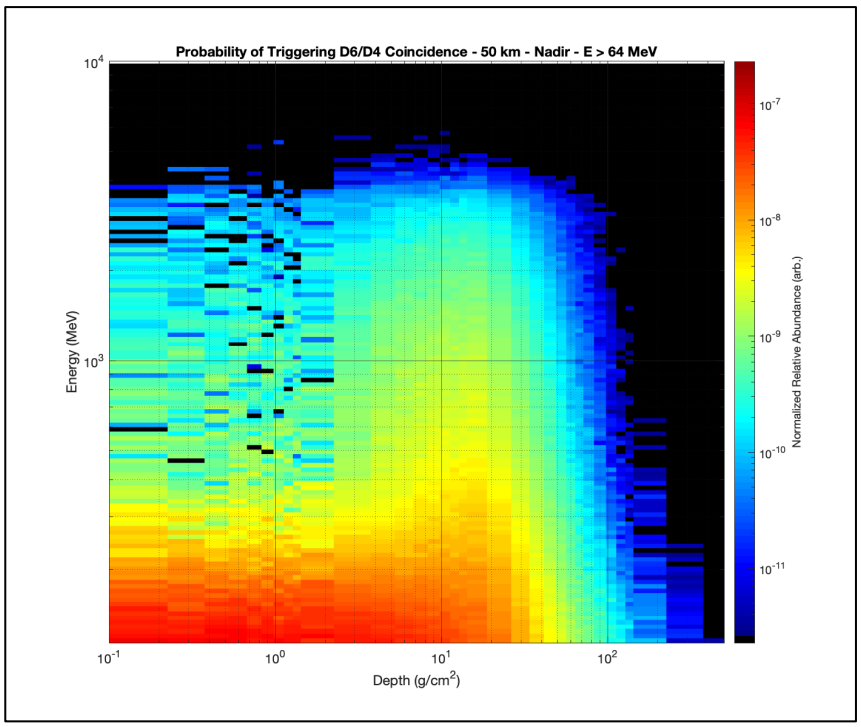

Figure 7.13. The maximum depth distribution of albedo protons emitted by a fully wet regolith and triggering D6/D4 coincidence when facing the lunar nadir at altitude of 50 km above the threshold energy of 65 MeV.

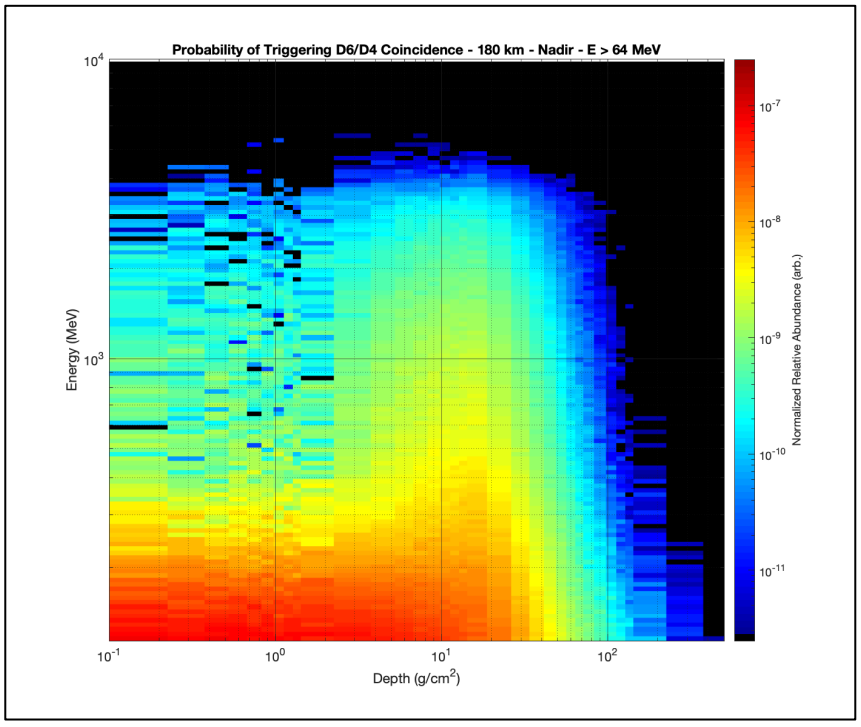

Figure 7.14. The maximum depth distribution of albedo protons emitted by a fully wet regolith and triggering D6/D4 coincidence when facing the lunar nadir at altitude of 180 km above the threshold energy of 65 MeV.

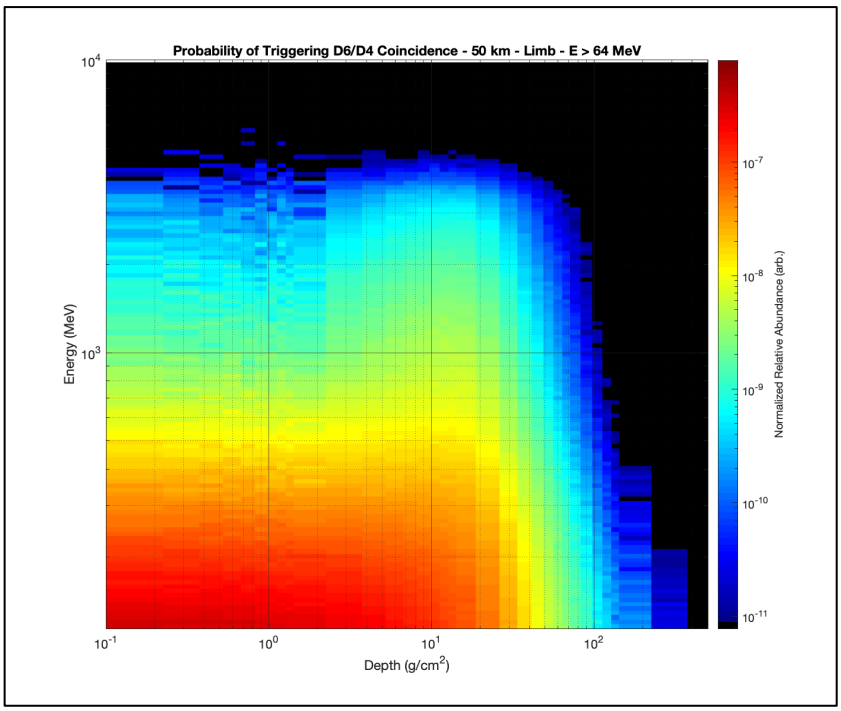

Figure 7.15. The maximum depth distribution of albedo protons emitted by a fully wet regolith and triggering D6/D4 coincidence when facing the lunar limb at altitude of 50 km above the threshold energy of 65 MeV.

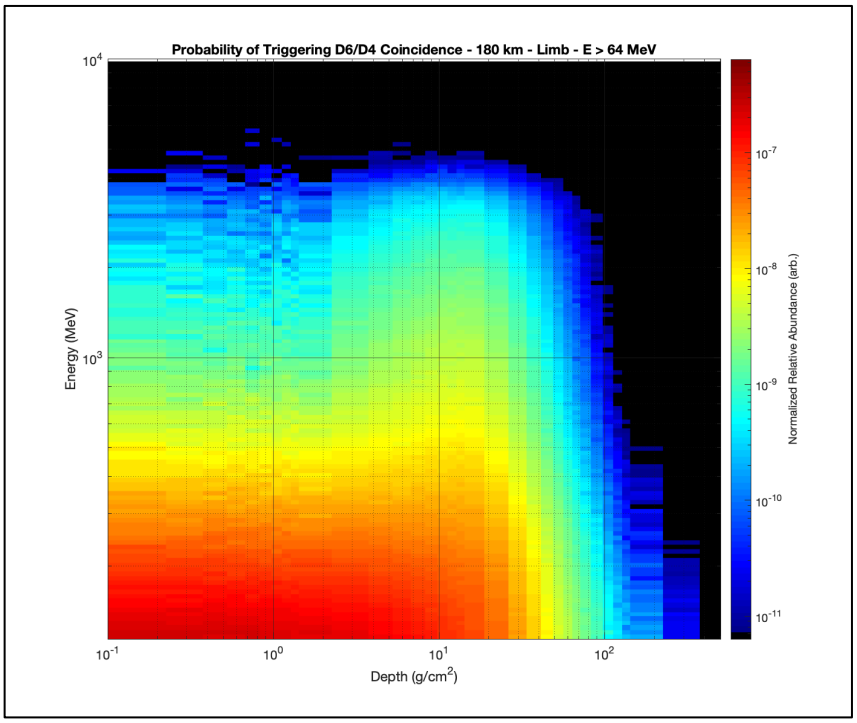

Figure 7.16. The maximum depth distribution of albedo protons emitted by a fully wet regolith and triggering D6/D4 coincidence when facing the lunar limb at altitude of 180 km above the threshold energy of 65 MeV.

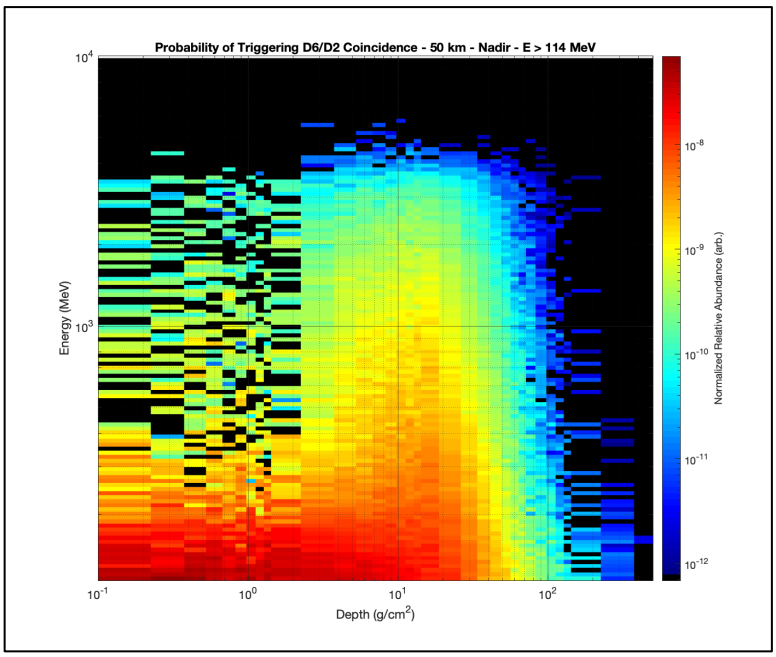

Figure 7.17. The maximum depth distribution of albedo protons emitted by a fully wet regolith and triggering D6/D2 coincidence when facing the lunar nadir at altitude of 50 km above the threshold energy of 114 MeV.

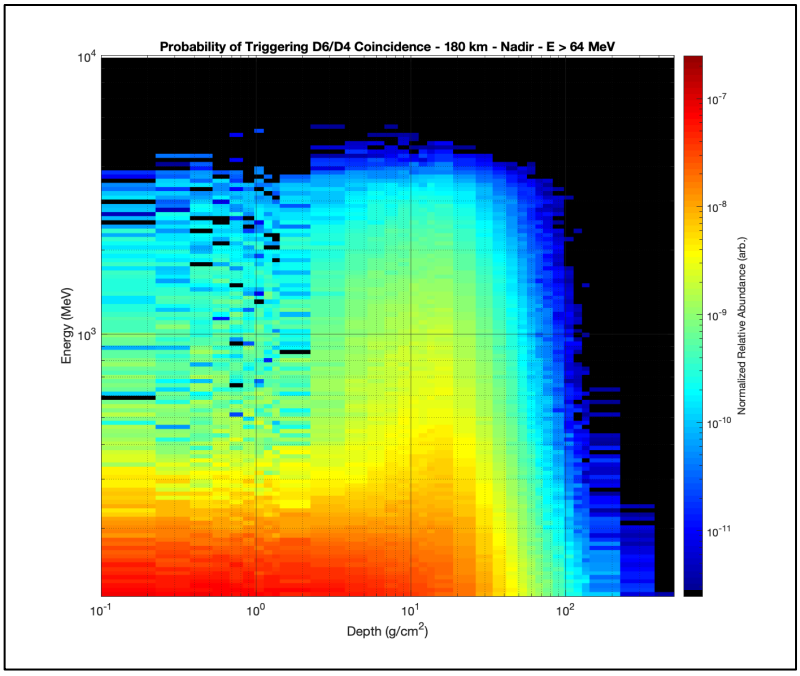

Figure 7.18. The maximum depth distribution of albedo protons emitted by a fully wet regolith and triggering D6/D2 coincidence when facing the lunar nadir at altitude of 180 km above the threshold energy of 114 MeV.

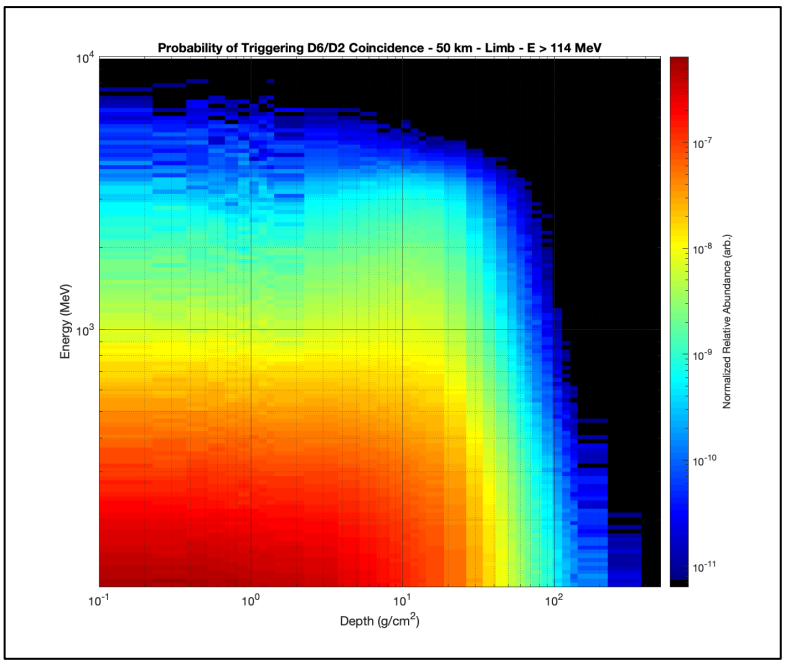

Figure 7.19. The maximum depth distribution of albedo protons emitted by a fully wet regolith and triggering D6/D2 coincidence when facing the lunar limb at altitude of 50 km above the threshold energy of 114 MeV.

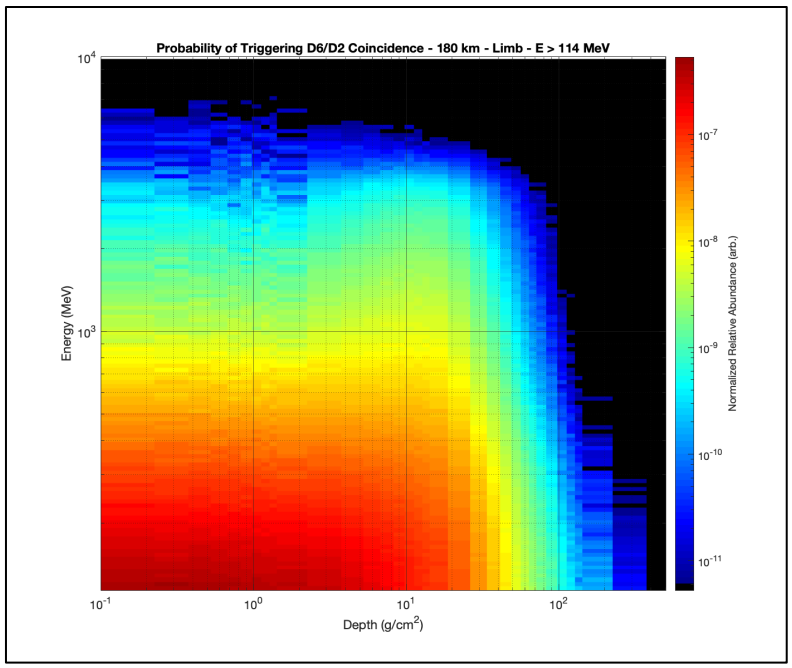

Figure 7.20. The maximum depth distribution of albedo protons emitted by a fully wet regolith and triggering D6/D2 coincidence when facing the lunar limb at altitude of 180 km above the threshold energy of 114 MeV.

7.3 Absorbed Dose[1]

Table 7.1 shows the total absorbed dose rates modeled by MCNP6 in the D1-D2 and the D5-D6 pairs and compares them with the measurements made by the CRaTER instrument between 19 June 2010 and 19 July 2010 for an estimated solar modulation potential of 500 MV obtained from the CRaTER dataset. The total absorbed dose rates resulting from MCNP6 simulations are within 5% of CRaTER measurements for the D1-D2 pair and within 1% for the D5-D6 pair.

Table 7.1 Dose rates (μGy/d) measured by CRaTER and simulated by MCNP6.

Detector Pair	CRaTER	MCNP
D1-D2	248.8	236.64 ± 2.6
D5-D6	245.1	245.76 ± 2.7

MCNP6 simulations show that albedo particles account for 19.9% of the total absorbed dose rate at LRO altitudes of 50 km in the D5-D6 detector pair. This is higher than the results reported by *Spence et al. [2013]*, which obtained an albedo contribution of 8.6% using Geant4. The key difference between these results is that MCNP6 shows a higher contribution from albedo photons than Geant4. However, the results for albedo protons, electrons, positrons, and neutrons are in reasonable agreement. The differences between the transport codes, which were also observed in Chapter 6, are likely due to the different nuclear models used in different transport codes.

Table 7.2 illustrates the contribution from each albedo species in the D5-D6 detector pair derived from MCNP6. Albedo photons have the highest contribution among albedo particles to

[1] Submitted as a presentation manuscript at the 70th International Astronautical Congress and in review for publication in *Acta Astronautica* as Zaman et al., "Absorbed Doses from GCR and Albedo Particles Emitted by the Lunar Surface".

the total absorbed dose (~8.8%). At the D1-D2 pair, the absorbed dose from albedo particles account for 16.2% of the total dose. The absorbed dose rate from GCR is higher in the upper detectors, while the absorbed dose rate from albedo particles is higher in the lower detectors, which is due to the shielding provided by the TEP material between the two pairs. Table 7.3 shows the modeled absorbed dose rates in D1-D2.

The addition of hydrogen to the lunar regolith in MCNP6 resulted in a slightly higher total absorbed dose rate in both detector pairs. Table 7.4 shows the dose rates generated from a wet regolith at the altitude of 50 km and compares them with the previously calculated dose rates from a dry regolith.

Table 7.2. Dose rates in the D5-D6 pair for GCR and albedo particles at 50 km derived from MCNP6 models.

	Absorbed Dose Rate (μGy/d)	Contribution to Total Dose Rate	Contribution to Total Albedo Dose Rate
GCR	196.86	80.1%	
Albedo Photons	21.7	8.81%	44.3%
Albedo Protons	12.2	4.97%	25.0%
Albedo Electrons	6.07	2.47%	12.4%
Albedo Positrons	4.64	1.89%	9.5%
Albedo Neutrons	2.87	1.17%	5.9%
Albedo Deuterons	1.22	0.50%	2.5%
Albedo Tritium Ions	0.16	0.07%	0.3%
Albedo Helium-3 Ions	0.05	0.02%	0.1%
Albedo Alphas	0.02	0.01%	0.04%
Total	245.76		

Table 7.3. Dose rates in the D1-D2 pair for GCR and albedo particles at 50 km derived from MCNP6 models.

	Absorbed Dose Rate (μGy/d)	Contribution to Total Dose Rate	Contribution to Total Albedo Dose Rate
GCR	198.34	83.8%	
Albedo Photons	20.9	8.81%	54.4%
Albedo Protons	6.21	2.62%	16.2%
Albedo Electrons	4.08	1.72%	10.6%
Albedo Positrons	3.42	1.45%	8.9%
Albedo Neutrons	3.50	1.48%	9.1%
Albedo Deuterons	0.22	0.09%	0.59%
Albedo Tritium Ions	0.010	0.004%	0.025%
Albedo Helium-3 Ions	0.003	0.001%	0.008%
Albedo Alphas	0.001	0.001%	0.004%
Total	236.64		

Table 7.4. Total absorbed dose rates (μGy/d) simulated by MCNP6 for dry and wet regolith.

Detector Pair	Dry Regolith	Wet Regolith
D1-D2	236.64 ± 2.6	239.45 ± 2.7
D5-D6	245.76 ± 2.7	247.75 ± 2.8

For the wet regolith, the albedo particles contribute to 21% of the total absorbed dose rate in the D5-D6 pair and 17% in the D1-D2 pair. Figure 7.21 illustrates the contributions of albedo dose rates to the total dose rates for both cases. The addition of hydrogen to the regolith increased the total dose rate by ~1% for both sets of detectors. Figure 7.22 shows the contribution of the individual albedo species to total albedo dose rate. The most significant variation between the dry and wet scenarios appears in the behavior of albedo protons and albedo photons. The presence of hydrogen leads to enhancement in albedo proton dose rate and suppression in albedo photon dose rate, as seen in Chapter 4. However, since the variation in albedo proton dose rate is higher with hydrogen in the regolith, a slight increase in total absorbed dose rate is observed. Other lighter ions

also show enhancements in the dose rate of wet regolith, but this relative increase appears to be insignificant since their total contribution is very small compared to the total absorbed dose rate.

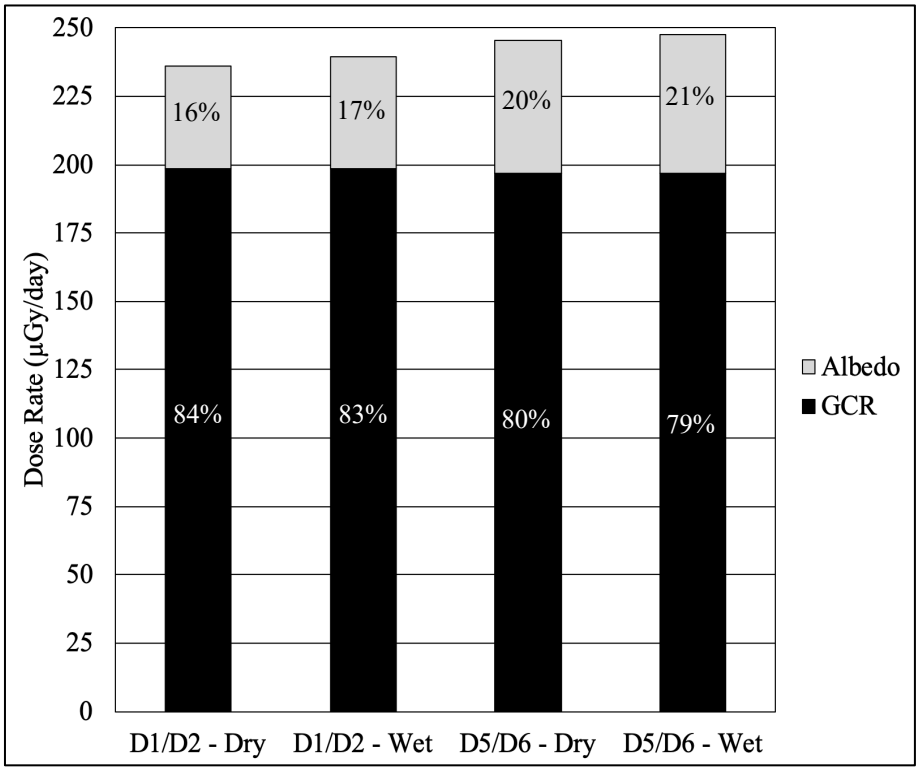

Figure 7.21. Simulated dose rates and dose rate contributions at 50 km altitude in CRaTER for dry and wet regolith in each detector pair.

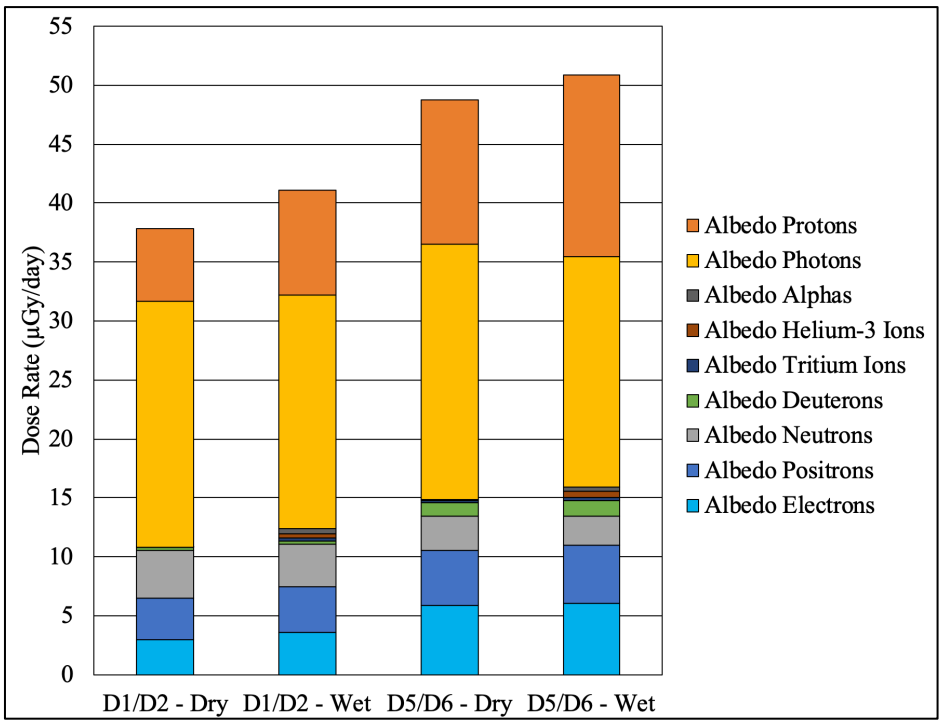

Figure 7.22. Simulated dose rates in each detector pair from albedo particles emitted by dry and wet regolith at 50 km altitude.

8. CONCLUSIONS AND FUTURE WORK

The energy and angular spectra of albedo particles produced by incident GCR ions as a function of maximum production depth were generated using MCNP6. The results show that the population of neutral particles dominates over most energies, and that they reach the lunar surface from processes occurring deeper in the lunar regolith compared to charged particles. Albedo protons stand out when it comes to the angular behavior of albedo particles since they are included in the source term unlike the other albedo particles that are only created in the regolith. With the exception of albedo photons, most energetic albedo particles leave the lunar surface at shallower angles.

Adding hydrogen to the regolith shows an enhancement in the population of high energy albedo protons in MCNP6, which are most likely hydrogen nuclei created by elastic scattering the energetic fragments of GCR ions heavier than protons. Studying the variations in the behavior of albedo particles in several scenarios, each with a regolith enriched with one of the major lunar elements, did not show significant changes in the behavior of albedo electrons, positrons, and protons with energies above 100 keV. The results from MCNP6 suggests that the best candidates for the characterization of the major lunar elements in the regolith are the low energy photons and neutrons. This is due to the increased cross sections of neutrons at lower energies, which is highly dependent on the type of the target isotope. Comparing the dry regolith results of MCNP6 with PHITS and HETC-HEDS shows a good agreement between the codes. However, there is less agreement when comparing the results of wet regolith.

Applying the generated spectra to the field of view of the CRaTER instrument shows that it is able to probe up to 10s of g/cm^2 deep in the regolith, with the limb orientation covering a

wider range of energies than the nadir orientation. However, the wet results from MCNP6 suggest that the nadir field of view might be the optimal orientation for detecting subsurface hydrogen.

Estimates of the contribution of albedo particles to total absorbed dose rate near the lunar surface shows that albedo particles contribute to ~20% of the total absorbed dose rate at an altitude of 50 km, with albedo photons and protons contributing to ~15%. Excluding photons, the results of this work are in reasonable agreement with the results obtained using Geant4. The calculated total dose rates in this work are within 5% of those measured by the CRaTER instrument.

Recommendations for future work are:

1. Investigate the source of the "knee" at 4 GeV in the albedo proton spectrum in dry regolith.
2. Perform calculations with MCNP6 and PHITS for albedo neutron production from dry regolith using the HETC-HEDS geometry, in order to determine if the differences are due to the different geometries utilized for the analyses.
3. Use CRaTER to confirm the asymmetric behavior of albedo protons.
4. Investigate the elastic scattering models in the different codes to determine if they are the source of variations in the behavior of the spectra of albedo protons and neutrons.

REFERENCES

Anderson, J. (2012). *Analyses of measurements from the CRaTER instrument on the LRO spacecraft using space radiation transport codes*. Thesis (Ph.D.)--University of Tennessee, Knoxville, 2012.

Armstrong, T. (1972). Calculation of the lunar photon albedo from galactic and solar proton bombardment. *Journal of Geophysical Research*, *77*(4), 524–536. https://doi.org/10.1029/JA077i004p00524

Carrier III, W. D., Mitchell, J. K., & Mahmood, A. (1973). The relative density of lunar soil. *Geochimica et Cosmochimica Acta (Suppl. 3)*, 2403-2411.

Case, A., Spence, H., Golightly, M., Kasper, J., Blake, J., Mazur, J., et al. (2010). GCR access to the Moon as measured by the CRaTER instrument on LRO. *Geophysical Research Letters*, *37*(19). https://doi.org/10.1029/2010GL045118

Charara, Y., Townsend, L., Gabriel, T., Zeitlin, C., Heilbronn, L., & Miller, J. (2008). HETC-HEDS Code Validation Using Laboratory Beam Energy Loss Spectra Data. *IEEE Transactions on Nuclear Science*, *55*(6), 3164–3168. https://doi.org/10.1109/TNS.2008.2006607

Crites, S., Lucey, P., & Lawrence, D. (2013). Proton flux and radiation dose from galactic cosmic rays in the lunar regolith and implications for organic synthesis at the poles of the Moon and Mercury. *Icarus*, *226*(2), 1192–1200. https://doi.org/10.1016/j.icarus.2013.08.003

Colaprete, A., Schultz, P., Heldmann, J., Wooden, D., Shirley, M., Ennico, K., et al. (2010). Detection of water in the LCROSS ejecta plume. *Science (New York, N.Y.)*, *330*(6003), 463–468. https://doi.org/10.1126/science.1186986

De Angelis, G., Badavi, F., Clem, J., Blattnig, S., Clowdsley, M., Nealy, J., et al. (2007). Modeling of the Lunar Radiation Environment. *Nuclear Physics B (Proceedings Supplements)*, *166*, 169–183. https://doi.org/10.1016/j.nuclphysbps.2006.12.034

de Wet, W. & Townsend, L. (2017). A calculation of the radiation environment on the Martian surface. *Life Sciences in Space Research*, *14*, 51–56. https://doi.org/10.1016/j.lssr.2017.07.008

de Wet, W. C., Zaman, F., Townsend, L., Schwadron, N., Spence, H. E., Wilson, J. K., et al. (2019). Lunar Albedo Protons and the Hunt for Subsurface Hydrogen. In *AGU Fall Meeting 2019*. AGU.

Elphic, R. C., Lawrence, D. J., Feldman, W. C., Barraclough, B. L., Maurice, S., Binder, A. B., & Lucey, P. G. (2000). Lunar rare earth element distribution and ramifications for FeO and TiO2: Lunar Prospector neutron spectrometer observations. Journal of Geophysical Research: Planets, 105(E8), 20333–20345. https://doi.org/10.1029/1999JE001176

Feldman, W., Maurice, S., Binder, A., Barraclough, B., Elphic, R., & Lawrence, D. (1998). Fluxes of Fast and Epithermal Neutrons from Lunar Prospector: Evidence for Water Ice at the Lunar Poles. *Science*, *281*(5382), 1496–1500. https://doi.org/10.1126/science.281.5382.1496

Gabriel, T. A., Bishop, B. L., Alsmiller, F. S., Alsmiller Jr, R. G., & Johnson, J. O. (2000). Calor95: Monte Carlo Code System for Design and Analysis of Calorimeter Systems, Spallation Neutron Source (SNS) Target Systems, etc. ORNL.

Gasnault, O., d'Uston, C., Feldman, W. C., & Maurice, S. (2000). Lunar fast neutron leakage flux calculation and its elemental abundance dependence. (2000). *Journal of Geophysical Research: Planets*, *105*(E2), 4263–4271. https://doi.org/10.1029/1999JE001124

Goorley, T., James, M., Booth, T., Brown, F., Bull, J., Cox, L., et al. (2016). Features of MCNP6.(Report). *Annals of Nuclear Energy*, *87*(P2), 772–783. https://doi.org/10.1016/j.anucene.2015.02.020

Hayatsu, K., Hareyama, M., Kobayashi, S., Yamashita, N., Miyajim, M., Sakurai, K., & Hasebe, N. (2008). Radiation Doses for Human Exposed to Galactic Cosmic Rays and Their Secondary Products on the Lunar Surface. *Biological Sciences in Space*, *22*(2), 59–66. https://doi.org/10.2187/bss.22.59

Honeycutt, J., Cianciola, C., & Wooten, L. (2019). NASA's Space Launch System: Artemis 1 Vehicle Nears Completion.

Lawrence, D., Feldman, W., Elphic, R., Hagerty, J., Maurice, S., Mckinney, G., & Prettyman, T. (2006). Improved modeling of Lunar Prospector neutron spectrometer data: Implications for hydrogen deposits at the lunar poles. *Journal of Geophysical Research: Planets*, *111*(E8). https://doi.org/10.1029/2005JE002637

Looper, M., Mazur, J., Blake, J., Spence, H., Schwadron, N., Golightly, M., et al. (2013). The radiation environment near the lunar surface: CRaTER observations and Geant4 simulations. *Space Weather*, *11*(4), 142–152. https://doi.org/10.1002/swe.20034

Matthiä, D., Ehresmann, B., Lohf, H., Köhler, J., Zeitlin, C., Appel, J., et al. (2016). The Martian surface radiation environment – a comparison of models and MSL/RAD measurements. *Journal of Space Weather and Space Climate*, *6*. https://doi.org/10.1051/swsc/2016008

Matthiä, D., Hassler, D., de Wet, W., Ehresmann, B., Firan, A., Flores-Mclaughlin, et al. (2017). The radiation environment on the surface of Mars - Summary of model calculations and comparison to RAD data. *Life Sciences in Space Research*, *14*, 18–28. https://doi.org/10.1016/j.lssr.2017.06.003

Mazur, J., Crain, W., Looper, M., Mabry, D., Blake, J., Case, A., et al. (2011). New measurements of total ionizing dose in the lunar environment. *Space Weather*, *9*(7). https://doi.org/10.1029/2010SW000641

Mazur, J., Zeitlin, C., Schwadron, N., Looper, M., Townsend, L., Blake, J., & Spence, H. (2015). Update on Radiation Dose from Galactic and Solar Protons at the Moon Using the LRO/CRaTER Microdosimeter. *Space Weather*, *13*(6), 363–364. https://doi.org/10.1002/2015SW001175

McKay, D., Heiken, G., Basu, A., Blanford, G., Simon, S., Reedy, R., et al. (1991). The lunar regolith. Lunar sourcebook, 285-356.

Mckinney, G., Lawrence, D., Prettyman, T., Elphic, R., Feldman, W., & Hagerty, J. (2006). MCNPX benchmark for cosmic ray interactions with the Moon. *Journal of Geophysical Research: Planets*, *111*(E6). https://doi.org/10.1029/2005JE002551

Mesick, K., Feldman, W., Coupland, D., & Stonehill, L. (2018). Benchmarking Geant4 for Simulating Galactic Cosmic Ray Interactions Within Planetary Bodies. *Earth and Space Science*, *5*(7), 324–338. https://doi.org/10.1029/2018EA000400

Niita, K., Sato, T., Iwase, H., Nose, H., Nakashima, H., & Sihver, L. (2006). PHITS—a particle and heavy ion transport code system. *Radiation Measurements*, *41*(9), 1080–1090. https://doi.org/10.1016/j.radmeas.2006.07.013

Ota, S., Kobayashi, S., Sihver, L., Yamashita, N., & Hasebe, N. (2011). Neutron production in the lunar subsurface from alpha particles in galactic cosmic rays. *Earth, Planets and Space*, *63*(1), 25–35. https://doi.org/10.5047/eps.2010.01.006

Panasyuk, M., Kuznetsov, N., & Tulupov, V. (2013). Radiation in space: Long-term cooperation between SINP MSU and the Lavochkin Association.(Report). *Solar System Research*, *47*(7), 594–600. https://doi.org/10.1134/S0038094613070125

Porter, J., Townsend, L., Spence, H., Golightly, M., Schwadron, N., Kasper, J., et al. (2014). Radiation environment at the Moon: Comparisons of transport code modeling and measurements from the CRaTER instrument. *Space Weather*, *12*(6), 329–336. https://doi.org/10.1002/2013SW000994

Pieters, C. M., Goswami, J. N., Clark, R. N., Annadurai, M., Boardman, J., Buratti, B., et al. (2009). Character and spatial distribution of OH/H2O on the surface of the Moon seen by M3 on Chandrayaan-1. *Science*, *326*(5952), 568-572. https://doi.org/10.1126/science.1178658

Prettyman, T., Hagerty, J., Elphic, R., Feldman, W., Lawrence, D., Mckinney, G., & Vaniman, D. (2006). Elemental composition of the lunar surface: Analysis of gamma ray spectroscopy data from Lunar Prospector. *Journal of Geophysical Research: Planets*, *111*(E12). https://doi.org/10.1029/2005JE002656

Puchalska, M., Sihver, L., Sato, T., Berger, T., & Reitz, G. (2012). Simulations of MATROSHKA experiment outside the ISS using PHITS. *Advances in Space Research*, *50*(4), 489–495. https://doi.org/10.1016/j.asr.2012.04.027

Ratliff, H., Smith, M., & Heilbronn, L. (2017). Simulation of the GCR spectrum in the Mars curiosity rover's RAD detector using MCNP6. *Life Sciences in Space Research*, *14*, 43–50. https://doi.org/10.1016/j.lssr.2017.07.003

Reedy, R. C. (1978). Planetary gamma ray spectroscopy. In *Gamma Ray Spectroscopy in Astrophysics* (p. 98).

Saal, A., Hauri, E., Cascio, M., Van Orman, J., Rutherford, M., & Cooper, R. (2008). Volatile content of lunar volcanic glasses and the presence of water in the Moon's interior. *Nature*, *454*(7201), 192–195. https://doi.org/10.1038/nature07047

Sato, T. & Niita, K. (2006). Analytical Functions to Predict Cosmic-Ray Neutron Spectra in the Atmosphere. *Radiation Research*, *166*(3), 544–555. https://doi.org/10.1667/RR0610.1

Sato, T., Iwamoto, Y., Hashimoto, S., Ogawa, T., Furuta, T., Abe, S., et al. (2018). Features of Particle and Heavy Ion Transport code System (PHITS) version 3.02. *Journal of Nuclear Science and Technology*, *55*(6), 1–7. https://doi.org/10.1080/00223131.2017.1419890

Schwadron, N., Baker, T., Blake, B., Case, A., Cooper, J., Golightly, M., et al. (2012). Lunar radiation environment and space weathering from the Cosmic Ray Telescope for the Effects of Radiation (CRaTER). *Journal of Geophysical Research: Planets*, *117*(E12). https://doi.org/10.1029/2011JE003978

Schwadron, N., Wilson, J., Looper, M., Jordan, A., Spence, H., Blake, J., et al. (2016). Signatures of volatiles in the lunar proton albedo. *Icarus*, *273*(C), 25–35. https://doi.org/10.1016/j.icarus.2015.12.003

Schwadron, N., Rahmanifard, F., Wilson, J., Jordan, A., Spence, H., Joyce, C., et al. (2018). Update on the Worsening Particle Radiation Environment Observed by CRaTER and Implications for Future Human Deep-Space Exploration. *Space Weather*, *16*(3), 289–303. https://doi.org/10.1002/2017SW001803

Sihver, L., Mancusi, D., Niita, K., Sato, T., Townsend, L., Farmer, C., et al. (2008). Benchmarking of calculated projectile fragmentation cross-sections using the 3-D, MC codes PHITS, FLUKA, HETC-HEDS, MCNPX_HI, and NUCFRG2. *Acta Astronautica*, *63*(7-10), 865–877. https://doi.org/10.1016/j.actaastro.2008.02.012

Slaba, T., O'Neill, P., & Golge, S. (2014). *Badhwar - O'Neill 2014 Galactic Cosmic Ray Flux Model Description*. Retrieved from http://hdl.handle.net/2060/20150003026

Spence, H., Case, A., Golightly, M., Heine, T., Larsen, B., Blake, J., et al. (2010). CRaTER: The Cosmic Ray Telescope for the Effects of Radiation Experiment on the Lunar Reconnaissance Orbiter Mission. *Space Science Reviews*, *150*(1-4), 243–284. https://doi.org/10.1007/s11214-009-9584-8

Spence, H., Golightly, M., Joyce, C., Looper, M., Schwadron, N., Smith, S., et al. (2013). Relative contributions of galactic cosmic rays and lunar proton "albedo" to dose and dose rates near the Moon. *Space Weather*, *11*(11), 643–650. https://doi.org/10.1002/2013SW000995

Townsend, L., Wilson, J., Nealy, J., & Simonsen, L. (1990). *Estimates of galactic cosmic ray shielding requirements during solar minimum - NASA-TM-4167*. Retrieved from http://hdl.handle.net/2060/19900008219

Townsend, L., Cucinotta, F., & Wilson, J. (1992). Interplanetary Crew Exposure Estimates for Galactic Cosmic Rays. *Radiation Research*, *129*(1), 48–52. https://doi.org/10.2307/3577902

Townsend, L., Charara, Y., Delauder, N., Pourarsalan, M., Anderson, J., Fisher, C., et al. (2010a). Parameterizations of the linear energy transfer spectrum for the CRaTER instrument during the LRO mission. *Space Weather*, *8*(3). https://doi.org/10.1029/2009SW000526

Townsend, L., Moussa, H., & Charara, Y. (2010b). Monte Carlo simulations of energy losses by space protons in the CRaTER detector. *Acta Astronautica*, *66*(5), 643–647. https://doi.org/10.1016/j.actaastro.2009.08.007

Turkevich, A. (1973). Average chemical composition of the lunar surface. *The Moon*, *8*(3), 365–367. https://doi.org/10.1007/BF00581730

Waters, L. S. (2002). MCNPX user's manual. *Los Alamos National Laboratory*.

Wilson, J., Spence, H., Kasper, J., Golightly, M., Bern Blake, J., Mazur, J., et al. (2012). The first cosmic ray albedo proton map of the Moon. *Journal of Geophysical Research: Planets*, *117*(E12). https://doi.org/10.1029/2011JE003921

Wilson, J., Spence, H., Schwadron, N., Case, A., Looper, M., Jordan, A., et al. (2020). Precise Detections of Solar Particle Events and a New View of the Moon. *Geophysical Research Letters*, *47*(1). https://doi.org/10.1029/2019GL085522

Yamashita, N., Hasebe, N., Miyachi, T., Kobayashi, M., Okudaira, O., Kobayashi, S., et al. (2008). Complexities of gamma-ray line intensities from the lunar surface. *Earth, Planets and Space*, *60*(4), 313–319. https://doi.org/10.1186/BF03352796

APPENDICES

APPENDIX A

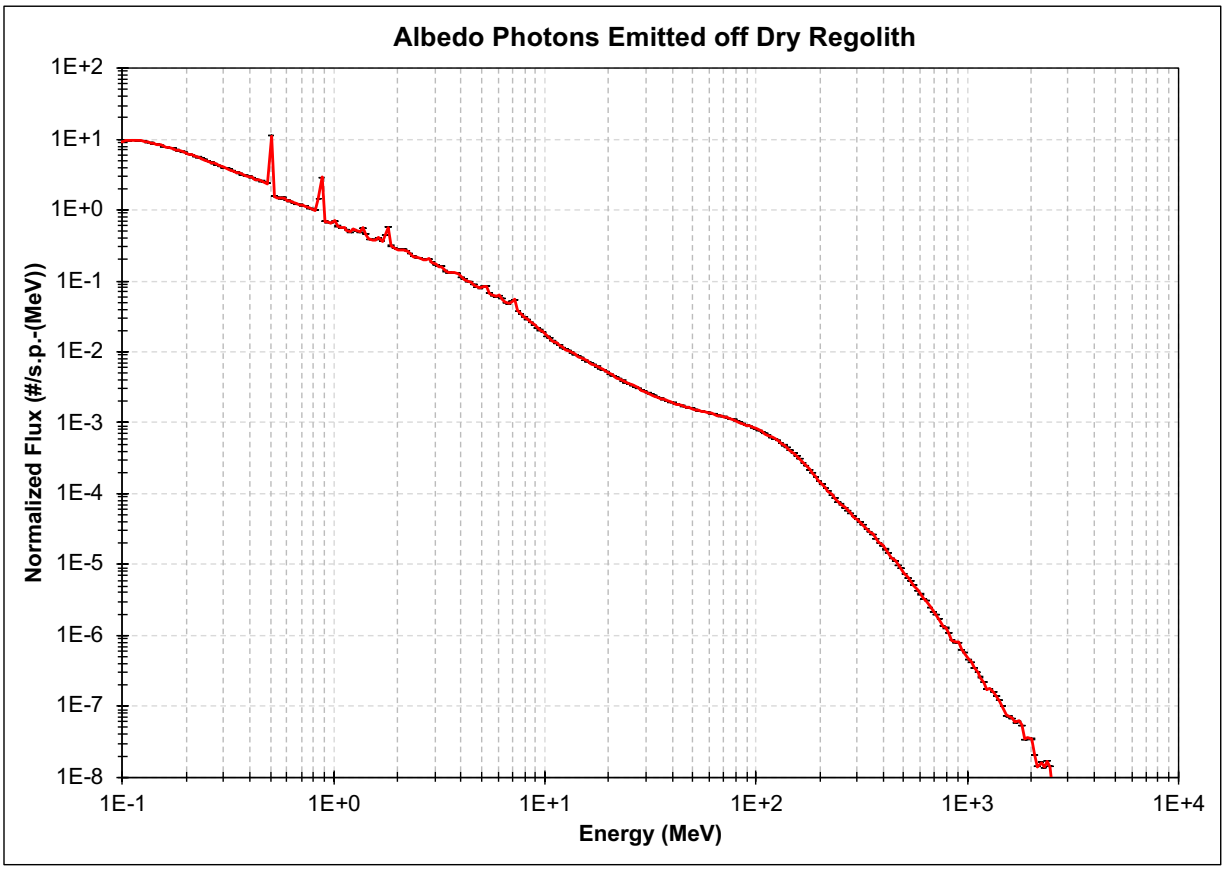

Figure A.1. The energy spectrum of albedo photons emitted off the lunar surface.

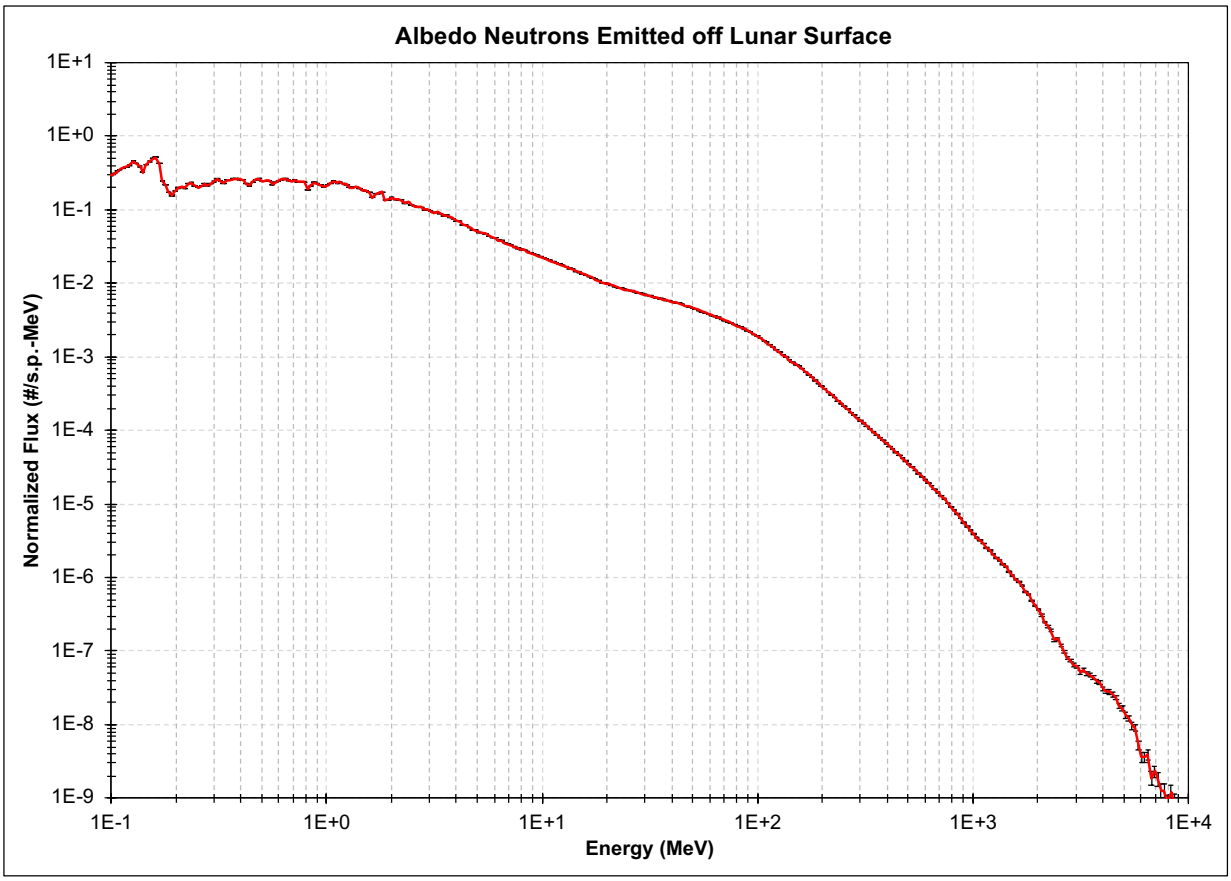

Figure A.2. The energy spectrum of albedo neutrons emitted off the lunar surface.

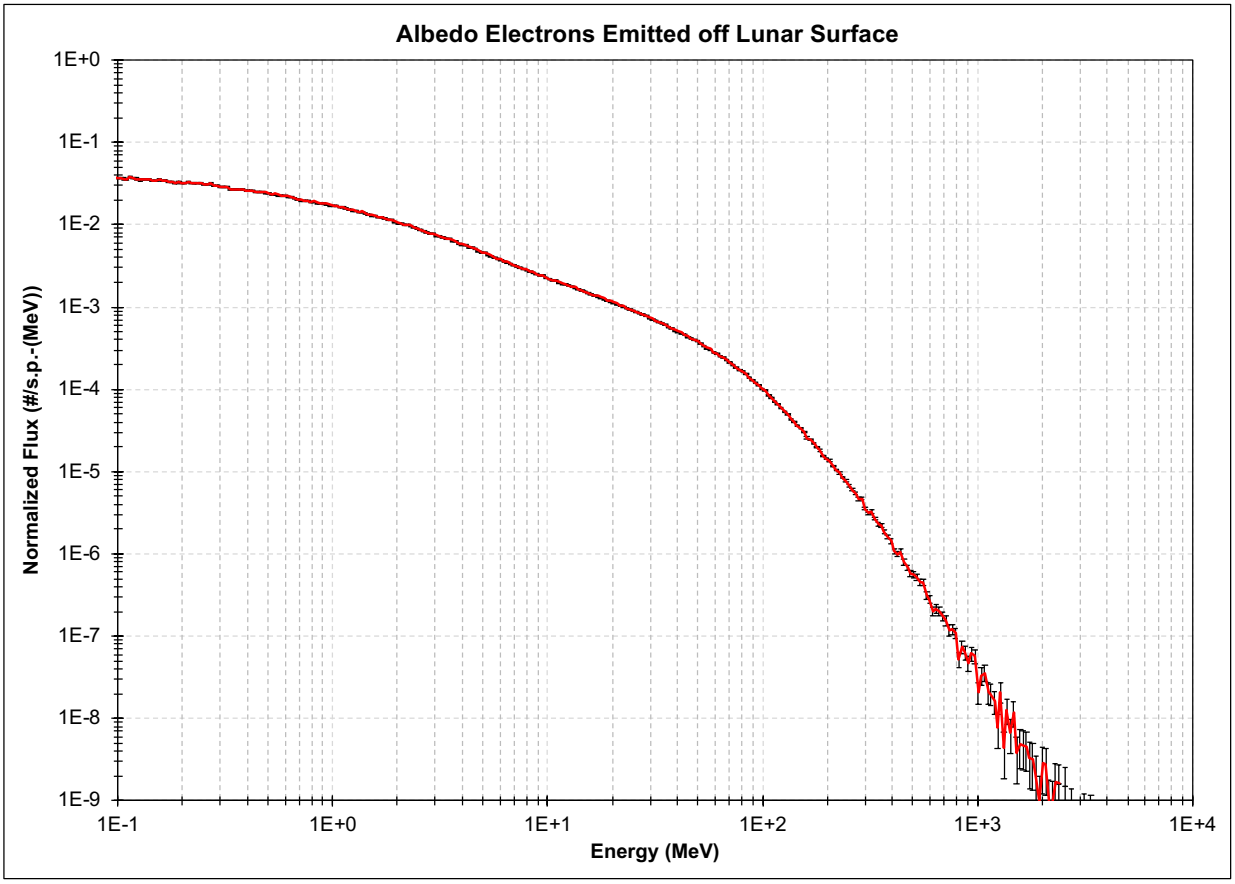

Figure A.3. The energy spectrum of albedo electrons emitted off the lunar surface.

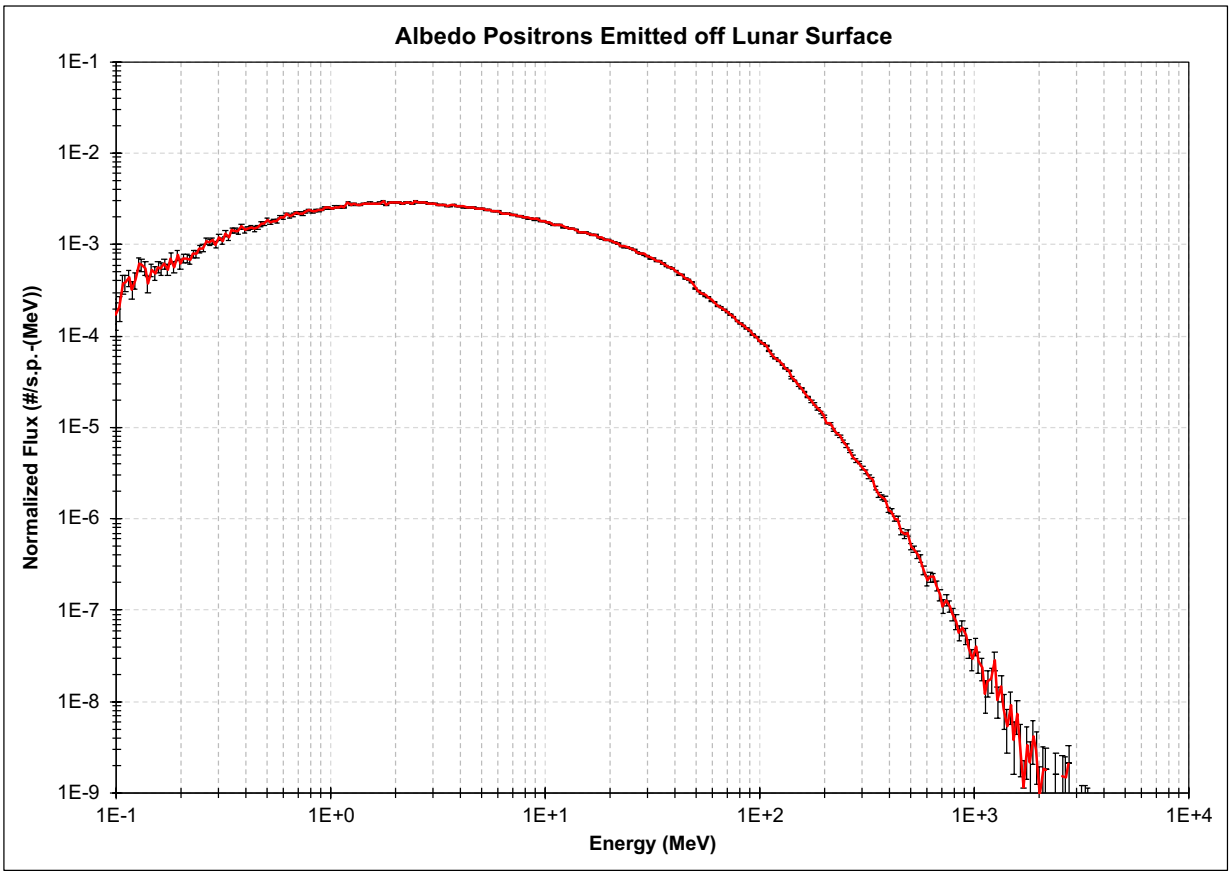

Figure A.4. The energy spectrum of albedo positrons emitted off the lunar surface.

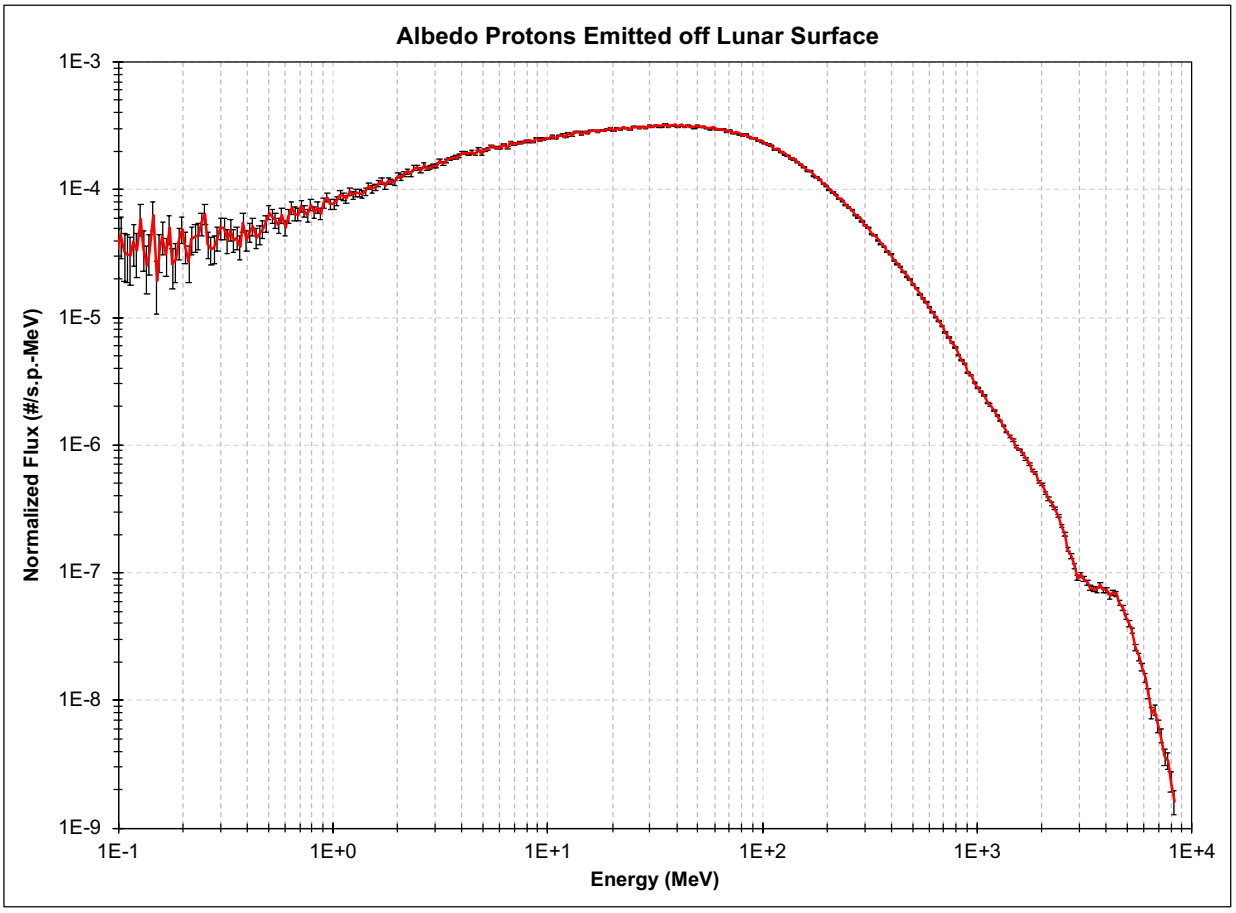

Figure A.5. The energy spectrum of albedo protons emitted off the lunar surface.

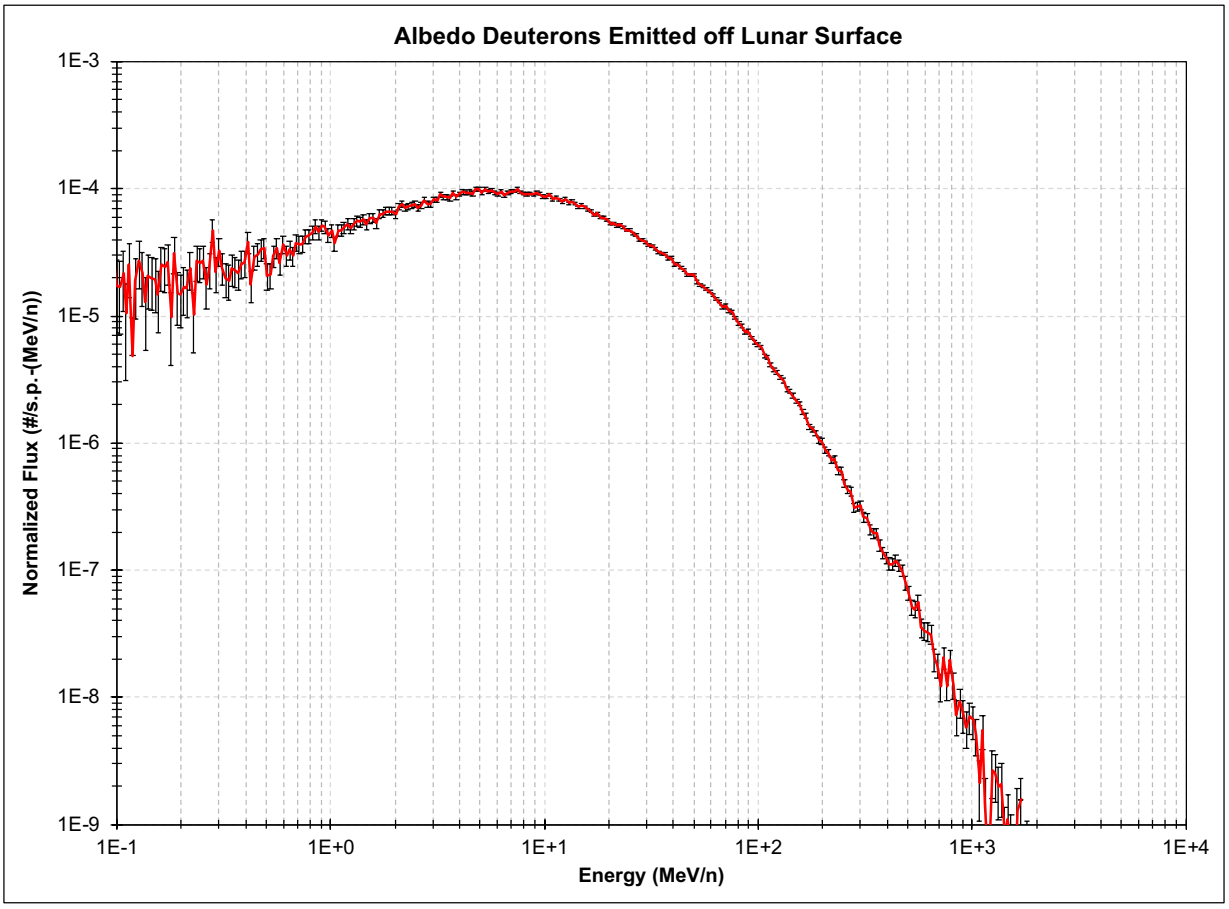

Figure A.6. The energy spectrum of albedo deuterons emitted off the lunar surface.

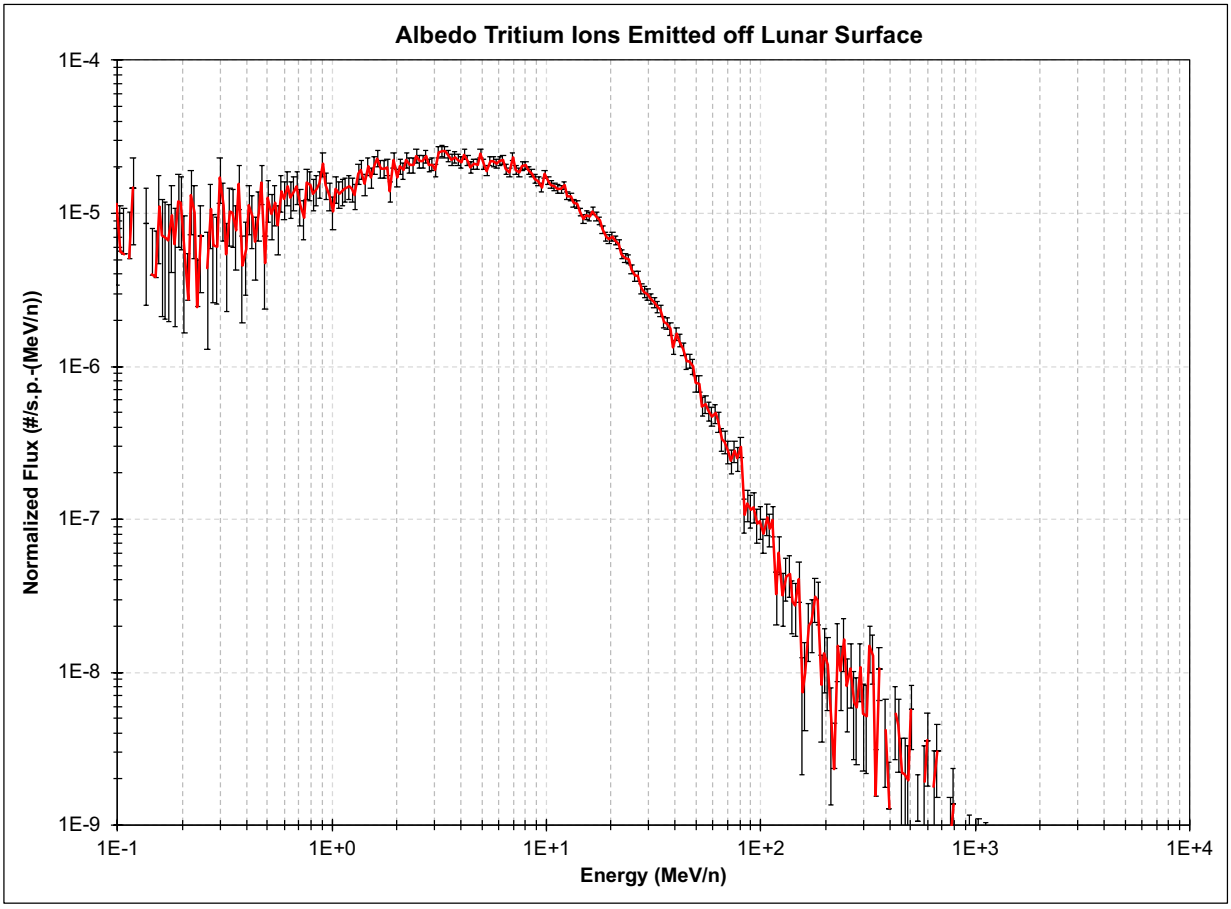

Figure A.7. The energy spectrum of albedo tritium ions emitted off the lunar surface.

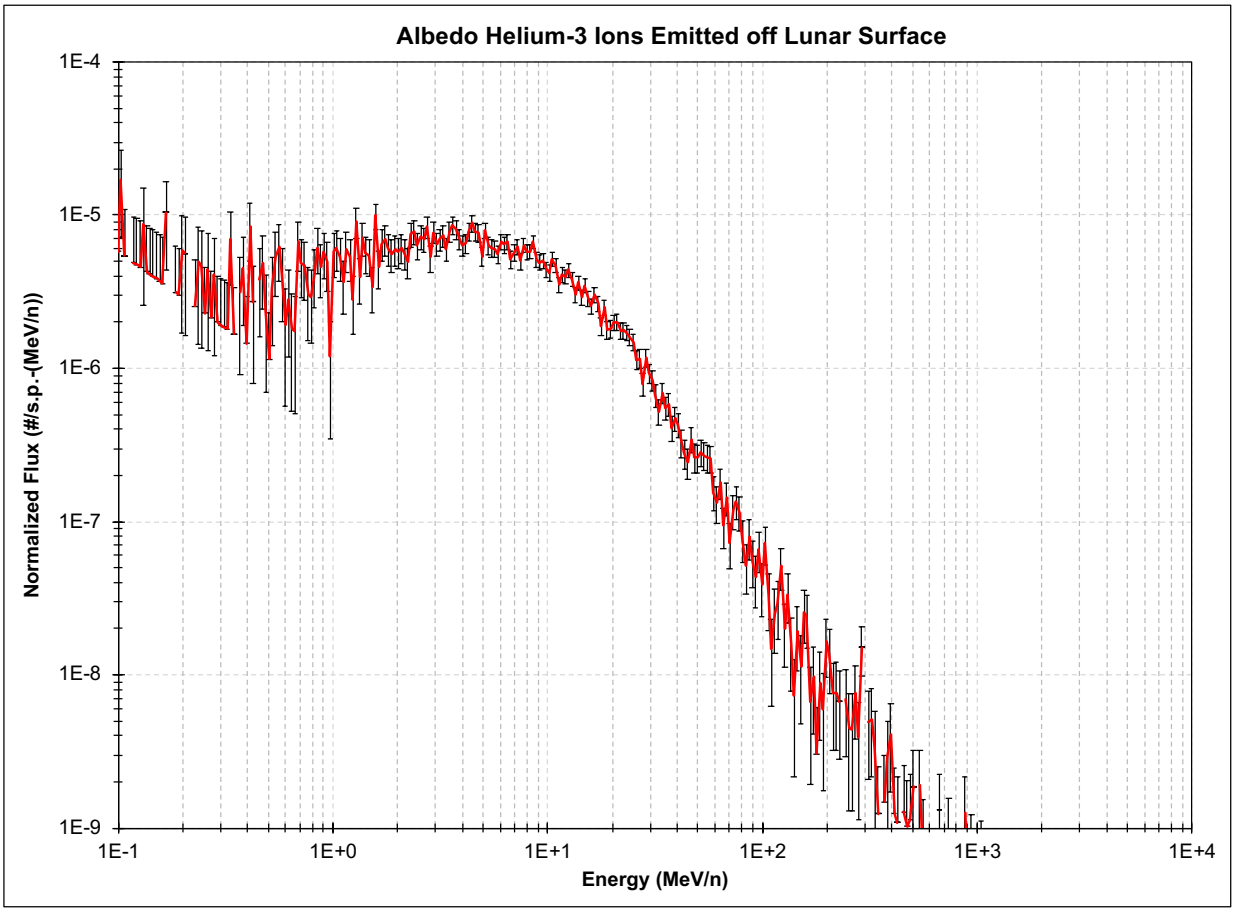

Figure A.8. The energy spectrum of albedo helium-3 ions emitted off the lunar surface.

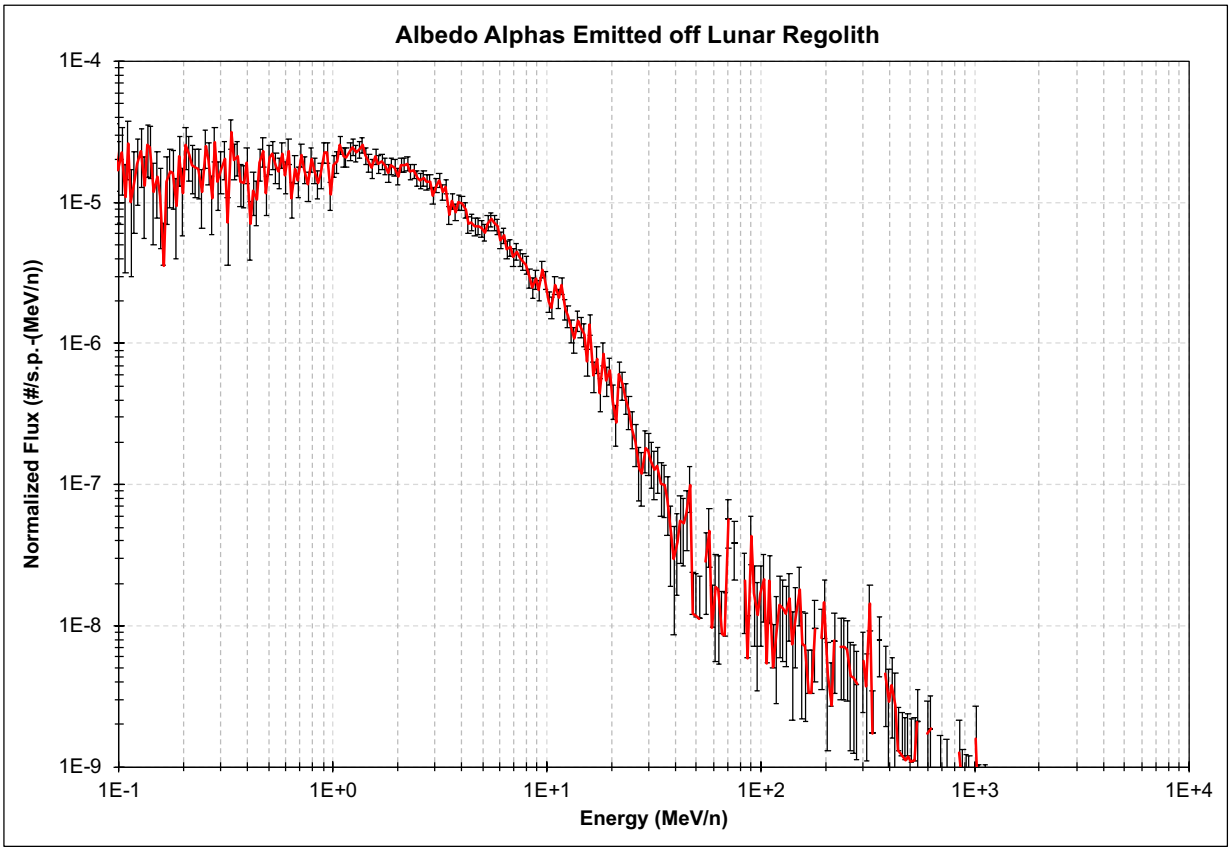

Figure A.9. The energy spectrum of albedo alphas emitted off the lunar surface.

APPENDIX B

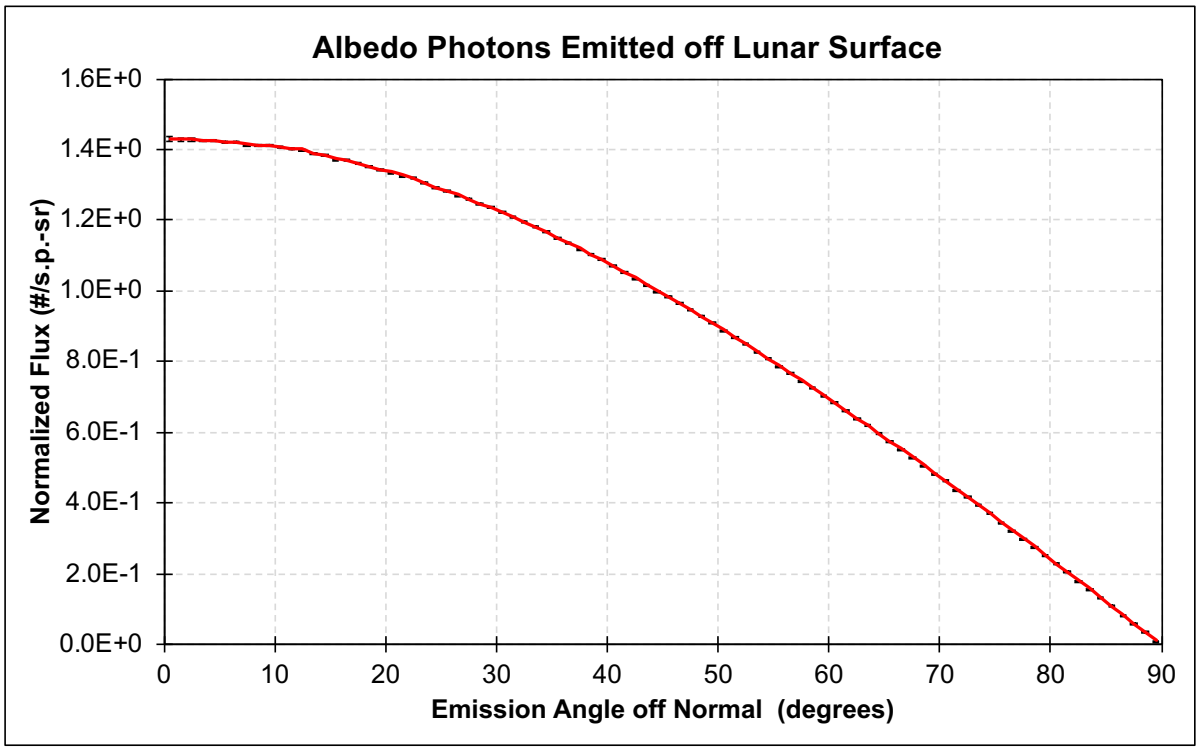

Figure B.1. The angular spectrum of albedo photons emitted off the lunar surface.

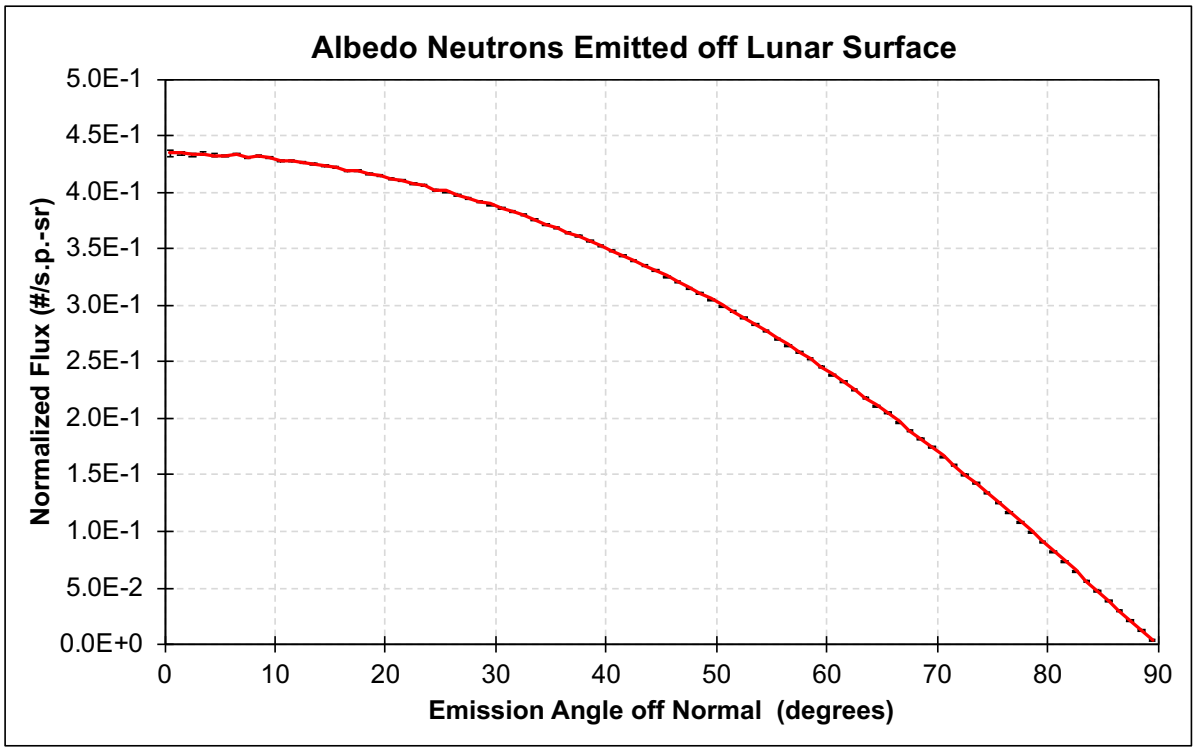

Figure B.2. The angular spectrum of albedo neutrons emitted off the lunar surface.

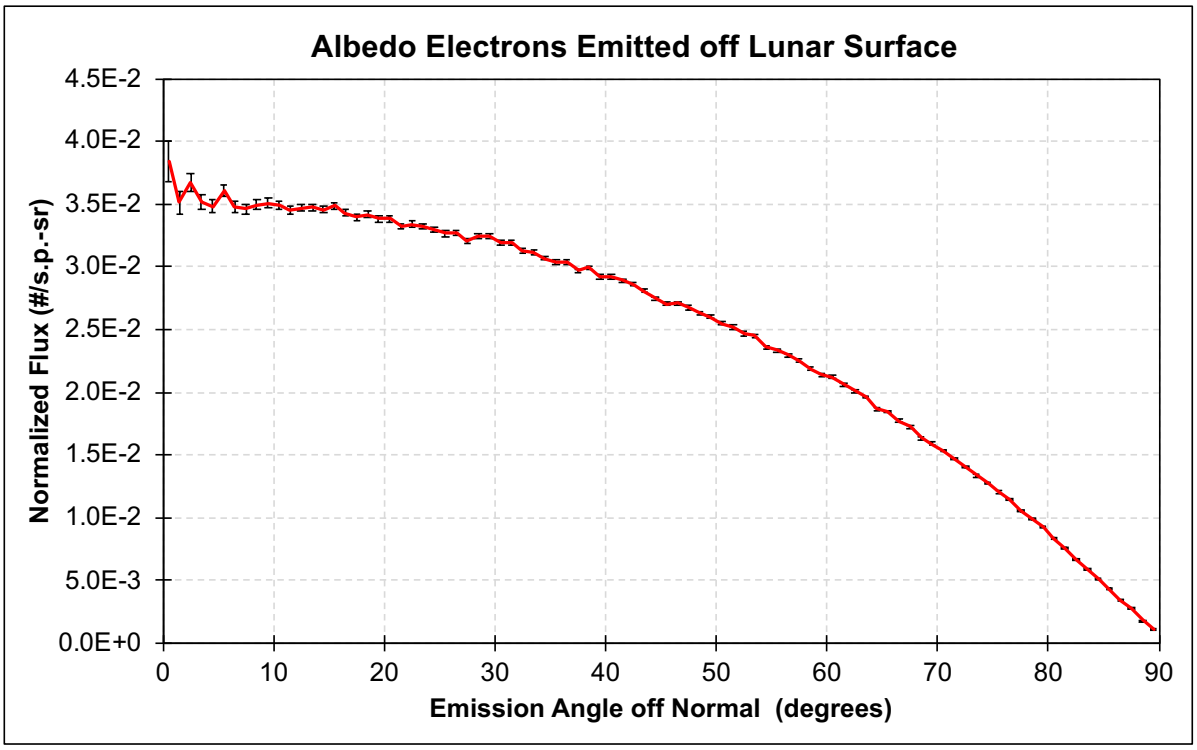

Figure B.3. The angular spectrum of albedo electrons emitted off the lunar surface.

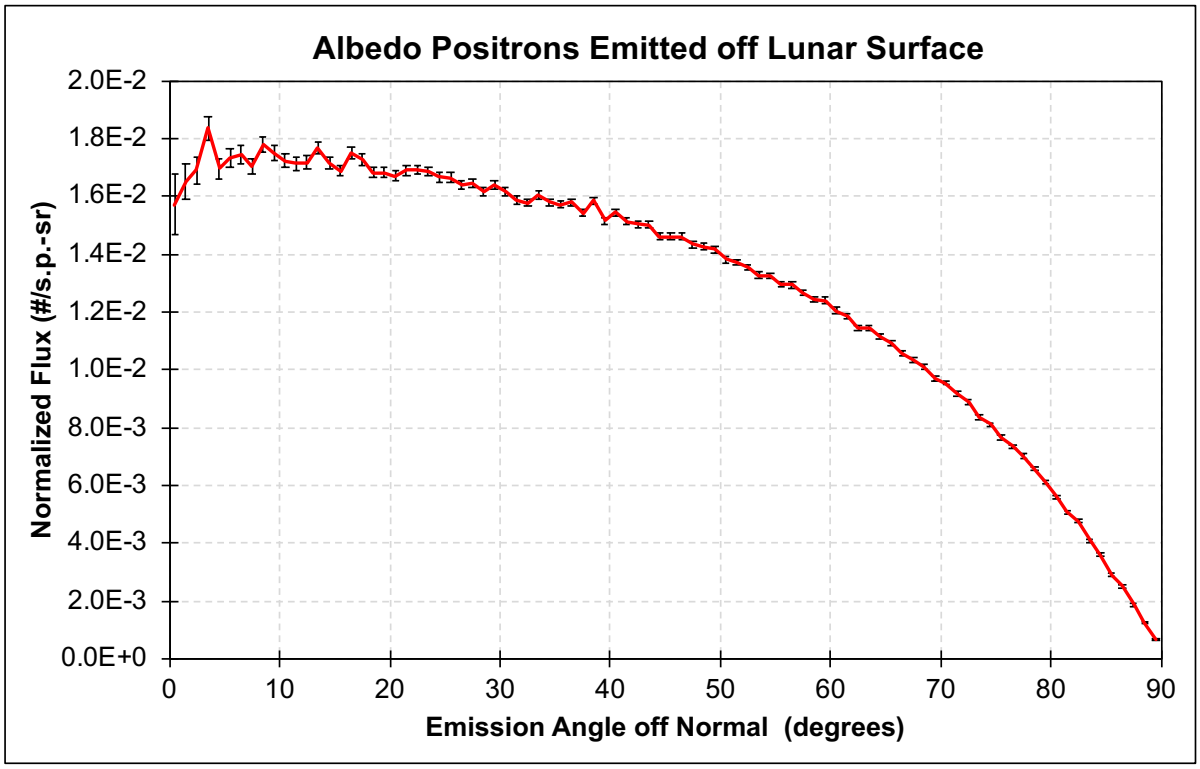

Figure B.4. The angular spectrum of albedo positrons emitted off the lunar surface.

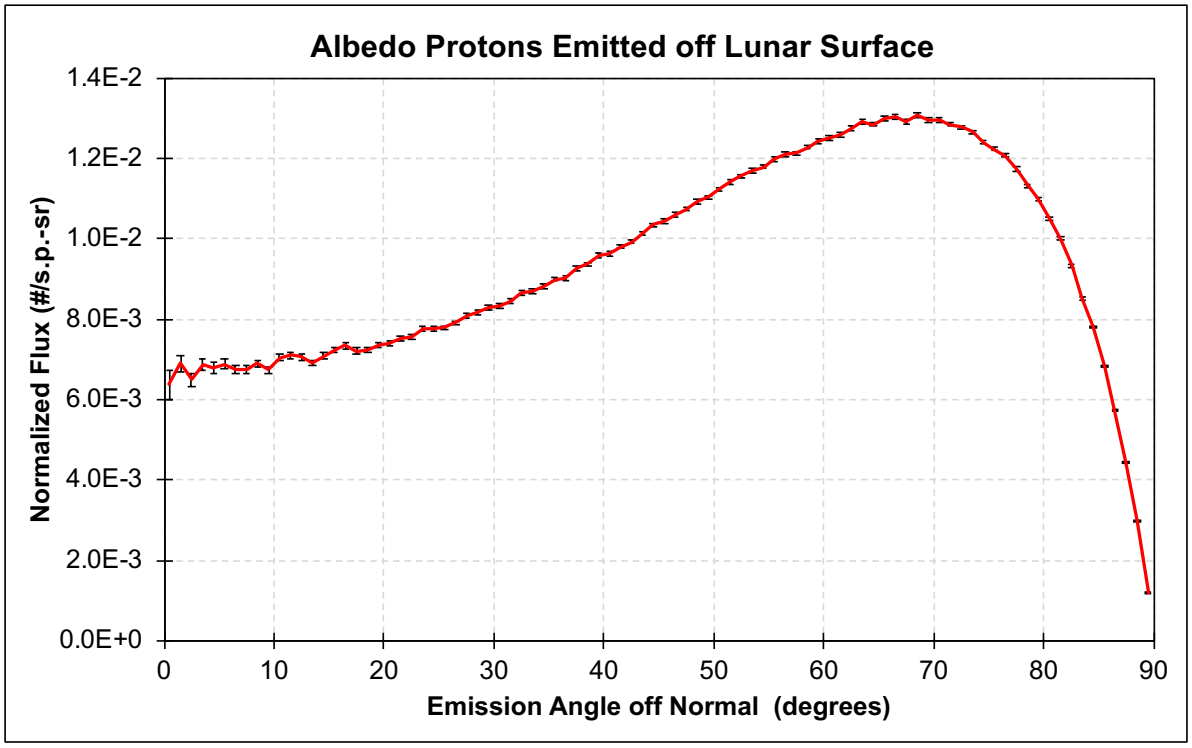

Figure B.5. The angular spectrum of albedo protons emitted off the lunar surface.

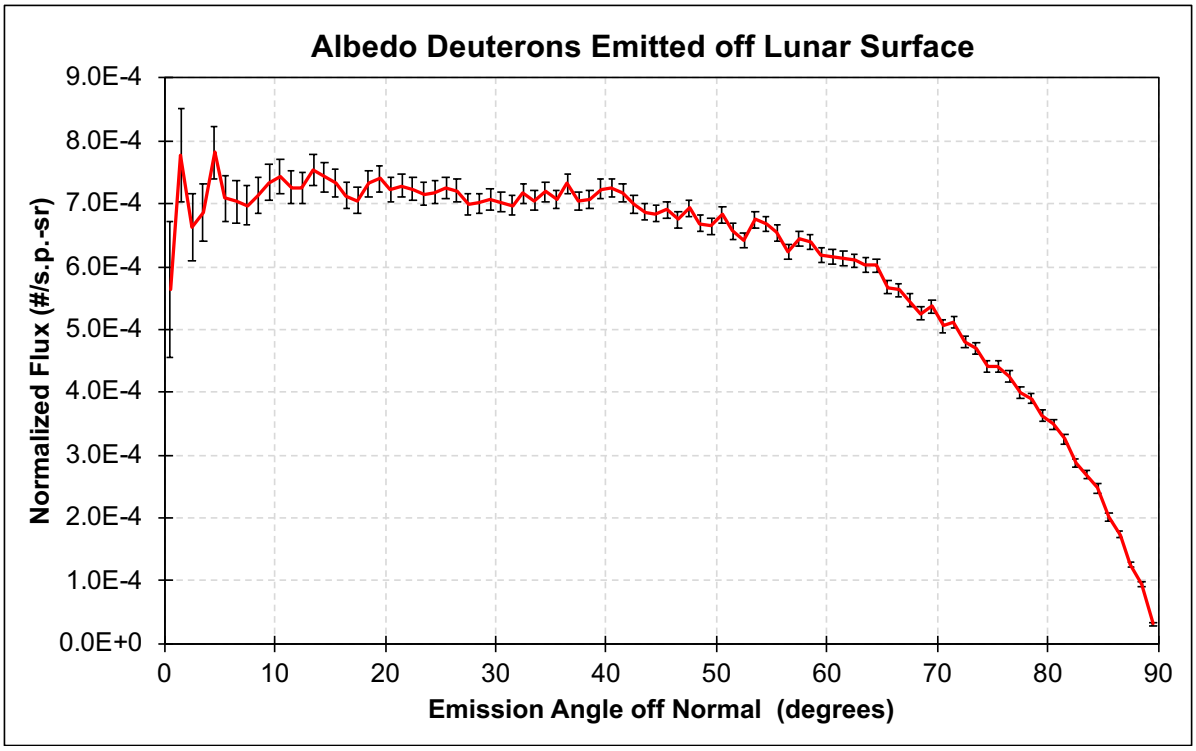

Figure B.6. The angular spectrum of albedo deuterons emitted off the lunar surface.

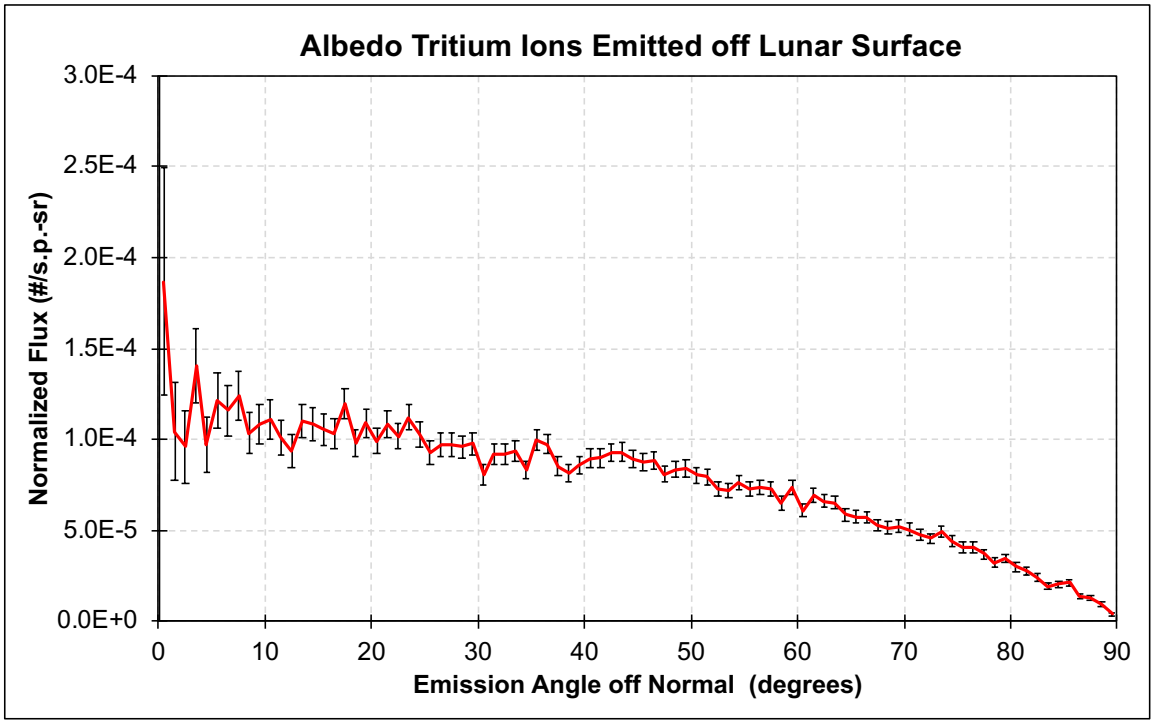

Figure B.7. The angular spectrum of albedo tritium ions emitted off the lunar surface.

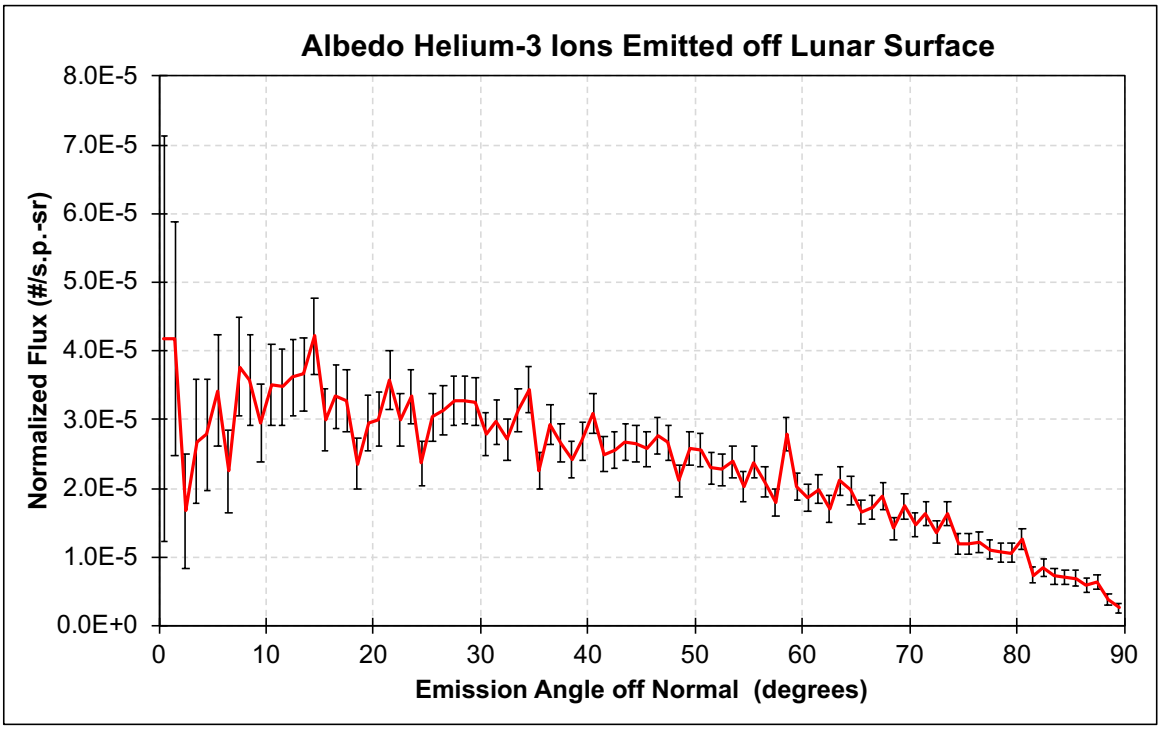

Figure B.8. The angular spectrum of albedo helium-3 ions emitted off the lunar surface.

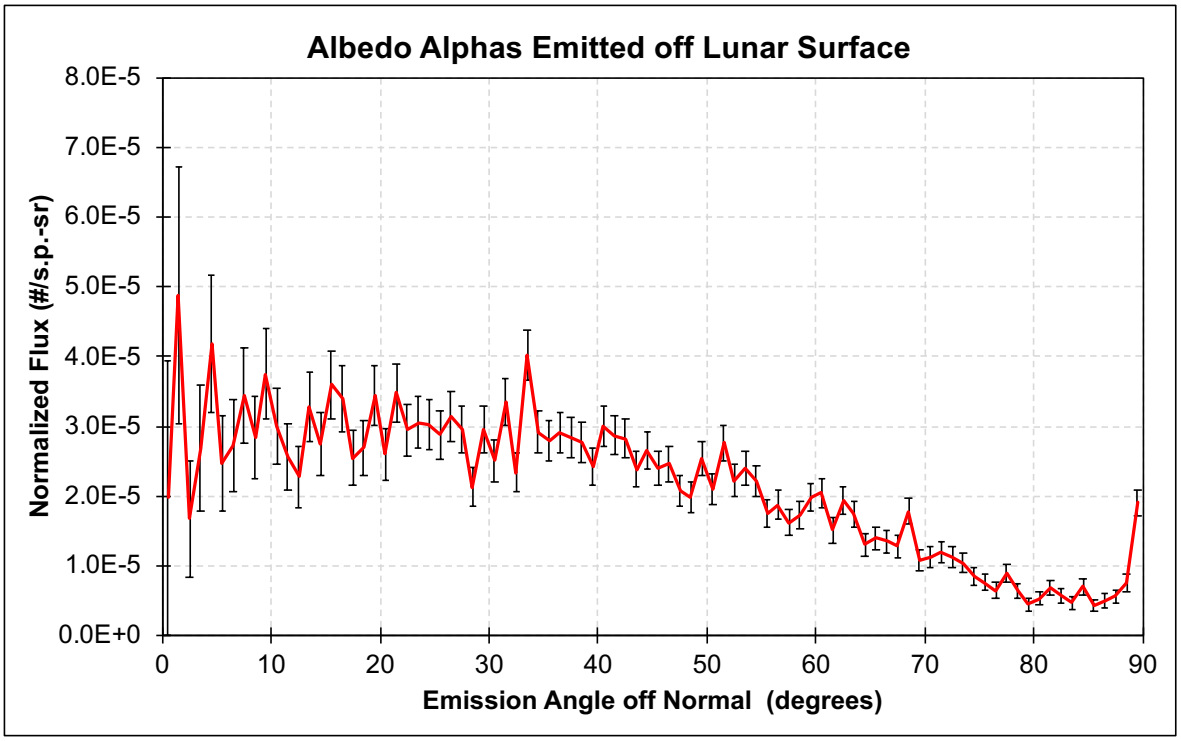

Figure B.9. The angular spectrum of albedo alphas emitted off the lunar surface.

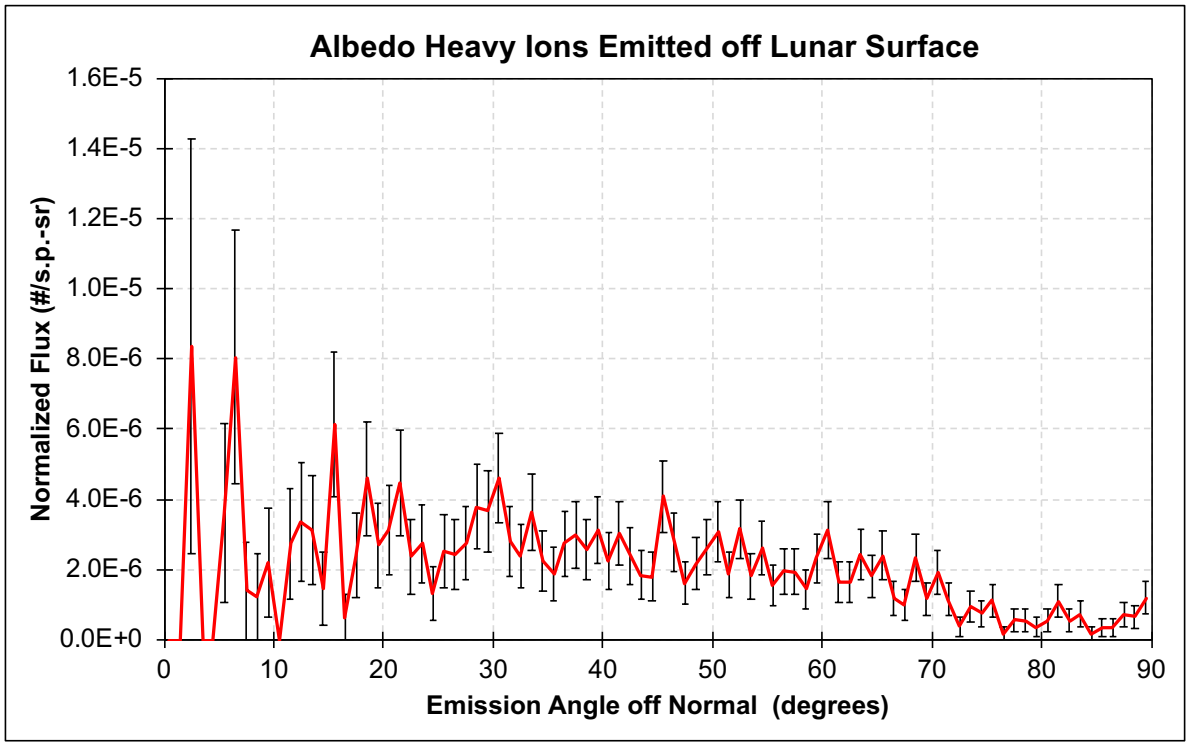

Figure B.10. The angular spectrum of albedo heavy ions emitted off the lunar surface.

APPENDIX C

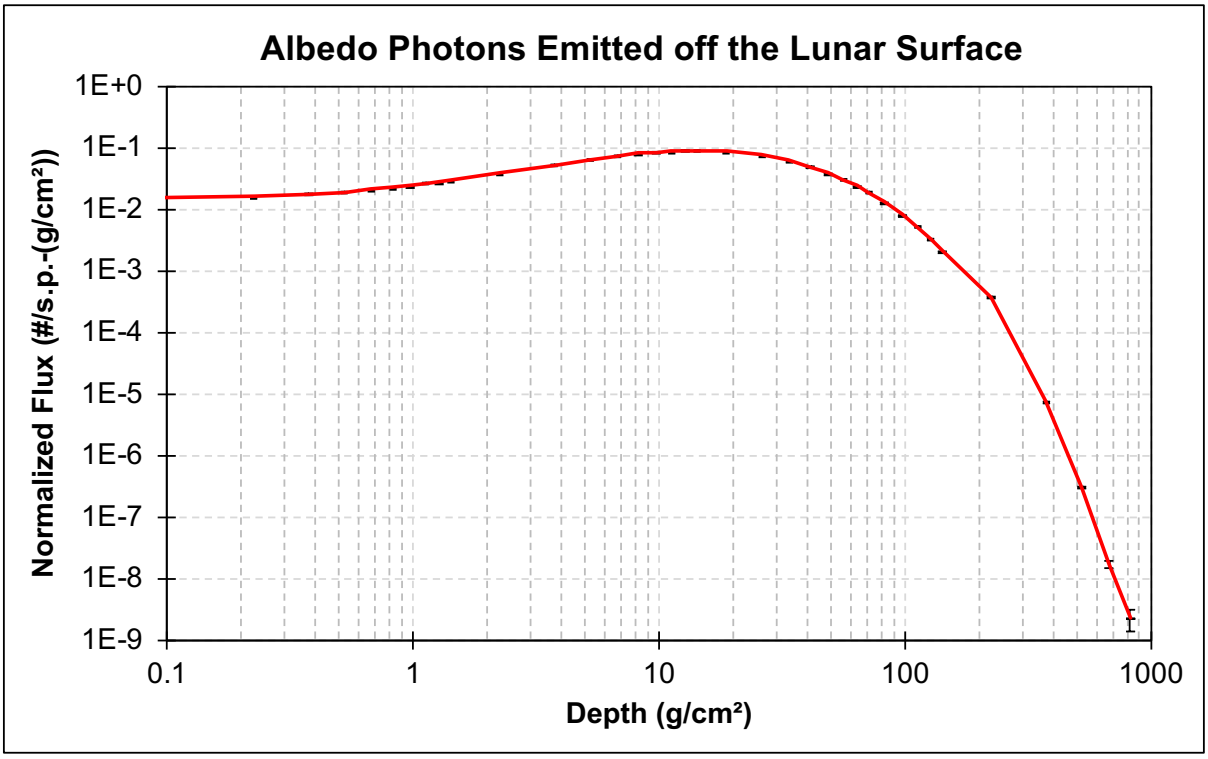

Figure C.1. The maximum production depth distribution of albedo photons.

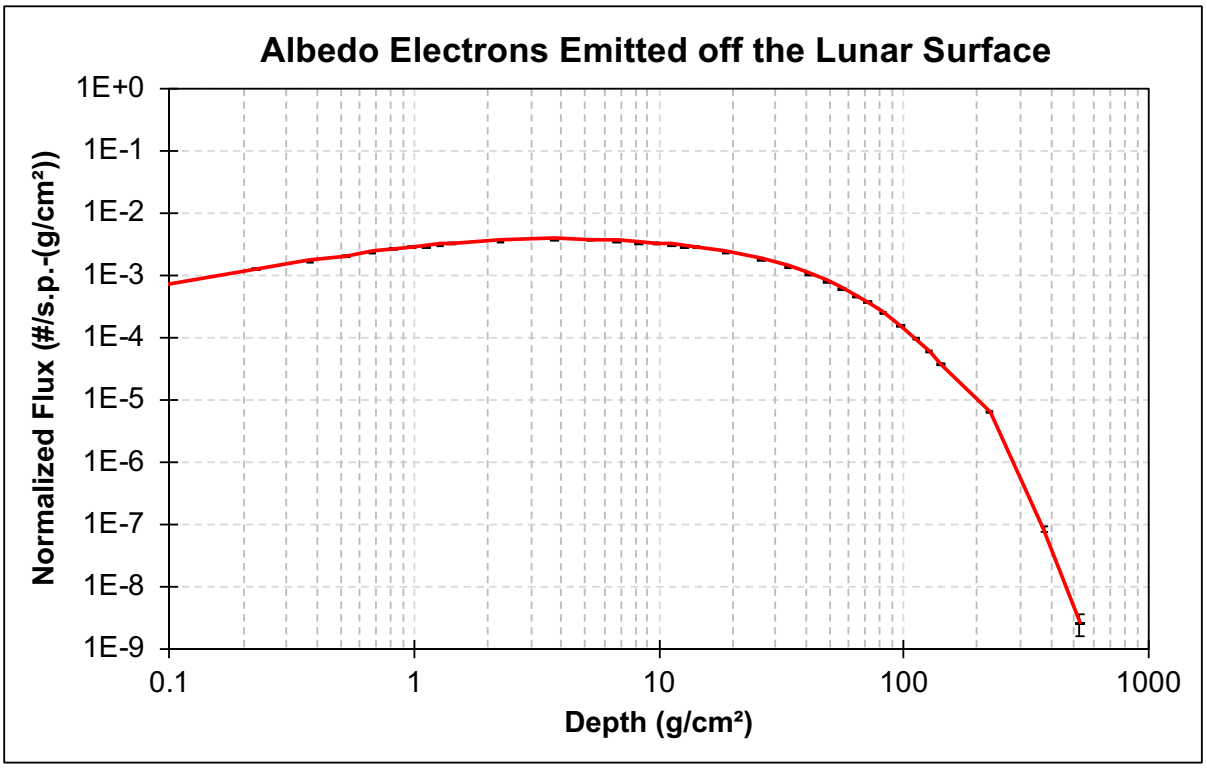

Figure C.2. The maximum production depth distribution of albedo electrons.

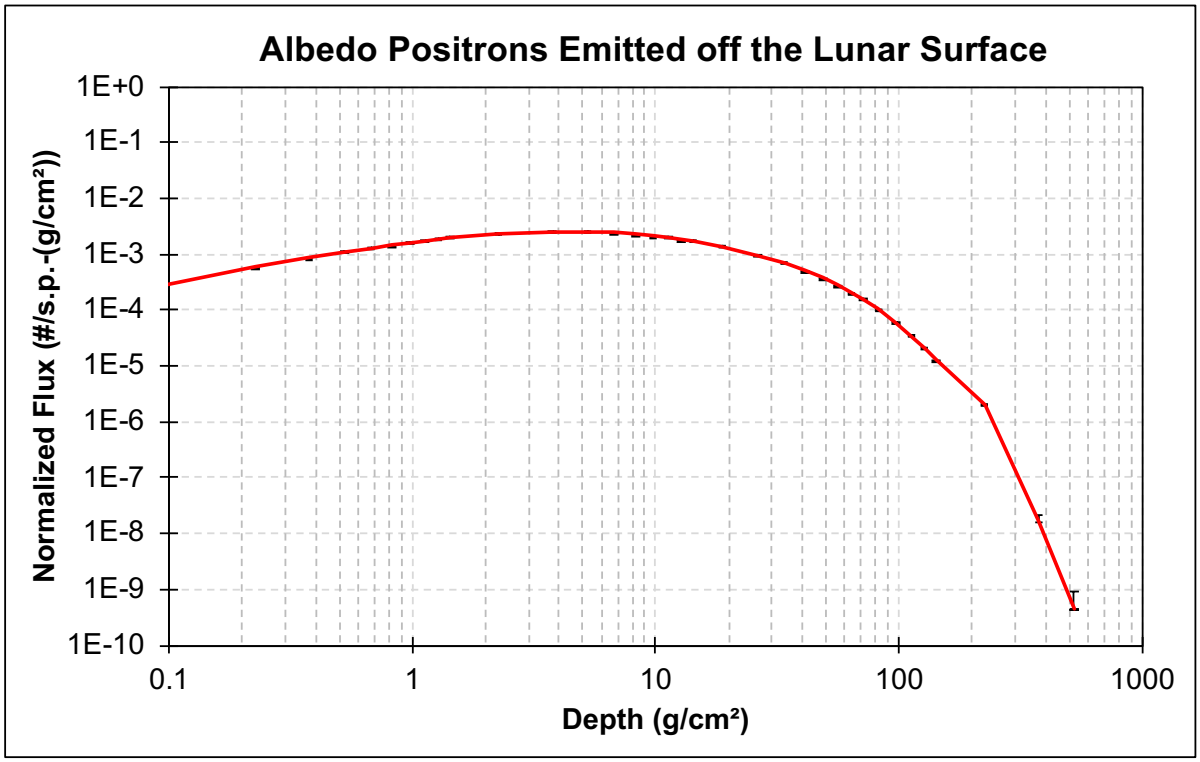

Figure C.3. The maximum production depth distribution of albedo positrons.

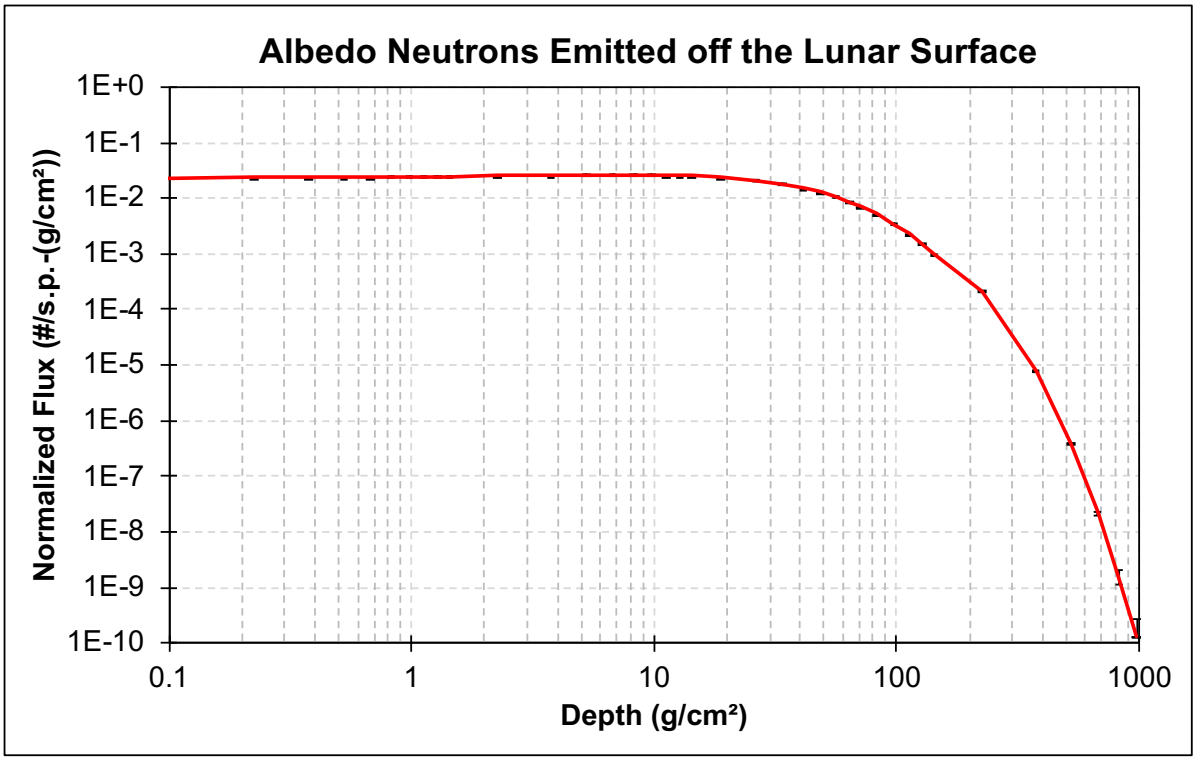

Figure C.4. The maximum production depth distribution of albedo neutrons.

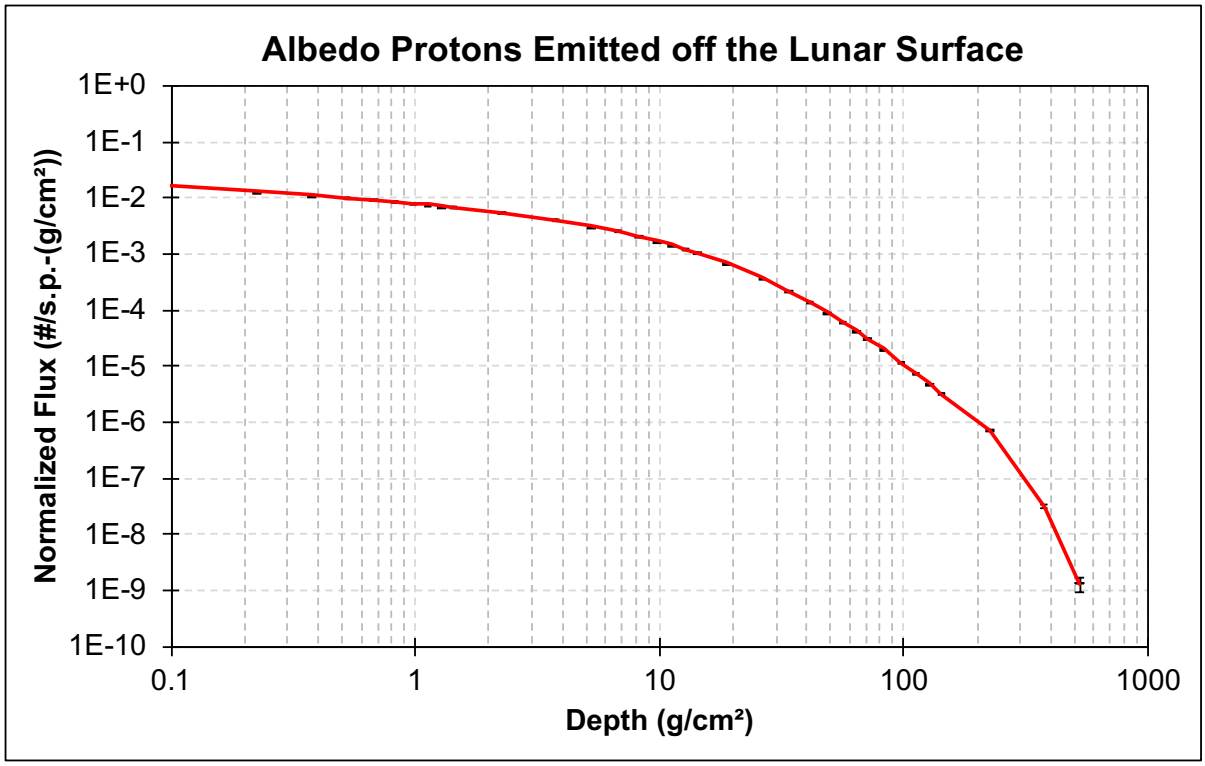

Figure C.5. The maximum production depth distribution of albedo protons.

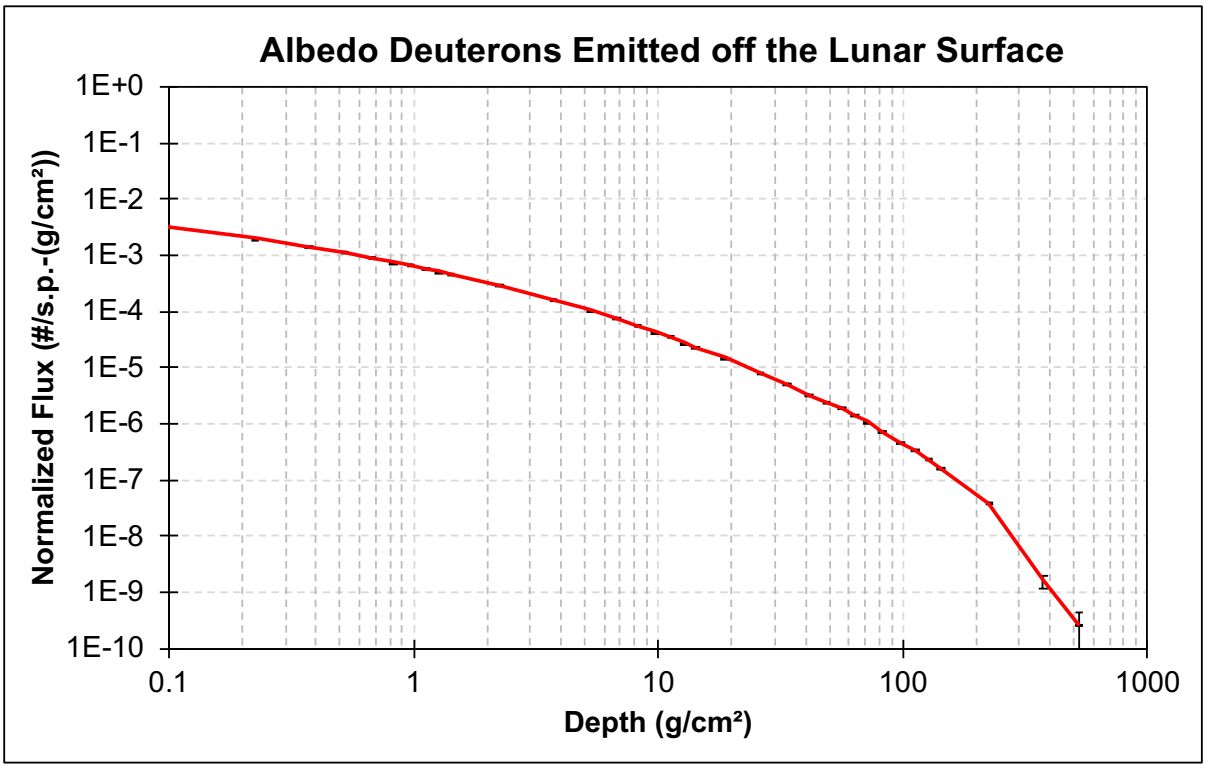

Figure C.6. The maximum production depth distribution of albedo deuterons.

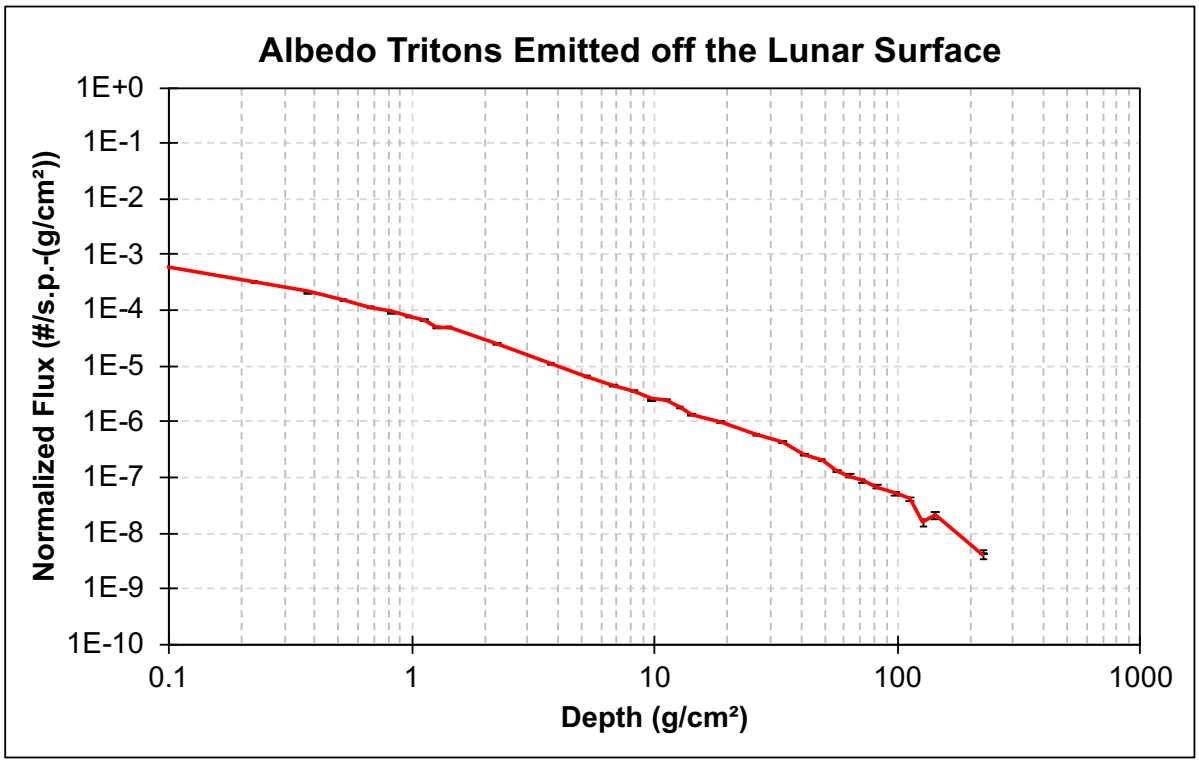

Figure C.7. The maximum production depth distribution of albedo tritium ions.

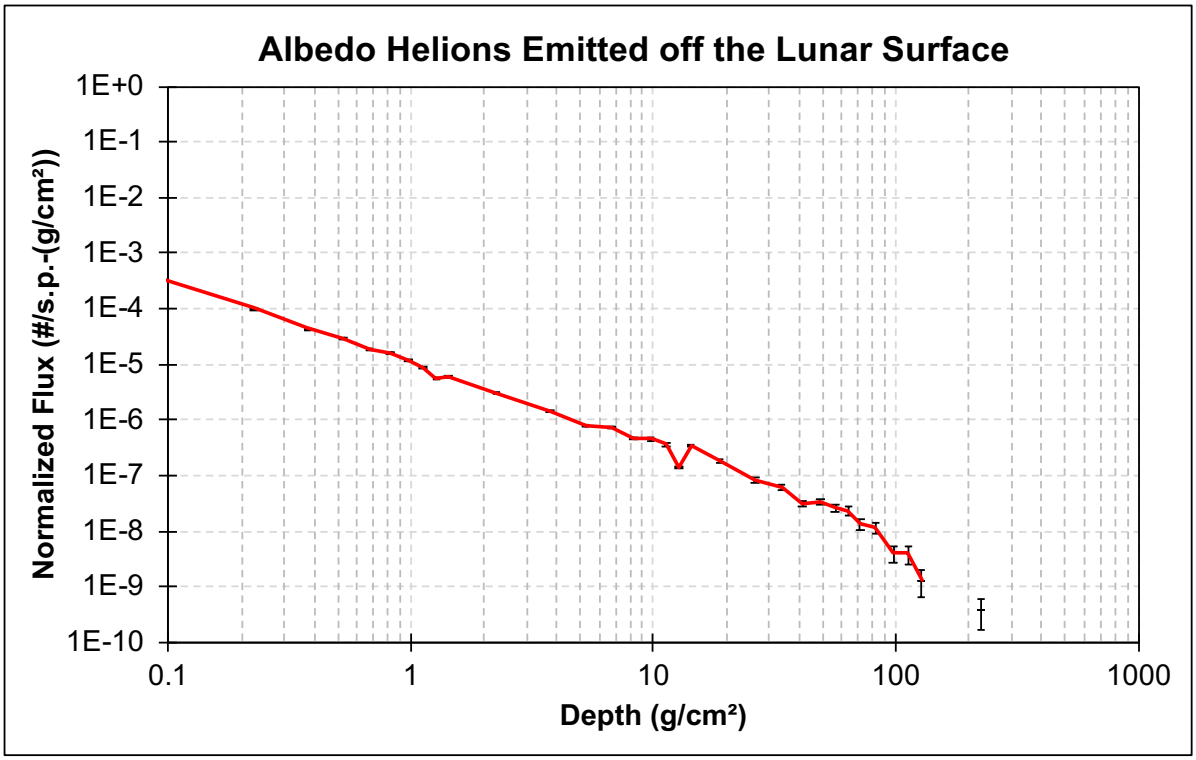

Figure C.8. The maximum production depth distribution of albedo helium-3 ions.

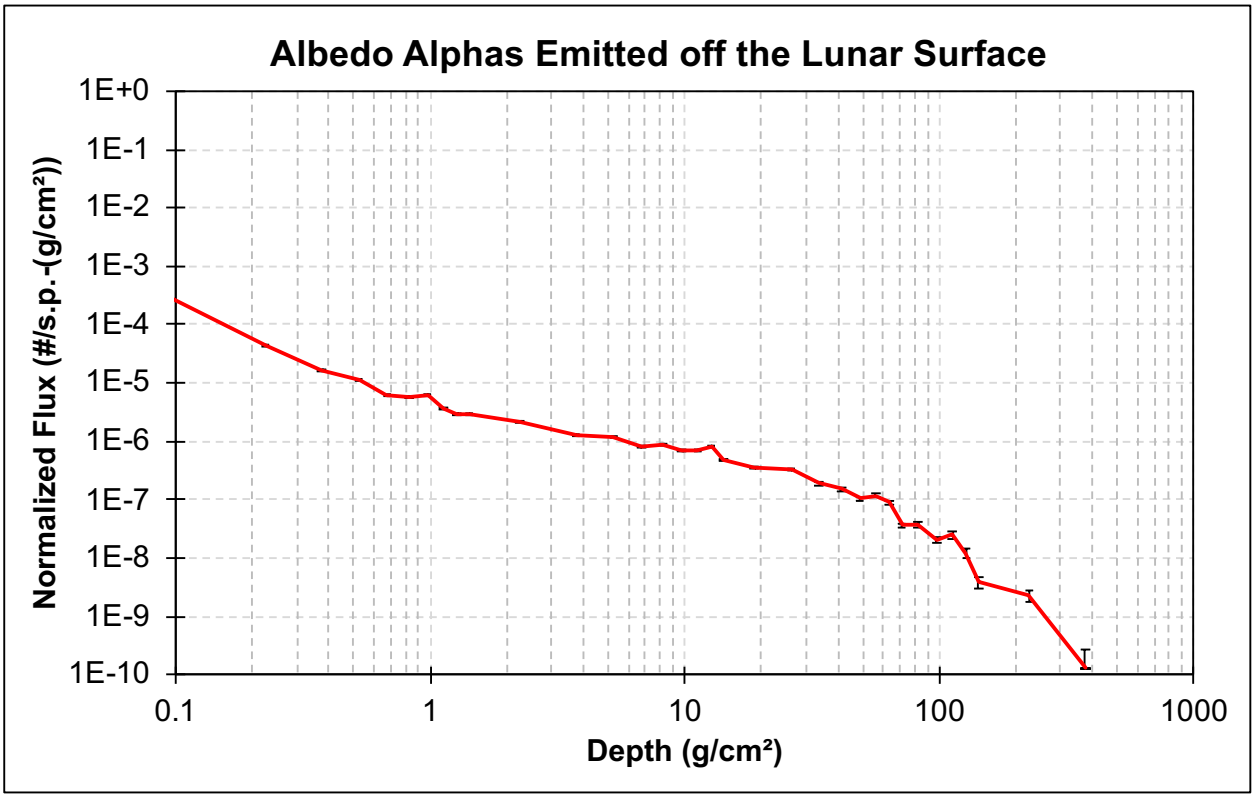

Figure C.9. The maximum production depth distribution of albedo alphas.

APPENDIX D

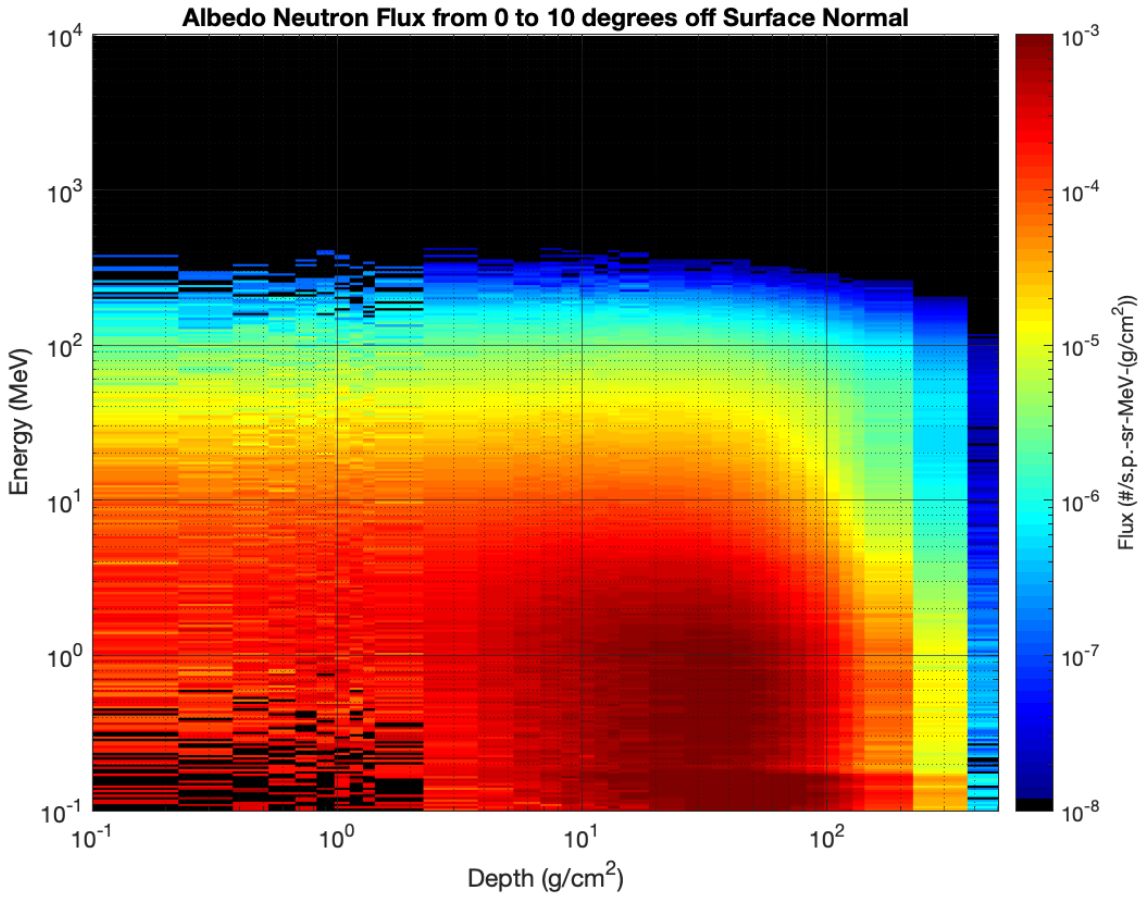

Figure D.1. Albedo neutron flux as a function of energy and maximum production depth for angles between 0 and 10 degrees off surface normal.

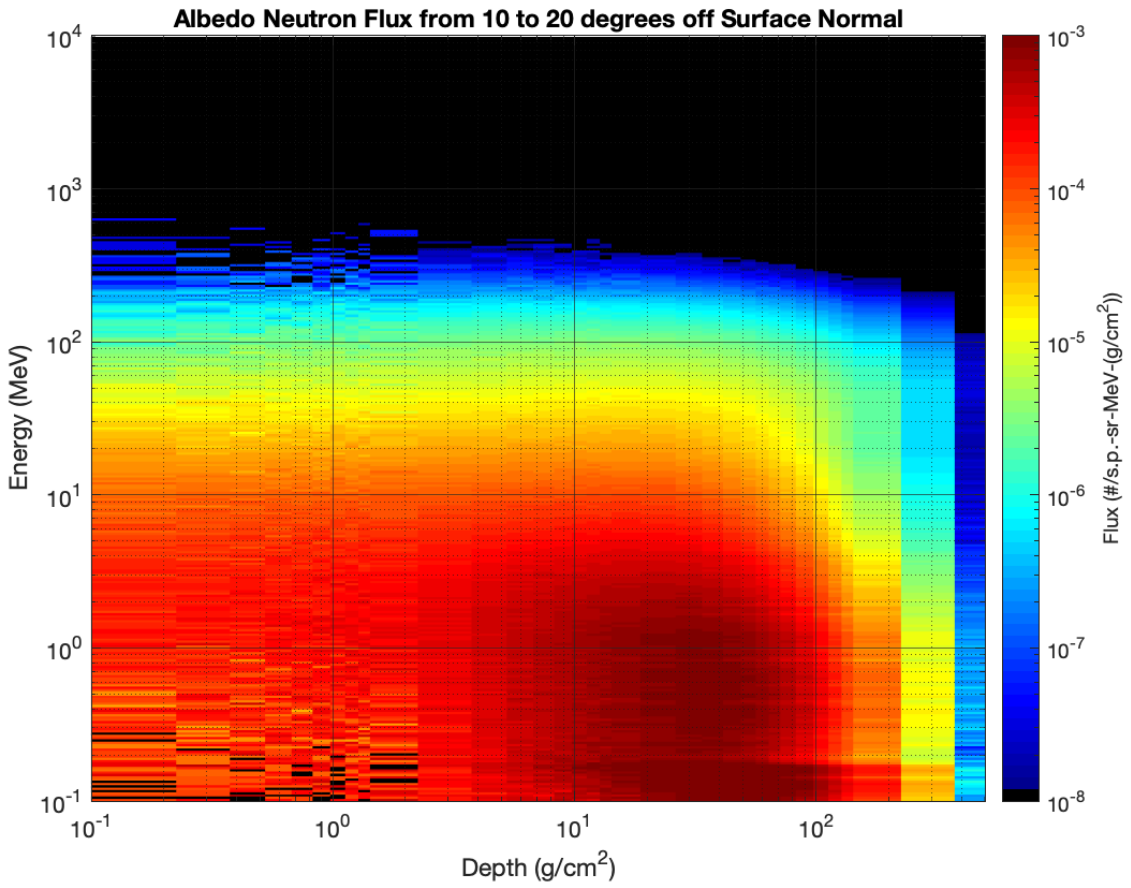

Figure D.2. Albedo neutron flux as a function of energy and maximum production depth for angles between 10 and 20 degrees off surface normal.

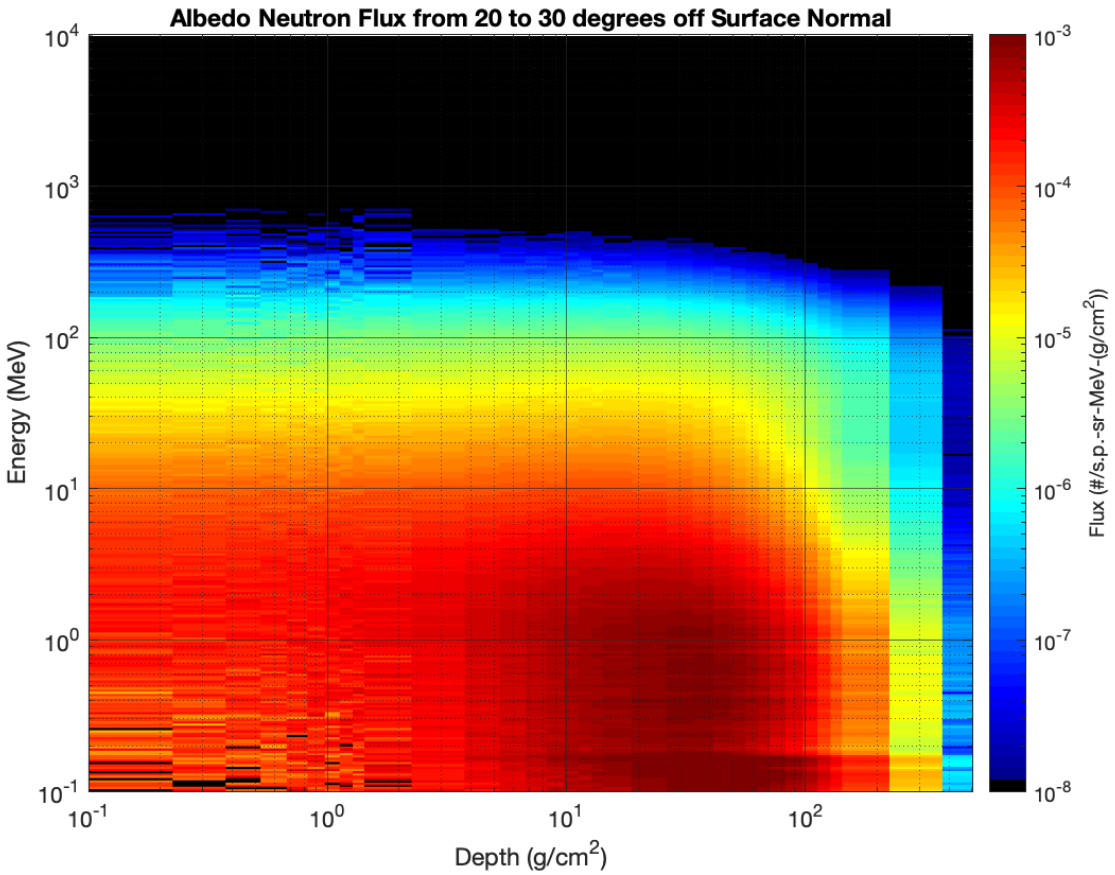

Figure D.3. Albedo neutron flux as a function of energy and maximum production depth for angles between 20 and 30 degrees off surface normal.

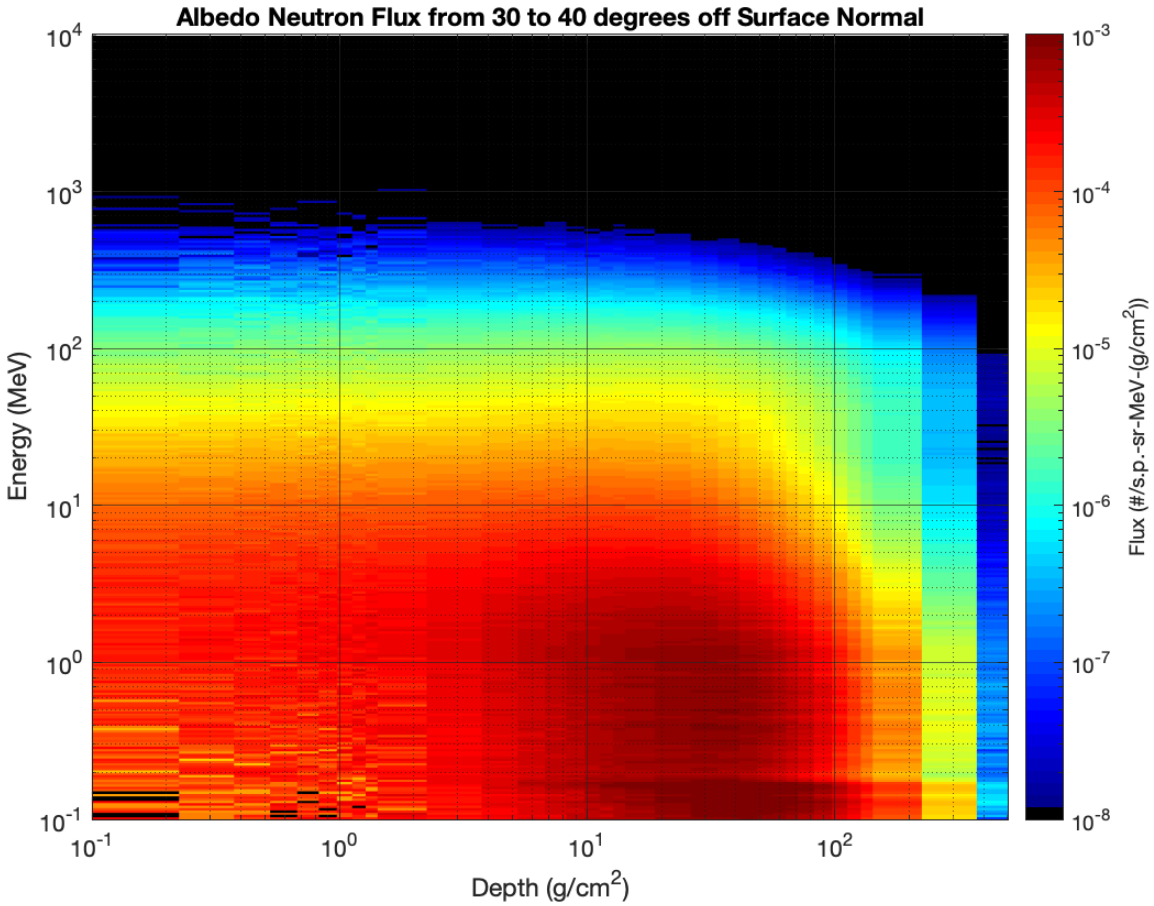

Figure D.4. Albedo neutron flux as a function of energy and maximum production depth for angles between 30 and 40 degrees off surface normal.

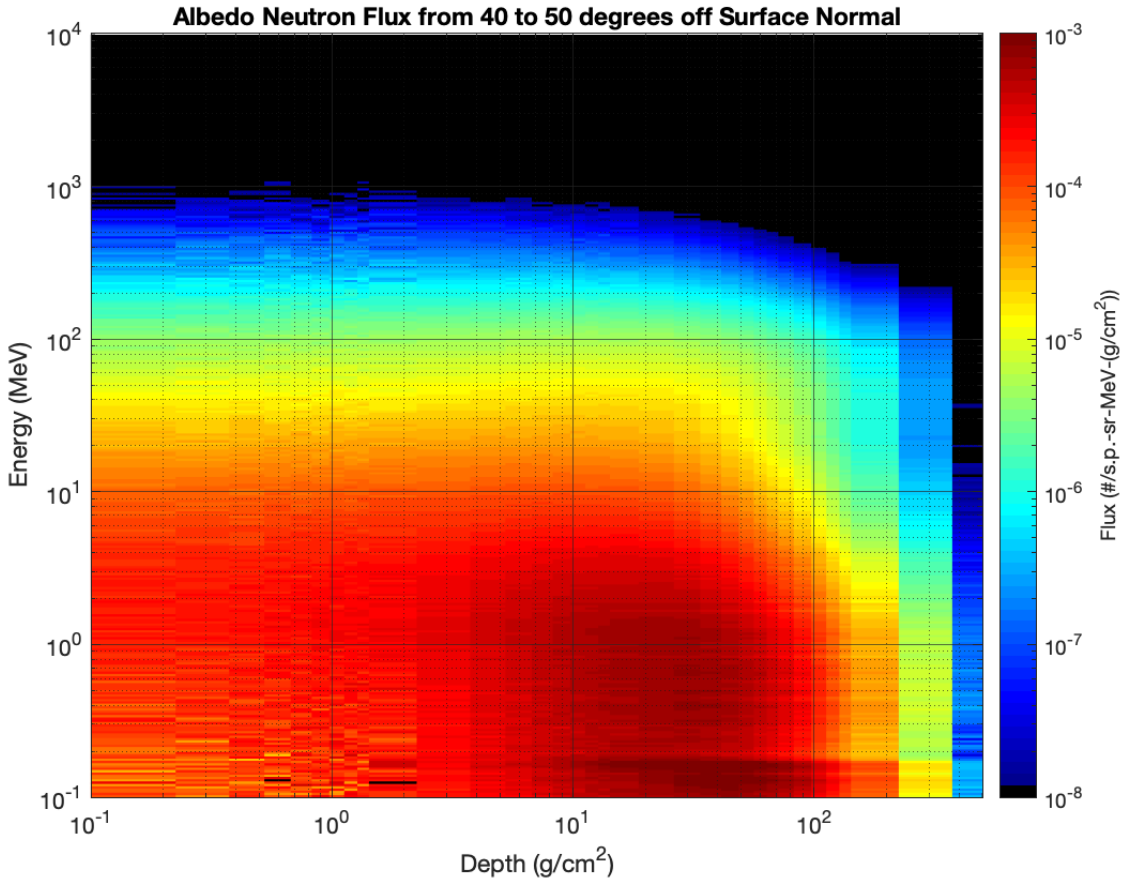

Figure D.5. Albedo neutron flux as a function of energy and maximum production depth for angles between 40 and 50 degrees off surface normal.

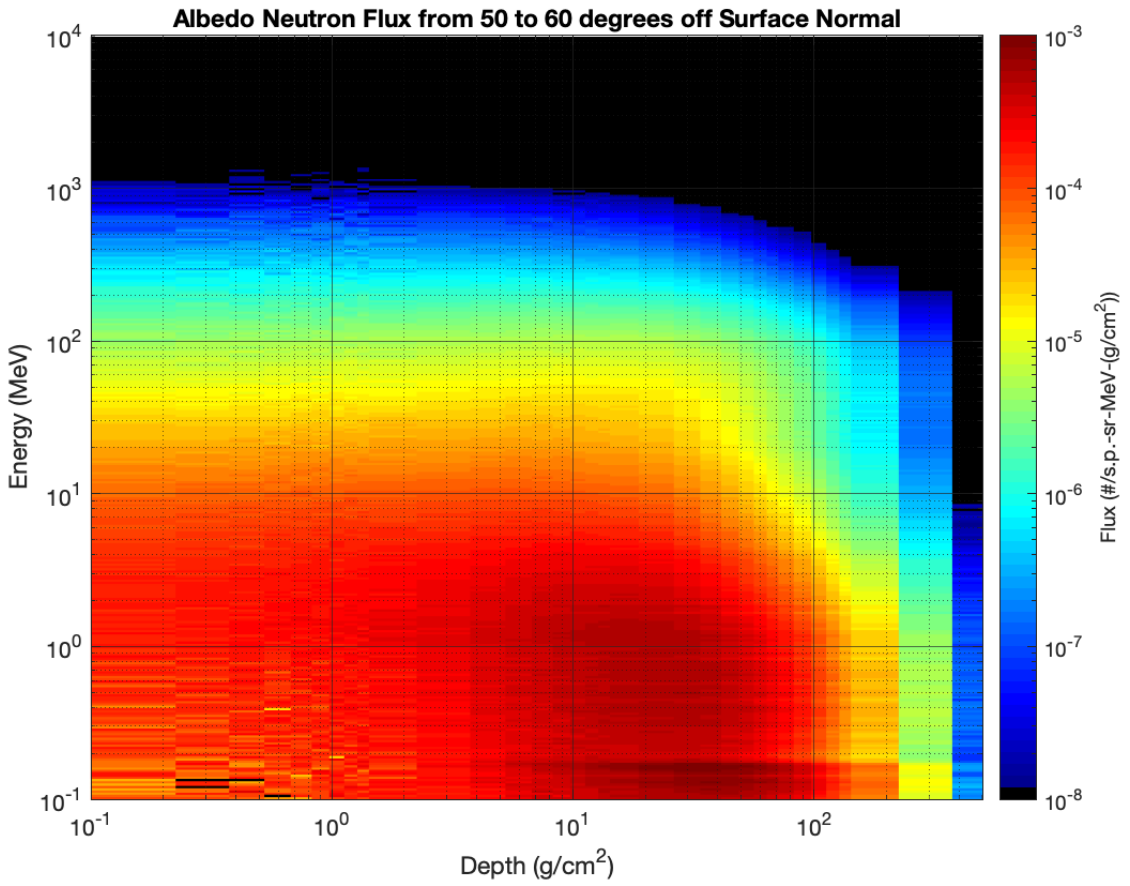

Figure D.6. Albedo neutron flux as a function of energy and maximum production depth for angles between 50 and 60 degrees off surface normal.

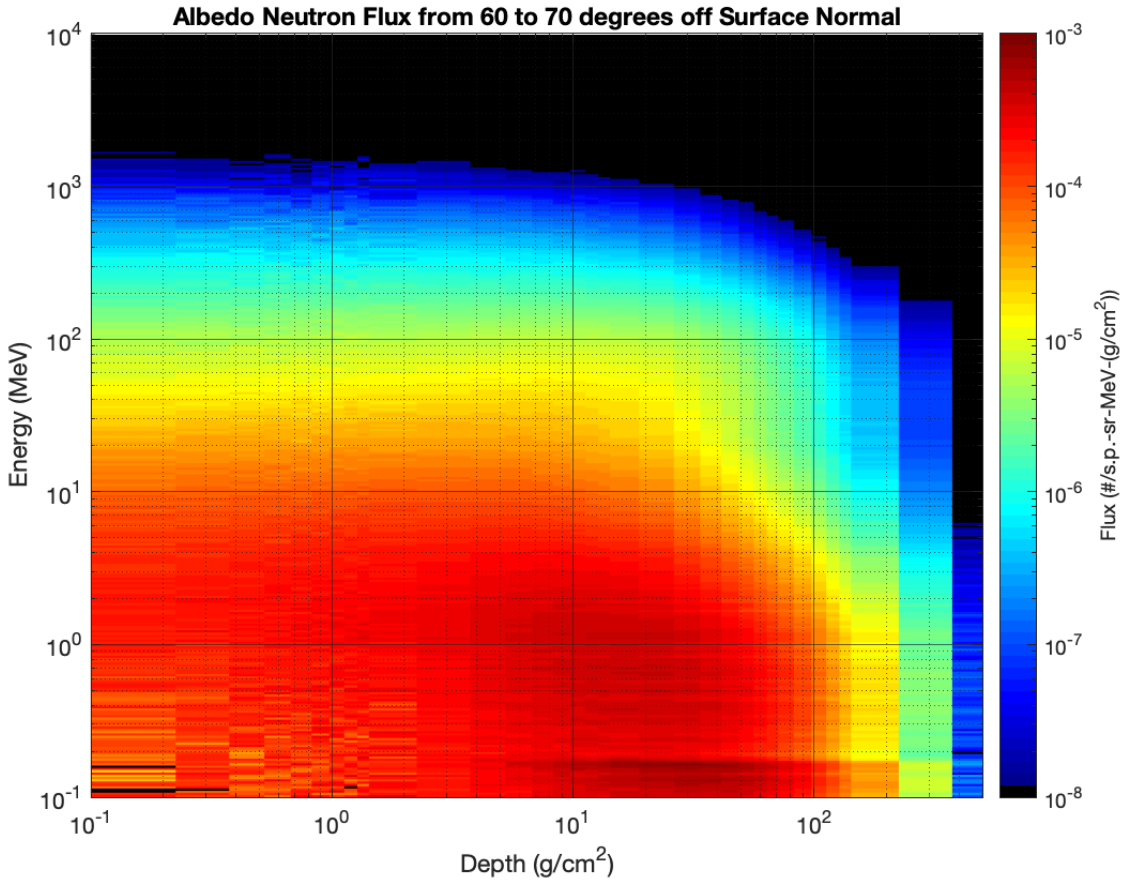

Figure D.7. Albedo neutron flux as a function of energy and maximum production depth for angles between 60 and 70 degrees off surface normal.

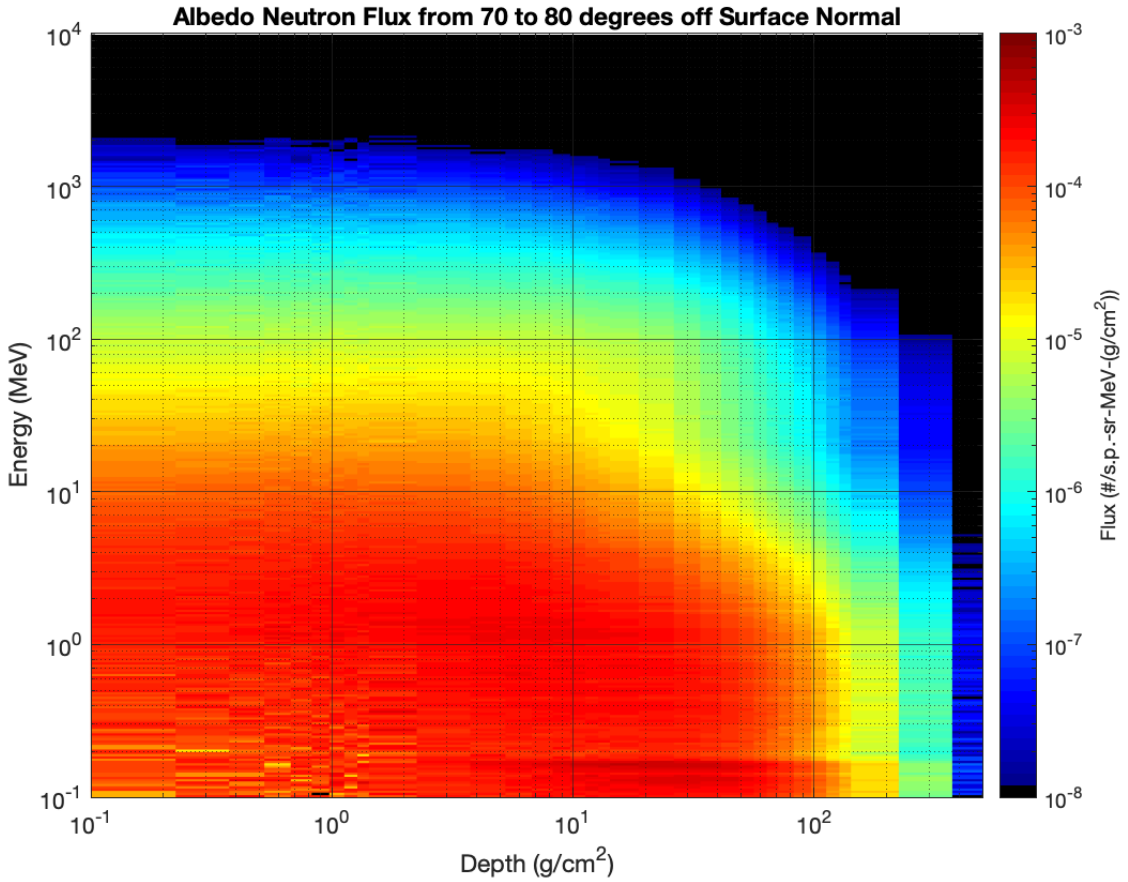

Figure D.8. Albedo neutron flux as a function of energy and maximum production depth for angles between 70 and 80 degrees off surface normal.

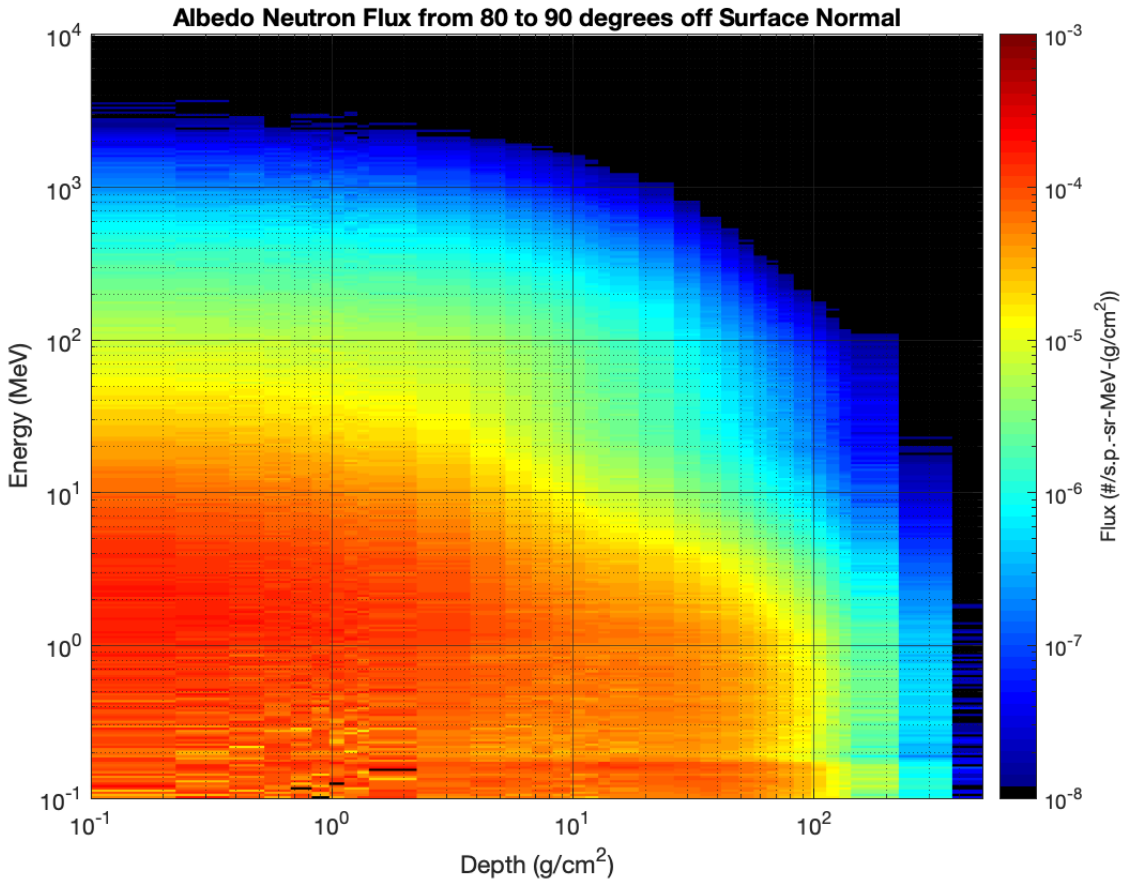

Figure D.9. Albedo neutron flux as a function of energy and maximum production depth for angles between 80 and 90 degrees off surface normal.

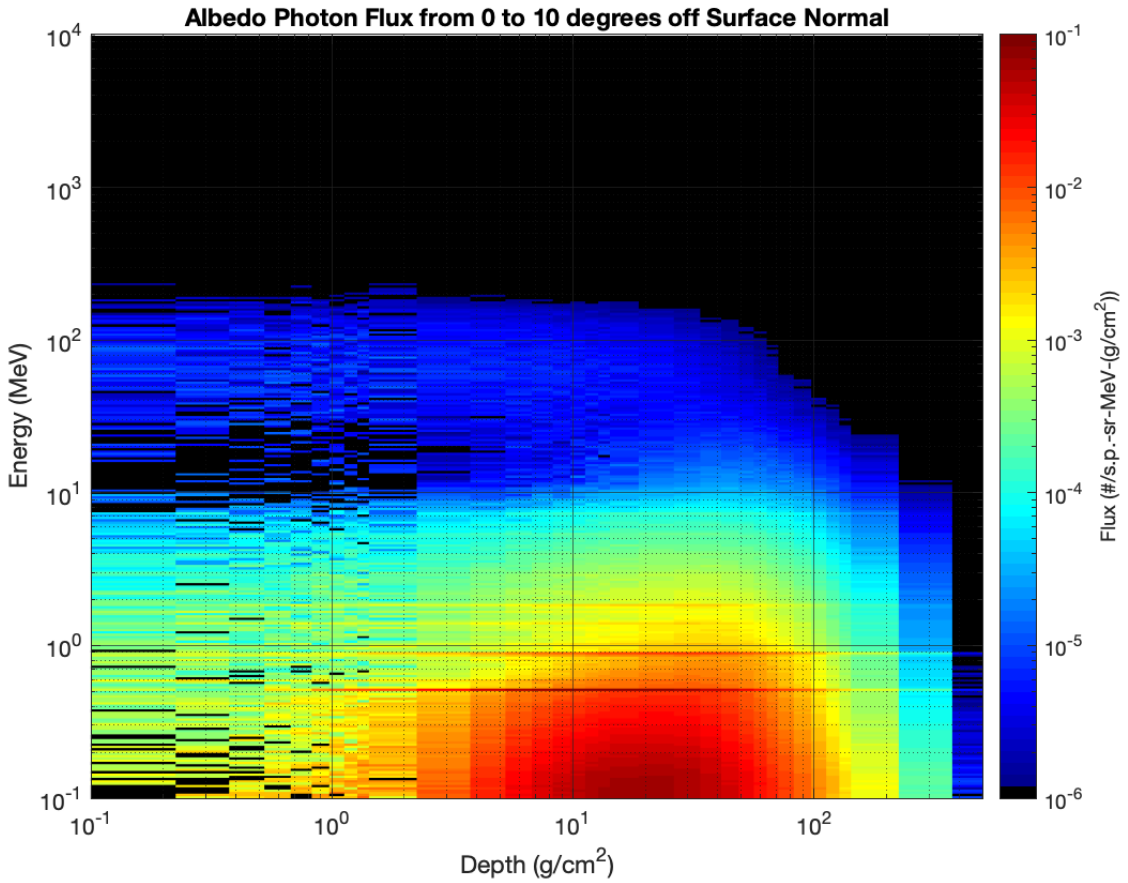

Figure D.10. Albedo photon flux as a function of energy and maximum production depth for angles between 0 and 10 degrees off surface normal.

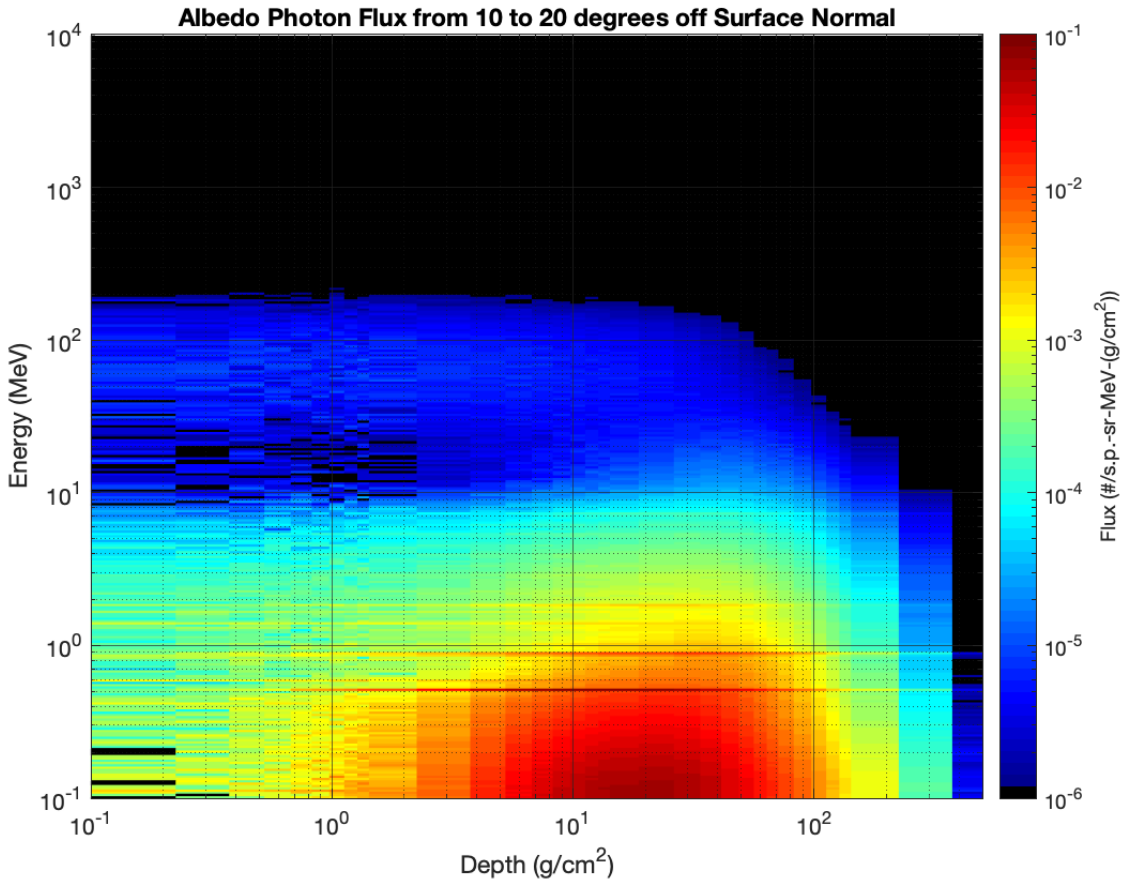

Figure D.11. Albedo photon flux as a function of energy and maximum production depth for angles between 10 and 20 degrees off surface normal.

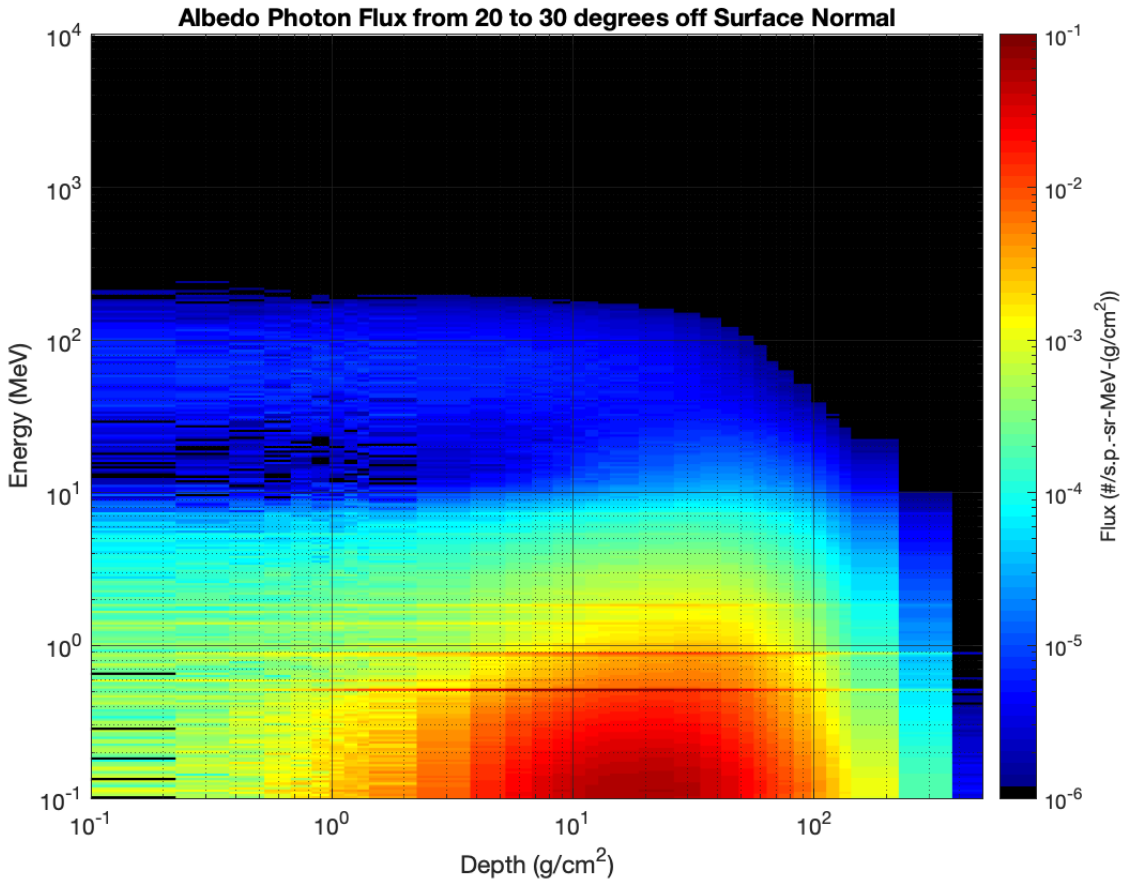

Figure D.12. Albedo photon flux as a function of energy and maximum production depth for angles between 20 and 30 degrees off surface normal.

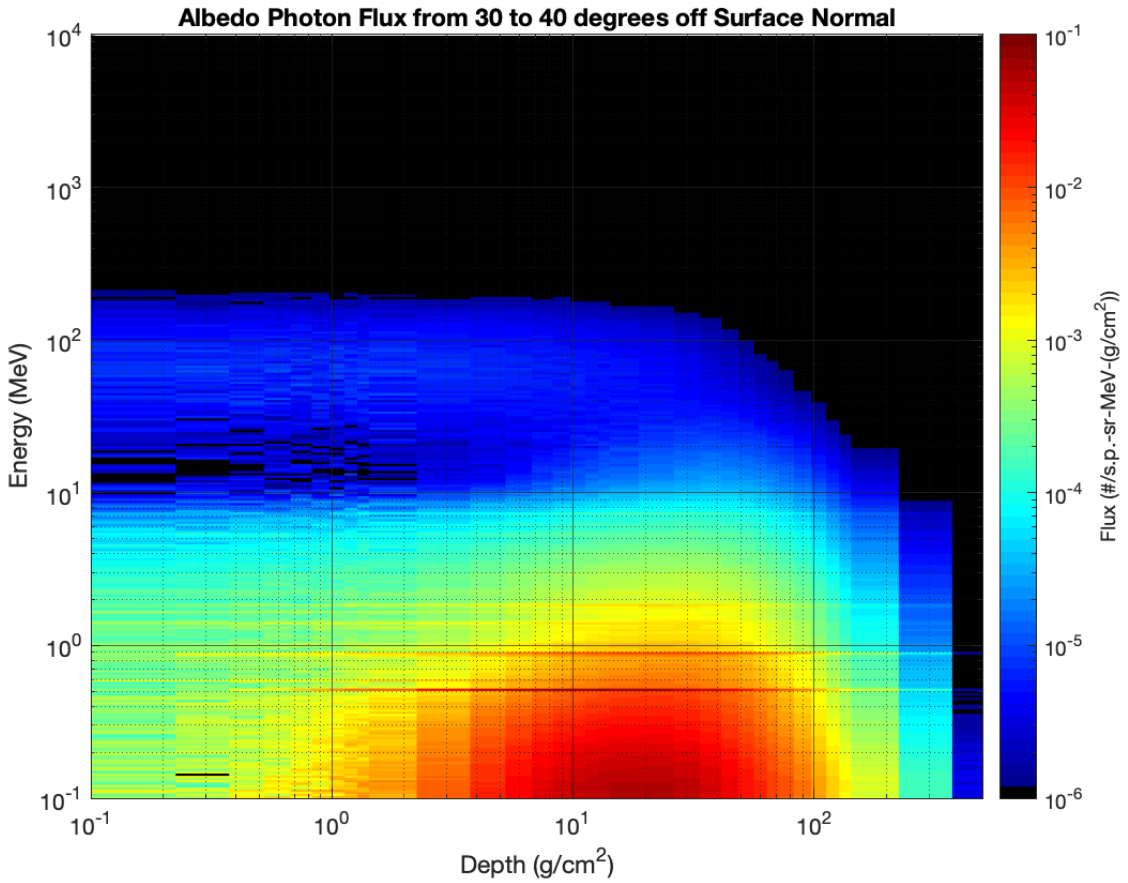

Figure D.13. Albedo photon flux as a function of energy and maximum production depth for angles between 30 and 40 degrees off surface normal.

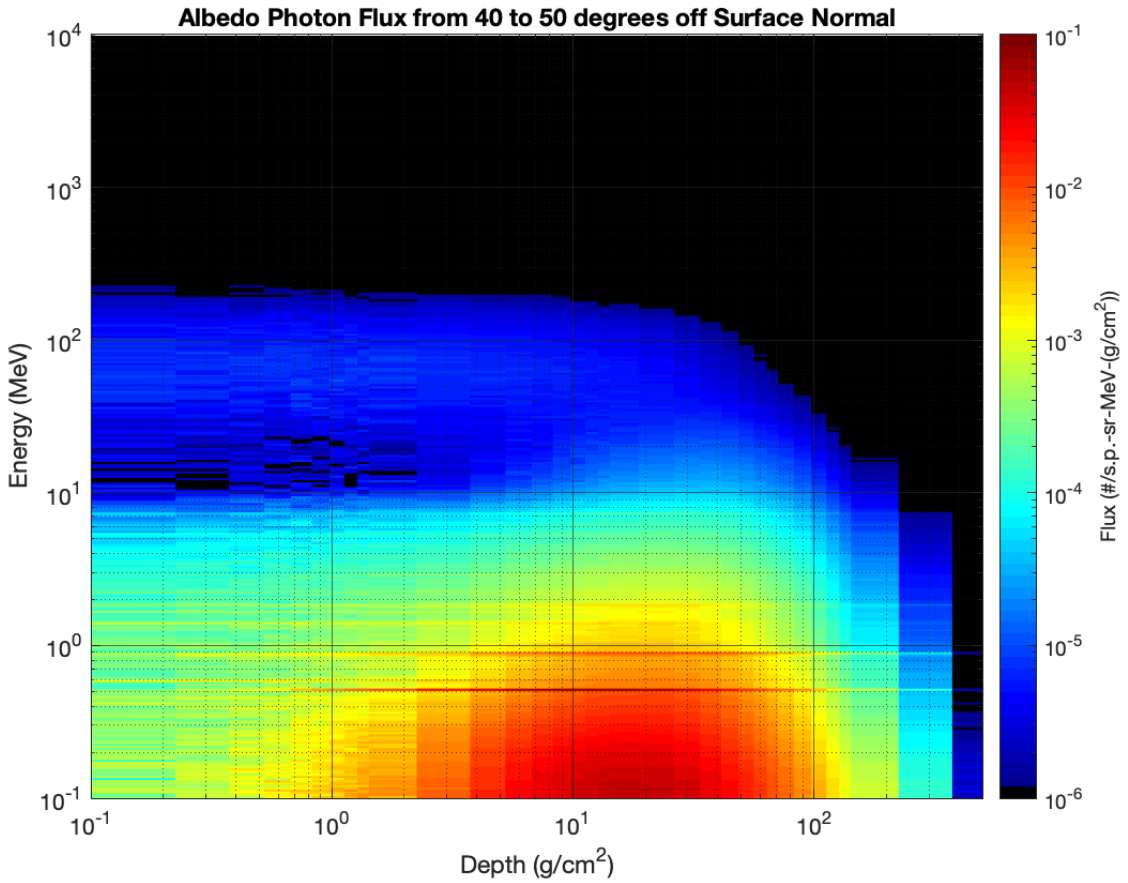

Figure D.14. Albedo photon flux as a function of energy and maximum production depth for angles between 40 and 50 degrees off surface normal.

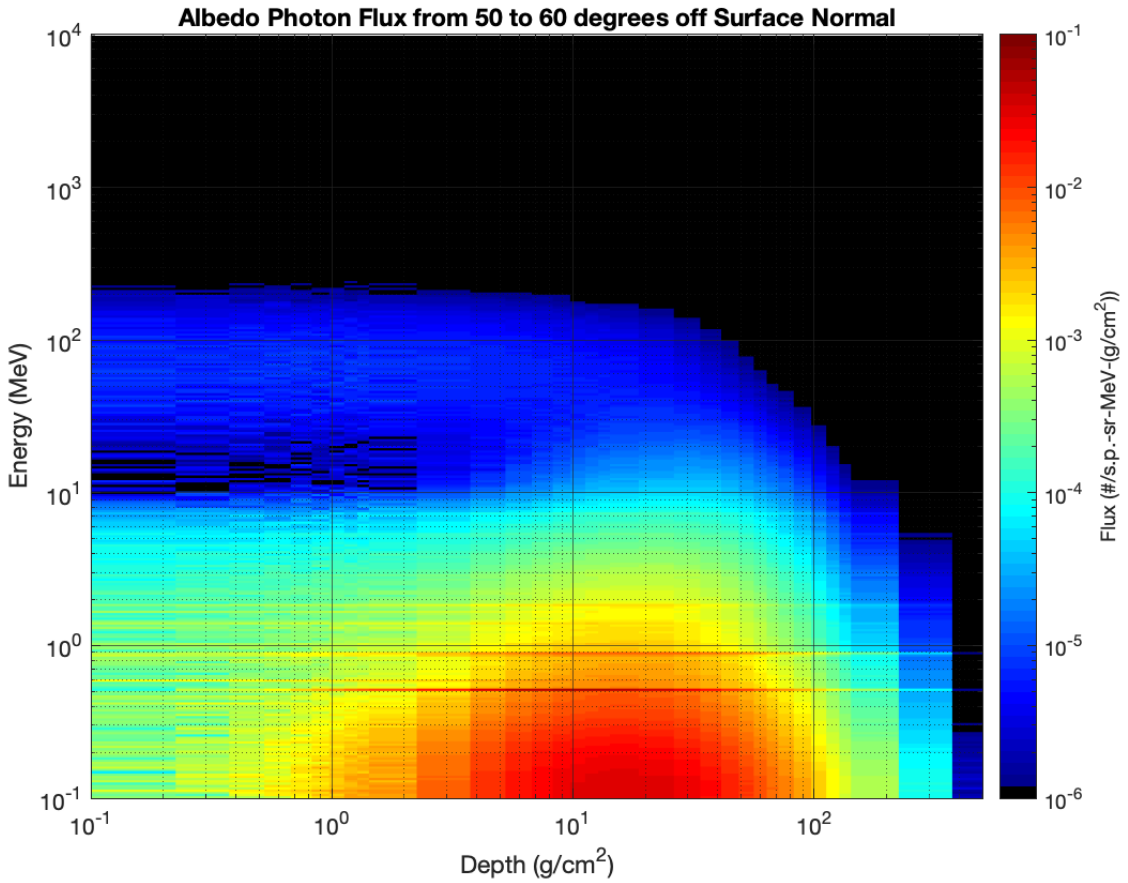

Figure D.15. Albedo photon flux as a function of energy and maximum production depth for angles between 50 and 60 degrees off surface normal.

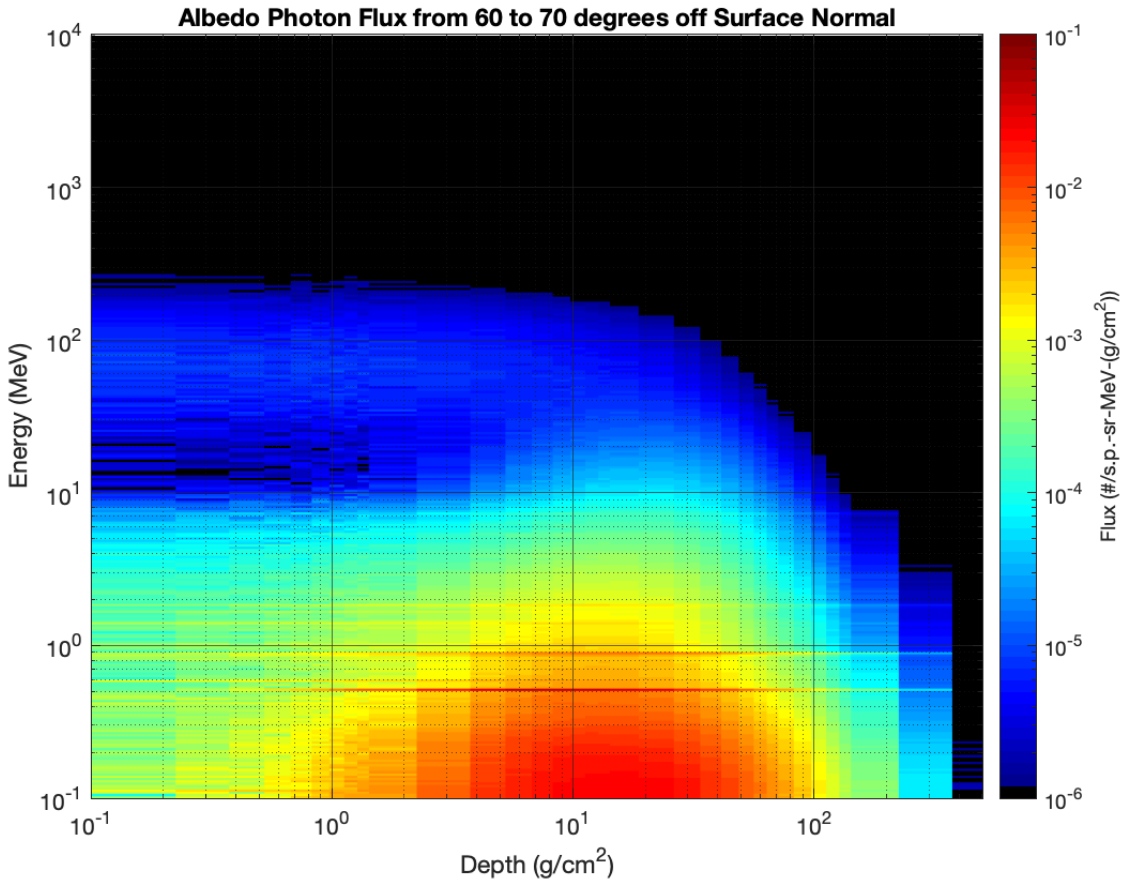

Figure D.16. Albedo photon flux as a function of energy and maximum production depth for angles between 60 and 70 degrees off surface normal.

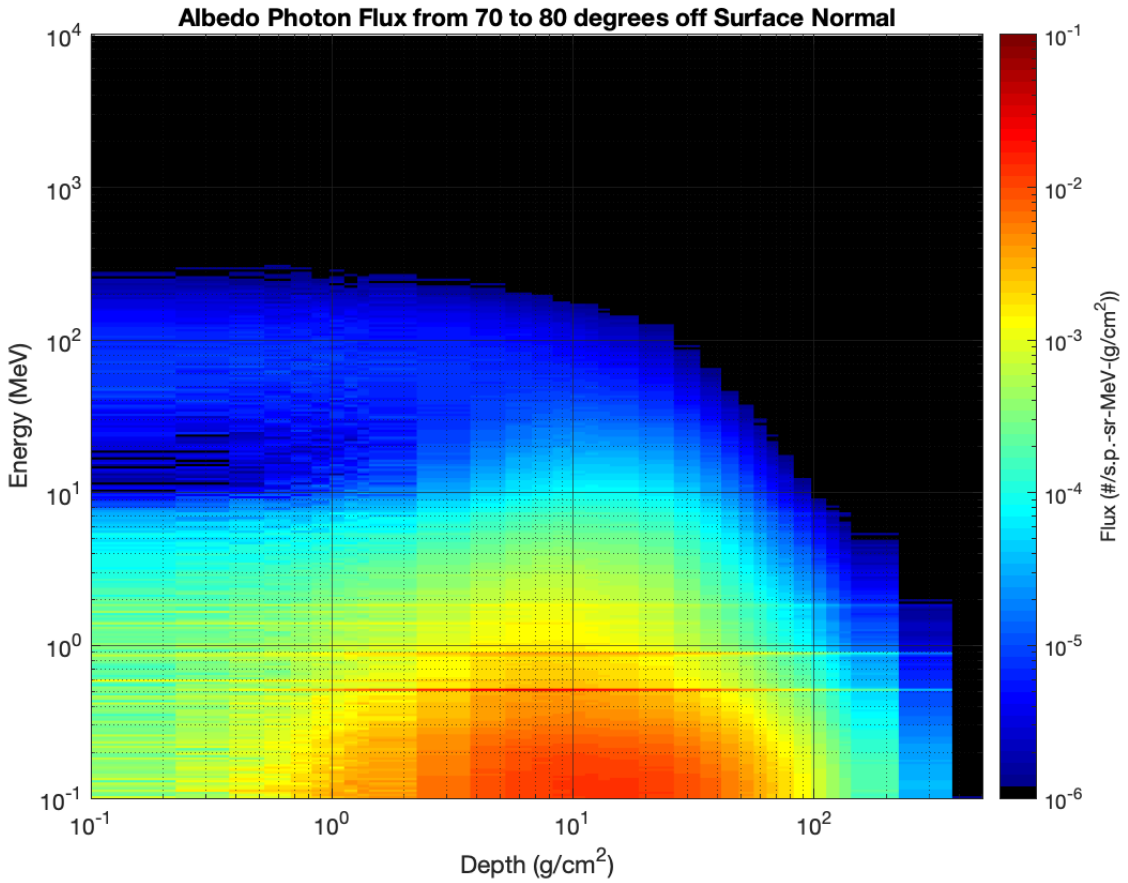

Figure D.17. Albedo photon flux as a function of energy and maximum production depth for angles between 70 and 80 degrees off surface normal.

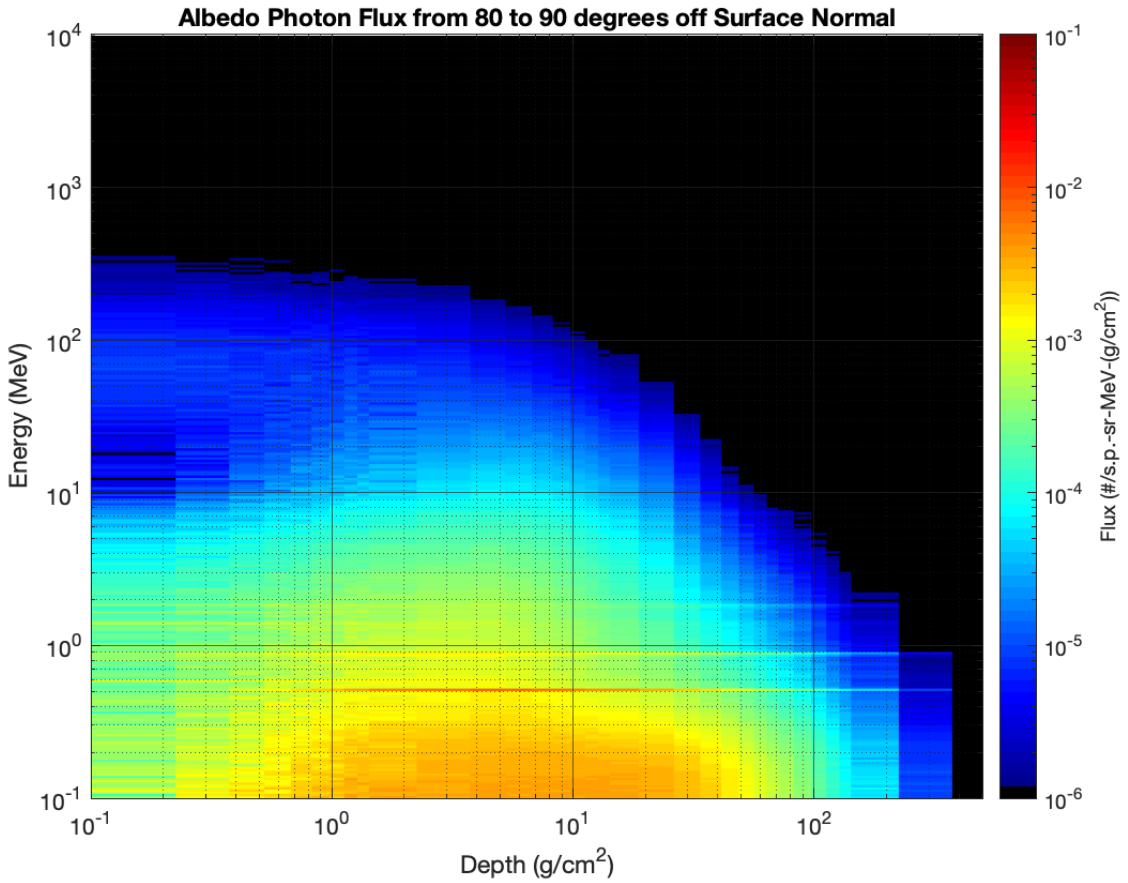

Figure D.18. Albedo photon flux as a function of energy and maximum production depth for angles between 80 and 90 degrees off surface normal.

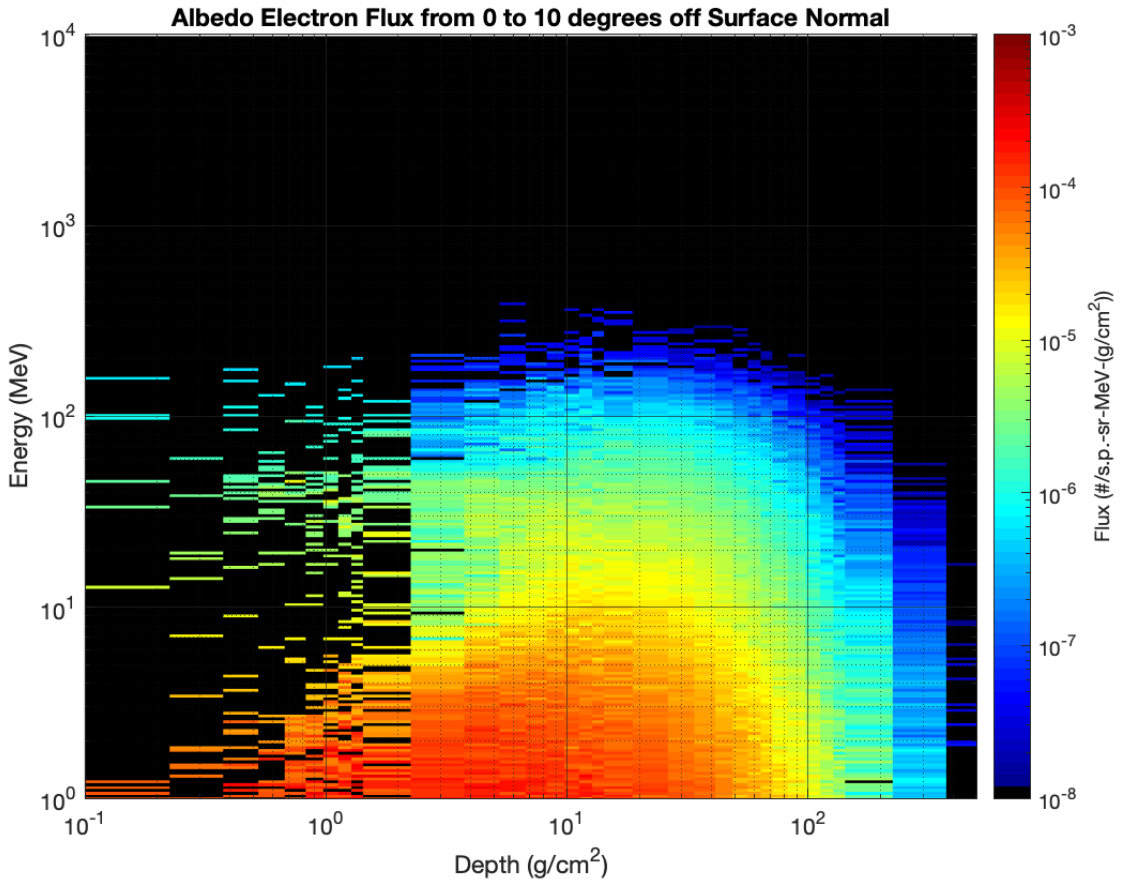

Figure D.19. Albedo electron flux as a function of energy and maximum production depth for angles between 0 and 10 degrees off surface normal.

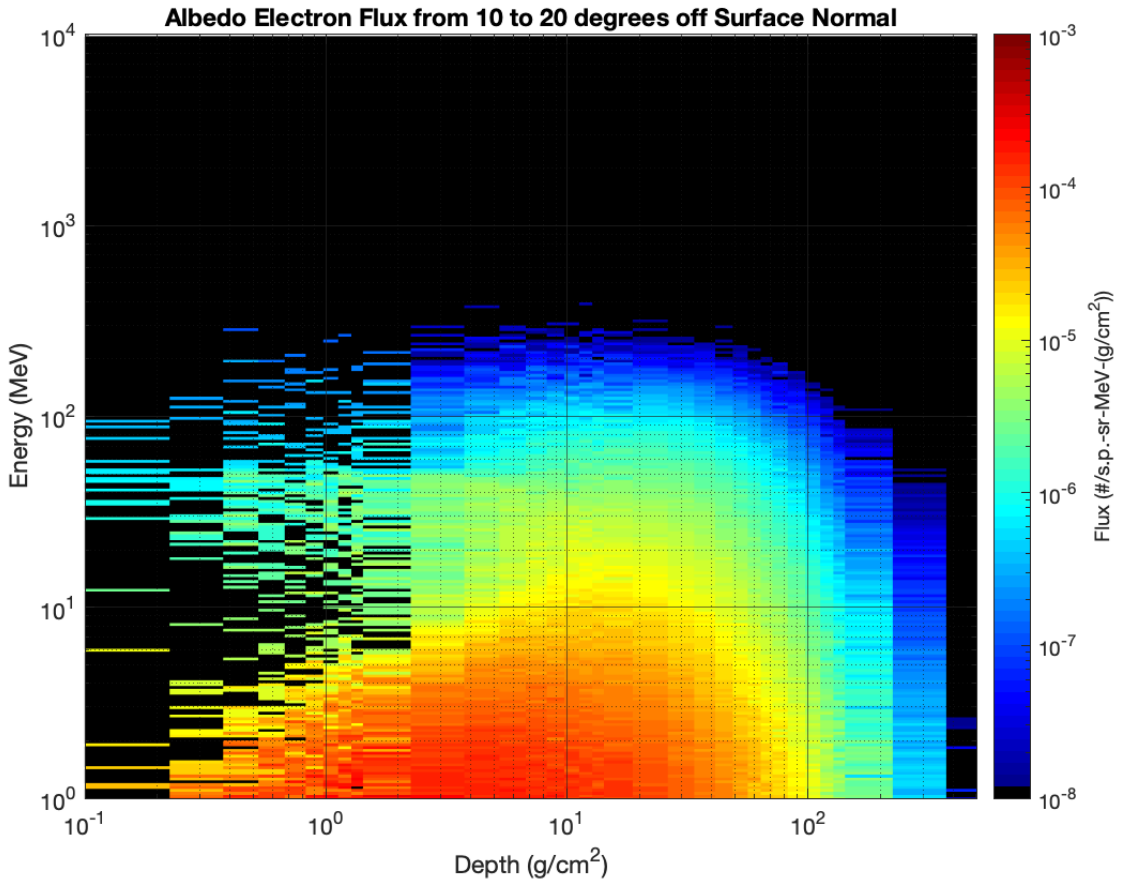

Figure D.20. Albedo electron flux as a function of energy and maximum production depth for angles between 10 and 20 degrees off surface normal.

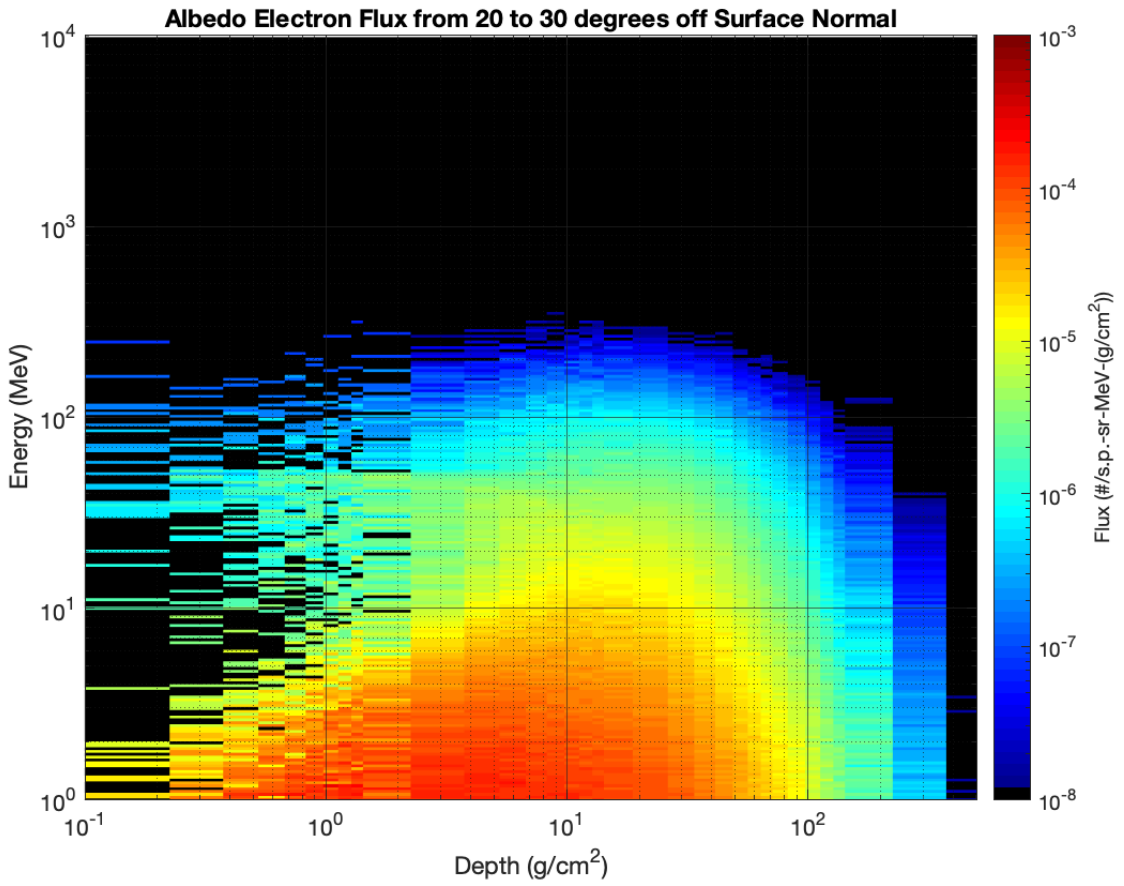

Figure D.21. Albedo electron flux as a function of energy and maximum production depth for angles between 20 and 30 degrees off surface normal.

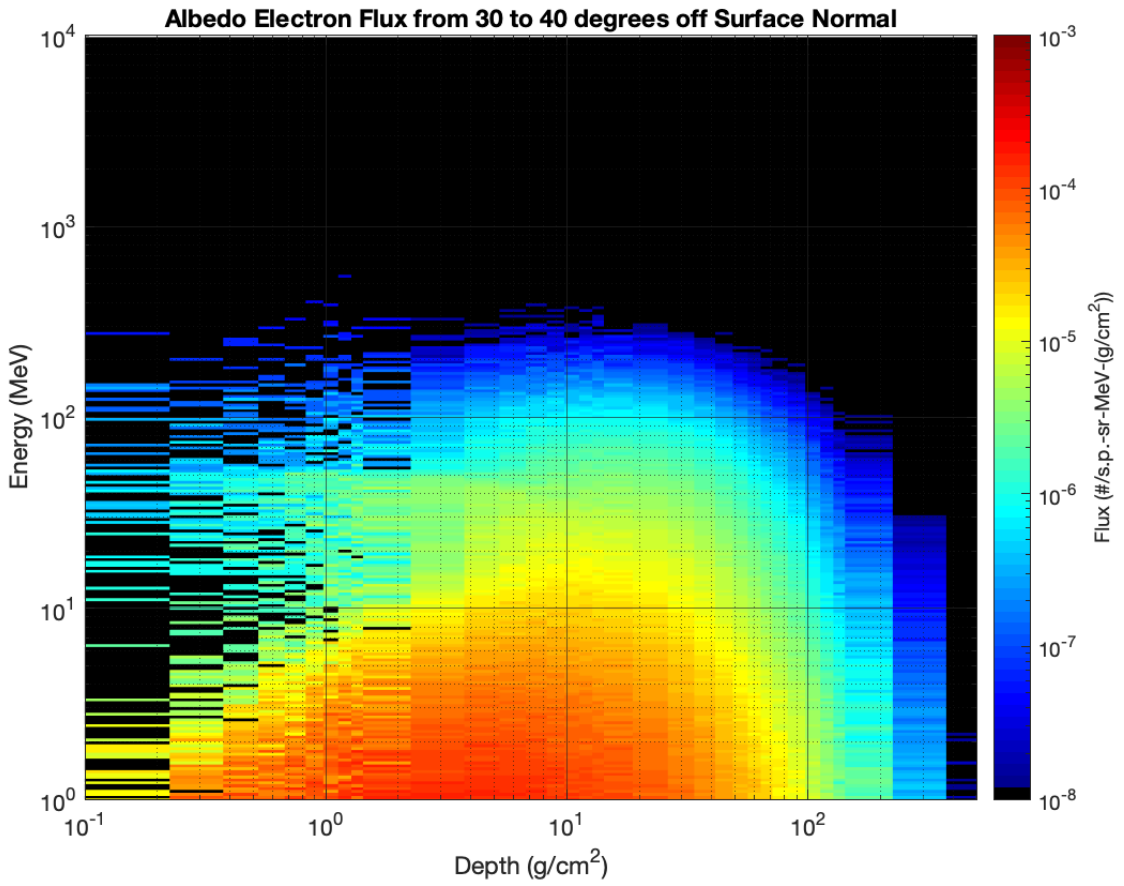

Figure D.22. Albedo electron flux as a function of energy and maximum production depth for angles between 30 and 40 degrees off surface normal.

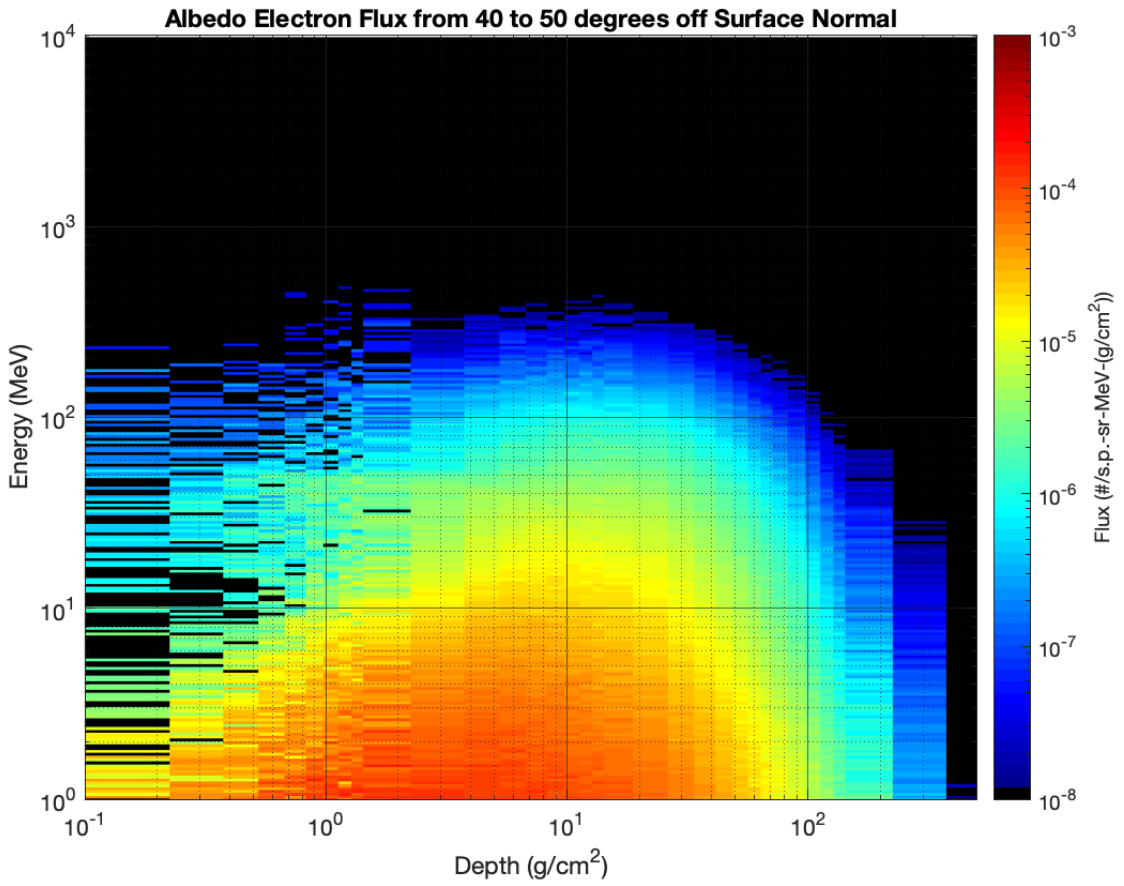

Figure D.23. Albedo electron flux as a function of energy and maximum production depth for angles between 40 and 50 degrees off surface normal.

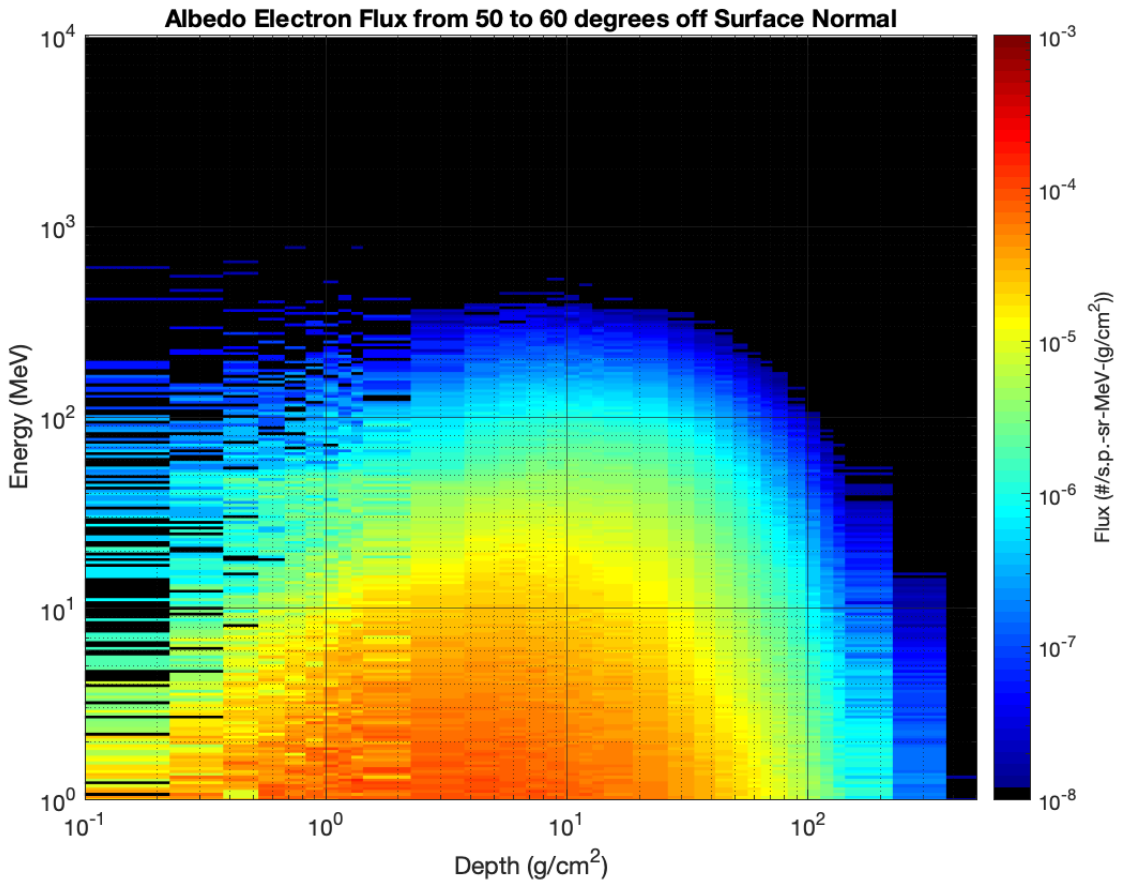

Figure D.24. Albedo electron flux as a function of energy and maximum production depth for angles between 50 and 60 degrees off surface normal.

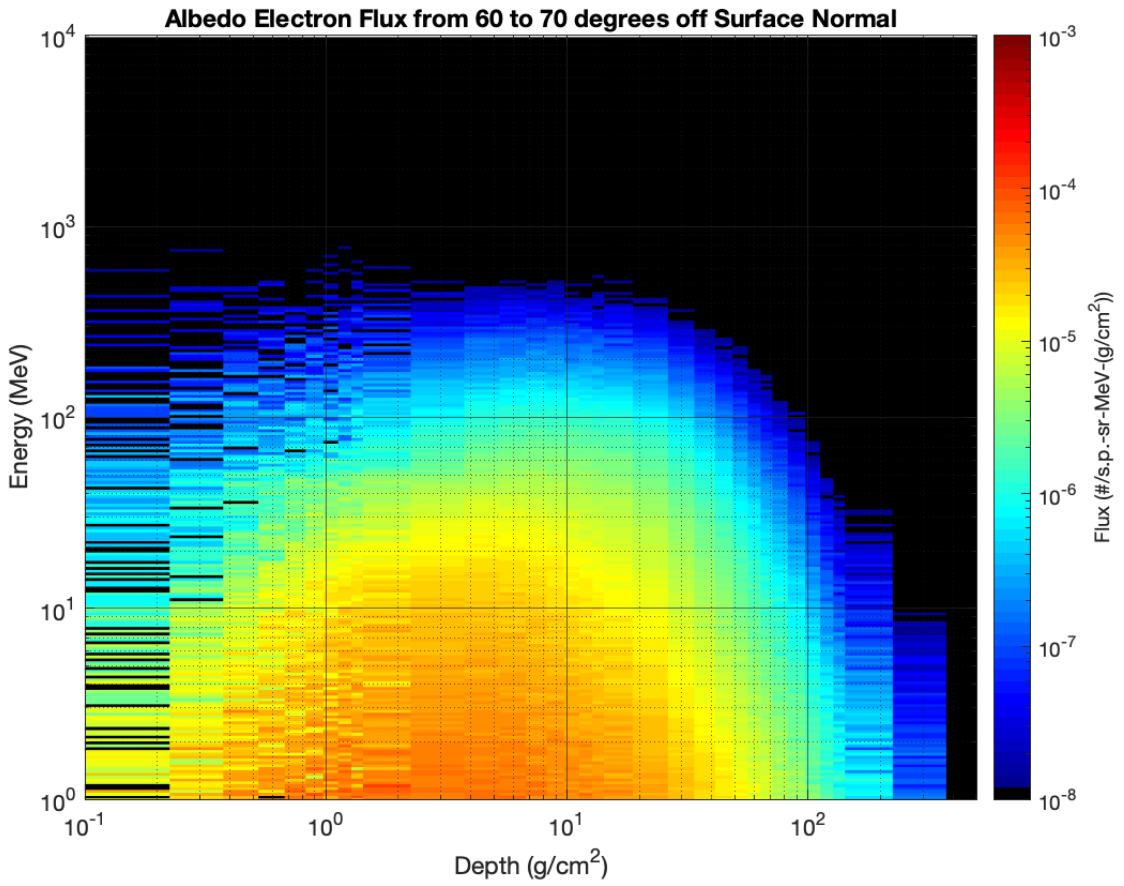

Figure D.25. Albedo electron flux as a function of energy and maximum production depth for angles between 60 and 70 degrees off surface normal.

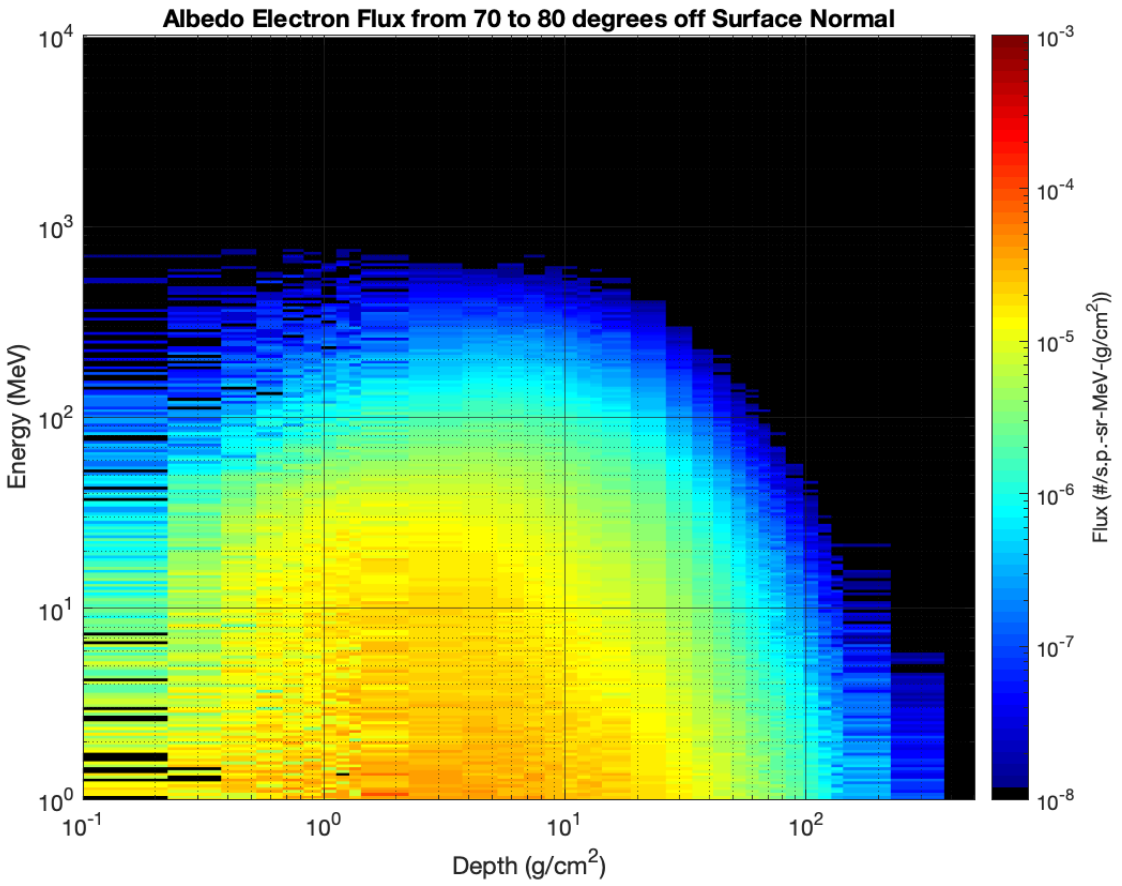

Figure D.26. Albedo electron flux as a function of energy and maximum production depth for angles between 70 and 80 degrees off surface normal.

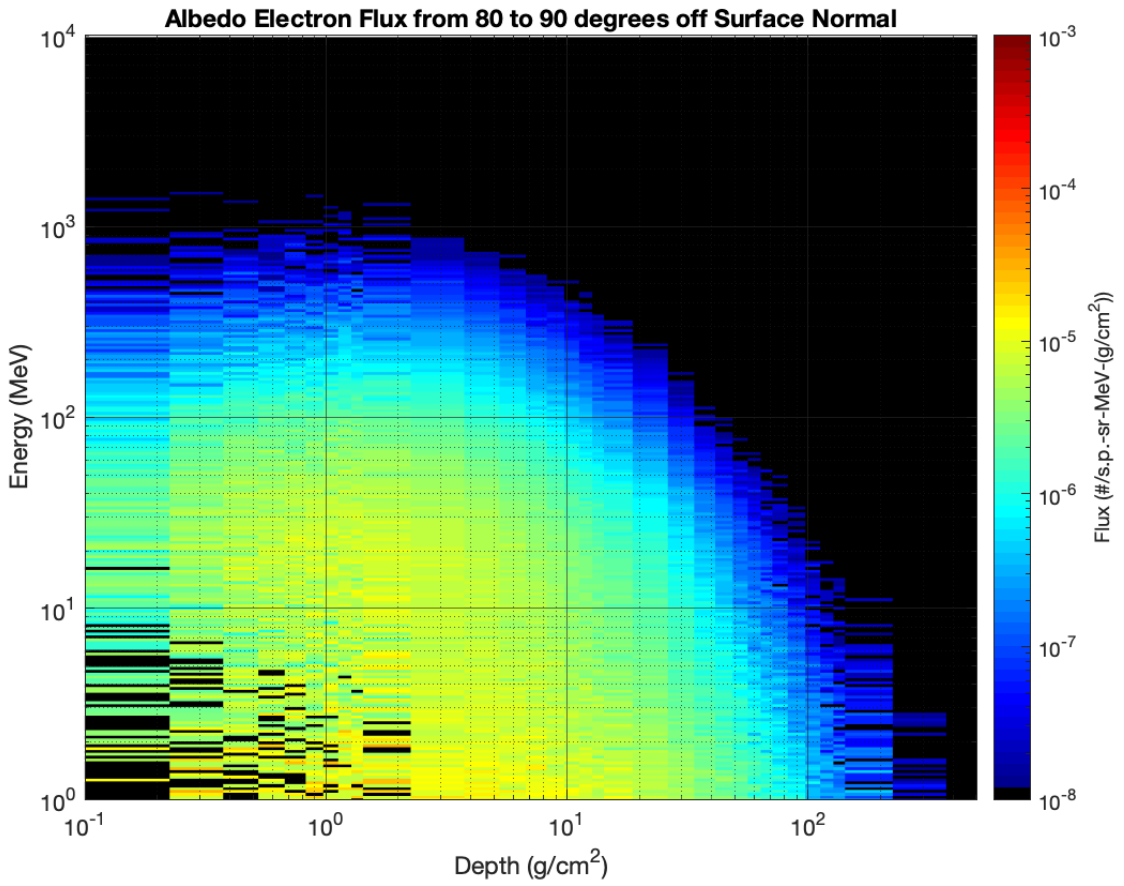

Figure D.27. Albedo electron flux as a function of energy and maximum production depth for angles between 80 and 90 degrees off surface normal.

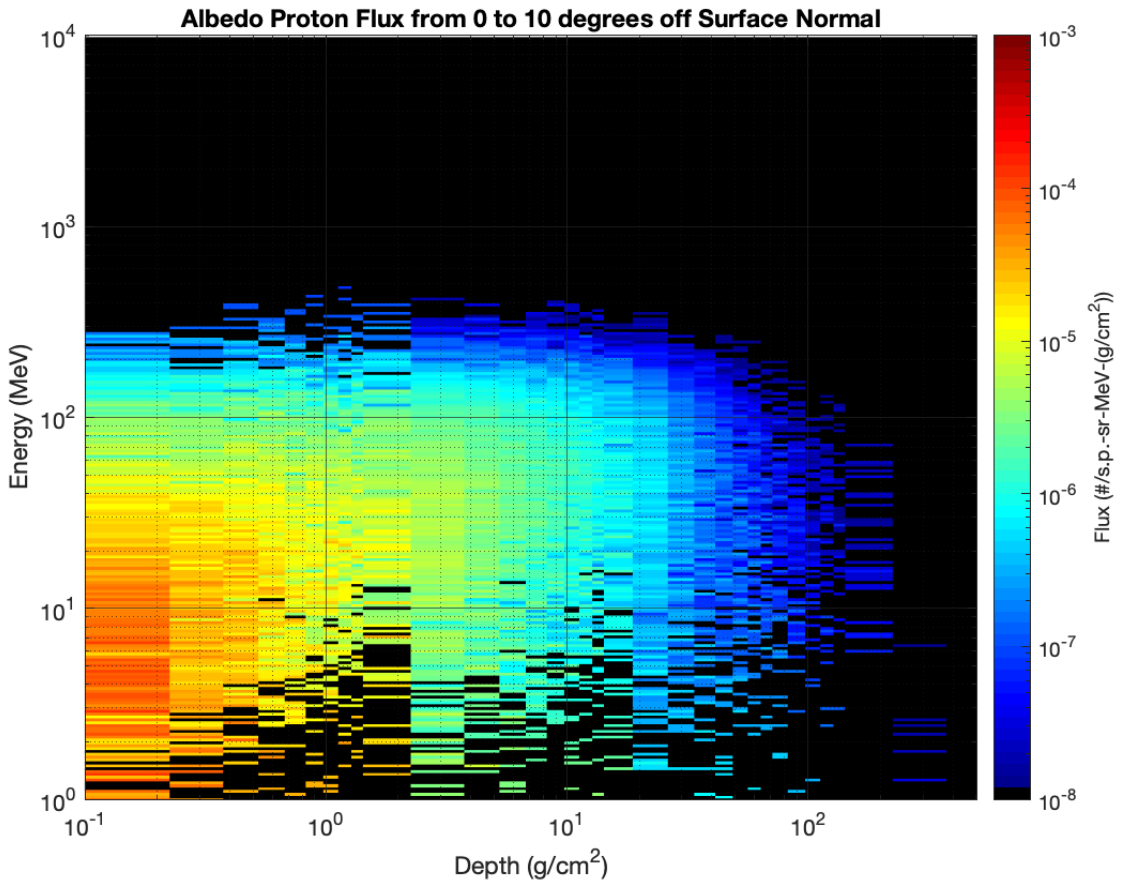

Figure D.28. Albedo proton flux as a function of energy and maximum production depth for angles between 0 and 10 degrees off surface normal.

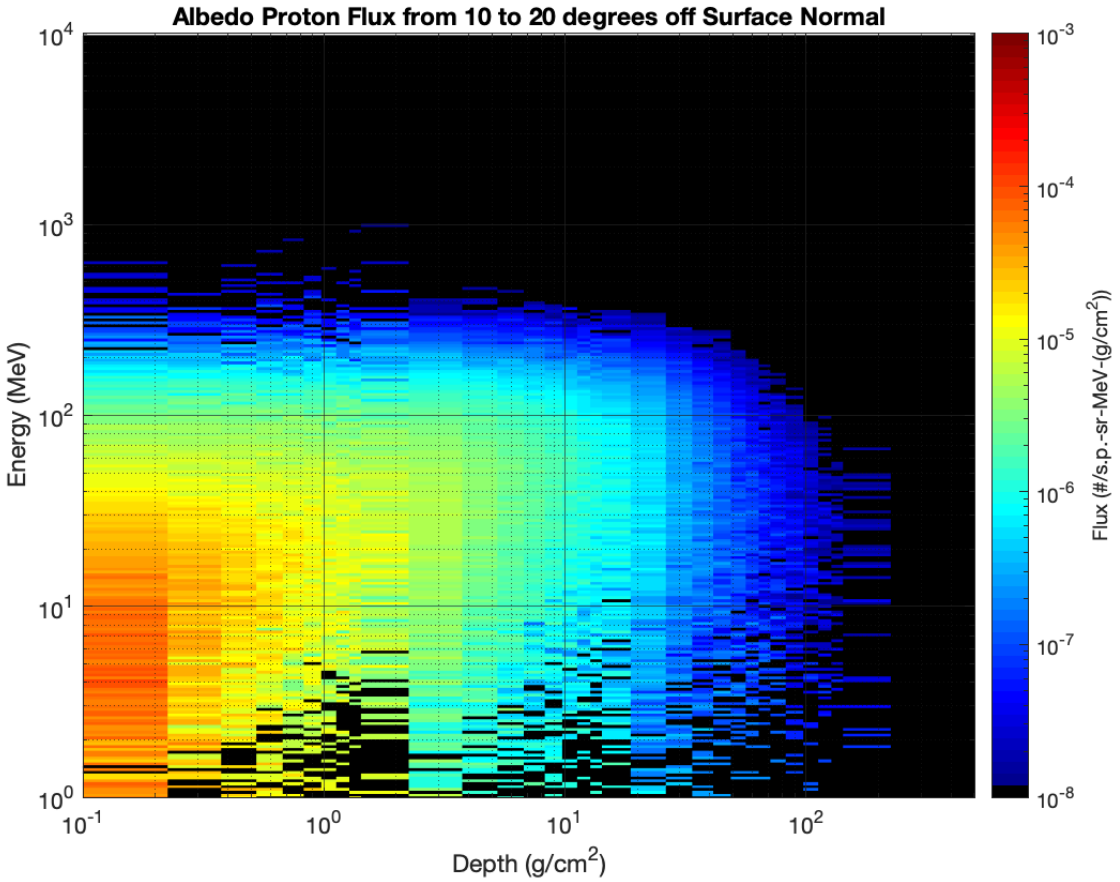

Figure D.29. Albedo proton flux as a function of energy and maximum production depth for angles between 10 and 20 degrees off surface normal.

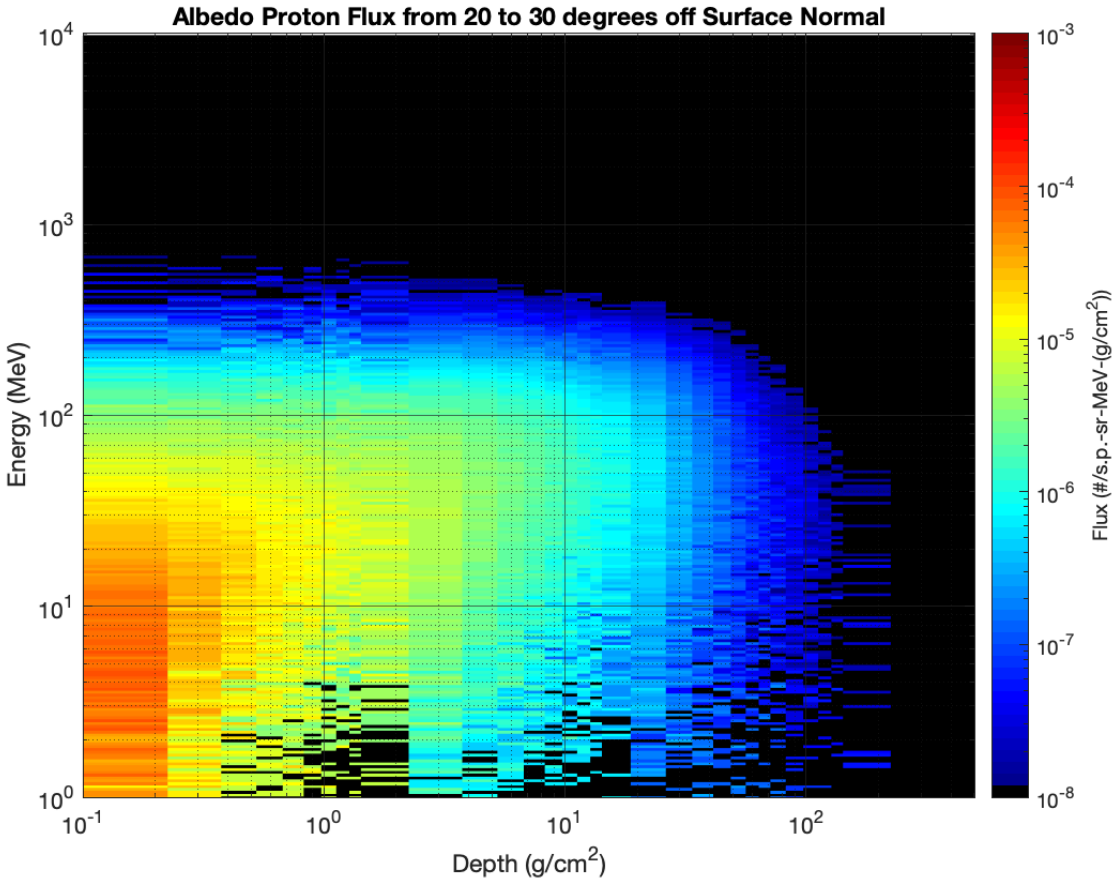

Figure D.30. Albedo proton flux as a function of energy and maximum production depth for angles between 20 and 30 degrees off surface normal.

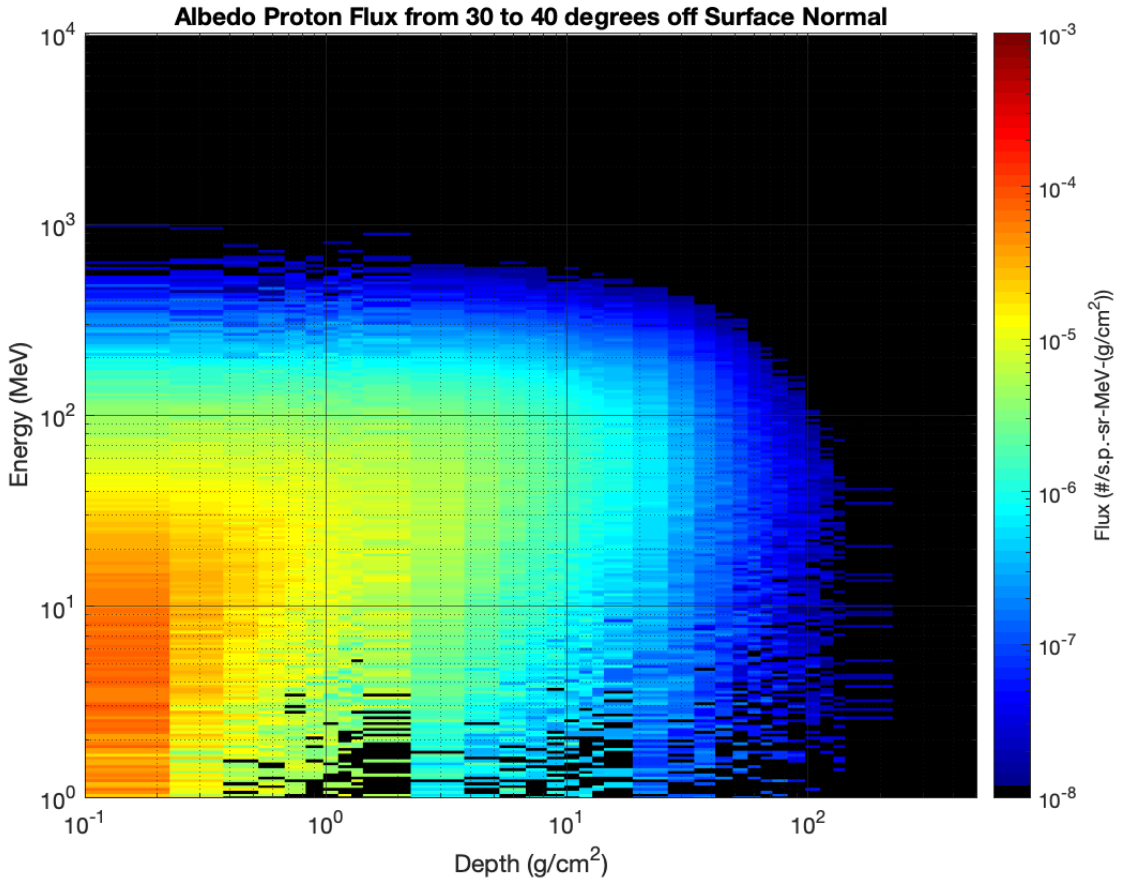

Figure D.31. Albedo proton flux as a function of energy and maximum production depth for angles between 30 and 40 degrees off surface normal.

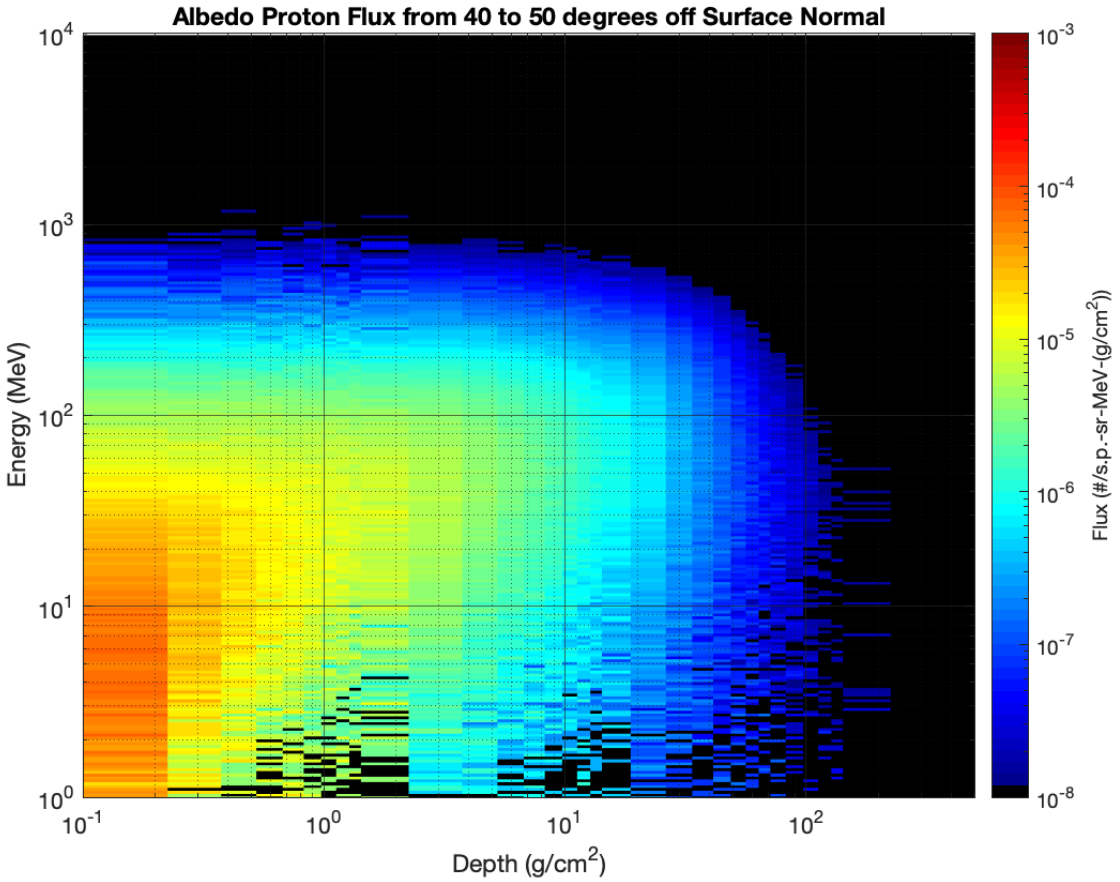

Figure D.32. Albedo proton flux as a function of energy and maximum production depth for angles between 40 and 50 degrees off surface normal.

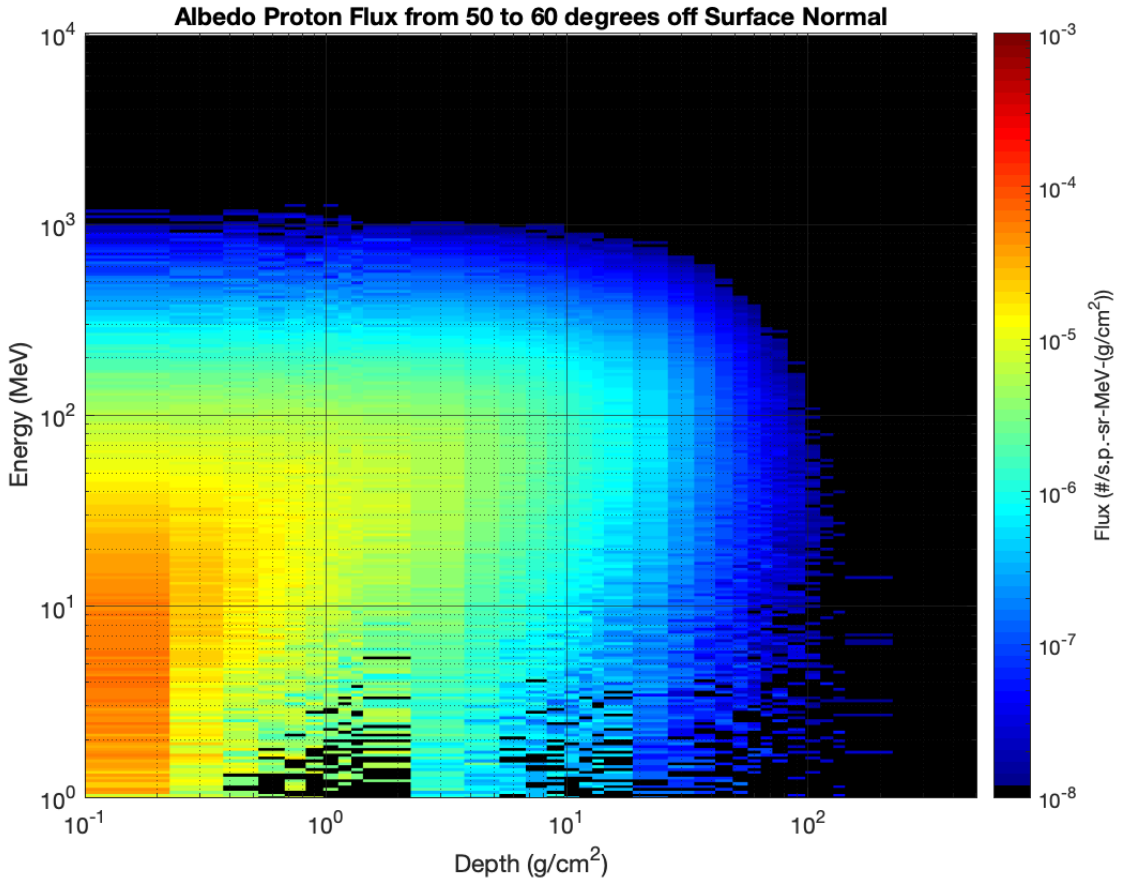

Figure D.33. Albedo proton flux as a function of energy and maximum production depth for angles between 50 and 60 degrees off surface normal.

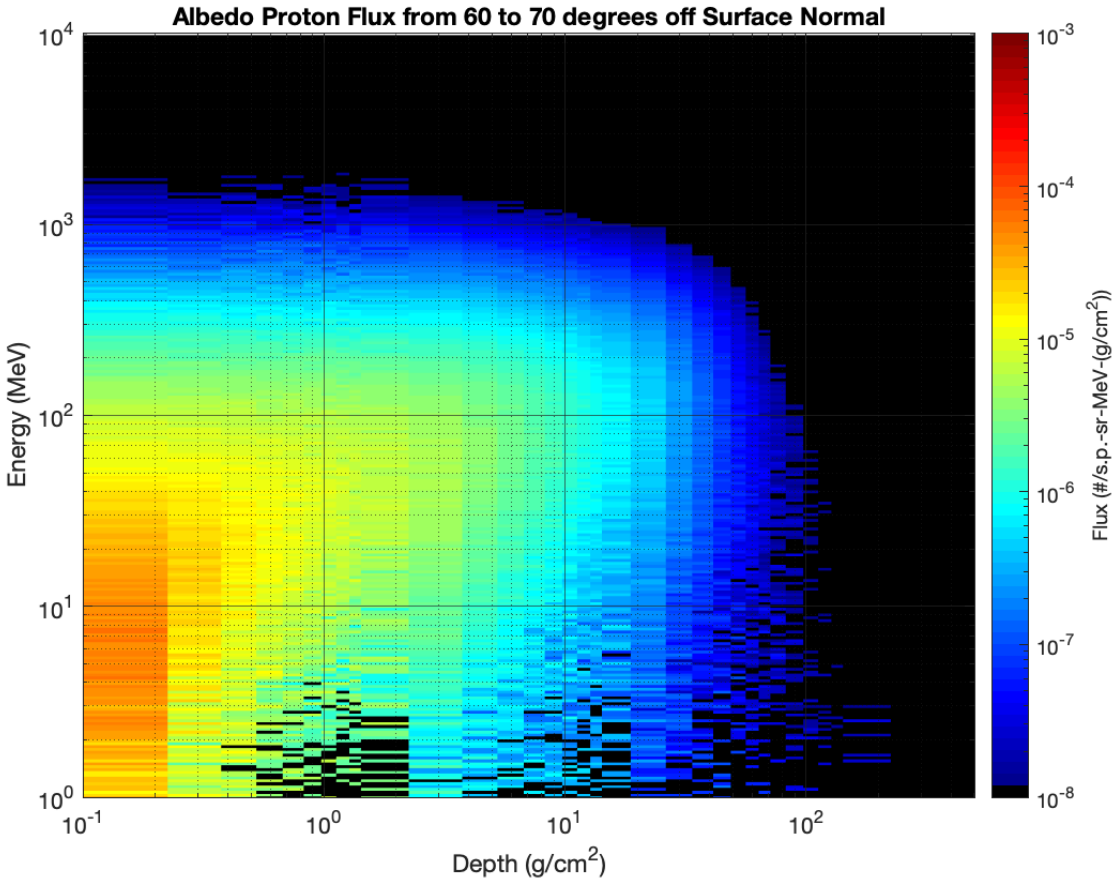

Figure D.34. Albedo proton flux as a function of energy and maximum production depth for angles between 60 and 70 degrees off surface normal.

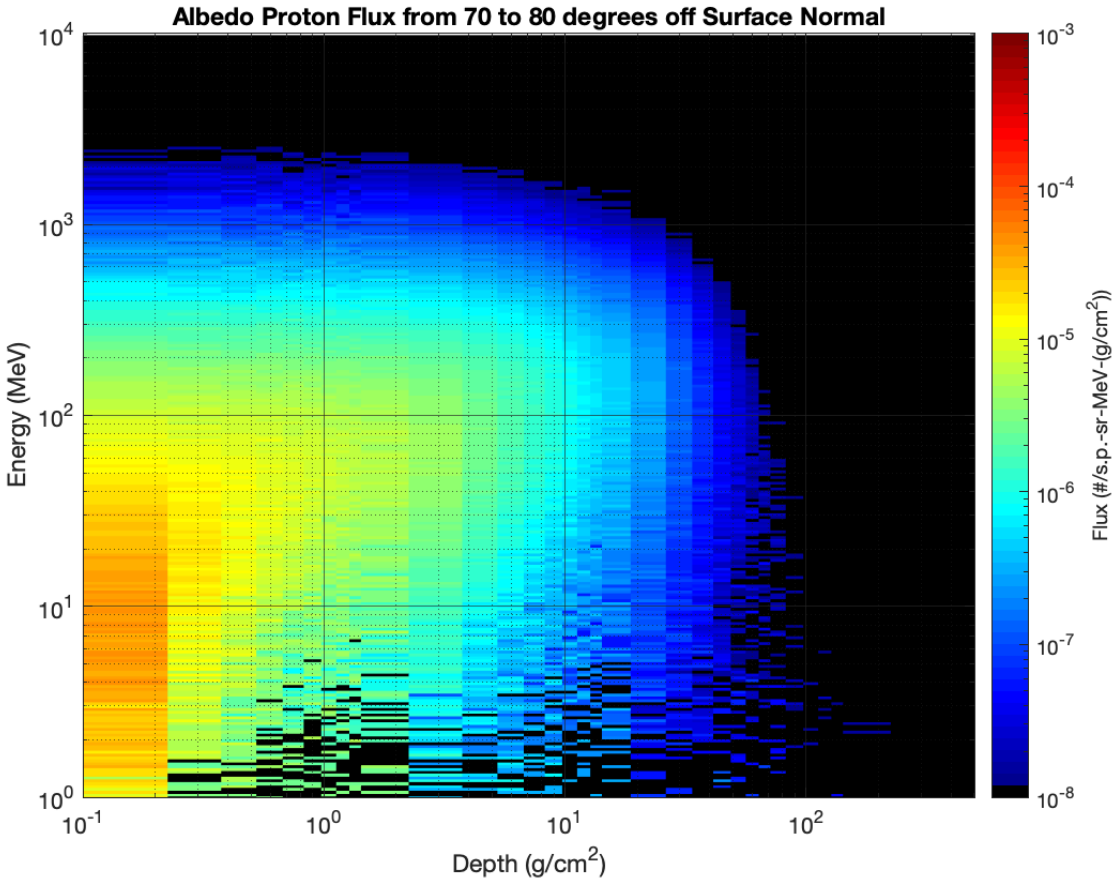

Figure D.35. Albedo proton flux as a function of energy and maximum production depth for angles between 70 and 80 degrees off surface normal.

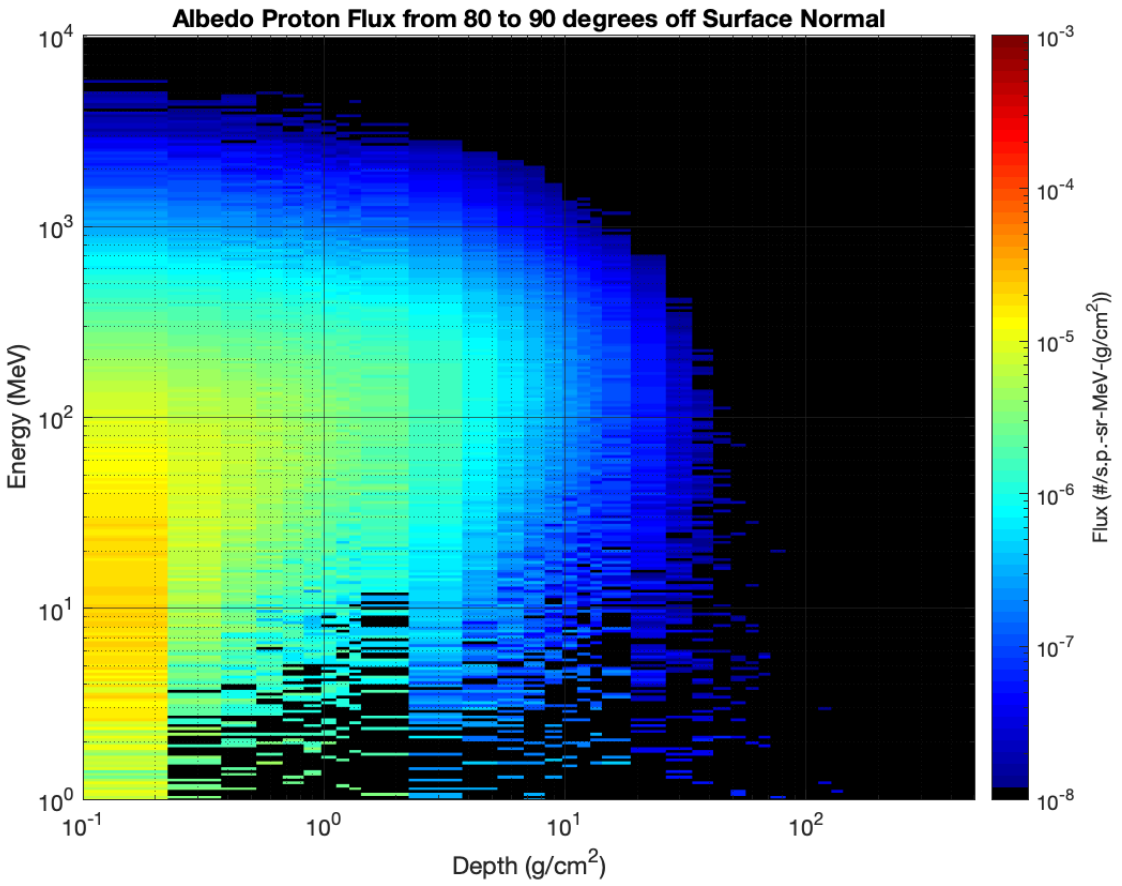

Figure D.36. Albedo proton flux as a function of energy and maximum production depth for angles between 80 and 90 degrees off surface normal.

VITA

Fahad Zaman was born in Kuwait City, Kuwait. He graduated from his high school in Kuwait in 2010 and then moved to Knoxville, Tennessee to complete his higher education. He received both a Bachelor of Science degree in Nuclear Engineering, Summa Cum Laude, in 2015, and a Master of Science degree in Nuclear Engineering in 2017 from the University of Tennessee.